NASA TECHNICAL MEMORANDUM

NASA TM X-3321

NASA TM X-3321

EXPERIMENTAL EVALUATION OF NACELLE-AIRFRAME INTERFERENCE FORCES AND PRESSURES AT MACH NUMBERS OF 0.9 TO 1.4

Daniel P. Bencze

Ames Research Center
Moffett Field, Calif. 94035

NATIONAL AERONAUTICS AND SPACE ADMINISTRATION · WASHINGTON, D. C. · MARCH 1977

1. Report No.	2. Government Accession No.	3. Recipient's Catalog No.
NASA TM X-3321		

4. Title and Subtitle	5. Report Date
EXPERIMENTAL EVALUATION OF NACELLE-AIRFRAME INTERFERENCE FORCES AND PRESSURES AT MACH NUMBERS OF 0.9 TO 1.4	March 1977
	6. Performing Organization Code
7. Author(s)	8. Performing Organization Report No.
Daniel P. Bencze	A-6344
	10. Work Unit No.
9. Performing Organization Name and Address	505-11-12
Ames Research Center Moffett Field, California 94035	11. Contract or Grant No.
	13. Type of Report and Period Covered
12. Sponsoring Agency Name and Address	Technical Memorandum
National Aeronautics and Space Administration Washington, D.C. 20546	14. Sponsoring Agency Code

15. Supplementary Notes

16. Abstract

Detailed interference force-and-pressure data were obtained on a representative supersonic transport wing-body-nacelle combination at Mach numbers of 0.9 to 1.4. The basic model consisted of a delta wing-body aerodynamic model with a length of 158.0 cm (62.2 in.) and a wingspan of 103.6 cm (40.8 in.) and four independently supported nacelles positioned beneath the model. The aerodynamic model was mounted on a six-component force balance and the left-hand wing was pressure instrumented. Similarly, each of the two right-hand nacelles was mounted on a six-component force balance housed in the thickness of the nacelle, while each of the left-hand nacelles was pressure instrumented. The nacelle support system provided the flexibility of varying the nacelle positions relative to the wing-body and to each other and controlling the mass flow through each nacelle.

The experimental program was conducted in the Ames 11- by 11-Foot Wing Tunnel at a constant unit Reynolds number of 9.8×10^6/m (3.0×10^6/ft). The primary variables examined included Mach number, angle of attack, nacelle position, and nacelle mass-flow ratio. Four different configurations were tested to identify various interference forces and pressures on each component. These included tests of the isolated nacelle, the isolated wing-body combination, the four nacelles as a unit, and the total wing-body-nacelle combination. Nacelle axial location, relative to both the wing-body and to other nacelles was the most important variable in determining the net interference among the components. Under the most favorable conditions, the net interference drag was equal to 50 percent the drag of four isolated nacelles at $M = 1.4$, 75 percent at $M = 1.15$, and 144 percent at $M = 0.90$. The overall interference effects were found to be rather constant over the operating angle-of-attack range of the configuration. The effects of mass-flow ratio on the interference pressure distributions were limited to the lip region of the nacelle and the local wing surface in the immediate vicinity of the nacelle lip. The net change in the measured interference forces resulting from variations in the nacelle mass-flow ratio were found to be quite small.

17. Key Words (Suggested by Author(s))	18. Distribution Statement
Transonic Aerodynamic interference Wing-body-nacelle	Unlimited STAR Category 02

19. Security Classif. (of this report)	20. Security Classif. (of this page)	21. No. of Pages	22. Price*
Unclassified	Unclassified	178	$7.00

*For sale by the National Technical Information Service, Springfield, Virginia 22161

"Page missing from available version"

SYMBOLS

A_{ac} nacelle aft balance cavity cross-sectional area

A_c nacelle capture area, πR_c^2

A_{fc} nacelle forward balance cavity cross-sectional area

A_{lip} nacelle internal lip cross-sectional area

A_{s1} first-order nacelle balance seal-force calibration constant

A_{s2} second-order nacelle balance seal-force calibration constant

A_{sf} nacelle internal-lip surface area

b wingspan, 103.6 cm (40.8 in.)

c wing chord

C'_A nacelle balance axial-force correction coefficient (table 5)

C_D drag coefficient, $\frac{\text{drag}}{q_\infty S}$

C_{D_N} nacelle drag coefficient, $\frac{\text{nacelle drag}}{q_\infty A_c}$

C_L lift coefficient, $\frac{\text{lift}}{q_\infty S}$

C_{L_N} nacelle lift coefficient, $\frac{\text{nacelle lift}}{q_\infty A_c}$

C_M pitching moment coefficient, $\frac{\text{pitching moment}}{q_\infty c_R S}$

C_{M_N} nacelle pitching moment coefficient, $\frac{\text{nacelle pitching moment}}{q_\infty L A_c}$

C_p pressure coefficient, $\frac{p - p_\infty}{q_\infty}$

c_R wing-body root chord, 71.99 cm (28.34 in.)

L nacelle length, 26.77 cm (10.54 in.)

L' theoretical nacelle length, 28.76 cm (11.32 in.)

L/D lift-to-drag ratio, $\frac{C_L}{C_D}$

M Mach number

MOC	method of characteristics
m/m_c	nacelle mass-flow ratio, $\frac{\text{mass flow}}{\rho_\infty V_\infty A_c}$
p	static pressure
q	dynamic pressure, $\frac{1}{2}\rho V^2$
R_c	nacelle capture (lip) radius
R_e	nacelle exit radius
R_{max}	maximum nacelle radius
$R_{N_{lip}}$	nacelle internal lip Reynolds number, based on local flow conditions and the distance from the nacelle lip to the balance seal
r	local nacelle radius
r'	boundary-layer recovery factor (table 5)
S	reference wing area, 0.412 m^2 (4.435 ft^2)
V	flow velocity
$\bar{X}$	length of NACA 1-series cowl
X	axial coordinate (model station) of wing-body configuration (fig. 2)
X_{ma}	axial coordinate of nacelle lip when the nacelle delta axial drive is at its most forward position
ΔX	axial position of the outboard nacelle lip relative to the inboard nacelle lip, $X_o - X_i$
x	local nacelle and local root-chord axial coordinate (figs. 3 and 4)
$\bar{Y}$	thickness of NACA 1-series cowl
Y	lateral coordinate of wing-body configuration (fig. 2)
y'	fraction of wing semispan, $\frac{Y}{(b/2)}$
ΔY	lateral postiion of the outboard nacelle centerline relative to the inboard nacelle centerline, $Y_o - Y_i$
Z	vertical coordinate of wing-body configuration (fig. 2)
z	local wing vertical coordinate

α	angle of attack
γ	ratio of specific heats, 1.4
δ_c	initial external cowl angle of the N_1 nacelle, 6.14° (fig. 4)
δ_β	final external boattail angle of the N_1 and N_2 nacelles, 9.74° (fig. 4)
θ	nacelle circumferential coordinate; 0° at top of the nacelle, looking downstream, clockwise is positive (fig. 5)
ρ	fluid density

Subscripts

ac	aft nacelle balance cavity
β	nacelle boattail
c	nacelle cowl lip
e	nacelle exit
fc	forward nacelle balance cavity
∞	free-stream value
I	interference quantity, measured value minus reference value
Iso	isolated condition
i,in	inboard nacelle
ℓ	wing lower surface
ℓe	wing leading edge
lip	nacelle lip
N	nacelle quantity
o,out	outboard nacelle
R	root chord
seal	nacelle balance seal
sf	skin friction
te	wing trailing edge

total	total quantity
u	wing upper surface

Superscripts

$(\bar{})$	average quantity

EXPERIMENTAL EVALUATION OF NACELLE-AIRFRAME INTERFERENCE FORCES AND PRESSURES AT MACH NUMBERS OF 0.9 TO 1.4

Daniel P. Bencze

Ames Research Center

SUMMARY

Detailed interference force-and-pressure data were obtained on a representative supersonic transport wing-body-nacelle combination at Mach numbers of 0.9 to 1.4. The basic model consisted of a delta wing-body aerodynamic model with a length of 158.0 cm (62.2 in.) and a wingspan of 103.6 cm (40.8 in.) and four independently supported nacelles positioned beneath the model. The aerodynamic model was mounted on a six-component force balance and the left-hand wing was pressure instrumented. Similarly, each of the two right-hand nacelles was mounted on a six-component force balance housed in the thickness of the nacelle, while each of the left-hand nacelles was pressure instrumented. The nacelle support system provided the flexibility of varying the nacelle positions relative to the wing-body and to each other and controlling the mass flow through each nacelle.

The experimental program was conducted in the Ames 11- by 11-Foot Wind Tunnel at a constant unit Reynolds number of 9.8×10^6/m (3.0×10^6/ft). The primary variables examined included Mach number, angle of attack, nacelle position, and nacelle mass-flow ratio. Four different configurations were tested to identify various interference forces and pressures on each component. These included tests of the isolated nacelle, the isolated wing-body combination, the four nacelles as a unit, and the total wing-body-nacelle combination. Nacelle axial location, relative to both the wing-body and to other nacelles was the most important variable in determining the net interference among the components. Under the most favorable conditions, the net interference drag was equal to 50 percent of the drag of the four isolated nacelles at $M = 1.4$, 75 percent at $M = 1.15$, and 144 percent at $M = 0.90$. The overall interference effects were found to be rather constant over the operating angle-of-attack range of the configuration. The effects of mass-flow ratio on the interference pressure distributions were limited to the lip region on the nacelle and the local wing surface in the immediate vicinity of the nacelle lip. The net change in the measured interference forces resulting from variations in the nacelle mass-flow ratio were found to be quite small.

Where applicable, comparisons were made with two available theoretical predictions; these included the equivalent body approach and a limited flow-field analysis based on the MOC. Although neither approach resulted in exceptional agreement with the measured results, both predicted the general trends and magnitude of the interference forces fairly well. The flow-field analysis, using the M.O.C. to predict the interference pressure distribution on the wing-body, yielded reasonable results at $M = 1.4$.

INTRODUCTION

To achieve a substantial increase in cruise speed of current subsonic transport aircraft, but avoid the overpressures associated with supersonic transport aircraft in the M = 2.0 to 3.0 range, recent efforts have been devoted to exploring the feasibility of a low supersonic transport aircraft which does not produce a noticeable overpressure at ground level (ref. 1). This is accomplished by taking advantage of the vertical temperature gradient in the atmosphere. Under the correct conditions, the cruise Mach number of an aircraft evaluated in terms of local speed-of-sound at ground level can be subsonic, although the cruise Mach number at altitudes is supersonic. Thus, a distinct shock wave cannot exist at ground level, eliminating the corresponding overpressures. The cruise Mach numbers for such aircraft vary from slightly greater than 1.0 to approximately 1.25 depending upon the exact atmospheric conditions. Furthermore, transport aircraft with high supersonic cruise Mach numbers could also fly within this Mach number range to eliminate the sonic boom problem while flying over populated areas.

Due to the inherently high drag and large interference effects associated with this range of cruise Mach numbers, the design of an efficient aircraft is critically dependent upon the integration of the various components. This is particularly true for the propulsion system design and integration, since the installed drag of the propulsion system must be included in the selection of the engine cycle to yield the most efficient aircraft. Preliminary studies (ref. 2) of the aerodynamic interference between the propulsion systems and airframe for a low supersonic transport have indicated that proper integration of the propulsion system can reduce the installed drag to less than one-half of the isolated propulsion system.

Presently, the aerodynamic analyses of the installation and integration of the propulsion system for such aircraft rely upon the equivalent body approach (ref. 3) or on limited flow-field analyses (refs. 2,4). The use of these methods has been substantiated (refs. 3,4) at the higher supersonic Mach numbers, however, little information is available at transonic and low supersonic Mach numbers. Therefore, an experimental program was formulated to obtain detailed interference data on a representative transport over this Mach number range. The principal objectives of this program were to evaluate the performance penalties associated with the propulsion system installation and operation and to acquire detailed force and pressure data to be used for the evaluation of the analytical techniques.

The wind-tunnel model consisted of a basic wing-body combination with four independently supported nacelles located beneath the model. Photographs of the model and support system installed in the Ames 11- by 11-Foot Wind Tunnel are shown in figures 1(a) and 1(b). Detailed force and pressure data were taken on both the wing-body combination and the individual nacelles. The primary variables were Mach number, angle of attack, nacelle position, and nacelle mass-flow ratio. The experimental program was conducted in the Ames 11- by 11-Foot Wind Tunnel over a Mach number range of 0.9 to 1.4. The unit

Reynolds number was held constant at 9.8×10^6/m (3.0×10^6/ft) over the Mach number range.

MODEL AND INSTRUMENTATION

Aero Model

The aerodynamic force model consisted of a delta wing-body combination. The general configuration is shown in figure 2, and was designated WB. The particular model was a 0.024-scale model of the final Boeing supersonic transport configuration (Boeing model SA1150). This model was selected because of its availability and because the general configuration represented a possible candidate for the type of transport aircraft under consideration. Although this particular configuration was not designed specifically for the transonic and low supersonic Mach number range, the large, highly contoured wing provided an ideal configuration for the investigation of detailed nacelle/wing interference forces and pressures.

The model had an overall length of 158.0 cm (62.2 in.) and a wingspan of 103.64 cm (40.8 in.). The wing is basically a delta wing with a leading-edge sweep of 50.5° and an inboard leading-edge extension with a sweep of 75.0°. The reference wing area and root chord are 0.412 m^2 (4.435 ft^2) and 71.99 cm (28.34 in.), respectively. The camber, twist, and thickness distribution were designed for a cruise Mach number of 2.7. The wing coordinates are tabulated in tables 1 and 2 and a detailed description of the wing and overall configuration is given in reference 5. To shorten the required nacelle support system (described in a later section), the horizontal and vertical tails were removed and the fuselage terminated at $X = 170.18$ cm (67.0 in.) for this test.

The model was supported by a six-component internal strain-gage balance. The moment center was located on the centerline of the model at $X = 134.44$ cm (52.92 in.) and at $Z = 12.80$ cm (5.04 in.), which corresponded to 62 percent of the reference root chord. The left-hand wing was modified to incorporate 126 static pressure orifices; 95 on the lower surface and 31 on the upper surface. The orifice locations are described in figure 3.

Nacelles

Two different nacelle geometries were tested and are described in figure 4. The basic nacelle configuration, designated N_1, was designed to produce low drag at low transonic Mach numbers while yielding a predictable flow field in the supersonic Mach number regime. The N_1 nacelle employed a sharp inlet lip and relatively long inlet and nozzle lengths which were equal to twice the inlet and nozzle diameters, respectively. The overall nacelle size was derived by using the engine and nacelle sizing procedures outlined in reference 6, and by assuming an engine bypass ratio of one and a cruise lift-to-drag ratio of 10, at a lift coefficient of 0.3. The nacelle had a capture

diameter of 4.32 cm (1.70 in.), a maximum diameter of 6.44 cm (2.54 in.), and a length, L, of 26.77 cm (10.54 in.). The external nacelle contours were defined using the following expressions for the forward and aft nacelle sections:

$$\frac{r}{R_{max}} = 1 - \left(1 - \frac{R_c}{R_{max}}\right)\left(1 - \frac{x}{x_{R_{max}}}\right)^{1.973}, \quad 0 \le x \le x_{R_{max}}$$

and

$$\frac{r}{R_{max}} = 1 - \left(1 - \frac{R_e}{R_{max}}\right)\left(\frac{L' - x}{L' - x_{R_{max}}}\right)^{1.508}, \quad x_{R_{max}} < x \le L'$$

where L' is the theoretical nacelle length, equal to 28.76 cm (11.32 in.). The exponents were dictated by the initial cowl and final boattail angles. The initial external cowl angle, δ_c, was selected to be the minimum value that would provide adequate nacelle thickness at the compressor face, while the final boattail angle, δ_β, was taken to be the average of the angles corresponding to conical and circular arc boattails. The specific values indicated in figure 4 for the N_1 nacelle were $\delta_c = 6.14°$ and $\delta_\beta = 9.74°$. To adequately support the nacelle while maintaining an unrestricted flow passage through the nacelle and support sting, the aft end of the nacelle was modified as illustrated in figure 4.

The second nacelle geometry, designated N_2, incorporated a slightly blunt lip as being more representative of an actual nacelle, reflecting the requirement for subsonic operation. The contours of the forward section of the N_2 nacelle ($0 \le x \le x_{R_{max}}$) corresponded to the NACA 1 series contours (ref. 7), with the cowl length X and cowl thickness Y equal to 19.49 cm (7.67 in.) and 0.98 cm (0.39 in.), respectively. The maximum diameter and aft portion of N_2 were identical to N_1. The overall nacelle contours are listed in figure 4.

Of the four individual nacelles supported beneath the wing-body model, the two on the left-hand side (looking upstream) were pressure instrumented and the two on the right-hand side were mounted individually on separate six-component internal strain-gage balances. Each of the pressure instrumented nacelles had 48 static-pressure orifices located in four rows equally spaced around the nacelles. Nacelle N_1 had 40 orifices on the external surface and 8 orifices located internally, while nacelle N_2 had 36 orifices located externally and 12 internally. The specific locations of the orifices are presented in figure 5.

The six component force balances used to support the right-hand nacelles were housed in the thickness of each nacelle. The balance is basically a two-shell flow-through force balance using four instrumented flexures located 90° apart at two axial locations, for a total of eight flexures. A schematic showing the balance installed within the contours of the N_1 nacelle is presented in figure 6. The moment center for each nacelle was located on the

centerline at x = 14.21 cm (5.59 in.). The balance was intended to measure only the aerodynamic forces on the external surface of the nacelle, however, for mechanical reasons it became necessary to include the aerodynamic forces on the initial 5.84 cm (2.30 in.) of the internal surface, as indicated in the schematic. This necessitated an additional balance correction which is discussed in a later section. To prevent flow through the balance cavity, thus ensuring a uniform pressure throughout the balance cavity, the metric and nonmetric components were bridged by a flexible rubber seal. The seal and its installation are detailed in figure 6. The seal was designed to produce negligible interference over the operating range of the balance and the expected pressure ratios across the seal. This was confirmed through detailed calibrations of the balance/seal combination with pressure ratios across the seal in excess of 3.0. To provide the necessary base area corrections for each nacelle, the pressure on the flow side of the seal were measured, as were the pressures in the forward and aft balance cavities. The pressure instrumentation is outlined in figure 6 and the balance corrections are described in the data reduction section.

Nacelle Support System

The nacelle support system was designed to independently support four nacelles beneath the wing-body combination while providing the flexibility of positioning the nacelles relative to both the wing-body combination and to each other. The support system also provided for the independent control and measurement of the mass flow through each nacelle. A schematic of the nacelle support system is presented in figure 7 and, as indicated earlier, figure 1(b) is a photograph of the support system mounted in the Ames 11- by 11-Foot Wind Tunnel.

The major components of the nacelle support system consisted of the main cross support, four vertical support and positioning units, and four flow-through nacelle stings and flow metering units. Eleven independent drives provided a three-dimensional nacelle positioning capability. These included two lateral drives which positioned the inboard and outboard nacelle pairs symmetrically about the vertical centerline. Four vertical drives were used to control the vertical position of the four nacelle stings. The axial position of each nacelle was controlled by two independent axial drive units. First, the main axial drive controlled the position of the main cross support and, hence, the position of all four nacelles as a single unit. Second, each nacelle sting had its own individual drive unit which allowed the position of each nacelle to be varied relative to the other three nacelles. Of the eleven drives, all were remotely controlled, except the four vertical drives which were manually operated. The maximum travel of each drive, relative to its midposition, is summarized in table 3 and the range of achievable nacelle positions, in the coordinate system of the wing-body model, is presented in table 4. A schematic drawing of possible nacelle positions is shown in figure 8.

Incorporated into each nacelle sting was a mass-flow control plug and appropriate pressure instrumentation to measure the flow through each nacelle. Each plug was remotely controlled. The pressure instrumentation consisted of a 16-tube total pressure rake (4 radial rakes, 4 probes per rake) and 4 exit static pressure orifices in each nacelle sting. The mass-flow characteristics of each nacelle sting were determined through static calibrations prior to installation in the wind tunnel. A final calibration was performed in the wind tunnel to account for the actual flow conditions at the flow exits.

DATA REDUCTION

Standard data reduction procedures were used to obtain the basic force and pressure data. The corrections applied to the nacelle balance forces, however, are dependent on the installation and require further discussion. Five separate corrections were applied to the measured nacelle axial-force balance readings to obtain the final aerodynamic data. The corrections, outlined in detail in table 5, included the pressure forces within the forward- and aft-balance cavities, on the forward lip cavity, across the balance seal, and the skin friction on the internal nacelle lip. The areas associated with each of these forces are identified in figure 6, and the specific values are given in table 5. The cross-sectional area associated with the forward- and aft-balance cavity forces and the forward lip forces were based on the physical geometry of the nacelles. The seal force was obtained through a calibration of the nacelle-balance system. The skin friction on the internal section of the nacelle from the lip to the seal was based on the average turbulent skin friction for this length. The skin-friction coefficient was calculated using the following relationship taken from reference 8:

$$C'_{A_{sf}} = \frac{\dfrac{0.455}{\left(\log_{10} R_{N_{lip}}\right)^{2.58}} - \dfrac{1050}{R_{N_{lip}}}}{1.0 + r' \dfrac{\gamma - 1}{2} M_{lip}^2} \tag{1}$$

where $R_{N_{lip}}$ and M_{lip} are the local values of Reynolds number and Mach number over the internal nacelle lip. The recovery factor, r', was taken to be 0.85. The term $1050/R_{N_{lip}}$ is a correction factor accounting for the initial laminar portion of the boundary layer. Typical values of these nacelle balance corrections, in terms of an axial-force coefficient as a function of nacelle mass-flow ratio, are presented in figure 9 for $M = 0.98$, 1.15, and 1.4. These corrections are subtracted from the balance axial-force coefficient to obtain the net nacelle-axial-force coefficient, which is also shown in figure 9 for reference. The dominant correction is the forward lip correction. The forward- and aft-balance cavity corrections tend to cancel each other, with their sum representing the base area correction associated with the clearance between the nacelle and support sting. The seal correction represents the other significant correction, while the skin friction correction is small and has little dependence upon the inlet mass-flow ratio.

It should be noted that, at $M = 1.4$, the discontinuity in the balance corrections at a mass-flow ratio of 1.0 is associated with the transition from local supersonic flow within the nacelle duct to subsonic flow.

TEST PROCEDURES

To ensure a turbulent boundary layer over the wing-body combination and nacelles, boundary-layer transition strips were applied to each of these components. The strips consisted of glass beads with a diameter range of 0.0119 to 0.0142 cm (0.0049 to 0.0058 in.). The transition strips, each 0.159 cm (0.0625 in.) wide, were located on the fuselage 3.71 cm (1.5 in.) downstream of the nose, on the upper and lower surfaces of the wing 1.91 cm (0.75 in.) behind and parallel to the wing leading edge, and on the nacelles 2.54 cm (1.00 in.) downstream of the nacelle lip. Sublimation tests using fluorene ($C_{13}H_{10}$) were conducted which validated that the boundary layer was tripped at the transition strip. Since only incremental results describing the interference forces and pressures were of interest, no attempt was made to establish or correct the results for the grit drag caused by the transition strips.

CONFIGURATIONS

To identify the various interference forces and pressures, tests of four different configurations were required. These included tests of the isolated nacelle, the isolated wing-body combination, the four nacelles as a unit, and the combination of the four nacelles and the wing-body.

The isolated nacelle forces and pressures were obtained by testing the two outboard nacelles with the two inboard nacelles and nacelle stings removed. To eliminate or minimize any interference between these two nacelles, they were positioned at their maximum outboard positions and staggered relative to each other. A maximum separation distance of 72.2 cm (24.5 in.) laterally and 20.3 cm (8.0 in.) axially was achieved. To determine whether the downstream nacelle was interfering with the upstream nacelle, force data were taken on the upstream nacelle as the position of the downstream nacelle was varied. The effects of the position of the downstream nacelle on the lift, drag, and pitching moment of the upstream nacelle are shown in figure 10 for the range of Mach numbers tested. The results are presented in terms of the increments in these forces relative to those measured with the downstream nacelle in its most aft position. Only at $M = 0.98$ do any interference effects appear noticeable on the upstream nacelle when the downstream nacelle is in its most aft position. In this case, it appears the axial force is reduced slightly as a result of the compression generated by the downstream nacelle impinging on the aft section of the upstream nacelle.

To accurately determine the interference effects between the wing-body and the nacelles, there must be no appreciable interference between the

nacelle support system and the wing-body combination that could be interpreted as aerodynamic interference between the components of interest. To assess the effects of the nacelle support system on the wing-body forces, the wing-body combination was tested with the nacelle support system mounted behind the model, but with all four nacelles and nacelle stings removed. The effects of the support system position on the wing-body lift, drag, and pitching moment at zero angle of attack are shown in figure 11 for the range of Mach numbers tested. For $M \geq 1.10$, the support system has very little effect for support positions corresponding to nacelle positions greater than X_{ma} = 111.76 cm (44 in.). For nacelle positions further forward than this, the interference effects of the support system become quite large. At $M = 0.98$, the interference effects of the support system are significant over the entire range of support positions, while at $M = 0.90$, the interference effects are minimal only at the extreme aft position of the support system. The effects of the nacelle support system position on the overall longitudinal aerodynamic characteristics of the wing-body combination are shown in figure 12 for $M = 1.4$ and 1.15. At $M = 1.4$, the longitudinal characteristics are essentially independent of the position of the support system, while at $M = 1.15$, the support system significantly alters these characteristics when positioned at its most forward location, X_{ma} = 10.16 cm (40 in.). In any area where the interference effects of the support system on the wing-body are significant, the data associated with these positions are judged questionable and hence, are not presented.

The actual interference data were obtained using the last two configurations: the four individual nacelles as a unit and the combination of the four nacelles and the wing-body. Photographs of these two configurations are presented in figure 1. Tests of the four individual nacelles identified the mutual nacelle/nacelle interference effects, while the final wing-body-nacelle configuration yielded the mutual wing-nacelle interference. A list of the specific configurations tested and their designations are given in table 6.

RESULTS AND DISCUSSIONS

The results have been divided into the following four major areas: (1) the isolated nacelle characteristics, (2) the isolated wing-body characteristics, (3) the nacelle-nacelle interference, and (4) the wing-body-nacelle interference. In each area, the effects of Mach number, angle of attack, nacelle mass-flow ratio, and relative position of the various components on both the force and pressure data are presented. In addition, where applicable, limited comparisons are made with various theoretical predictions of the interference forces and pressures. A more complete documentation of the actual wind-tunnel data is contained in references 9 and 10.

Isolated Nacelle Characteristics

The effects of nacelle mass-flow ratio on the nacelle drag coefficients of the N_1 and N_2 nacelles are presented in figure 13 for the range of

Mach numbers tested. The drag coefficient presented here represents the net force on the external surface of the nacelles. However, in the case of the N_2 nacelle, it also includes the pressure force on the internal cowl lip. This latter force is not present on the N_1 nacelle, since this nacelle has essentially a sharp lip, and, hence, has no internal cowl lip area. Both nacelles produce considerable cowl suction at lower mass-flow ratios, thereby reducing the drag of the nacelle. Generally, this reduction in nacelle drag with reduced mass-flow ratio increases with decreasing Mach number. At subsonic Mach numbers and at low mass-flow ratios, the net drag on the nacelles is negative which actually represents a thrust on the nacelle surface. Using these data and the procedure outlined in reference 11 to calculate the additive drag, the net spillage drag for the N_1 nacelle was obtained and is presented in figure 14. This net spillage drag is equal to drag on the nacelle itself, plus the additive drag minus the drag at a reference mass-flow ratio, which, in this case, was chosen to be 1.0. For the lower Mach numbers, the drag at a mass-flow ratio of 1.0 was obtained by extrapolating the available data, presented in figure 13, to a mass-flow ratio of 1.0. In terms of the actual spillage drag, the drag of the nacelle is always positive. The increase in drag with reduced mass-flow ratio is less at the lower Mach numbers, reflecting the lower additive drag and the greater levels of cowl suction that exist at these lower Mach numbers. Comparable spillage drag results were not computed for the N_2 nacelle because the location of the stagnation point on the nacelle lip was not precisely known and comparable additive drag results could not be computed.

The reference drag, defined to be the drag of the nacelle at a mass-flow ratio of one and associated with the spillage drag for the N_1 nacelle, is presented in figure 15 as a function of Mach number. These results are compared to various theoretical predictions of the nacelle drag. The nacelle skin friction drag was computed by assuming turbulent flow over the entire nacelle. The skin-friction coefficient was obtained from the formulation given in reference 12. Three predictions for the nacelle wave drag are given. The method of characteristics results were obtained from the computer program described in reference 13. Since this approach required that the entire flow field be supersonic, only predictions at the high Mach numbers were obtained. The equivalent-body results were obtained by the method described in reference 3, while the results based on the small-disturbance technique were obtained from a computer program based on the analysis of reference 14. At the higher Mach numbers, the best agreement between the predicted and measured values is obtained from the method of characteristics. At the lower supersonic Mach numbers, the small-disturbance technique yields the better agreement. In addition, the results based on the small-disturbance approach reflect the overall trends with Mach number better than those based on the equivalent body approach.

The nacelle surface pressure distributions for the N_1 nacelle over the Mach number range tested are given in figure 16, in terms of the average pressure coefficient along the length of the nacelle. These data correspond to the highest mass-flow ratios achievable at each Mach number. The specific mass-flow ratio for each Mach number is noted in the figure. Applicable theoretical predictions from the method of characteristic and the

small-disturbance technique are also presented. The pressure distributions are similar at all Mach numbers. The initial compression on the forward portion of the nacelle is followed by a slow expansion to a nearly constant pressure at the maximum diameter. In all cases, a rapid expansion exists over the aft portion of the nacelle. At supersonic Mach numbers, the low-pressure region extends to nearly the trailing edge of the nacelle; while subsonicly, the presence of an embedded shock wave downstream of the maximum diameter of the nacelle is quite evident. At $M = 1.4$, fairly good agreement is achieved between the data and both theoretical predictions, with the small-disturbance approach giving slightly better results. However, better agreement between the measured and predicted levels of drag is achieved using the method of characteristics as illustrated in figure 15. This discrepancy is probably due to the combined inaccuracies involved in the prediction of both the skin-friction and wave-drag components, rather than a discrepancy between the wave drag calculated using either theoretical approach. At $M = 1.15$, agreement between the measured and predicted pressure distributions is slightly less than at $M = 1.4$. Over the forward portion of the nacelle, it appears that the flow separates from the cowl lip and then reattaches at approximately $x/R_c = 3.0$. In addition, the expansion of the flow over the aft portion of the nacelle is delayed slightly relative to that obtained at the higher Mach numbers and from the theoretical predictions.

The effects of mass-flow ratio on the N_1 nacelle surface pressure distribution at $M = 1.4$, 1.15, 0.98, and 0.90 are shown in figure 17. Reductions in mass-flow ratio cause a decrease in the local pressures on the forward section of the nacelle. This accounts for the decrease in drag with reduced mass-flow ratio illustrated in figure 13. At all Mach numbers, variations in m/m_c affect only the surface pressure distributions on approximately the forward third of the nacelle, with little if any, effect on the aft two thirds of the nacelle. Similar results are shown in figure 18 for the N_2 nacelle. The internal pressures are also presented for the N_2 nacelle to help interpret the pressures in the region of the lip. Substantial negative pressures are generated in the region of the lip at the lower mass-flow ratios with a rather gentle recompression at all Mach numbers except at 0.90. In this case, the flow recompresses quite rapidly immediately downstream of the lip. This is reflected in the drag versus mass-flow characteristics of the N_2 nacelle that are presented in figure 13(b). Note, the slope of the drag versus mass-flow curve at $M = 0.90$ is slightly less than at the other Mach numbers.

The longitudinal aerodynamic characteristics of lift, drag, and pitching moment of the N_1 nacelle are shown in figure 19 for $M = 1.4$, 1.15, and 0.98.

Isolated Wing-Body Characteristics

As discussed in the test procedure section, the isolated wing-body combination was tested with the nacelle support system mounted behind the model. The longitudinal characteristics of the wing-body combination at $M = 1.4$ and 1.15 were presented previously in figure 12 for various nacelle support system positions. In addition, the effects of the support system position on the

lift, drag, and pitching moment at nominally zero angle of attack are shown in figure 11. As noted earlier, in those areas where substantial interference exists between the support system and the wing-body combination, the data were judged questionable and are not presented. A summary of the longitudinal characteristics at M = 1.4, 1.15, and 0.90 are presented in figure 20 for the most aft position of the nacelle support system.

Nacelle-Nacelle Interference

The nacelle-nacelle interference drag characteristics are presented in terms of the net interference drag normalized by the corresponding isolated drag of the nacelles. For the individual nacelles, the interference drag is given by

$$\frac{C_{D_{N_I}}}{C_{D_{N_{Iso}}}} = \frac{C_{D_N} - C_{D_{N_{Iso}}}}{C_{D_{N_{Iso}}}} = \frac{C_{D_N}}{C_{D_{N_{Iso}}}} - 1.0$$

while for the four nacelles the interference drag is

$$\frac{C_{D_{N_I}}}{4C_{D_{N_{Iso}}}} = \frac{2\left(C_{D_{N_I}} + C_{D_{N_o}}\right) - 4C_{D_{N_{Iso}}}}{4C_{D_{N_{Iso}}}} = \frac{C_{D_{N_I}} + C_{D_{N_o}}}{2C_{D_{N_{Iso}}}} - 1.0$$

The isolated drag of the N_1 and N_2 nacelles corresponded to the values at the maximum measured mass-flow ratio as indicated in figures 13(a) and (b), respectively.

The net interference drag among the four N_1 nacelles as a function of the position of outboard nacelle relative to the inboard nacelle is presented in figure 21 for M = 1.4, 1.15, 0.98, and 0.90. A schematic showing the relative positions of the nacelles is included in figure 21. The interference drag of the individual inboard and outboard nacelles, corresponding to the results in figure 21, are presented in figure 22. At M = 1.4, the net interference drag among the four nacelles is small over the entire range of nacelle positions tested. The interference effects among the four nacelles increases considerably as the Mach number is decreased. The net interference drag at M = 1.15 is primarily unfavorable, while at M = 0.98 and 0.90, significant levels of favorable interference drag are achieved. Because of the possible interference effects of the tapered aft section of the inboard nacelle sting on the outboard nacelle, the data corresponding to the most aft nacelle positions (maximum $\Delta X/R_c$) for these two lower Mach numbers may be questionable.

The increase in the interference drag with decreasing Mach number is more strongly illustrated in the interference characteristics of the individual nacelles, shown in figure 22. At all Mach numbers, the interference drag on

the inboard nacelle tends to be of one sign while the interference drag on the outboard nacelle tends to be of the opposite sign. The net interference drag of the four nacelles corresponds to one-half the sum of these two values. At $M = 1.4$, the interference drag on the inboard and outboard nacelles tend to cancel one another, resulting in little net interference drag among the four nacelles. The interference drag on the individual nacelles at the lower Mach numbers is quite large with the interference effects being generally highly favorable on the outboard nacelle and highly unfavorable on the inboard nacelle. For example, in the case of the outboard nacelle at $M = 0.98$, the most favorable interference occurs at $\Delta X/R_c = 5.0$ and corresponds to approximately 0.90 of the isolated nacelle drag. However, the unfavorable interference on the inboard nacelle is 0.66 of the isolated nacelle drag, yielding only a net favorable interference among all four nacelles equal to

$$\frac{C_{D_{N_I}}}{4C_{D_{N_{Iso}}}} = -0.12$$

as indicated in figure 21.

The interference pressure distributions associated with the force data presented in figures 21 and 22 on both the inboard and outboard nacelles at $\Delta X/R_c = 0.0$, 4.71, and 9.42 are shown in figures 23, 24, and 25, respectively. The results are presented in terms of the interference pressure coefficient

$$C_{P_I} = C_P - C_{P_{Iso}}$$

where C_P is the local pressure coefficient and $C_{P_{Iso}}$ is the average isolated nacelle pressure presented in figure 16. Both the average interference pressure coefficient $\overline{C_{P_I}}$ and the individual interference pressure coefficients at $\theta = 0°$, 90°, 180°, and 270° are presented. To aid in interpreting the interference pressure distributions, the corresponding distributions of the local average interference drag coefficient

$$\overline{2C_{P_I}} \frac{r}{R_c} \frac{dr}{dx}$$

are presented in figure 26. These data were faired realizing the value of the local drag coefficient must be zero at the maximum diameter of the nacelles where

$$\frac{dr}{dx} = 0 \quad \text{at} \quad \frac{x}{R_c} = 9.02$$

As the outboard nacelle is positioned farther aft of the inboard nacelle, the shift in both the local interference forces and pressures aft on the inboard nacelle and forward on the outboard nacelle is quite evident. In

addition, the influence of the large negative slopes on the aft portion of the nacelle is significant, as reflected by the fact that the local forces being generated in this region of the nacelle are larger than the local forces being generated on the forward portion.

To assess how accurately these distributions of local drag coefficient represent the actual interference forces, these distributions were integrated over L. This required the data to be extrapolated to the forward and aft ends of the nacelle. These extrapolations are shown in figure 26. A comparison of the interference forces obtained from the force measurements and from the integration of the average interference pressure distributions is presented in figure 27. Although, the quantitative agreement between the two is less than desired, there is a good qualitative agreement between the two results, which indicates that the distribution of the local interference drag coefficient fairly accurately represents the interference effects between the nacelles. The discrepancy between the two results is probably due to the rather coarse definition of the pressure distributions and to the extrapolations to the nacelle lip and trailing edge. In addition, any skin-friction drag variations caused by the interference effects are not reflected in the integration of the interference pressure distribution.

The effects of nacelle lateral position on the nacelle-nacelle interference are illustrated in figure 28. The net interference drag of the four nacelles is presented as a function of the axial position of the outboard nacelles relative to the inboard nacelles for three different lateral nacelle positions. In general, the magnitude of the interference effects, both favorable and unfavorable, tend to increase as the lateral separation of the inboard and outboard nacelles is reduced. This increase is due to both the change in position of the nacelles relative to the interference pressure field and the greater intensity of this pressure field near the generating body.

To illustrate these effects more clearly and to generalize the results, the individual inboard and outboard nacelle interference drags are shown in figure 29 as a function of $(\Delta X - \Delta Y\sqrt{M_\infty^2 - 1})/R_c$. Here, ΔX is the axial distance and ΔY is the lateral distance of the outboard nacelle relative to the inboard nacelle. This presentation, which uses the Mach lines as a coordinate, eliminates the interference-force variations that result from changes in the position of the nacelles relative to the pressure field generated by the adjacent nacelle on the same side of the model. Variations in the interference drag at a constant value of $(\Delta X - \Delta Y\sqrt{M_\infty^2 - 1})/R_c$ are then attributable to variations in the intensity of the interference pressure field or to the interference effects of the nacelles on the opposite side of the model. At $M = 1.4$, the theoretical interference drag on a single nacelle based on an isolated nacelle pair is also presented for each of the three lateral positions. The theoretical results were obtained from the M.O.C. program described in reference 13. The program was used to generate the pressure field at the nacelle location; this pressure distribution was then integrated over the surface of the nacelle to obtain the interference drag. The agreement between the data and the predicted results is fairly good, especially for negative values of $(\Delta X - \Delta Y\sqrt{M_\infty^2 - 1})/R_c$. Under these conditions, the interference effects of the nacelles on the opposite side of the model are small or

nonexistent, thus the data essentially corresponds to the interference of an isolated nacelle pair and should agree with the predicted results. For near zero and positive values of $(\Delta X - \Delta Y\sqrt{M_\infty^2 - 1})/R_c$, there is more scatter in the data and less agreement with the analytical results. For these nacelle positions, the larger variations in the interference forces at a constant value of $(\Delta X - \Delta Y\sqrt{M_\infty^2 - 1})/R_c$ are primarily due to variation in the intensity of the interference pressures as a function of lateral position, while the disagreement between the data and the predicted results is believed to result from the interference effects of the nacelles on the opposite side of the model. The variations in the intensity of the interference pressure field are illustrated in figure 30 in the form of the interference pressure distributions and the corresponding distributions of the local interference drag coefficient on the outboard nacelle. The results are shown for three lateral nacelle positions but for a nearly constant value of $(\Delta X - \Delta Y\sqrt{M_\infty^2 - 1})/R_c$ equal to approximately 1.0. At the closer lateral spacings, the interference pressures, in terms of $\bar{C}_{p_I}$ are greater in both the positive and negative directions over the length of the nacelle. These greater interference pressures result in increases in the local drag coefficient and, ultimately, in higher levels of interference drag. As noted in figure 30, the actual interference drag obtained from the direct force measurements agrees well with the integration of the interference pressure distributions. Thus, these results illustrate that variations in the intensity of the interference flow field caused by variations in lateral nacelle separation can have a significant effect on the interference drag among the nacelles.

The results at $M = 1.15$ follow the same general trend as the results at $M = 1.4$. However, because of the greater interference of the nacelles on the opposite side of the model at this lower Mach number, there is more scatter over the entire range of nacelle positions. The data at $M = 0.98$ have been plotted in the same fashion, but assuming the term $\Delta Y\sqrt{M_\infty^2 - 1}$ to be equal to zero. These results show the same characteristics as the higher Mach number data, but at greater magnitudes, especially in the region of favorable interference. The effects of the variations in the intensity of the interference pressure field with lateral nacelle separation are also evident at $M = 0.98$. At the closer lateral nacelle spacings, both the favorable and unfavorable interference drag is greatest over the entire range of nacelle positions tested. As the lateral spacing is increased the interference effects are reduced in magnitude.

Figure 31 presents a comparison between the measured and predicted nacelle-nacelle interference drag among the four nacelles at $M = 1.4$ and 1.15. At $M = 1.4$, both the equivalent body approach and the method of characteristics were used to predict the results, while at $M = 1.15$ only the equivalent body approach was applicable. The method of characteristics was used to predict the interference drag on each nacelle caused by the remaining three nacelles. Each nacelle pair analyzed was assumed to be an isolated pair and the effects of any intervening nacelle was neglected. Both methods predict the general magnitude and trends of the data. At $M = 1.4$, the results based on the M.O.C. appear to agree better with the test results than those based on the equivalent body approach.

By using the M.O.C. at $M = 1.4$, the interference pressure distribution on the nacelles can be estimated. Typical results are shown in figures 32 and 33. These results were obtained by summing the individual interference pressure fields generated by each of the remaining three nacelles at the location of the nacelles being analyzed. Any intervening nacelles were assumed to be transparent to an intersecting pressure disturbance. In figure 32, the average interference pressure on the nacelles is compared to the analytical results, while figure 33 compares the corresponding individual interference pressures at $\theta = 0°$, 90°, 180°, and 270° to these predictions. In the case of the average interference pressures, the agreement between the two sets of results is fair. The measured pressure rises tend to be smeared out because of the averaging of the four pressures around the nacelle. Hence, the agreement in these areas tends to be the poorest. In the expansion region with the smaller pressure gradients, the agreement between the predicted and measured results is considerably better. By comparing the individual interference pressures to the predicted results, the best agreement is obtained at the top and bottom of the nacelle ($\theta = 0°$ and 180°) where there is no reflection of the pressure field or blocking of it by the nacelle itself.

The effects of nacelle mass-flow ratio on the net interference drag of the four nacelles are shown in figure 34 for $M = 1.4$, 1.15, and 0.98 and the nacelle position indicated. The results are plotted as a function of the average mass-flow ratio of the nacelles. The reduction in nacelle mass-flow ratio at all Mach numbers had little effect on the net interference drag of the four nacelles. The effects of mass flow changes, therefore, appear to be localized, affecting only the individual nacelles.

Wing-Body-Nacelle Interference

Force data — The overall longitudinal aerodynamic characteristics of the WBN_1N_1 configuration are presented in figures 35, 36 and 37. For $M = 1.4$ and 1.15, the results are presented at two nacelle positions, $X_{in} = X_{out} = 142.24$ cm (56 in.) and 121.92 cm (48 in.), while the results at Mach number 0.9 are presented only at $X_{in} = X_{out} = 142.24$ cm (56 in.). The spanwise positions of the inboard and outboard nacelles were held fixed at $y_i' = 0.25$ and $y_o' = 0.55$, respectively. In addition, the vertical positions of the nacelles were held constant; the centerlines of the inboard nacelles were located at $Z = 6.20$ cm (2.44 in.) and the centerlines of the outboard nacelles at $Z = 7.67$ cm (3.02 in.). In each case, data for the isolated wing-body, the wing-body in the presence of the nacelles, and the wing-body-nacelle combination are given to illustrate the various interference effects among the components.

At $M = 1.4$ and 1.15, the presence of the nacelles at $X_{in} = X_{out} = 142.24$ cm (56 in.) results in a large reduction in drag and an increase in lift of the wing-body combination relative to the isolated characteristics. These results are maintained over the entire range of angle of attack and also remain fairly constant. The maximum L/D of the wing-body

combination in the presence of the nacelles is increased by an increment of approximately 1.5 at both Mach numbers, while the angle of attack at a constant lift coefficient is decreased by 0.5°. If the net forces on the four nacelles are included, however, the performance of the overall wing-body-nacelle configuration is reduced to a level below that of the isolated wing-body. At $M = 1.4$, the net reduction in maximum L/D between the isolated wing-body and the overall wing-body-nacelle combination is 0.7, and, at $M = 1.15$, it is 0.5.

Based solely on isolated wing-body and nacelle characteristics, the corresponding reductions in maximum L/D, as indicated in figures 35(a) and 36(a), are 1.5 and 1.2 at $M = 1.4$ and 1.15, respectively. Since the measured loss in performance is considerably less than the estimated value based on isolated data, a significant amount of favorable interference exists among the wing-body combination and nacelles.

With the nacelles moved forward to $X_{in} = X_{out} = 121.92$ cm (48 in.) the results, as indicated in figures 35 (b) and 36 (b), are essentially reversed at $M = 1.4$ and 1.15. The presence of the nacelles increases the drag of the wing-body combination and results in a zero or slightly negative increment in lift. Thus, the maximum L/D of the wing-body combination in the presence of the nacelles is reduced. At $M = 1.4$, the reduction in maximum L/D is 0.65, while at $M = 1.15$, the reduction is 1.0. As shown, including the nacelle forces, the maximum L/D of the overall wing-body-nacelle combination is reduced to a level considerably below the estimated value based on the isolated characteristics of the components. Furthermore, the incremental changes in maximum L/D associated with including the nacelle forces are greater than the corresponding reductions based on the isolated wing-body and nacelle characteristics. Therefore, at this nacelle position, both the interference of the nacelles on the wing-body and the wing-body on the nacelles are unfavorable, resulting in significant reductions in overall performance.

At $M = 0.9$ with the nacelles positioned at $X_{in} = X_{out} = 142.24$ cm (56 in.), the interference effects, as presented in figure 37, are similar to results for the forward nacelle position $X_{in} = X_{out} = 121.92$ cm (48 in.) at the higher Mach numbers. At maximum L/D, there is an unfavorable interference effect of the nacelles on the wing-body combination. However, including the nacelle forces resulted in only a small reduction in maximum L/D, with the maximum value L/D of the wing-body-nacelle combination being greater than the estimated value based on the isolated component characteristics. Thus, there is considerable favorable interference of the wing-body combination on the nacelles under these conditions.

The effects of nacelle position on the interference drag, lift, and pitching moments of the wing-body and wing-body-nacelle combination are shown in figures 38, 39, and 40 for $M = 1.4$, 1.15, and 0.90, respectively. The results presented are for zero angle of attack and with the inboard and outboard nacelles positioned at a spanwise location of $y_i' = 0.25$ and $y_o' = 0.55$, respectively. At $M = 1.4$ and 1.15, results are presented for three different values of stagger between the inboard and outboard nacelles: $\Delta X/R_c = 0.0$, 4.71, and 9.41, while at $M = 0.9$, only data at $\Delta X/R_c = 0$ are

presented. The wing-body interference corresponds to the interference on the wing-body caused by the presence of the nacelles, and the wing-body-nacelle interference corresponds to the net interference among all the components.

Before discussing the aerodynamic characteristics of the data, it is appropriate to note that this configuration was also used to assess the interference effects of the support system and to reduce the uncertainty associated with the presence of the support system. Because of the dual axial drive capability of the support system, which consisted of the main axial drive and the individual nacelle axial drives, it was possible to position the nacelles at a specific location relative to the wing-body model with different positions of the main support system. This was done at all Mach numbers for $\Delta X/R_c = 0$. These results are also presented in figures 38, 39, and 40.

The data represented by the open symbols correspond to the most aft position of the main axial drive and the most forward position of the nacelle delta axial drives that would yield the desired nacelle position. This configuration should produce the minimum support interference. Moving the main support system forward 10.16 cm (4 in.) while maintaining a constant nacelle position resulted in the data represented by the filled symbols. As indicated in figures 38 and 40, at $M = 1.4$ and 0.9, the change in position of the main support system has essentially no effect on the interference lift, drag, and pitching moment. At $M = 1.15$ (fig. 39), there is a small shift in the data at the forward nacelle positions, indicating the presence of an interference effect resulting from the change in position of the main support system. However, the magnitude of these support interference effects are quite small. Therefore, the basic data with the support system in its most aft position, consistent with the desired nacelle position, is believed to be an accurate description of the true interference effects at these conditions.

The actual interference drag as a function of nacelle position, as presented in figures 38, 39, and 40, show similar characteristics at all the Mach numbers. At the aft nacelle positions, both the interference of the nacelles on the wing-body and the wing-body on the nacelles is favorable, resulting in a substantial level of favorable interference. The most favorable interference occurs with the nacelles abreast and located as far aft as possible. As the nacelles are moved forward, both of these interference components become unfavorable and produce a net unfavorable interference. By comparing the magnitude of the maximum favorable interference drag to the drag of four isolated nacelles, it was found that approximately 50 percent of the nacelle drag at $M = 1.4$ would be recovered under the most favorable conditions. At $M = 1.15$, the most favorable interference recovers approximately 75 percent of the drag of the isolated nacelles, while at the subsonic condition at $M = 0.90$, the most favorable interference exceeds the isolated drag of the nacelles, recovering 144 percent of the isolated nacelle drag. At the forward nacelle locations, the unfavorable interference is considerably greater than the most favorable interference and consistently represents a drag increment greater than the isolated drag of the nacelles. This is especially true at $M = 0.9$, where the greatest unfavorable interference represents a drag increment equal to 2.78 times the isolated drag of the nacelles.

The interference lift and pitching moment at M = 1.4 and 1.15 are comparable in both magnitude and variation with nacelle position. At the aft nacelle positions, only the positive pressure field generated by the forward portion of the nacelle intersects the wing and creates a positive increment in lift and a negative increment in pitching moment. As the nacelles are moved forward, more of the positive pressure field intersects the wing and increases the positive lift and negative pitching moments. At the forward nacelle positions, the negative pressure field generated by the expansion of the flow over the aft section of the nacelles intersects the wing, and results in negative lift and positive pitching moment increments. At M = 0.90, the variations in the interference lift and pitching moment tend to be the reverse of those at supersonic Mach numbers. As the nacelles are moved forward from the most aft location, the interference lift decreases and the pitching moment increases. Apparently, at this subsonic Mach number, the flow accelerates in the area between the nacelles and lower wing surface and causes negative interference pressures rather than positive pressures generated under supersonic conditions. This is clearly illustrated in the pressure data which are presented in the following section.

The interference drag, lift, and pitching moment of the wing-body combination on the individual inboard and outboard nacelle pairs are presented in figures 41, 42, and 43 for M = 1.4, 1.15, and 0.90, respectively. These data correspond to the overall results presented in the three previous figures. The sum of these interference forces on the inboard and outboard nacelle pairs represents the difference between the wing-body and wing-body-nacelle results shown in figures 38, 39, and 40. Generally, there is little difference between the forces on the inboard and outboard nacelles, although some differences do arise at the more forward nacelle locations or when the nacelles are highly staggered. At the supersonic Mach numbers of 1.4 and 1.15, the interference drag is almost entirely unfavorable, except at the most aft nacelle position where it becomes slightly favorable. The interference lift on the nacelles tends to be favorable over the range of nacelle positions and Mach numbers tested but is quite small and represents only approximately 1 percent of the estimated cruise lift coefficient of the vehicle at this Mach number.

The methods available to predict these various interference forces are limited because of the complex nature of the flow field involved. The most conventional method employed is the equivalent body approach (ref. 3) which is basically a far-field analysis of the drag of the overall configuration. By analyzing various combinations of the components of the configuration, a prediction of the interference drag can be made. With this approach, the interference drag at M = 1.4 and 1.15 was predicted; the predicted results are compared to the experimental results in figure 44. The interference drag was computed with and without the use of image nacelles to simulate the reflection of the interference flow field generated by the nacelles on the lower surface of the wing. Both sets of results are presented in figure 44. Generally, there is fairly good agreement between the predicted and measured values. However, which of the two theoretical predictions agree better with the data is not well defined. At M = 1.4, the results employing the image nacelles agree better with the data, while at M = 1.15, the results without the image nacelles appears to agree better, especially when the nacelles are staggered.

An alternate method of estimating some of the interference forces is described in references 2 and 4. By utilizing the flow field generated by an isolated nacelle and a reflection plane to simulate the wing, this method is capable of predicting the interference lift, drag, and pitching moment on the wing-body combination resulting from the presence of the nacelles. The approach as described in reference 2, which uses the M.O.C. to generate the flow field of the isolated nacelle, the interference forces on the wing-body were computed and compared with the experimental results in figure 45. Fairly good agreement was obtained at all nacelle positions for each of the interference parameters: lift, drag, and pitching moment. Since the approach used here employed the M.O.C., only those conditions with an entirely supersonic flow field could be analyzed. Therefore, only the results at $M = 1.4$ could be computed.

Both the effects of nacelle spanwise position and the alternate nacelle contour, N_2, were small relative to reference spanwise positions and the basic N_1 nacelle contour. The effects of nacelle spanwise position are shown in figure 46 and the results with the N_2 nacelle contour are presented in figure 47, at $M = 1.4$ and 1.15. Both sets of results are presented in terms of the interference lift, drag, and pitching moment for $\Delta X/R_c = 0$ and compared to the basic results with the N_1 nacelles positioned at spanwise locations $y_i' = 0.25$ and $y_o' = 0.55$. As illustrated by these results, neither change had a significant effect on the interference forces.

One area of concern regarding the operation of the propulsion system in this Mach number regime is the effects of nacelle airflow variations on the interference forces. To investigate this, the airflow through the nacelles was varied and the results are shown in figure 48 for $M = 1.4$, 1.15, and 0.90. The interference lift, drag, and pitching moment are shown as functions of the average mass-flow ratio of the nacelles. Both the wing-body and wing-body-nacelle data are presented. In determining the wing-body-nacelle interference drag, the drag of the isolated nacelle was evaluated at the average nacelle mass-flow ratio to eliminate the effects of reduced mass flow on the drag of the isolated nacelles. The data show very little effect of mass-flow ratio on any of the interference forces over the range of Mach numbers or nacelle positions presented. The largest effect measured is in the interference lift at $M = 1.4$ for the nacelles positioned at $X_{in} = X_{out} = 142.2$ cm (56 in.). Under these conditions, the interference lift increases by 50 percent as the mass-flow ratio is decreased from the maximum value of approximately 78 percent. However, on an absolute basis, this increase represents only a 0.013 increment in lift coefficient or a 3- to 4-percent change in cruise lift coefficient.

The overall trends of the interference forces with Mach number are shown in figure 49 for a number of nacelle axial positions. Generally, the interference forces tend to increase, either favorably or unfavorably, as M is reduced from 1.4 to 1.0. As indicated earlier, the data taken near $M = 1.0$ were questionable because of the interference effects of the support system and are not presented. The variations in the interference forces with Mach number, spanwise nacelle position, nacelle shape, and nacelle mass-flow ratio are not as great as the interference forces resulting from changes in the axial position of the nacelles, as illustrated in figures 38, 39, and 40. Therefore,

it appears nacelle axial position is the most significant variable in determining the interference forces.

Pressure Data — The interference pressure distributions on the lower surface of the wing-body combination and on the inboard and outboard nacelles at selected data points corresponding to the force data previously shown are presented in this section. The effects of Mach number, nacelle spanwise and axial position, angle of attack, and nacelle mass-flow ratio are presented. A summary of the interference pressure data showing the values of the primary variables and associated figure numbers is presented in table 7.

By using the flow field analysis described in reference 2, which is based on M.O.C. and a reflection plane, the interference pressure distributions on the lower surface of the wing-body combination at $M = 1.4$ can be estimated. These results are compared to the experimental data in figures 50, 52, 54, and 55 for various nacelle positions. The theoretical results described by the solid lines represent the net interference pressures, generated by the nacelles, that can directly influence the lower surface of the wing-body without intersecting an intervening nacelle. The results described by the dashed line represent the net interference generated by all four nacelles, based on the assumption that any intervening nacelles were transparent to any pressure disturbance generated by an adjacent nacelle. In all cases, the net interference pressure was taken to be the algebraic sum of the interference pressures generated by the individual nacelles included in the analysis.

For the results presented in figure 50 with the nacelles positioned aft at $X_{in} = X_{out} = 142.2$ cm (56 in.), only the nacelles on either side of the orifice row were capable of influencing the pressure at these locations. There is generally fair to good agreement between the theoretical and measured results, except in the region of the intersection of the shock waves and the wing surface. In this region, the boundary layer on the wing surface tends to smear out the pressure rise at the shock wave. There is very little difference between the interference pressure distributions at the two angles of attack. However, at the higher angle of attack, the measured shock position, as indicated by the initial pressure rise, tends to be farther forward than at zero angle of attack. This is probably because of the lower average Mach number that exists beneath the wing at the higher angle of attack.

The individual nacelle-interference pressure distributions are shown in figure 51. The average interference pressures (averaged around the circumference) are shown in figure 51(a), and the individual interference pressures are presented in figures 51(b) and (c). The average pressure distributions are rather flat at both angles of attack, but do show a positive shift between zero and the higher angle of attack. This shift again illustrates the reduced Mach number or greater compression beneath the wing at the higher angle of attack. The detailed pressure distributions at the four circumferential locations show greater variations than the average distribution and generally

follow the same characteristics found for this nacelle configuration under isolated conditions without the wing-body combination being present. These results were previously presented in figure 23. The higher angle of attack results in a net positive shift in the interference pressures, but does not appreciably change the shape of the pressure distribution.

With the nacelles located farther forward at $X_{in} = X_{out} = 121.9$ cm (48 in.), the resultant interference pressure distribution on the wing-body, shown in figure 52, are considerably more complex. In all cases, at least three and, in one case, all four of the nacelles can affect the pressure distribution measured along any one row of orifices. In addition to the pressure rises resulting from the shock waves generated by the nacelles, the expansion of the flow around the aft end of the nacelles is strongly felt on the wing-body. The agreement between the theoretical and measured values is fairly good, particularly at zero angle of attack, which is the basic flow field being modeled. However, it is not clear whether it is appropriate to include the effects of the nacelles that can influence a particular area only after passing around an intervening nacelle. Obviously, the nacelles directly influencing a particular area dominate the interference pressure distribution, while those nacelles indirectly affecting the particular area result in much less of a perturbation of the pressure distribution. Furthermore, in some cases, the agreement between the theoretical and measured results is enhanced by including these indirect effects and, in others, it is not. The individual nacelle pressure distributions, shown in figure 53, exhibit considerably more variation along the nacelle length than when the nacelles were positioned aft at $X_{in} = X_{out} = 142.2$ cm (56.0 in.). The individual nacelle pressure distributions are dominated by the wing flow field and show little relation to the comparable nacelle pressure distribution measured without the wing-body combination present (fig. 23).

The interference pressure distributions on the wing-body with the nacelles staggered are shown in figures 54 and 55. These results show similar agreement between the theoretical predictions and measured data, as in the previous cases. However, for these configurations, when the effects of the nacelles that indirectly affect the pressure distribution were included, there was a general improvement in the agreement between the theoretical and experimental results.

The effects of nacelle spanwise location on the wing-body and nacelle interference pressures are shown in figures 56 and 57, respectively. The wing-body pressure distributions are comparable for all three spanwise nacelle positions. The small changes in the wing-body interference pressures reflect the relative proximity of the nacelles to the particular row of orifices. The nacelle interference pressures shown in figure 57 exhibit variations with nacelle spanwise position similar to those measured on the four nacelles tested without the wing-body combination present (fig. 23). For both the wing-body and nacelles, the greatest interference pressures are experienced when the inboard and outboard nacelles are at their closest position, which corresponds to the spanwise positions $y_i' = 0.30$ and $y_o' = 0.50$.

As indicated in figure 48, reducing the mass-flow ratio of the nacelles had little effect on the net interference forces. The wing interference

pressures also show a relatively small dependence on the nacelle mass flow ratio. Figures 58(a) and (b) present the wing-body interference pressures at two mass flows for the nacelles positioned at $X_{in} = X_{out} = 142.2$ cm (56 in.) and 121.9 cm (48 in.), respectively. In both cases, the only major change in the wing-body pressure distribution is in the region where the detached shock wave at the lower mass-flow ratio intersects the wing surface. Here, there is a large pressure rise which is generally followed by a rapid drop in pressure. However, outside of this change, the downstream pressure distributions at both mass-flow ratios are very similar and practically identical in many cases. This is essentially the same result found in the case of the isolated nacelles; namely, the effects of reduced mass-flow are concentrated locally only around the forward portion of the nacelles with very little effect on the aft section.

The wing-body and nacelle interference pressure distributions at $M = 1.15$, comparable to the $M = 1.4$ data, are presented in figures 59 through 67, and are outlined in table 7. As expected, the interference pressures are greater in magnitude and the pressure rises occur farther upstream at $M = 1.15$ than at $M = 1.4$. Except for these two differences, the same general characteristics are exhibited in the data at these two Mach numbers.

A limited amount of subsonic data at $M = 0.90$ is presented in figures 68 through 72 and is outlined in table 7. Only the wing-body and nacelle interference pressures at $X_{in} = X_{out} = 142.2$ cm (56 in.) and 121.9 cm (48 in.) are shown along with the wing interference pressures at a reduced mass-flow ratio with the nacelles located at $X_{in} = X_{out} = 142.2$ cm (56 in.). Subsonically, with no shock waves present to create rapid pressure changes, the interference pressure distributions are much smoother and extend further upstream. This is quite obvious in figure 68, which shows the wing interference pressures with the nacelles located at $X_{in} = X_{out} = 142.2$ cm (56 in.). As found earlier and as illustrated in figure 69, the higher angle of attack produced essentially a net shift in the nacelle interference pressure distribution. In this case, only the portion of the nacelle located forward of the wing trailing edge at $X = 163.0$ cm (64.2 in.) was affected by the change in angle of attack and is reflected in the net shift in the nacelle interference pressure distribution. The pressure distribution on the portion of the nacelle aft of the wing trailing edge shows very little dependence on the angle of attack. The wing pressure distributions at a reduced nacelle mass-flow ratio are shown in figure 72 and exhibit a large negative pressure peak immediately downstream of the nacelle lip. This is apparently because of the expansion of the flow around the nacelle lip at this reduced mass-flow ratio.

SUMMARY OF RESULTS

The effect of Mach number, angle of attack, nacelle position, and nacelle mass-flow ratio on the net interference forces and pressures on a representative delta wing-body-nacelle combination are presented. By using the equivalent body approach and a limited flow-field analysis based on the method of characteristics, comparisons are made between the predicted and measured interference forces and pressures. Of all the variables studied, the nacelle

axial position, relative to the wing-body combination, had the greatest effect on the overall interference forces. With the most favorable nacelle axial position, the net interference drag was favorable and recovered 50 percent of the drag of the four isolated nacelles at $M = 1.4$, 75 percent at $M = 1.15$, and 144 percent at $M = 0.9$. In contrast, at the most unfavorable nacelle position, the net interference drag was highly unfavorable and resulted in a drag increase corresponding to 102 percent of the drag of the four isolated nacelles at $M = 1.4$, 129 percent at $M = 1.15$, and 278 percent at $M = 0.9$. The net interference drag was approximately equally divided between the interference of the nacelles on the wing-body and the wing-body on the nacelles. The net interference drag was most favorable when both components were favorable, while the opposite was true for the unfavorable interference. The interference lift was generally positive over the range of Mach numbers and nacelle positions tested, with the most favorable lift interference corresponding to approximately 10 percent of the cruise lift coefficient. The interference forces remained fairly constant over the operating angle of attack range of the configuration. Variations in nacelle mass-flow ratio were found to have very little effect on the net interference forces on the four nacelles as a unit or on the wing-body-nacelle combination. Based on the interference pressure distributions on the wing-body, the effects of reduced mass-flow ratio were essentially limited to the forward third of the nacelle and the wing surface in the immediate vicinity of the nacelle lip.

The predicted results based on both theoretical approaches agreed fairly well with the measured data. Although neither approach produced exceptional agreement, both predicted the magnitude and variations of the interference forces with nacelle position reasonably well. According to the limited flow-field analysis, the interference pressure distributions predicted agree with the measured values. Because of the wing boundary layer, the agreement was better in the expansion regions than in the compression regions that correspond to the shock-wave impingements. Comparisons between the measured and predicted interference pressure distributions indicated the nacelles directly adjacent to the measured pressures dominated the pressure distribution. However, the comparisons did not clearly identify the necessity of including the effects of those nacelles not directly adjacent to the measured pressures in the definition of the theoretical pressure distributions.

Ames Research Center
National Aeronautics and Space Administration
Moffett Field, California 94035, August 4, 1976

REFERENCES

1. Bradley, E. S.; Johnson, W. M.; and Von Keszycki, C. H.: Passenger Transport at Low Supersonic Speeds. AIAA Paper 69-776, July 1969.

2. Bencze, D. P.: Nacelle-Airframe Interference at Low Supersonic Mach Numbers. AIAA Paper 72-1113, Nov. 1972.

3. Harris, Roy V., Jr.: An Analysis and Correlation of Aircraft Wave Drag. NASA TM X-947, 1964.

4. Mack, R. J.: A Numerical Method for Evaluation and Utilization of Supersonic Nacelle-Wing Interference. NASA TN D-5057, 1968.

5. Manro, M. E.; Moulijn, J. P.; and Knittel, J. D.: Pressure Distribution on a Delta Wing-Horizontal Stabilizer Combination at Mach Numbers from 0.3 to 2.9. FAA-SS-72-30-8, Federal Aviation Administration, vol. 8, July 15, 1972. (Limited to government agencies only.)

6. Gerend R. P.; and Roundhill, J. P.: Correlation of Gas Turbine Engine Weights and Dimensions. AIAA Paper 70-669, June 1970.

7. Baals, Donald D.; Smith, Normal F.; and Wright, John B.: The Development and Application of High-Critical-Speed Nose Inlets. NACA TR-920, 1948.

8. Schlichting, Hermann: Boundary Layer Theory. McGraw Hill Book Co., 1968.

9. Bencze, D. P.: Wind Tunnel Investigation of Nacelle-Airframe Interference at Mach Numbers of 0.90 to 1.4 - Data Report - Force Data. NASA TM X-62,489, 1976.

10. Bencze, D. P.: Wind Tunnel Investigation of Nacelle-Airframe Interference at Mach Numbers of 0.90 to 1.4 - Data Report - Pressure Data. Volume I - NASA TM X-73,149, Volume II - NASA TM X-73,088, 1976.

11. Sibulkin, Merwin: Theoretical and Experimental Investigations of Additive Drag. NACA TR-1187, 1954.

12. Neal, Luther, Jr.; Bertram, Mitchell H.: Turbulent-Skin-Friction and Heat-Transfer Charts Adapted From the Spalding and Chi Method. NASA TN D-3969, 1967.

13. Sorensen, Virginia L.: Computer Program for Calculating Flow-Fields in Supersonic Inlets. NASA TN D-2897, 1965.

14. Krupp, J. A.; and Murman, E. M.: Computation of Transonic Flows Past Lifting Airfoils and Slender Bodies. AIAA Journal, vol. 10, no. 7, July 1972, pp. 880-886.

TABLE 1.- WING PLANFORM

Y/(b/2), percent	Y		Chord		z_{le}		z^{a}_{te}	
	cm	in.	cm	in.	cm	in.	cm	in.
0	0	0	101.30	39.88	-1.440	-0.567	-0.749	-0.295
9.80	5.08	2.0	81.79	32.20	-1.918	-.755	.097	.038
19.61	10.16	4.0	64.16	25.26	-1.684	-.663	.914	.360
29.41	15.24	6.0	54.46	21.44	-.673	-.265	1.758	.692
39.22	20.32	8.0	47.60	18.74	-.157	-.062	2.139	.842
49.02	25.40	10.0	41.20	16.22	.112	.044	2.032	.800
58.82	30.48	12.0	35.05	13.80	.216	.085	1.750	.689
68.63	35.56	14.0	28.83	11.35	.234	.092	1.415	.557
78.43	40.64	16.0	22.71	8.94	.244	.096	1.153	.454
88.24	45.72	18.0	16.43	6.47	.259	.102	.864	.340
98.04	50.80	20.0	9.09	3.58	.224	.088	.635	.250

[a] z measured relative to the wing design plane at Z = 11.89 cm (4.68 in.).

TABLE 2.- WING THICKNESS DISTRIBUTION - z/c,[a] percent

Y/(b/2), percent / x/c, percent	0		9.80		19.61		29.41		39.22		49.02	
	Upper	Lower	Upper	Lower	Upper	Lower	Upper	Lower	Upper	Lower	Upper	Lower
0	0	0	0	0	0	0	0	0	0	0	0	0
5	1.17	0.48	0.99	0.21	0.62	0.19	0.29	0.36	0.34	0.34	0.27	0.33
10	1.77	.60	1.16	.36	1.07	.42	.52	.66	.54	.66	.45	.64
15	2.11	.72	2.05	.49	1.50	.66	.73	.93	.72	.92	.63	.91
20	2.28	.83	2.31	.63	1.19	.95	.92	1.16	.88	1.15	.80	1.12
30	2.31	1.01	2.50	.92	2.25	1.48	1.23	1.55	1.10	1.57	1.04	1.48
40	2.15	1.16	2.51	1.19	2.76	1.89	1.39	1.81	1.21	1.81	1.16	1.70
50	2.07	1.31	2.37	1.43	2.58	2.13	1.38	1.94	1.21	1.93	1.18	1.18
60	1.81	1.46	2.09	1.59	2.19	1.91	1.25	1.89	1.11	1.87	1.13	1.75
70	1.46	1.52	1.65	1.55	1.67	1.49	1.03	1.64	.96	1.60	1.00	1.52
80	.99	1.29	1.10	1.27	1.15	1.06	.74	1.20	.71	1.16	.78	1.08
90	.45	.75	.51	.79	.64	.57	.40	.64	.43	.62	.48	.55
100	0	0	0	0	0	0	0	0	0	0	0	0

Y/(b/2), percent / x/c, percent	58.82		68.63		78.43		88.24		98.04	
	Upper	Lower	Upper	Lower	Upper	Lower	Upper	Lower	Upper	Lower
0	0	0	0	0	0	0	0	0	0	0
5	0.27	0.33	0.34	0.30	0.26	0.31	0.29	0.32	0.89	0.34
10	.47	.60	.53	.57	.43	.58	.47	.63	1.14	.68
15	.68	.83	.73	.81	.62	.83	.64	.86	1.36	.93
20	.86	1.04	.91	1.00	.92	1.03	.81	1.15	1.61	1.19
30	1.15	1.36	1.22	1.33	1.15	1.33	1.09	1.37	1.88	1.55
40	1.32	1.56	1.43	1.45	1.33	1.52	1.34	1.56	1.99	1.70
50	1.36	1.65	1.49	1.53	1.39	1.60	1.42	1.61	1.98	1.70
60	1.28	1.59	1.54	1.49	1.33	1.53	1.42	1.53	1.92	1.60
70	1.09	1.43	1.22	1.31	1.15	1.33	1.35	1.31	1.64	1.49
80	.79	1.13	.93	1.02	.89	.99	1.12	.95	1.30	1.13
90	.43	.60	.53	.54	.55	.54	.82	.50	.93	.67
100	0	0	0	0	0	0	0	0	0	0

[a] z measured normal to local chord line.

TABLE 3.- RANGE OF TRAVEL OF THE NACELLE DRIVES

Drive	Range relative to midposition
Inboard lateral[a]	±5.33 cm (±2.10 in.)
Outboard lateral[b]	±5.33 cm (±2.10 in.)
Vertical	±6.35 cm (±2.50 in.)
Main axial	±15.24 cm (±6.00 in.)
Delta axial	±10.16 cm (±4.00 in.)

[a]Outboard lateral drive at outboard limit.
[b]Inboard lateral drive at inboard limit.

TABLE 4.- RANGE OF NACELLE POSITIONS RELATIVE TO MODEL COORDINATES

Position	Range
Inboard lateral[a]	10.36 cm (4.08 in.) ≤ Y ≤ 21.03 cm (8.28 in.)
Outboard lateral[b]	20.42 cm (8.04 in.) ≤ Y ≤ 31.09 cm (12.24 in.)
Vertical	-5.00 cm (-1.97 in.) ≤ Z ≤ 7.70 cm (3.03 in.)
Axial[c]	101.60 cm (40.0 in.) ≤ X ≤ 152.40 cm (60.0 in.)

[a]Outboard lateral drive at outboard limit.
[b]Inboard lateral drive at inboard limit.
[c]Maximum axial separation of any two nacelles limited to 20.32 cm (8.0 in.).

TABLE 5.- NACELLE BALANCE CORRECTIONS

Correction[a]	Symbol	Equation
Aft balance cavity	$C'_{A_{ac}}$	$-(p_{ac} - p_\infty)\, A_{ac}/qA_c$
Forward balance cavity	$C'_{A_{fc}}$	$(p_{fc} - p_\infty)\, A_{fc}/qA_c$
Lip cavity	$C'_{A_{lip}}$	$(p_{lip} - p_\infty)\, A_{lip}/qA_c$
Seal	$C'_{A_{seal}}$	$\dfrac{(p_{fc} - p_{lip})\, A_{S1} + (p_{fc} - p_{lip})^2\, A_{S2}}{qA_c}$
Skin friction	$C'_{A_{sf}}$	$\dfrac{0.455/\left(\log_{10} R_{N_{lip}}\right)^{2.58} - \left(1050/R_{N_{lip}}\right)}{1.0 + \left\{0.85[(\gamma - 1)/2]M^2_{lip}\right\}} \dfrac{A_{sf}}{A_c}$
Total	$C'_{A_{total}}$	$C'_{A_{ac}} + C'_{A_{fc}} + C'_{A_{lip}} + C'_{A_{seal}} + C'_{A_{sf}}$

Constants:

$A_{ac} = 6.187$ cm^2 (0.959 in.^{2})

$A_{fc} = 7.361$ cm^2 (1.141 in.^{2})

$A_{lip} = 3.645$ cm^2 (0.565 in.^{2})

$A_{S1} = 5.206\times10^{-3}$ cm^2 (0.807×10^{-3} in.^{2}), inboard
7.703×10^{-3} cm^2 (1.194×10^{-3} in.^{2}), outboard

$A_{S2} = 1.59\times10^{-11}$ cm^4/dyne (0.17×10^{-6} in.^{4}/lb), inboard
2.81×10^{-11} cm^4/dyne (0.30×10^{-6} in.^{4}/lb), outboard

$A_{sf} = 79.245$ cm^2 (12.283 in.^{2})

[a] Balance correction subtracted from nacelle balance axial force.

TABLE 6.- CONFIGURATION DESCRIPTION

No.	Configuration	Left-hand outboard	Nacelles inboard	Right-hand inboard	Nacelles outboard	Wing-body
1	N_1	N_1	*a*	*a*	N_1	*b*
2	N_2	N_2	*a*	*a*	N_2	*b*
3	N_2N_2	N_2	N_2	N_2	N_2	*b*
4	N_1N_1	N_1	N_1	N_1	N_1	*b*
5	WBN_1N_1	N_1	N_1	N_1	N_1	WB
6	WBN_1N_1	N_2	N_2	N_2	N_2	WB
7	WB[c]	*a*	*a*	*a*	*a*	WB

[a] Nacelle and nacelle sting not installed.
[b] Wing-body not installed, sting fairing installed.
[c] Nacelle support system installed, but nacelles and nacelle stings not installed.

TABLE 7.- WING-BODY-NACELLE PRESSURE DATA

Figure no.	M_∞	α, deg	X_i, cm (in.)	X_o, cm (in.)	y_i'	y_o'	m/m_c	Wing-body data	Nacelle data
50	1.40	0, 5.24	142.2 (56)	142.2 (56)	0.25	0.55	max.	X	
51	↓	0, 5.24	142.2 (56)	142.2 (56)	↓	↓	↓		X
52	↓	0, 5.33	121.9 (48)	121.9 (48)	↓	↓	↓	X	
53	↓	0, 5.33	↓	121.9 (48)	↓	↓	↓		X
54	↓	0.32	↓	132.1 (52)	↓	↓	↓	X	
55	↓	0.02	↓	142.2 (56)	↓	↓	↓	X	
56	↓	~0	↓	121.9 (48)	variable	variable	↓	X	
57	↓	↓	↓	121.9 (48)	variable	variable	↓		X
58(a)	↓	↓	142.2 (56)	142.2 (56)	0.25	0.55	0.959, 0.779	X	
58(b)	↓	↓	121.9 (48)	121.9 (48)	↓	↓	1.00, 0.795	X	
59	1.15	0, 5.65	142.2 (56)	142.2 (56)	↓	↓	max.	X	
60	↓	0, 5.65	142.2 (56)	142.2 (56)	↓	↓	↓		X
61	↓	0, 5.72	121.9 (48)	121.9 (48)	↓	↓	↓	X	
62	↓	0, 5.72	↓	121.9 (48)	↓	↓	↓		X
63	↓	0.13	↓	132.1 (52)	↓	↓	↓	X	
64	↓	0.11	↓	142.2 (56)	↓	↓	↓	X	
65	↓	~0	↓	121.9 (48)	variable	variable	↓	X	
66	↓	↓	↓	121.9 (48)	variable	variable	↓		X
67(a)	↓	↓	142.2 (56)	142.2 (56)	0.25	0.55	0.968, 0.787	X	
67(b)	↓	↓	121.9 (48)	121.9 (48)	↓	↓	0.988, 0.801	X	
68	0.90	0, 5.33	142.2 (56)	142.2 (56)	↓	↓	max.	X	
69	↓	0, 5.33	142.2 (56)	142.2 (56)	↓	↓	↓		X
70	↓	-0.03	121.9 (48)	121.9 (48)	↓	↓	↓	X	
71	↓	-0.03	121.9 (48)	121.9 (48)	↓	↓	↓		X
72	↓	0.20	142.2 (56)	142.2 (56)	↓	↓	0.955, 0.636	X	

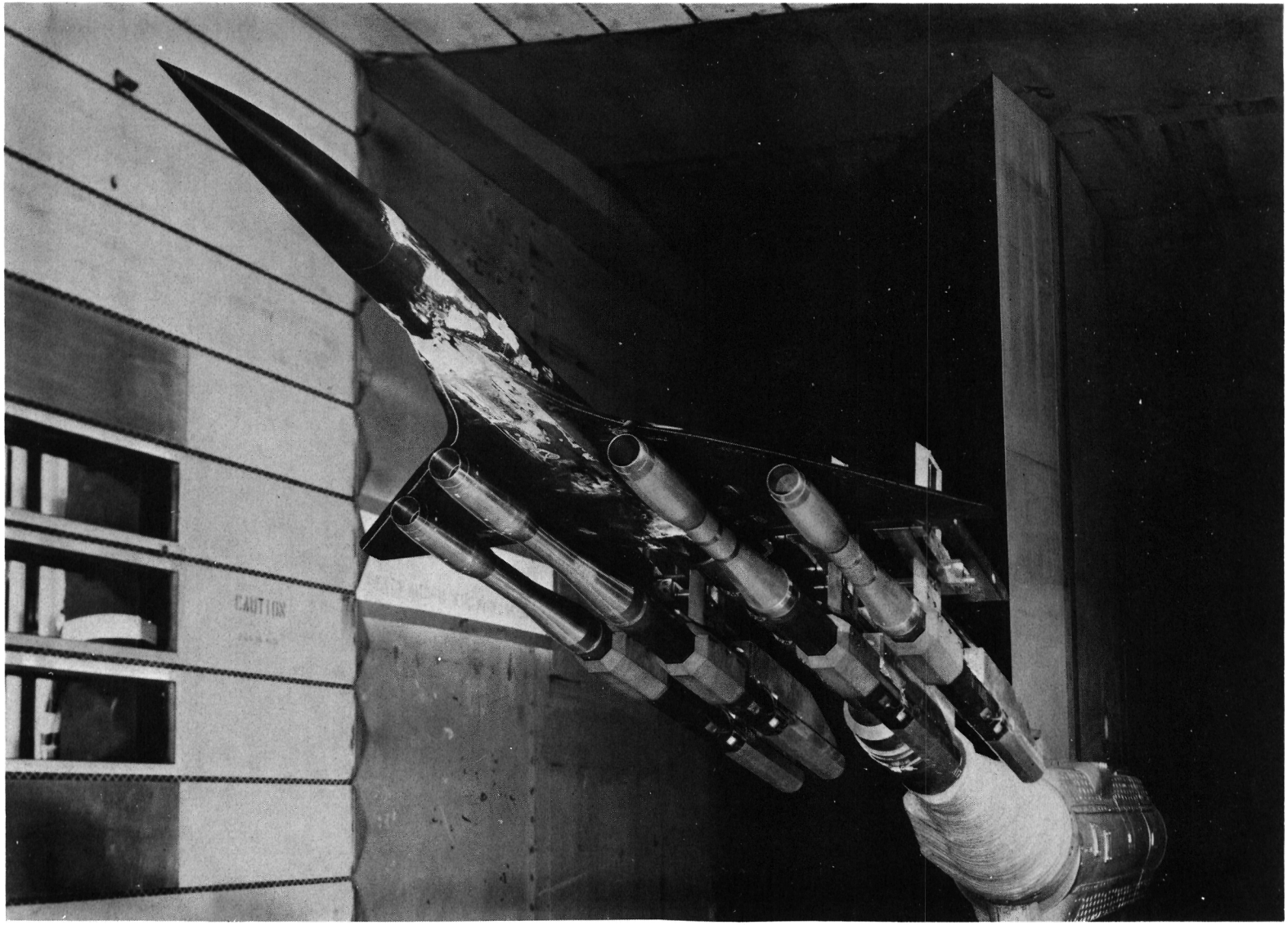

(a) Wing-body-nacelle configuration with nacelle support system.

Figure 1.- Model installed in the Ames 11- by 11-Foot Wind Tunnel.

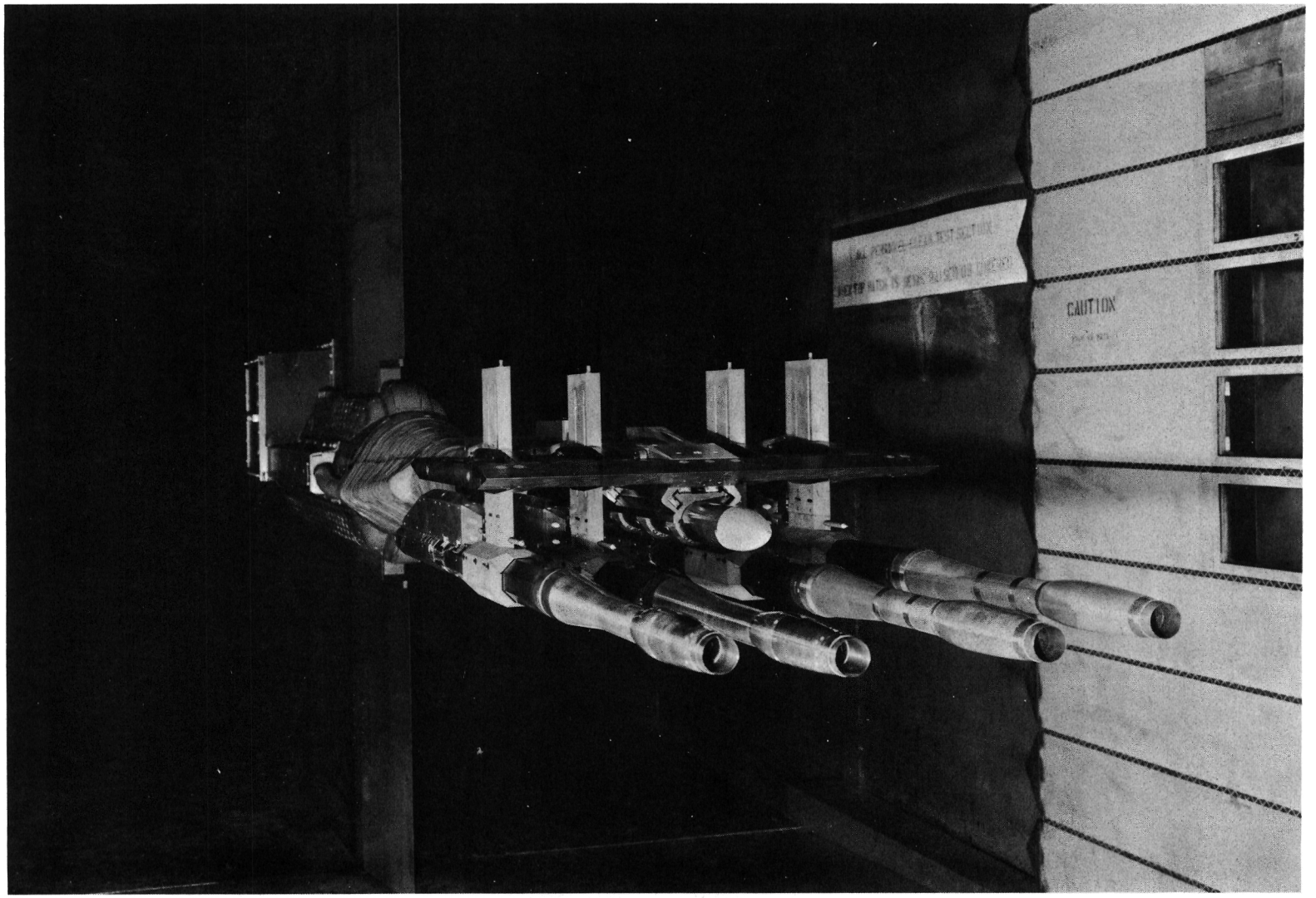

(b) Nacelle support system.

Figure 1.- Concluded.

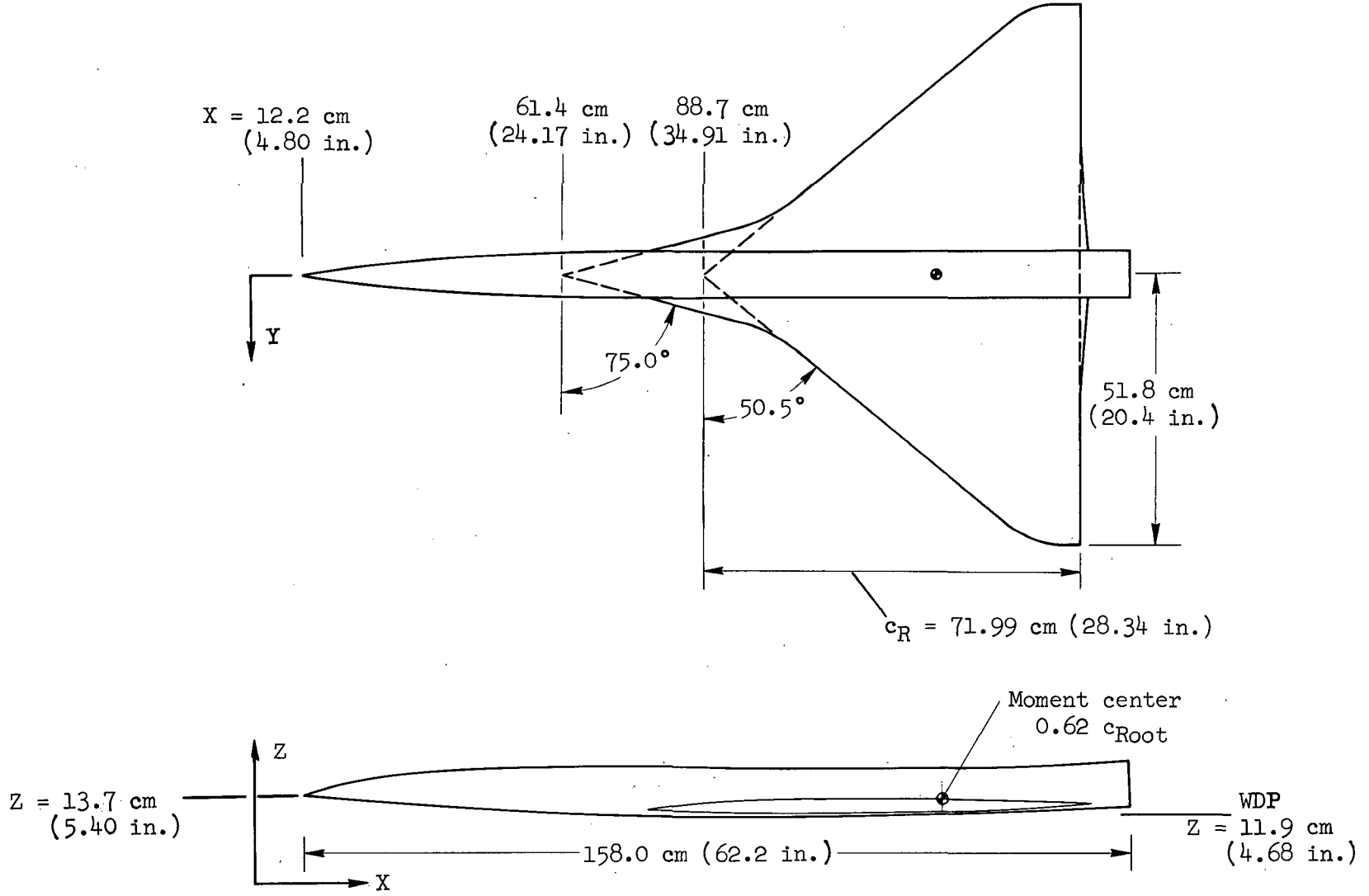

Figure 2.- General wing-body configuration.

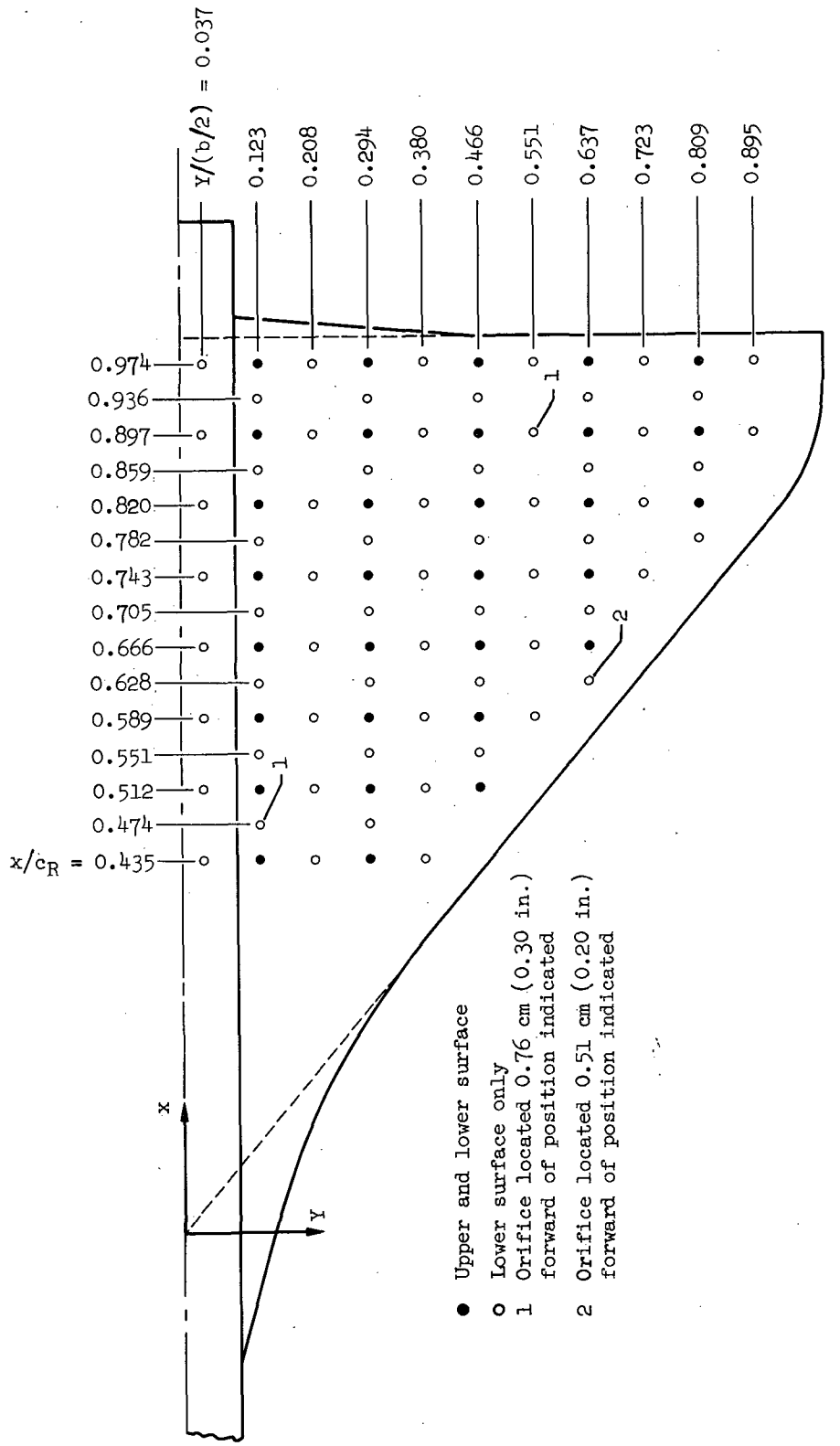

Figure 3.- Wing pressure instrumentation.

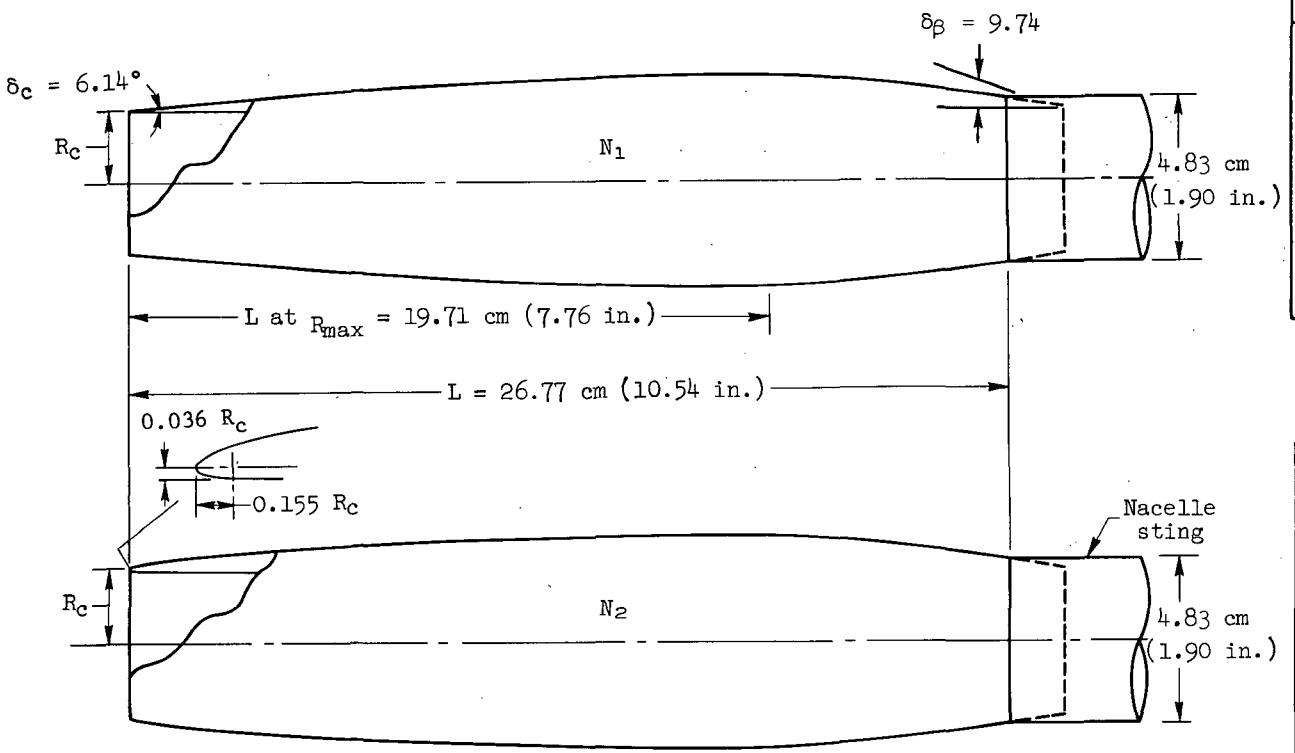

Nacelle, N_1

x/R_c	r/R_c	x/R_c	r/R_c
0.000	1.000	7.326	1.474
0.666	1.069	7.992	1.486
1.332	1.133	8.658	1.492
1.998	1.192	9.026	1.492
2.664	1.246	9.325	1.484
3.331	1.294	9.991	1.441
3.996	1.337	10.656	1.379
4.662	1.375	11.322	1.302
5.328	1.407	11.988	1.213
5.994	1.435	12.654	1.113
6.660	1.458	13.320	1.004

R_c = 2.16 cm (0.850 in.)

Nacelle, N_2

x/R_c	r/R_c	x/R_c	r/R_c
0.000	1.000	4.349	1.362
0.130	1.056	5.654	1.401
0.384	1.094	6.524	1.417
0.609	1.129	7.393	1.431
1.002	1.167	8.698	1.438
1.218	1.192	8.986	1.430
1.478	1.212	9.628	1.389
1.739	1.230	10.270	1.329
2.262	1.264	10.912	1.255
2.783	1.294	11.553	1.169
3.192	1.320	12.195	1.073
4.001	1.349	12.837	1.067

R_c = 2.25 cm (0.885 in.)

Figure 4.- Nacelle geometries.

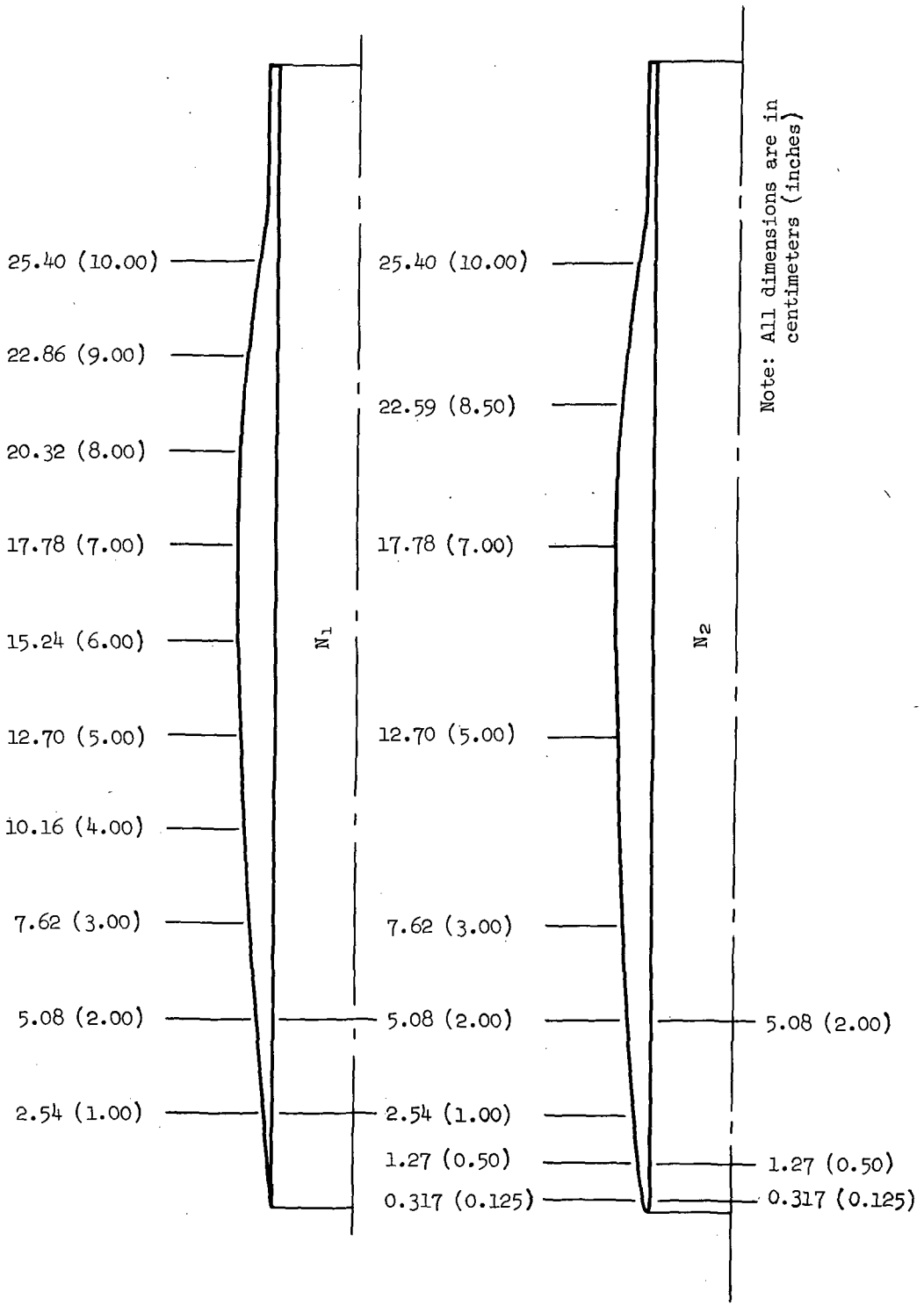

Figure 5.- Nacelle pressure instrumentation.

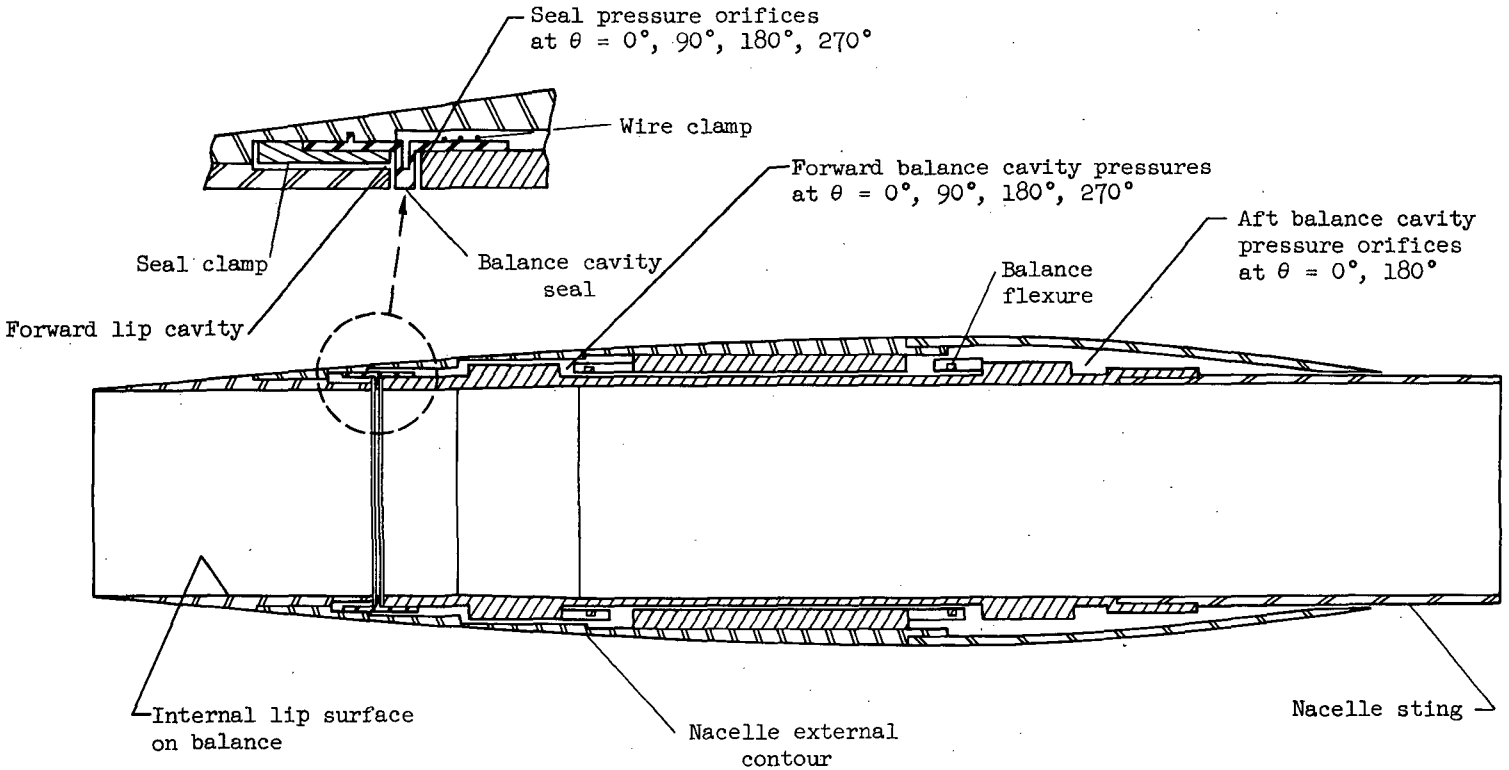

Figure 6.- Nacelle flow-through balance.

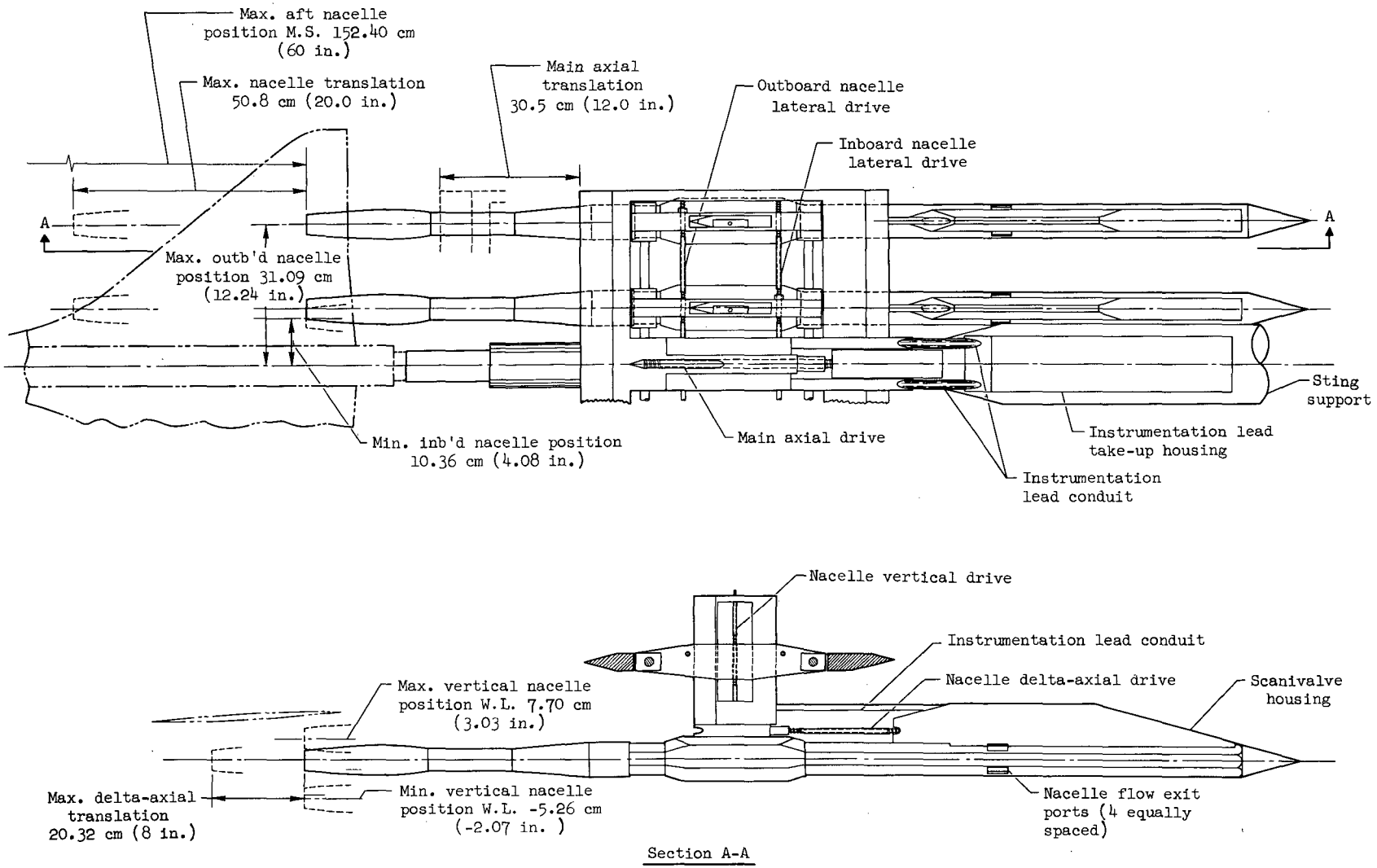

Figure 7.- Nacelle support system.

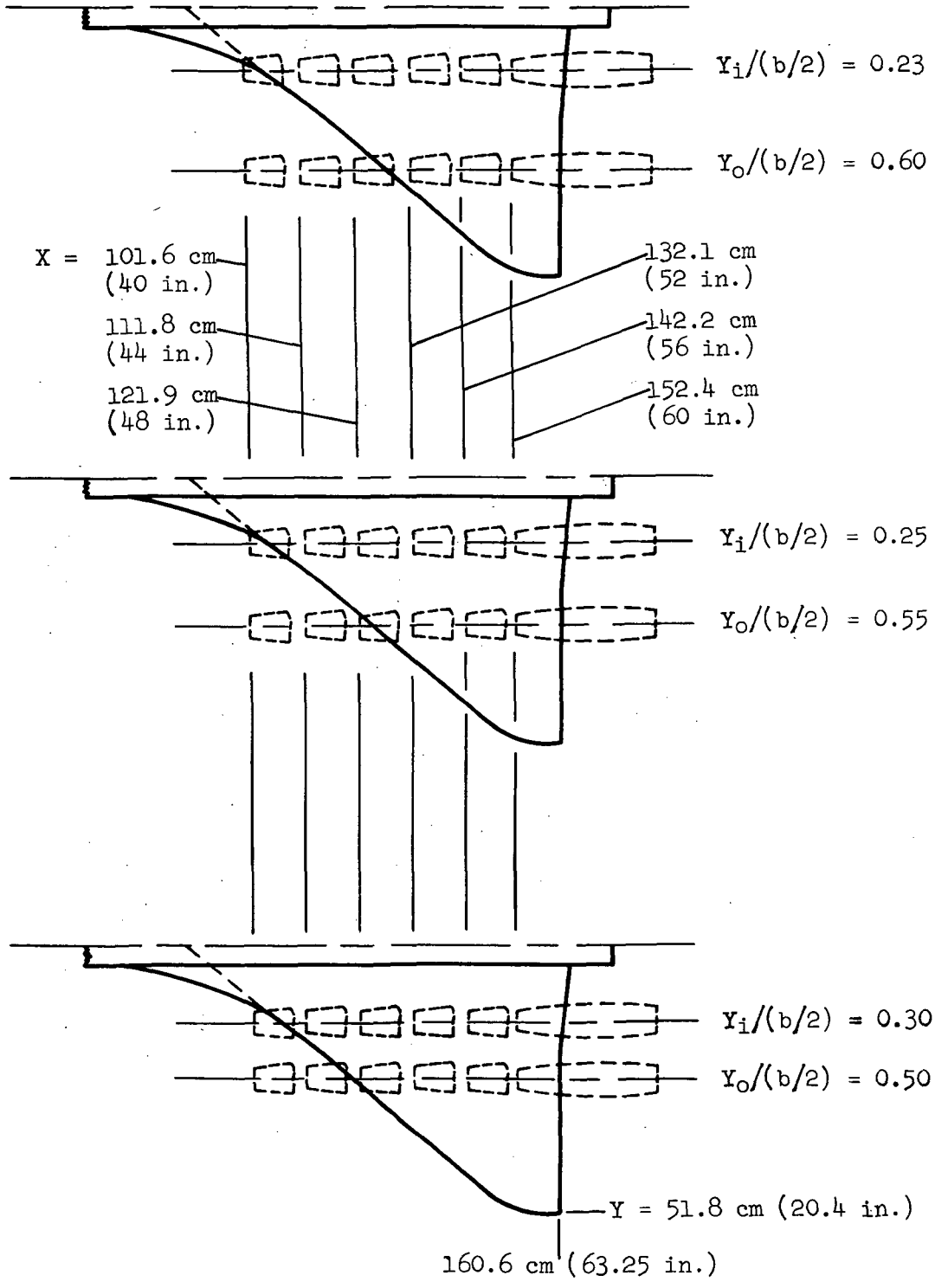

Figure 8.- Nacelle position relative to wing-body model.

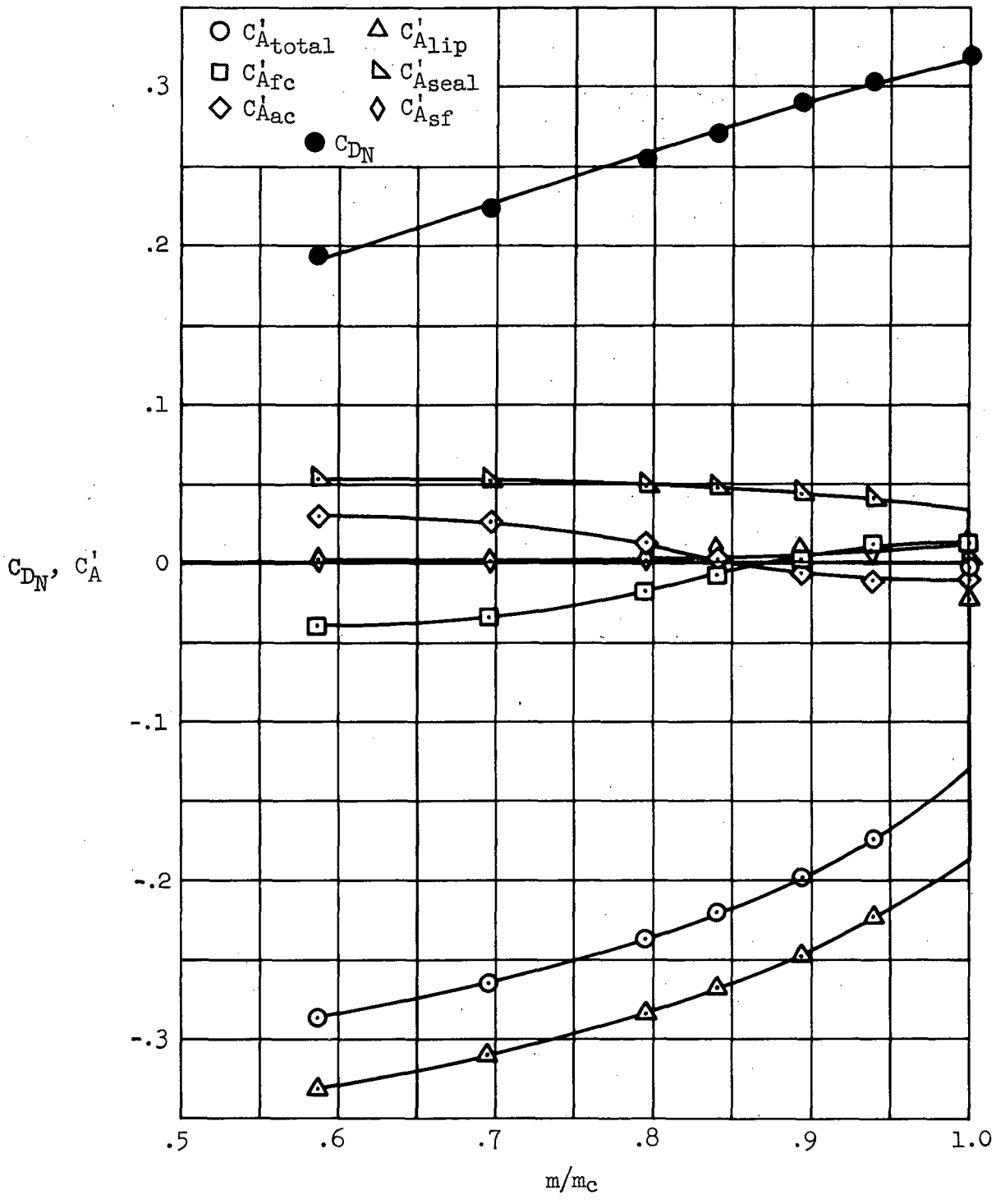

(a) $M_\infty = 1.40$, $\Delta X/R_c = 9.41$

Figure 9.- Nacelle balance tares; configuration N_1N_1, $\alpha = 0°$, $y'_i = 0.25$, $y'_o = 0.55$.

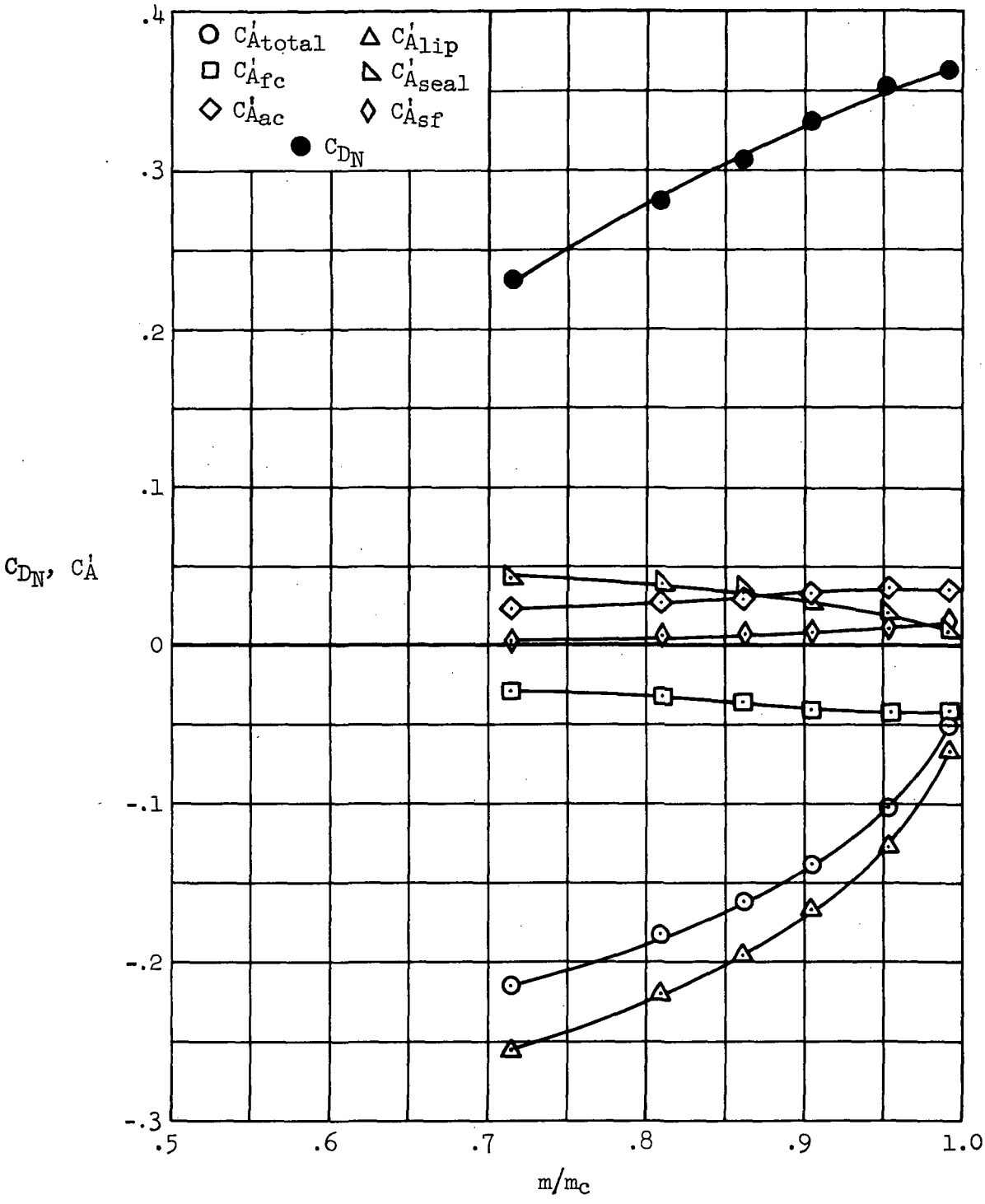

(b) $M_\infty = 1.15$, $\Delta X/R_c = 9.41$

Figure 9.- Continued.

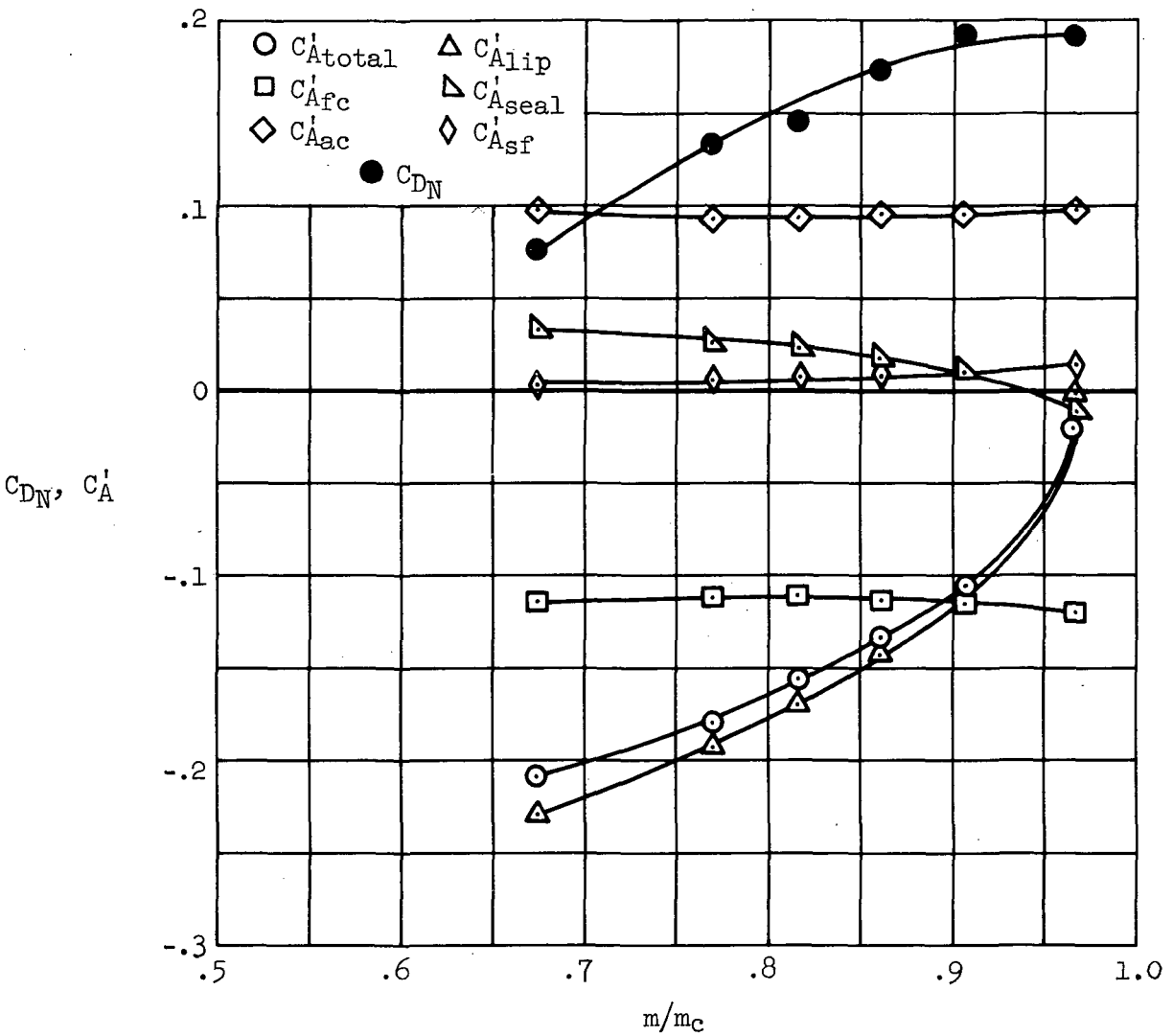

(c) $M_\infty = 0.98$, $\Delta X/R_c = 0$

Figure 9.- Concluded.

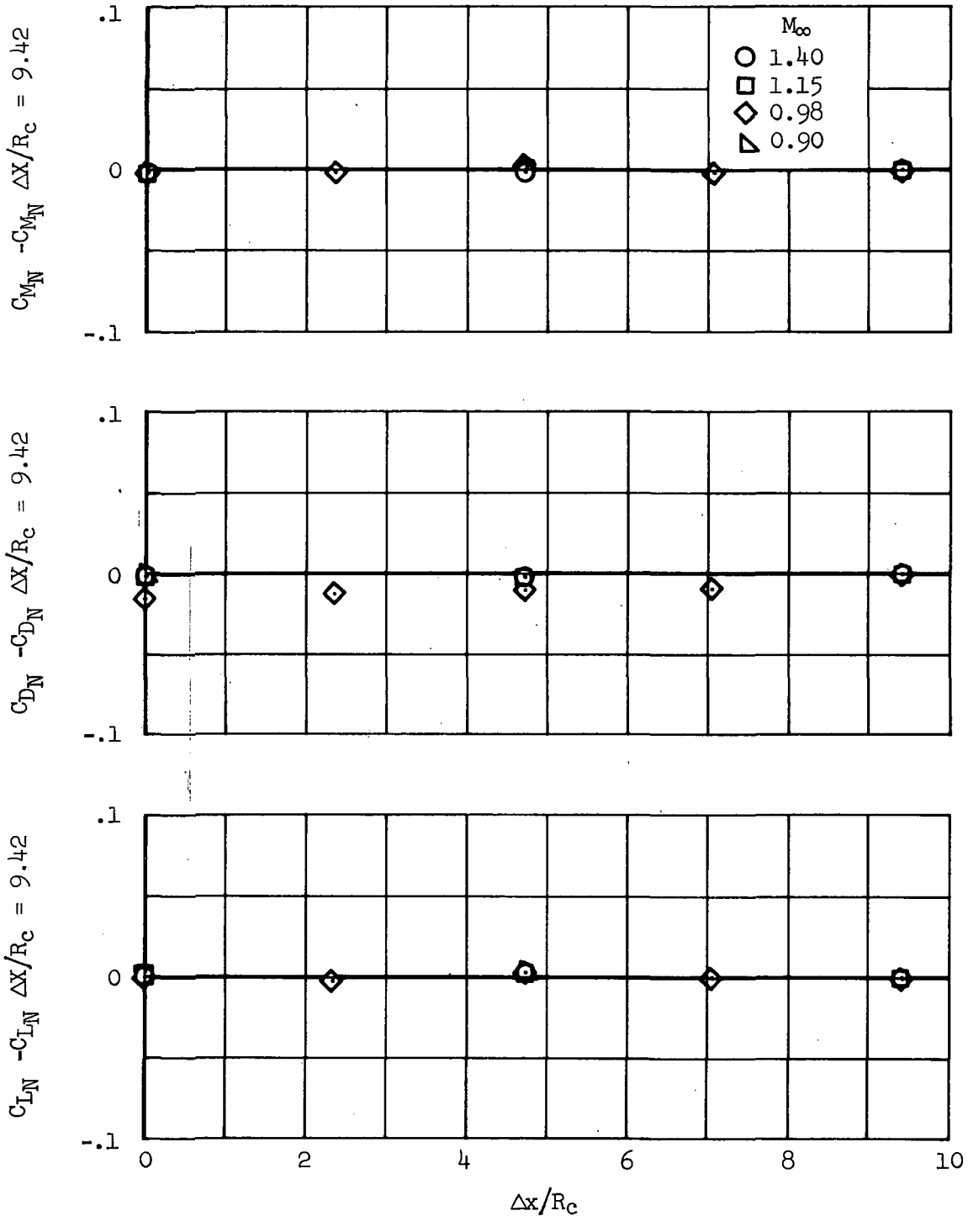

Figure 10.- Interference of downstream nacelle on upstream nacelle; configuration N_1, $\alpha = 0°$, $y_i' = 0.23$, $y_o' = 0.60$, maximum m/m_c.

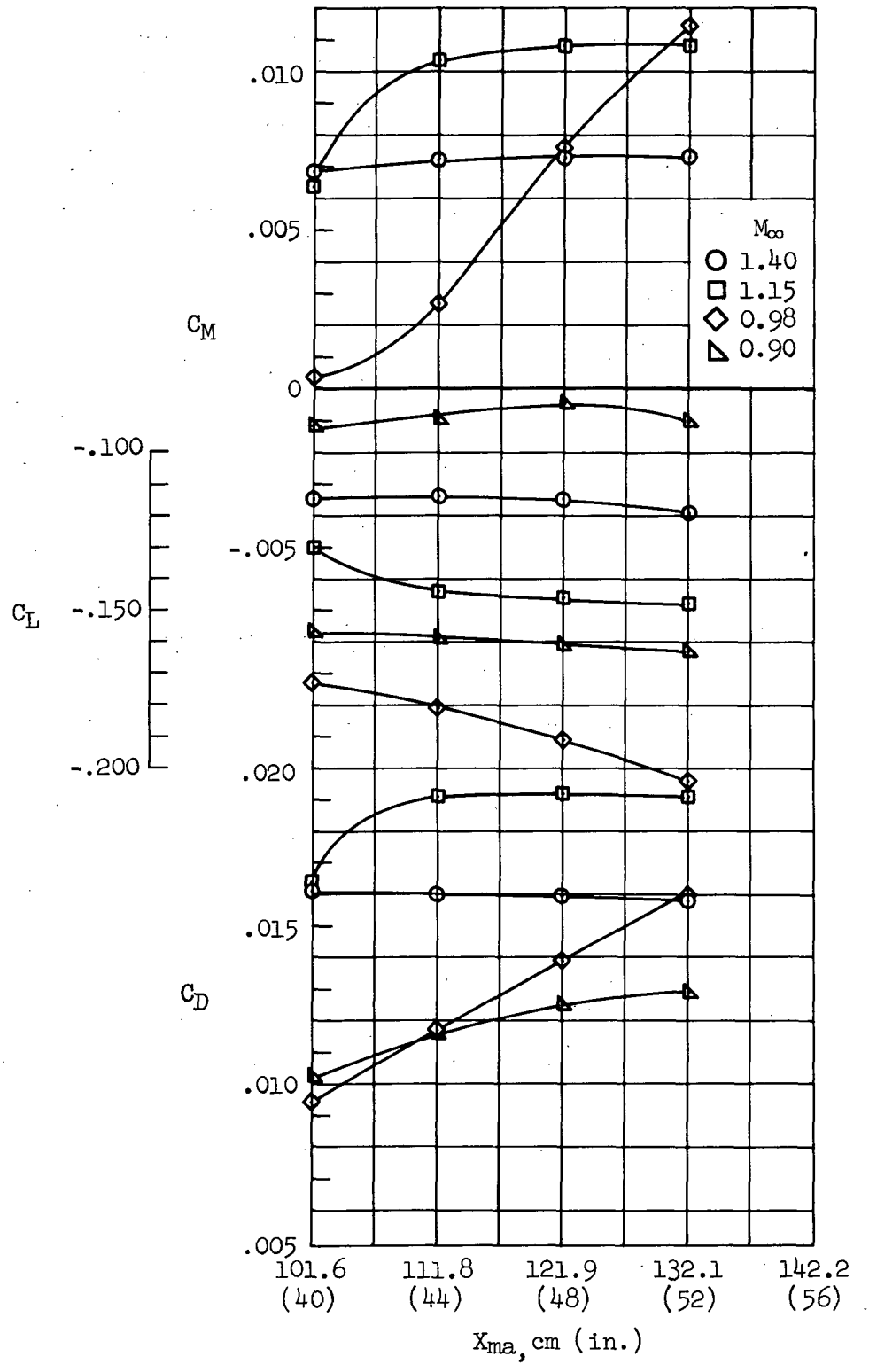

Figure 11.- Interference of nacelle support system on the wing-body; configuration WB, $\alpha = 0°$, $y_i' = 0.25$, $y_o' = 0.55$, maximum m/m_c.

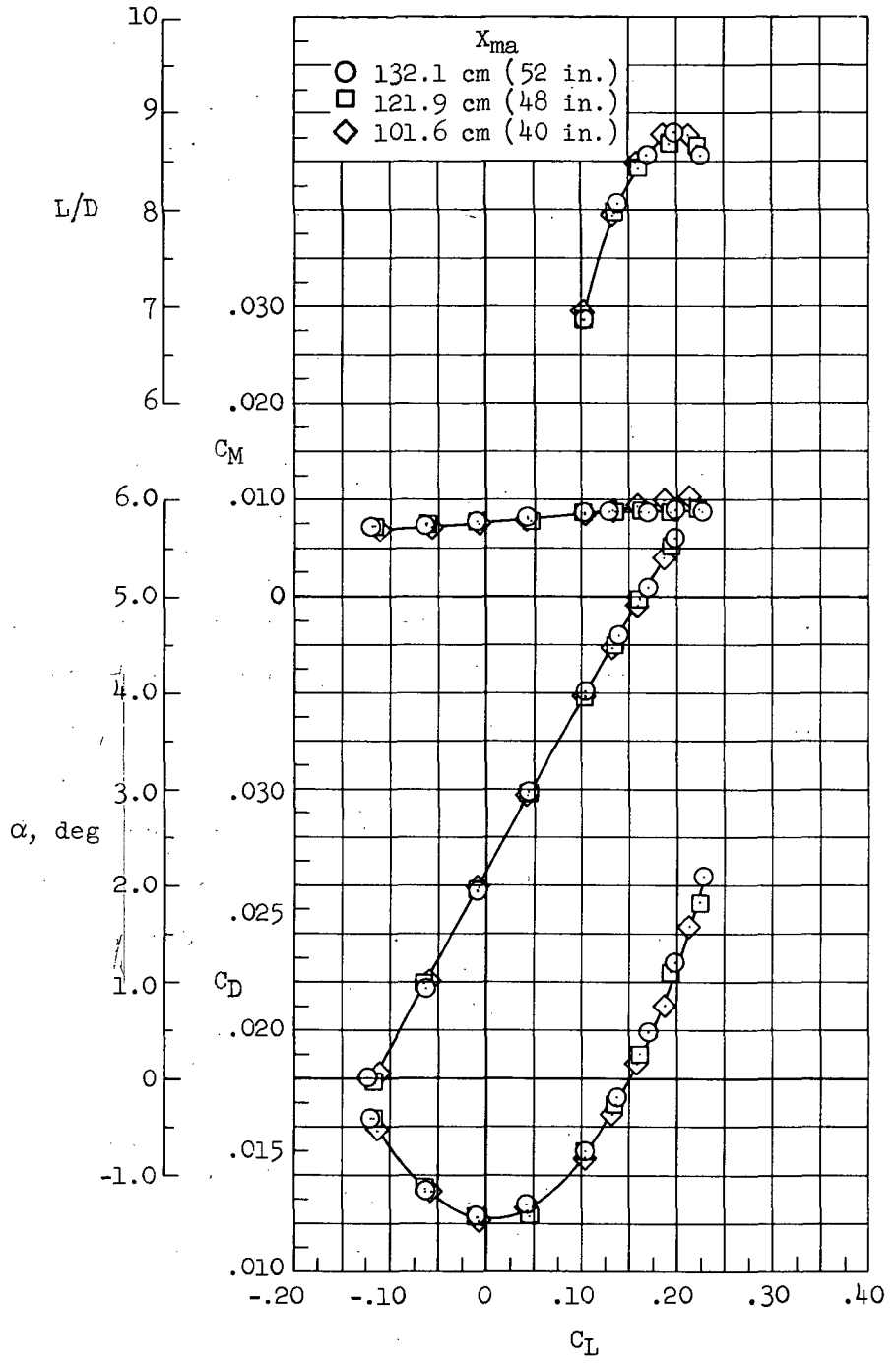

(a) $M_\infty = 1.40$

Figure 12.- Interference of nacelle support system on the longtudinal characteristics of the wing-body; configuration WB, $y_i' = 0.25$, $y_o' = 0.55$, maximum m/m_c.

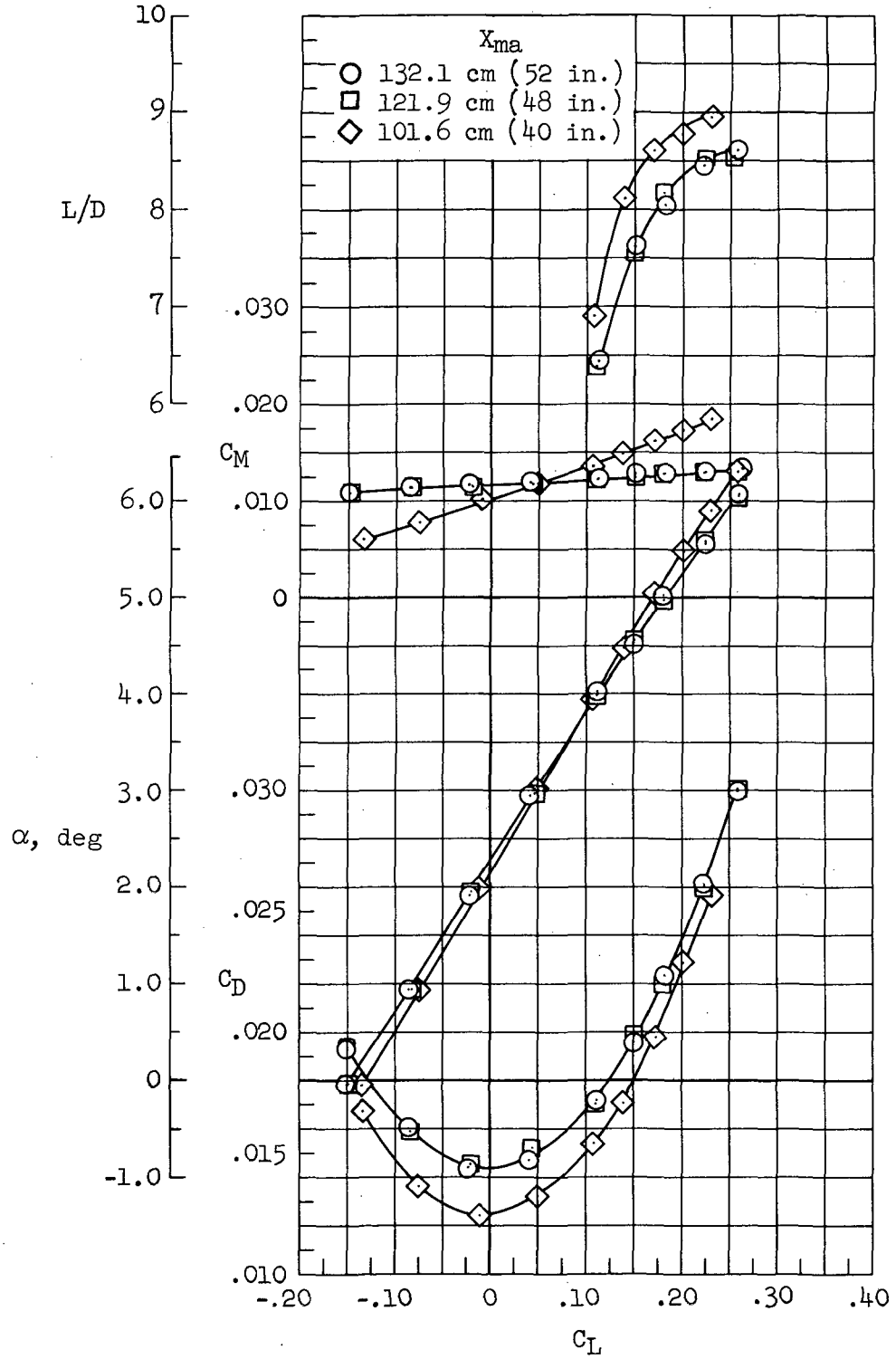

(b) $M_\infty = 1.15$

Figure 12.- Concluded.

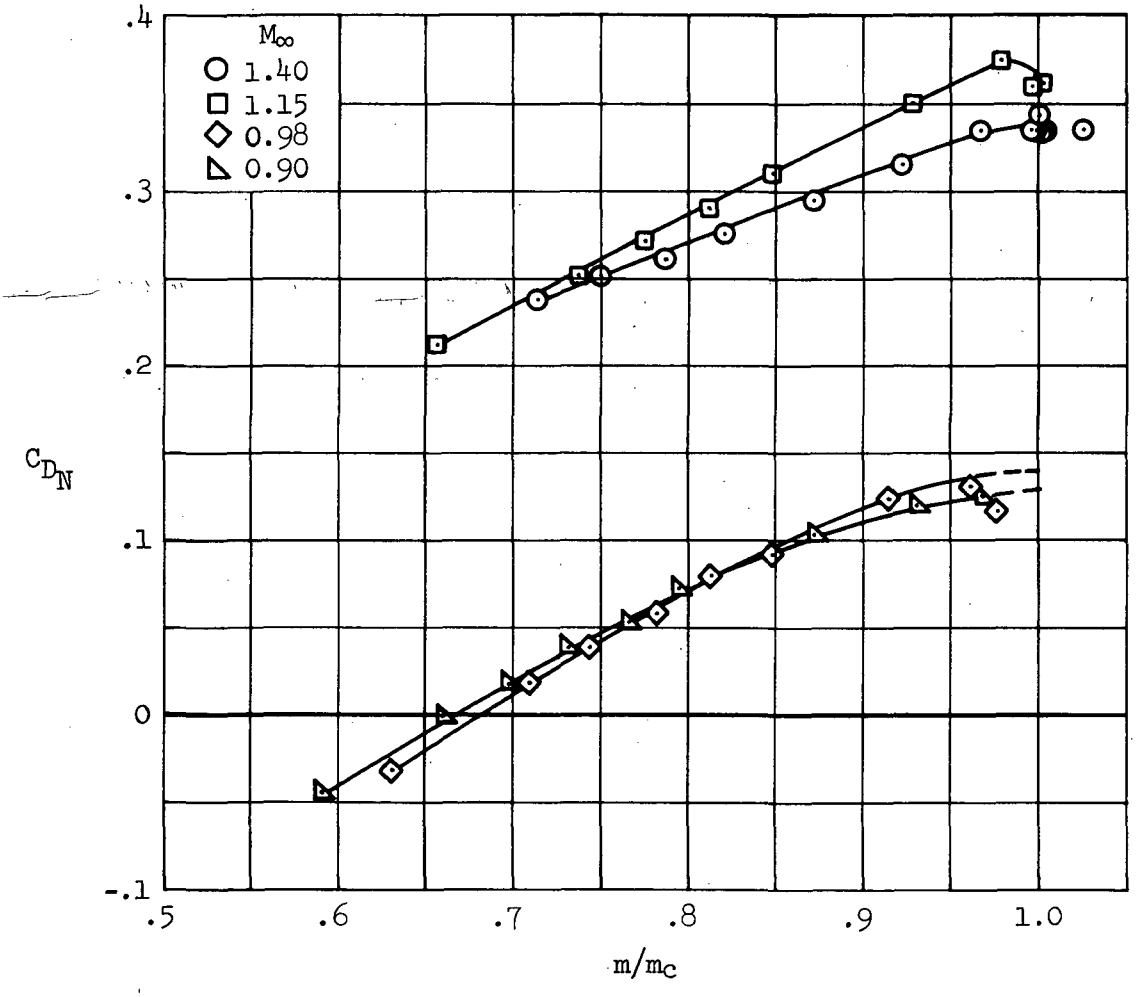

(a) Nacelle N_1.

Figure 13.- Nacelle drag variations with mass-flow ratio, $\alpha = 0°$.

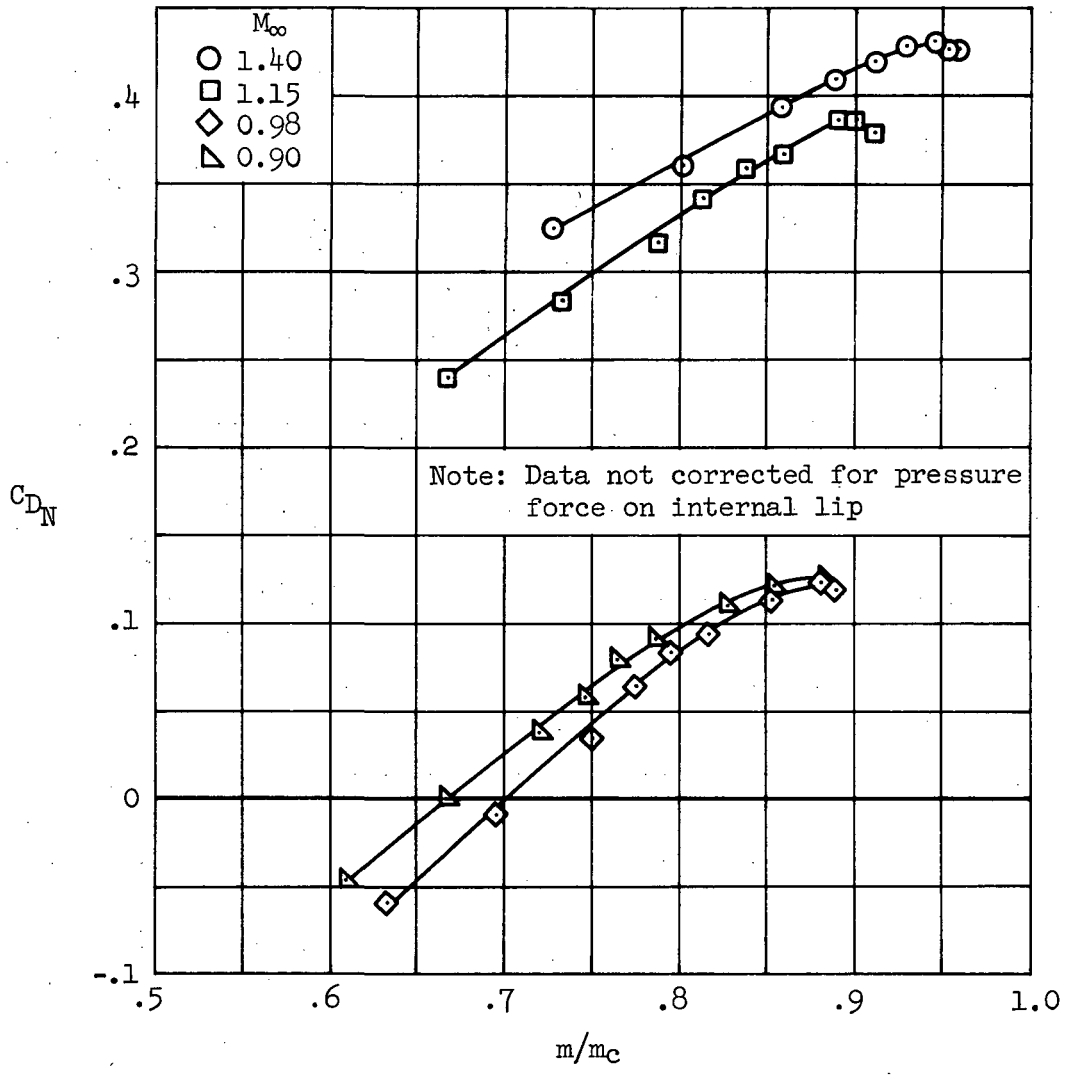

(b) Nacelle N_2.

Figure 13.- Concluded.

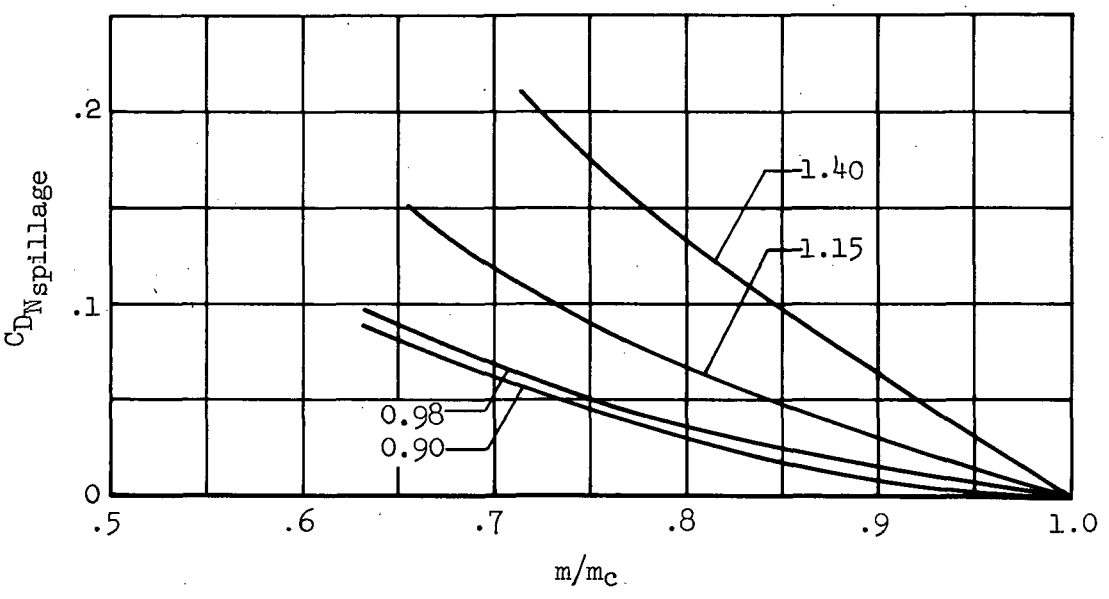

Figure 14.- Nacelle spillage drag; nacelle N_1, $\alpha = 0°$.

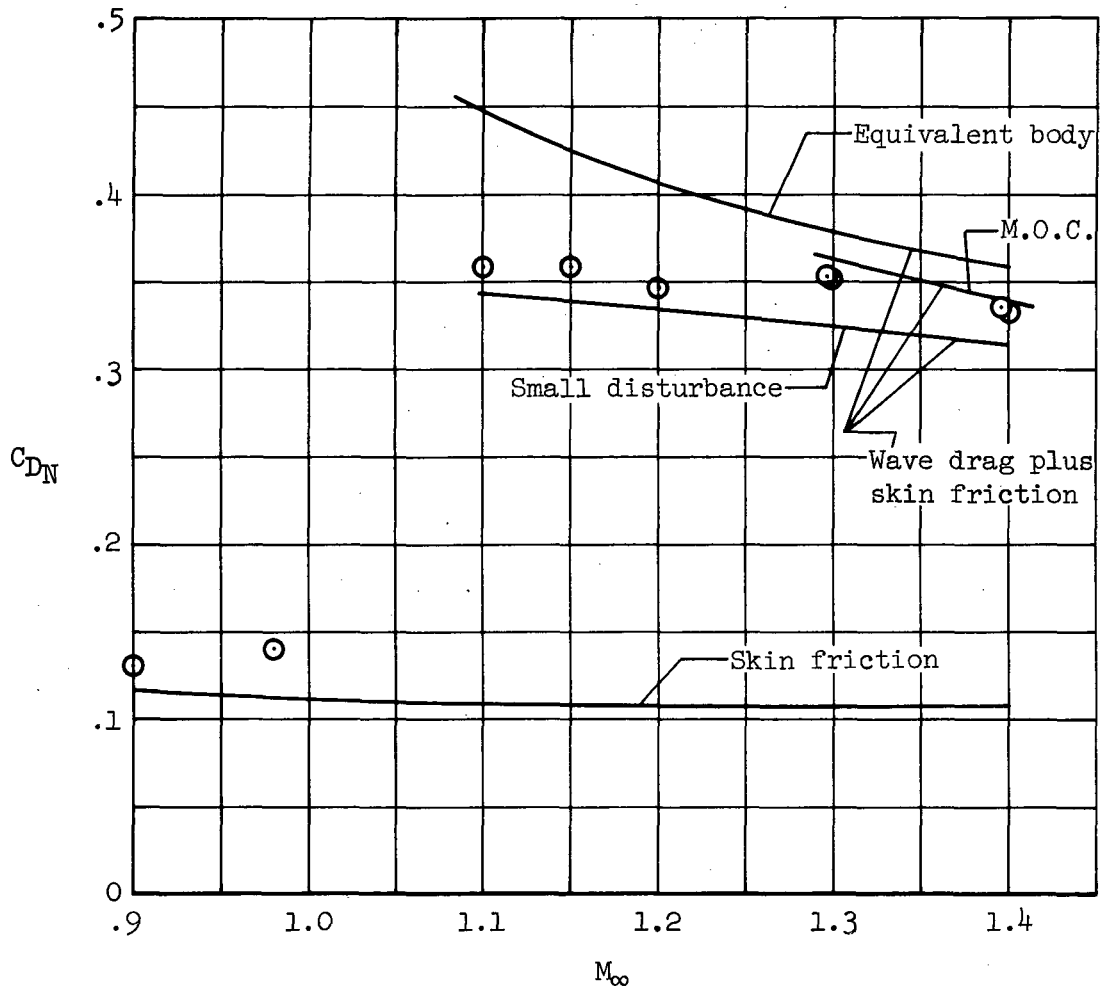

Figure 15.- Isolated nacelle drag; nacelle N_1, $\alpha = 0°$, $m/m_c = 1.0$.

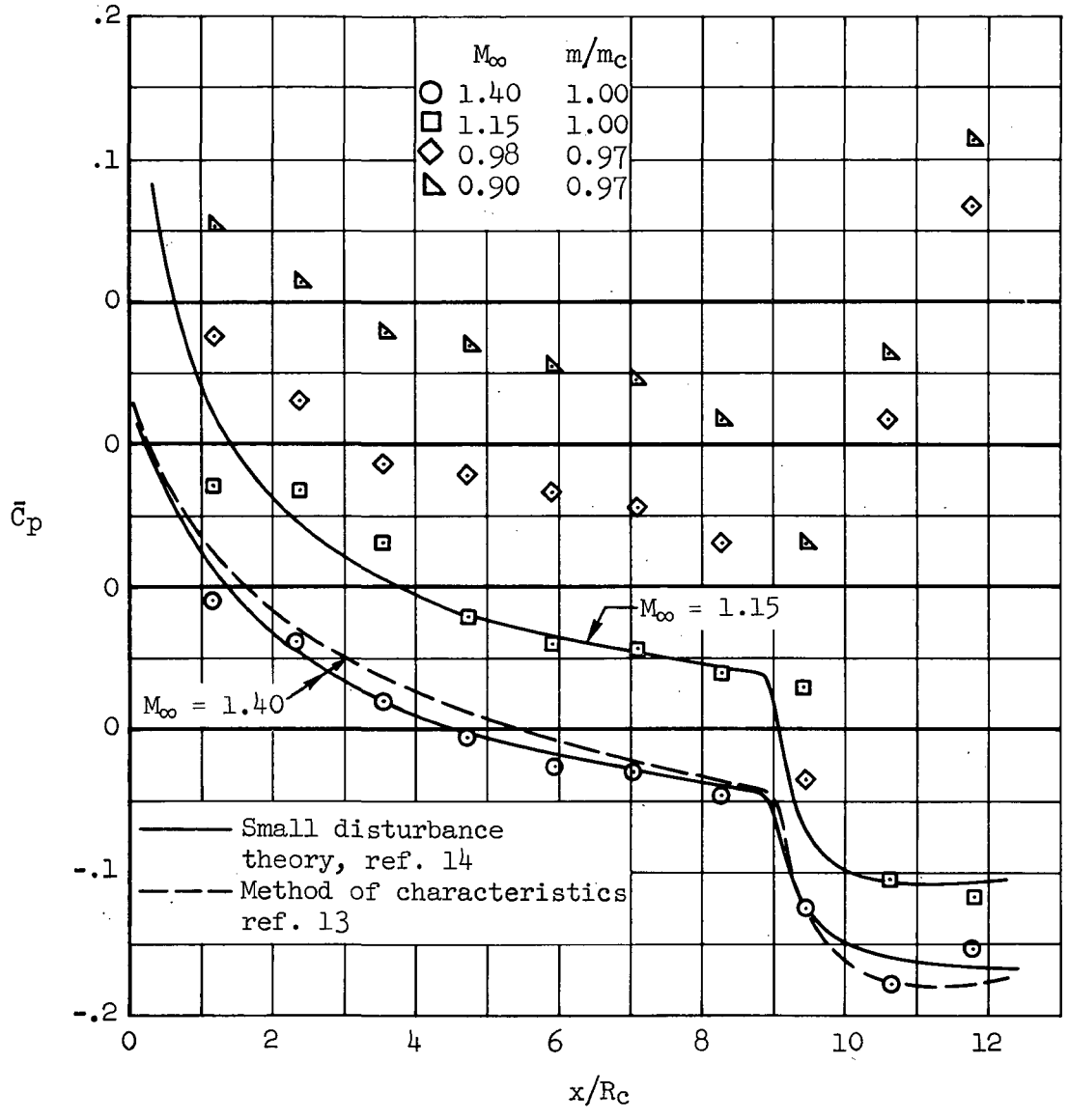

Figure 16.- Isolated nacelle surface pressure distributions; nacelle N_1, $\alpha = 0°$, maximum m/m_c.

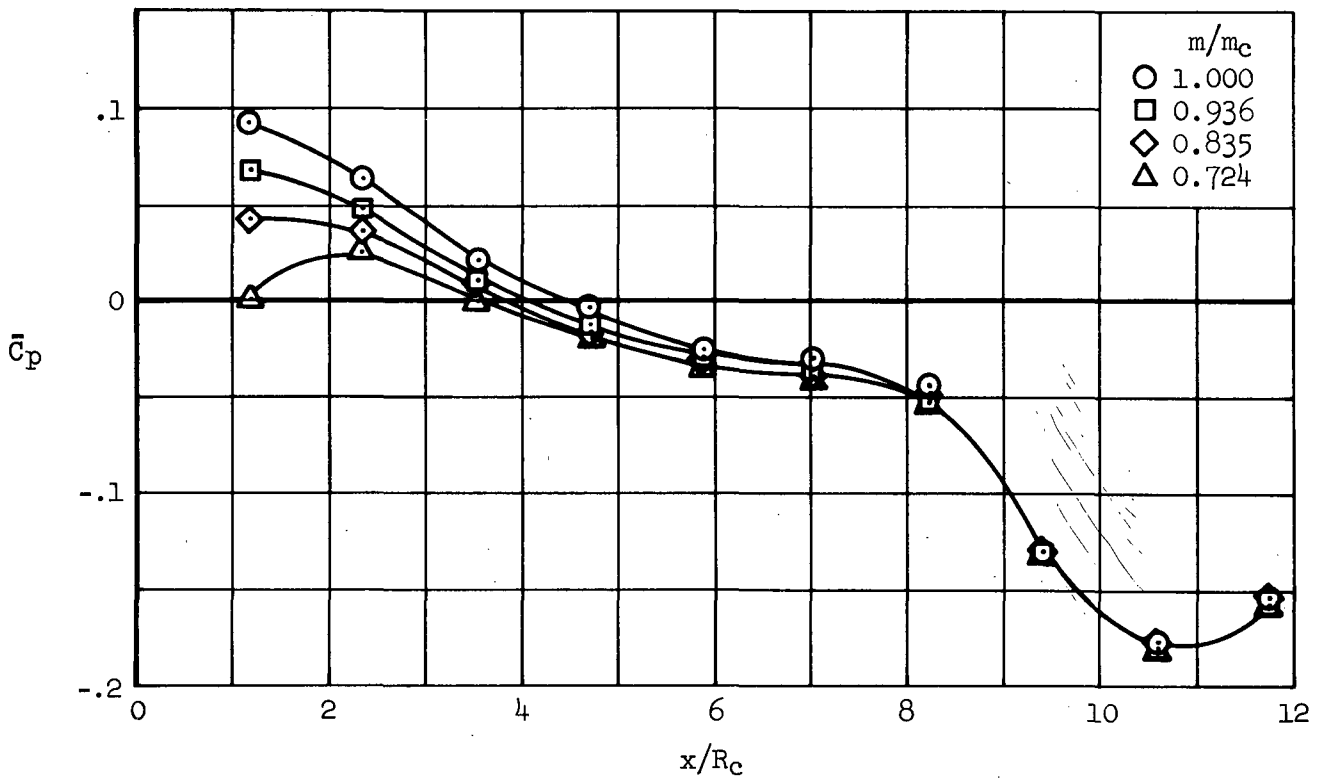

(a) $M_\infty = 1.40$

Figure 17.- Isolated nacelle surface pressure distributions; nacelle N_1, $\alpha = 0°$.

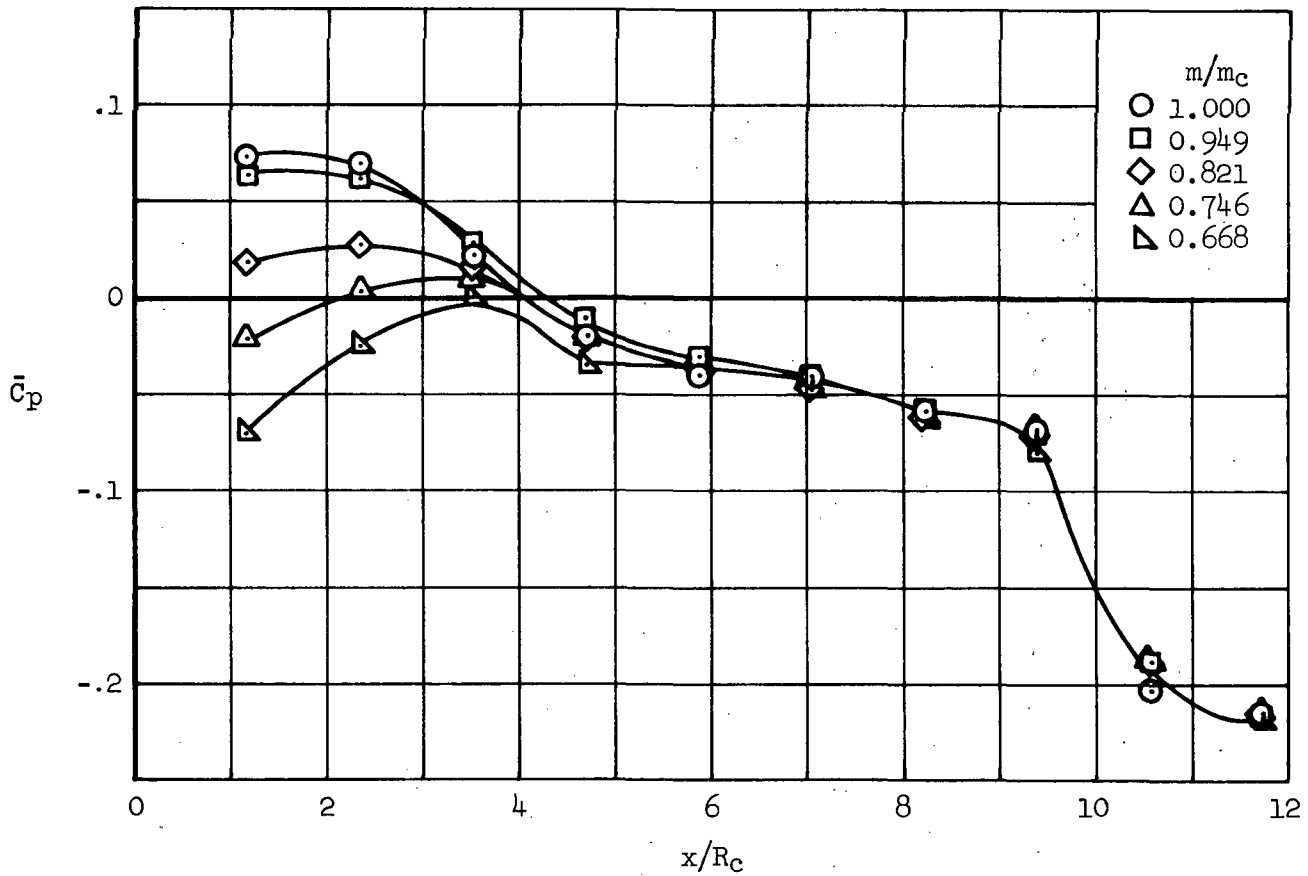

(b) $M_\infty = 1.15$

Figure 17.- Continued.

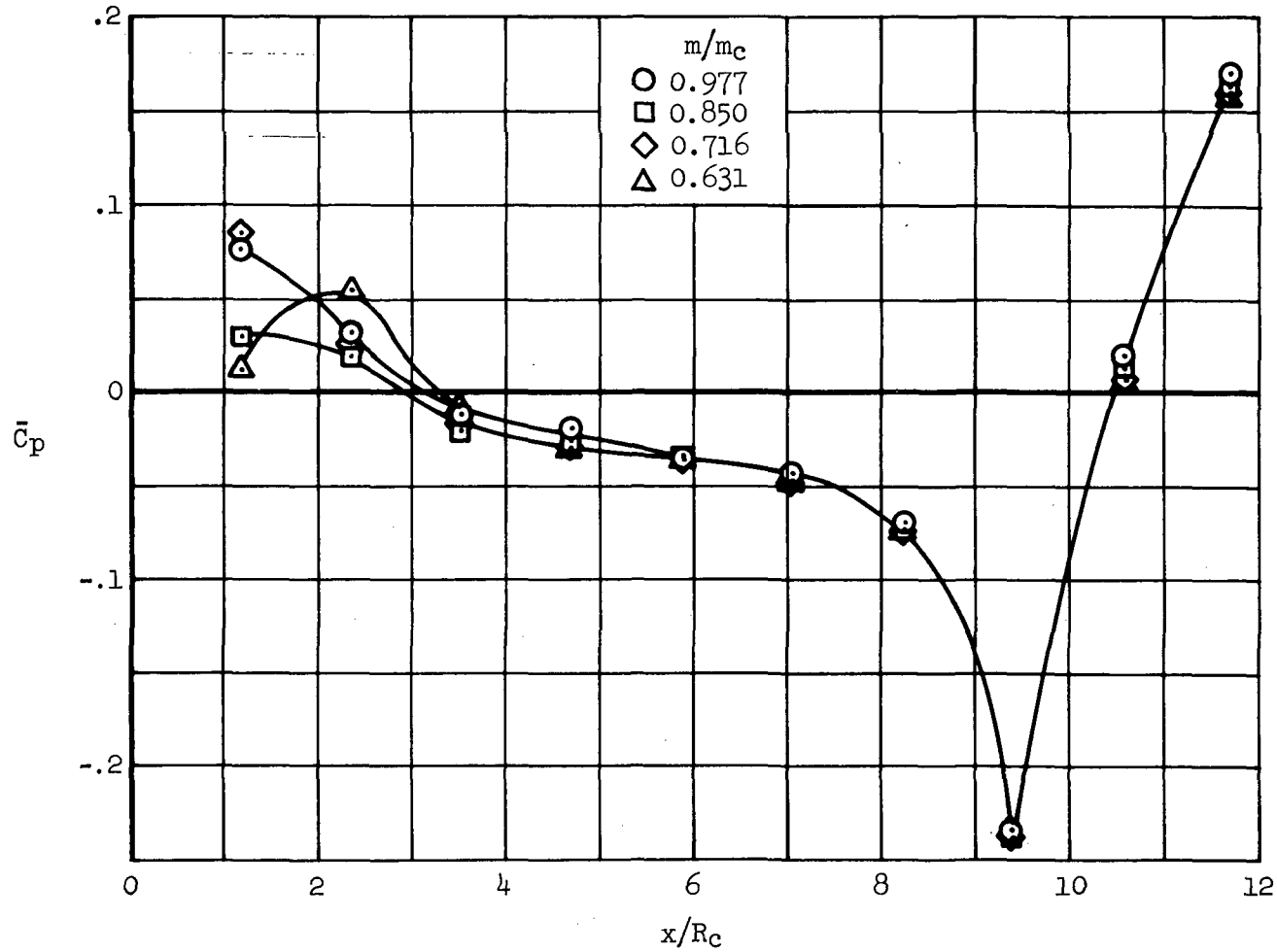

(c) $M_\infty = 0.98$

Figure 17.- Continued.

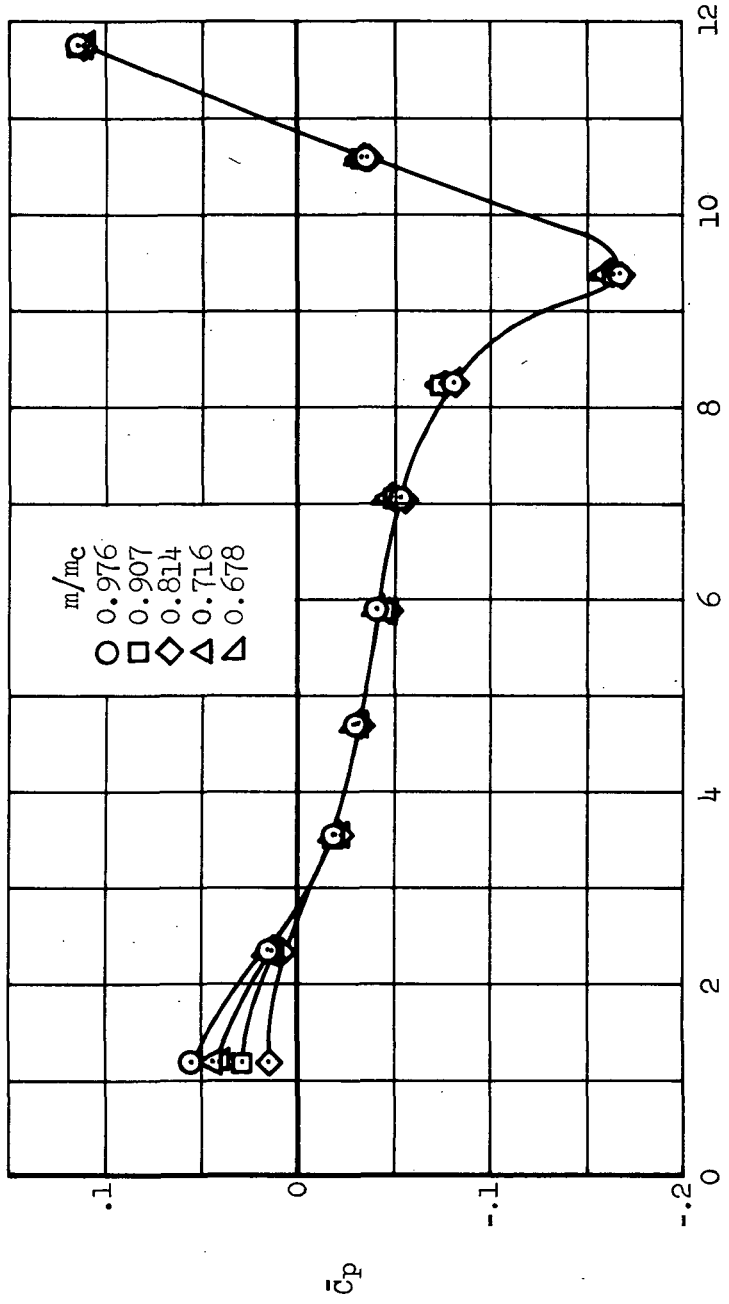

(d) $M_\infty = 0.90$

Figure 17.- Concluded.

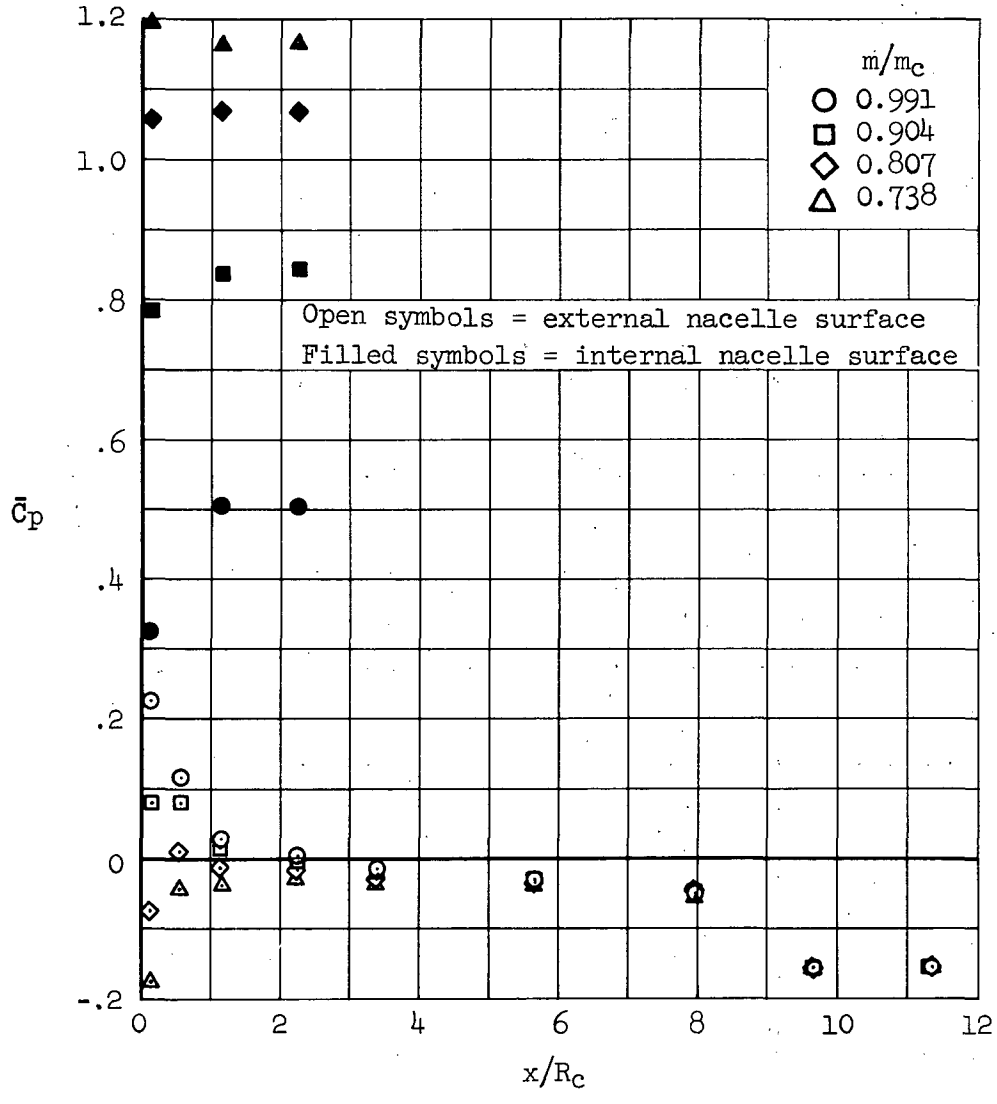

(a) $M_\infty = 1.40$

Figure 18.- Isolated nacelle surface pressure distributions; nacelle N_2, $\alpha = 0°$.

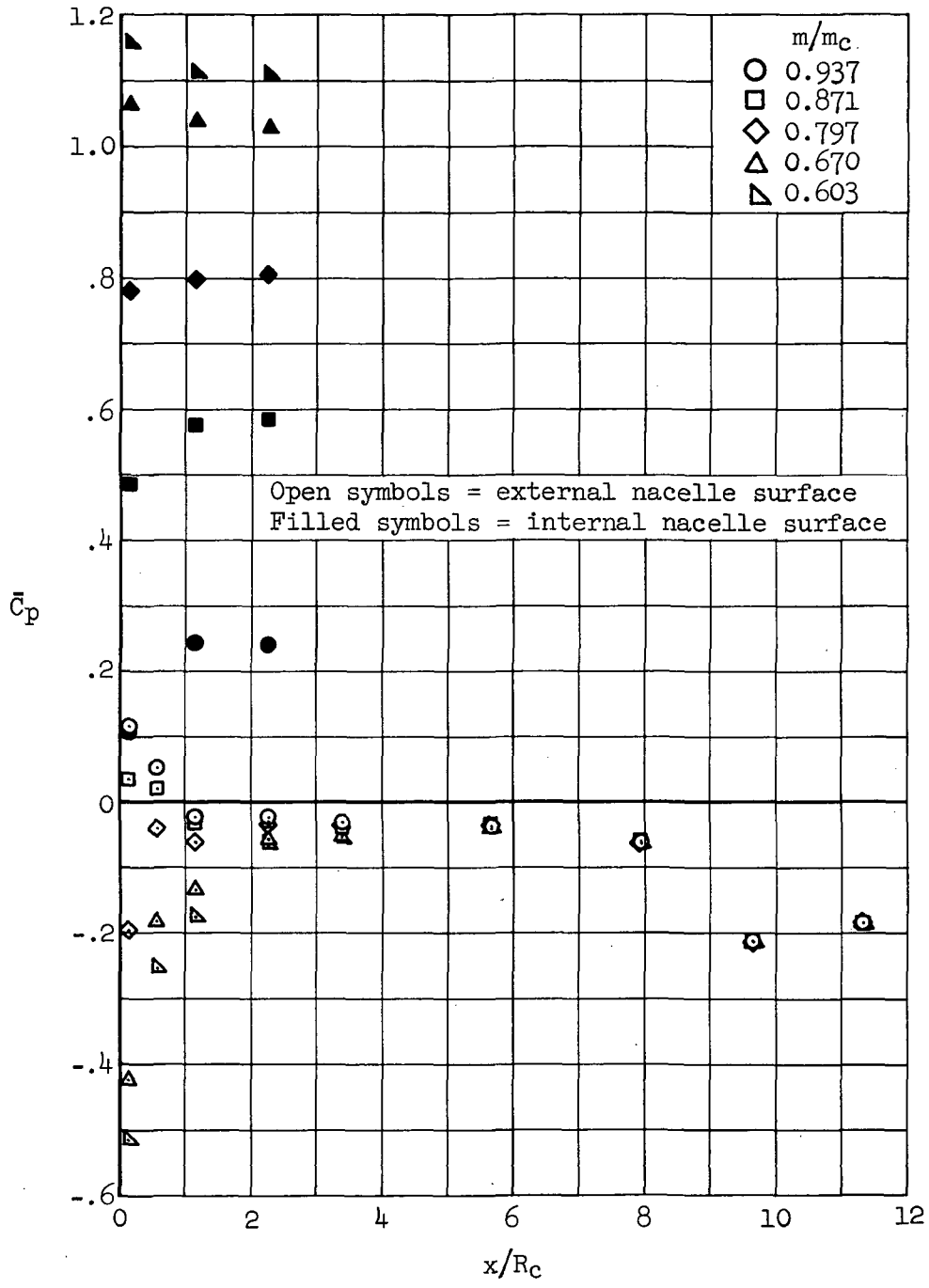

(b) $M_\infty = 1.15$

Figure 18.- Continued.

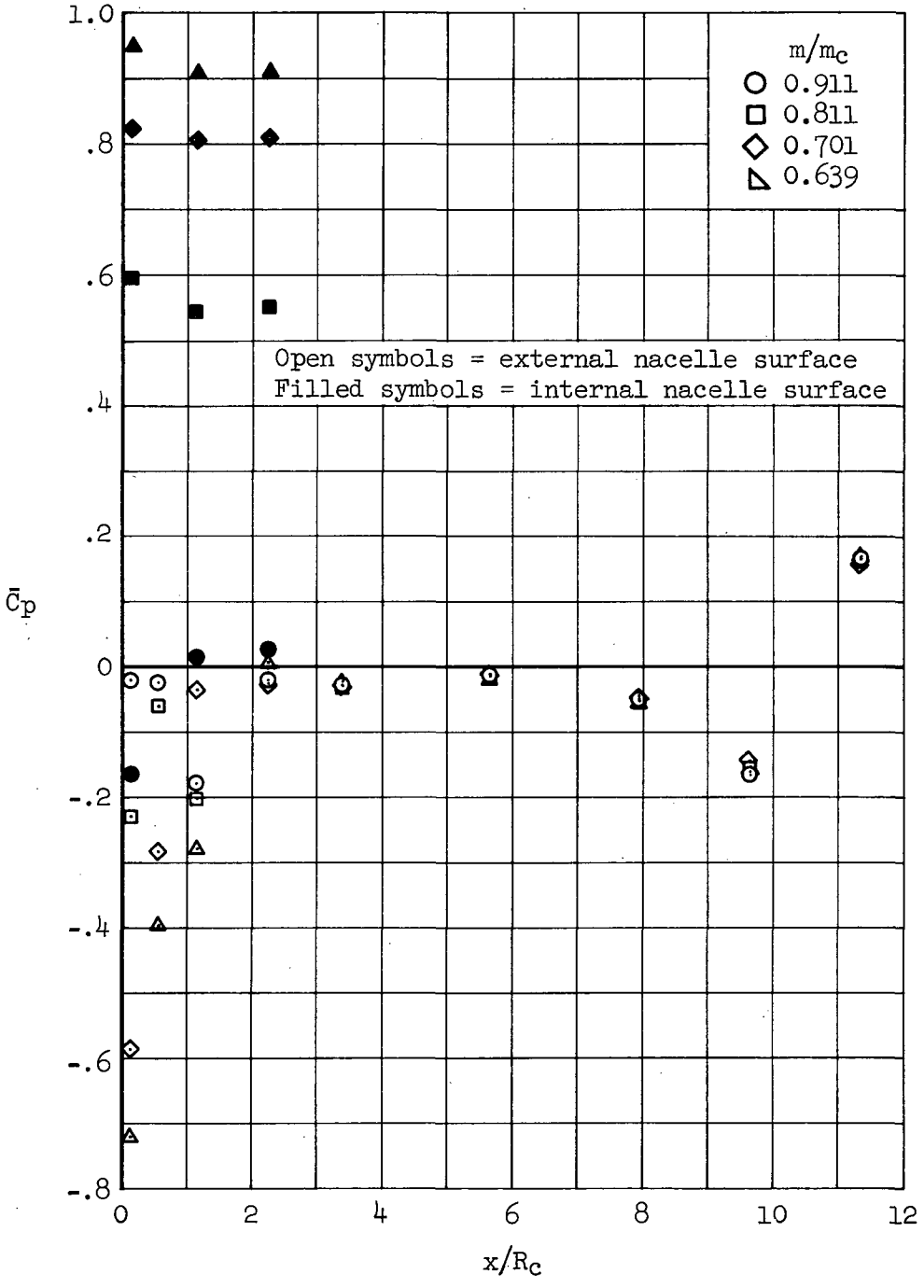

(c) $M_\infty = 0.98$

Figure 18.- Continued.

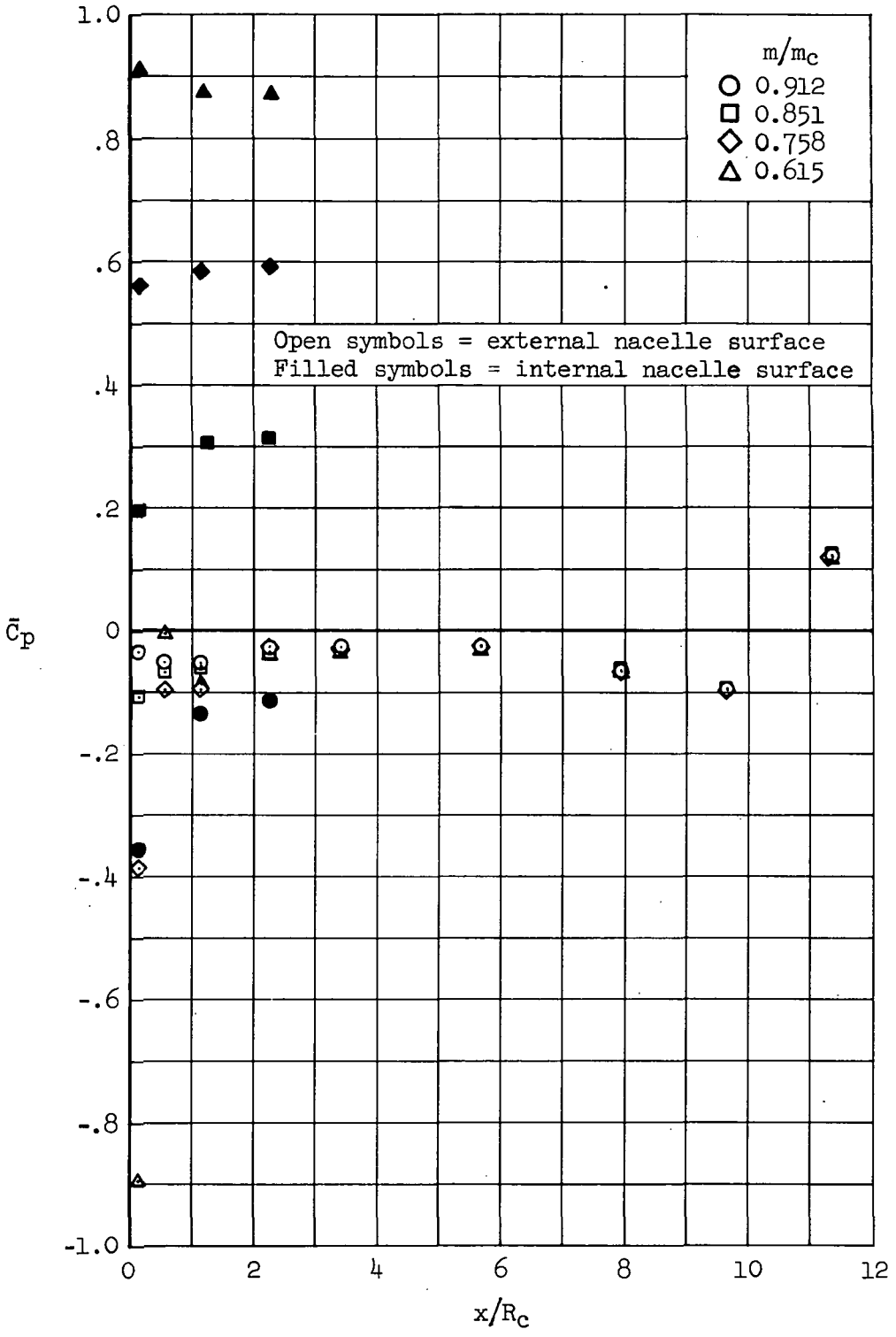

(d) $M_\infty = 0.90$

Figure 18.- Concluded.

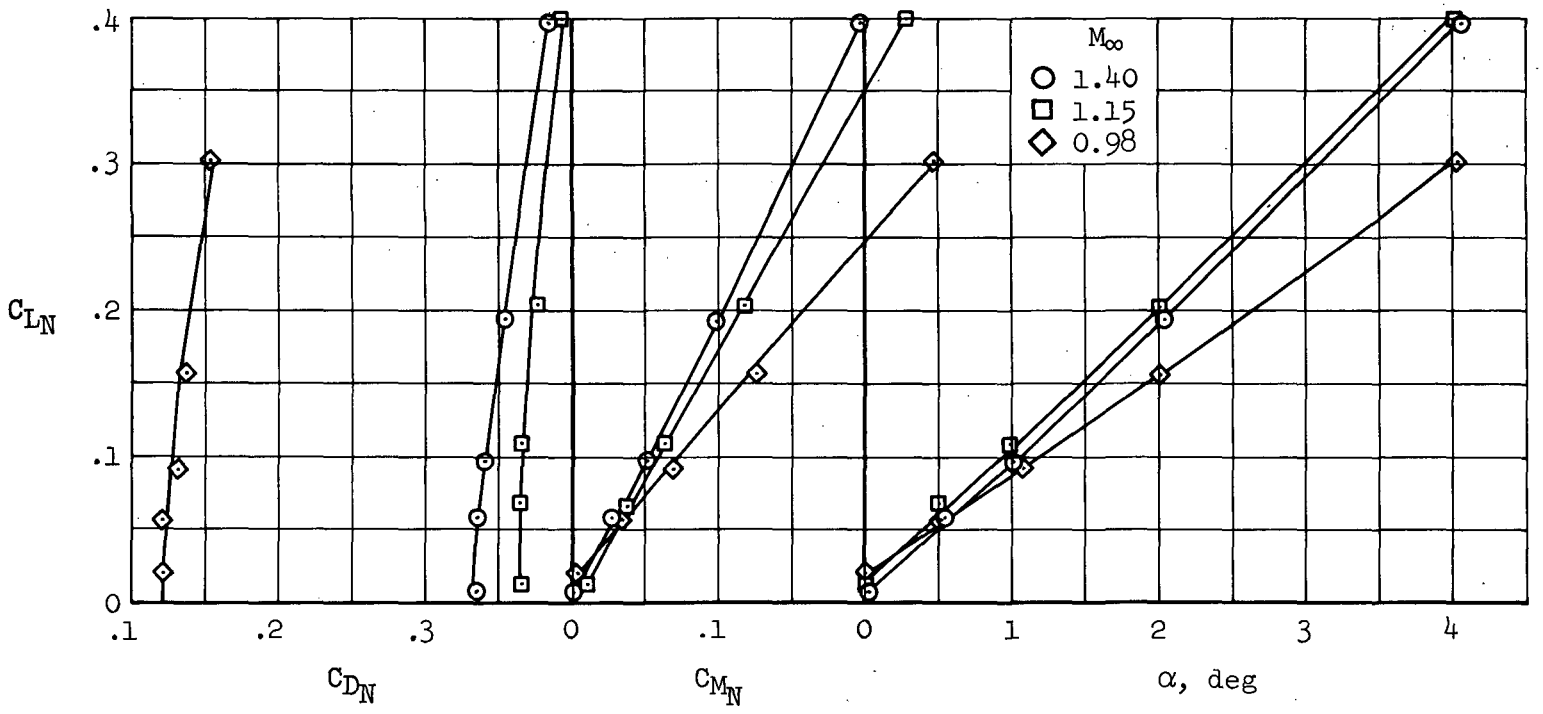

Figure 19.- Isolated nacelle longitudinal characteristics; nacelle N_1, maximum m/m_c.

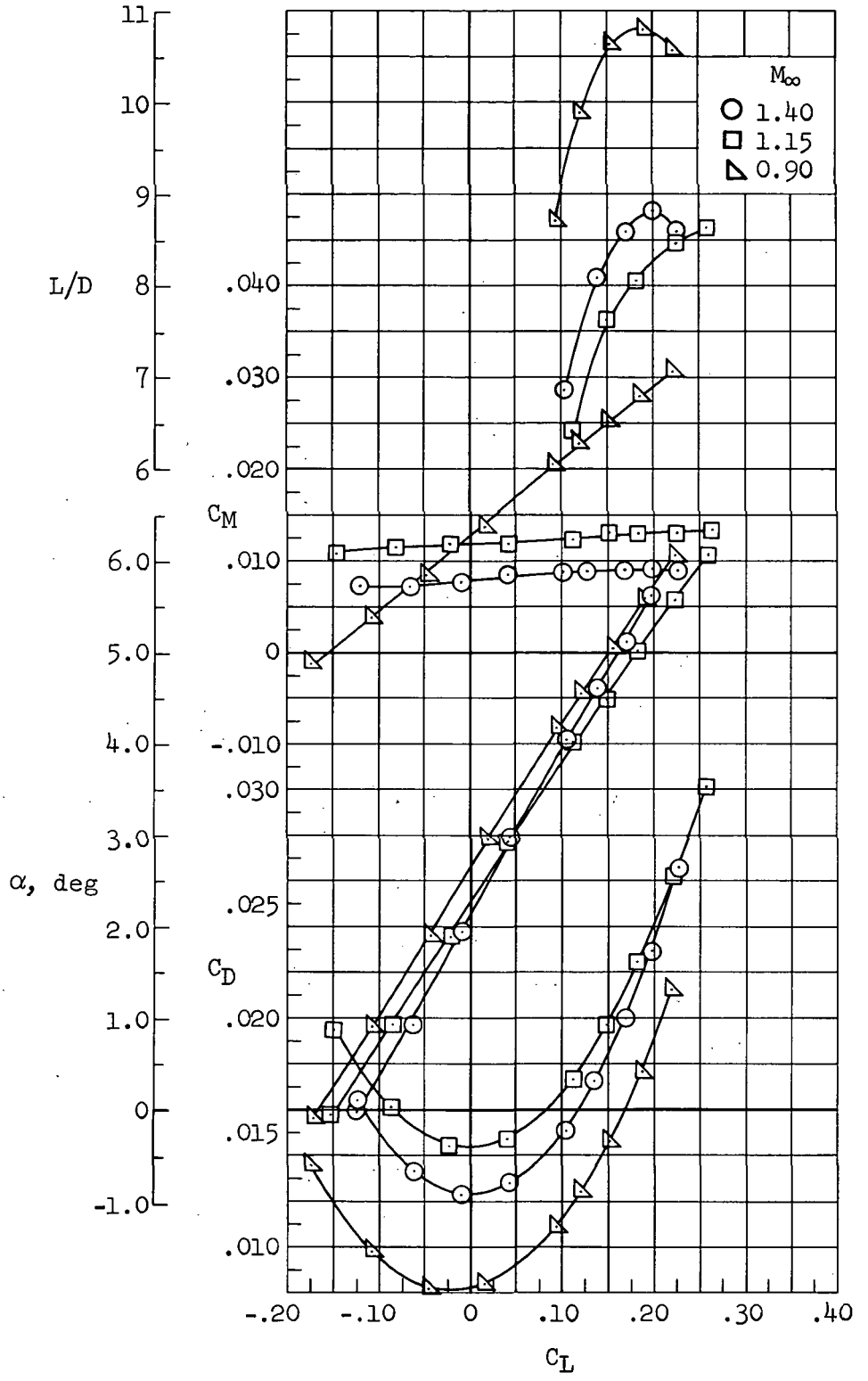

Figure 20.- Isolated wing-body longitudinal characteristics; configuration WB, X_{ma} = 132.1 cm (52 in.).

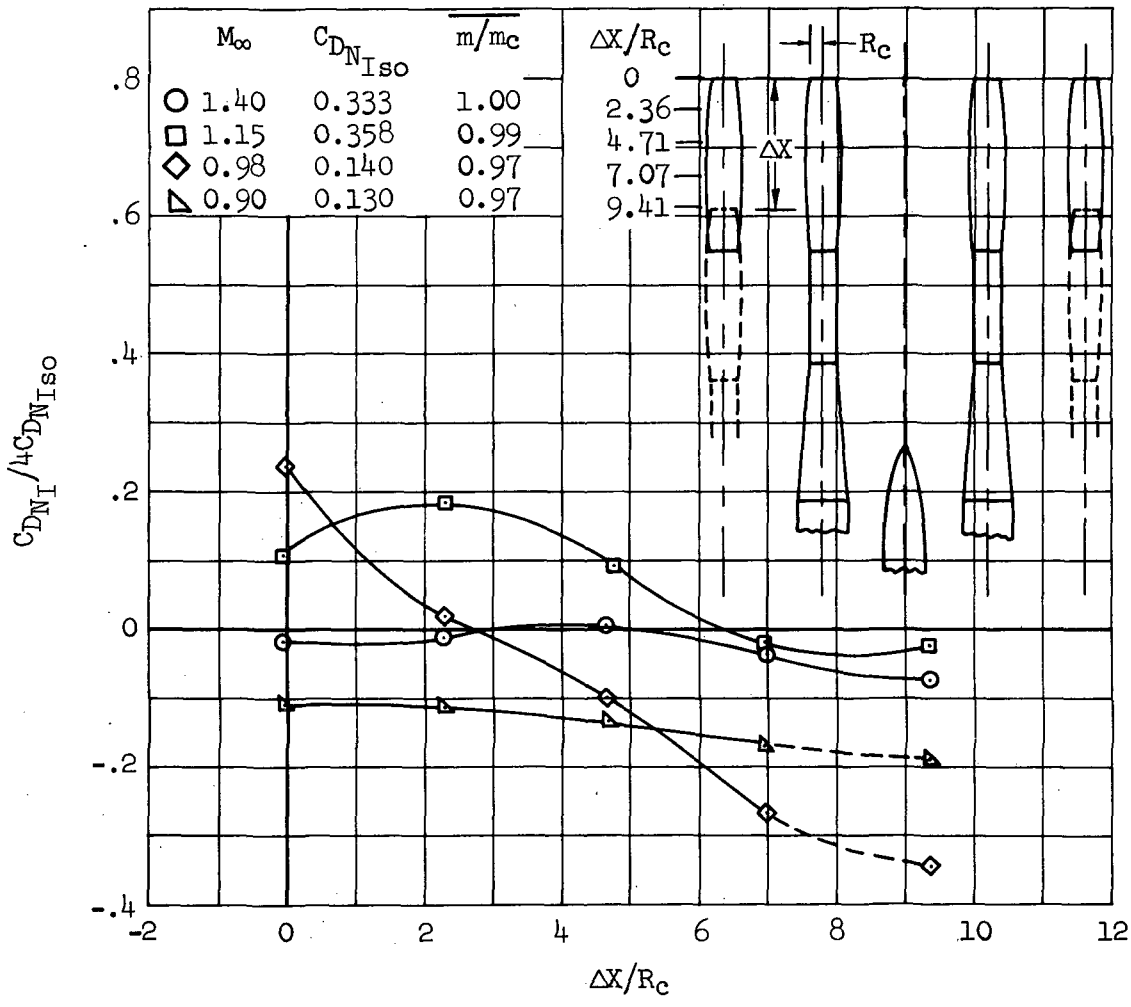

Figure 21.- Nacelle-nacelle interference drag; configuration N_1N_1, $\alpha = 0°$, $y_i' = 0.25$, $y_o' = 0.55$, maximum m/m_c.

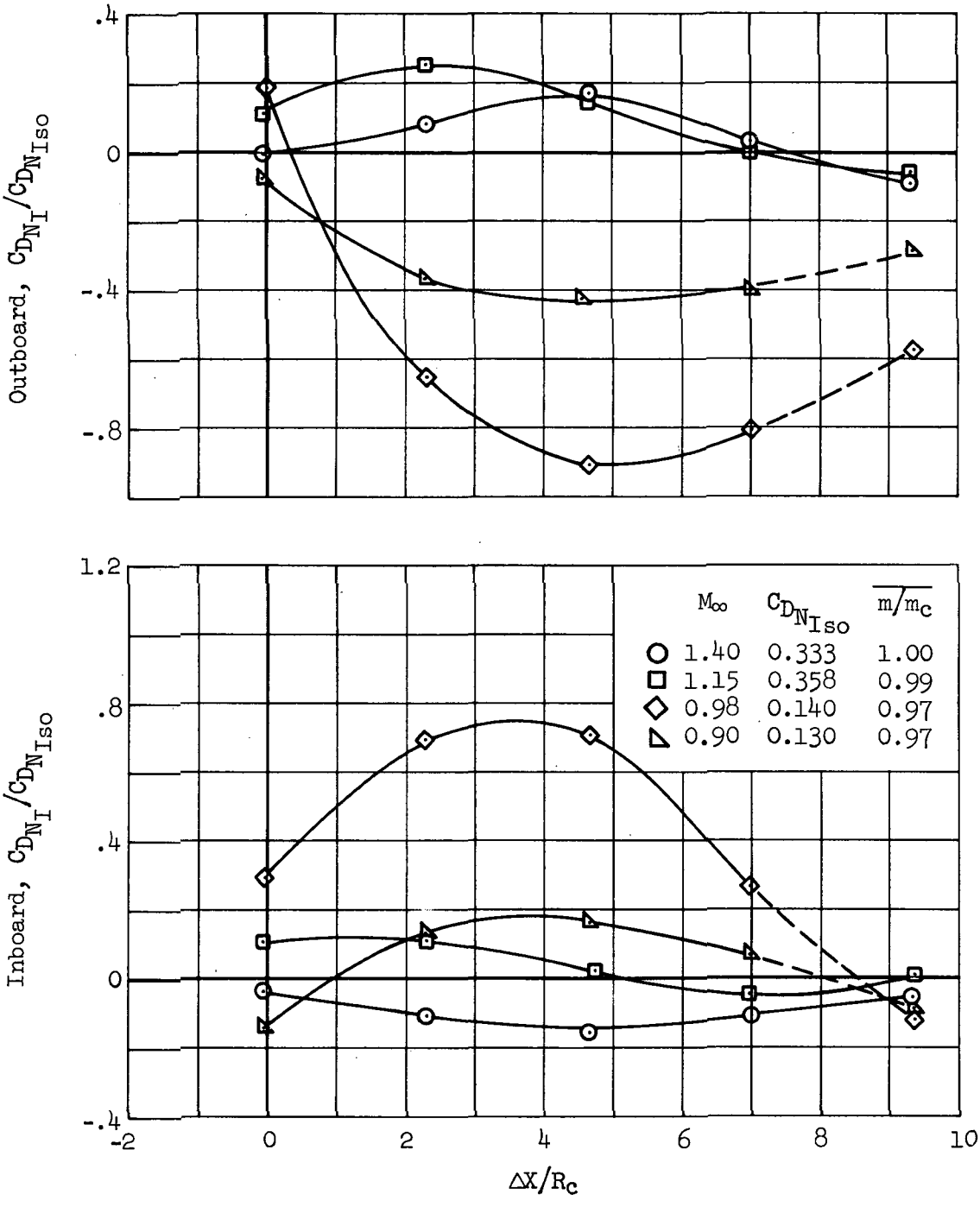

Figure 22.- Interference drag on individual nacelles; configuration N_1N_1, $\alpha = 0°$, $y_i' = 0.25$, $y_o' = 0.55$, maximum m/m_c.

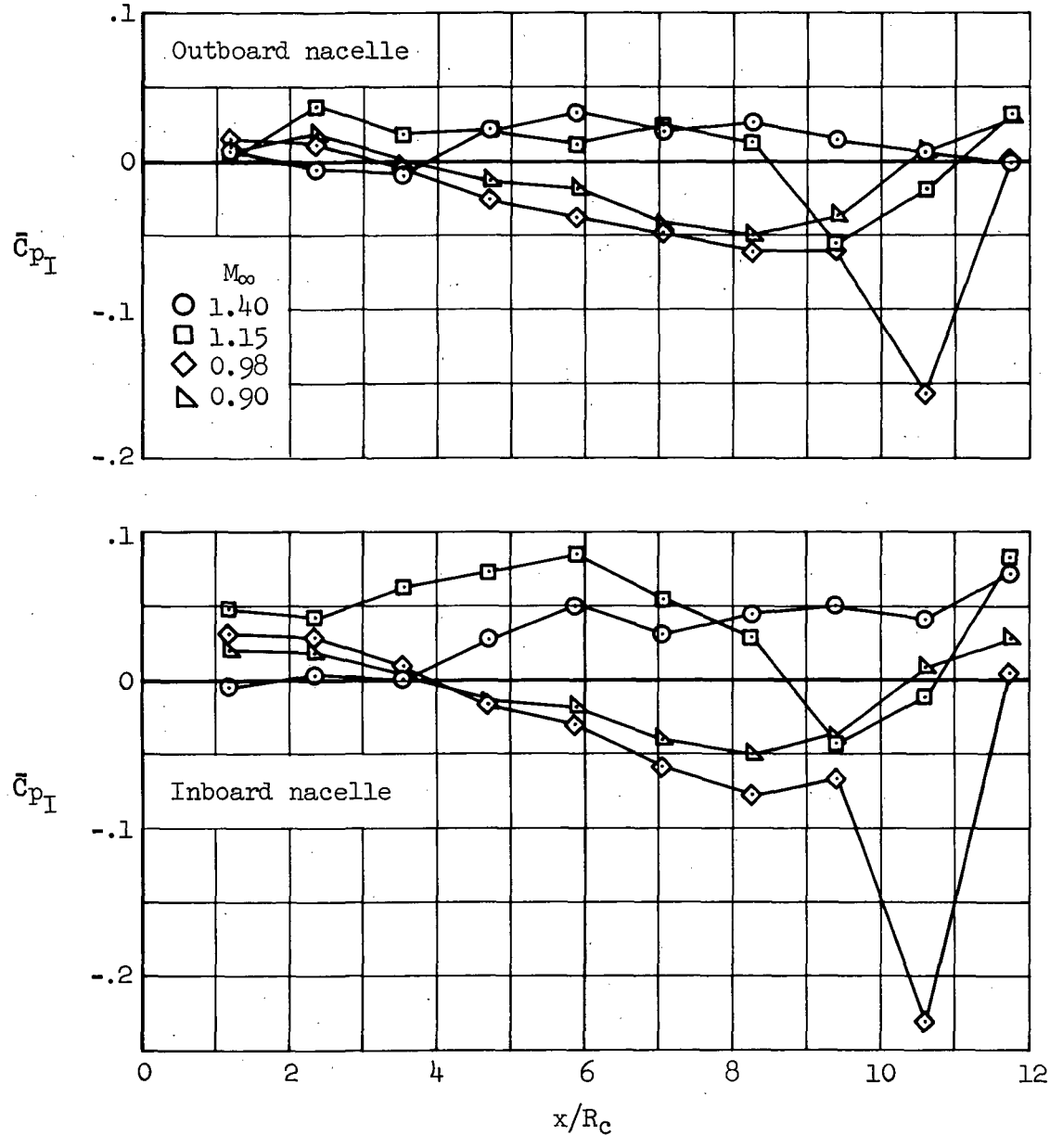

(a) Inboard and outboard nacelles, $\bar{C}_{p_I}$.

Figure 23.- Nacelle interference pressure distributions; configuration N_1N_1, $\alpha = 0°$, $\Delta X/R_c = 0$, $y_i' = 0.25$, $y_o' = 0.55$, maximum m/m_c.

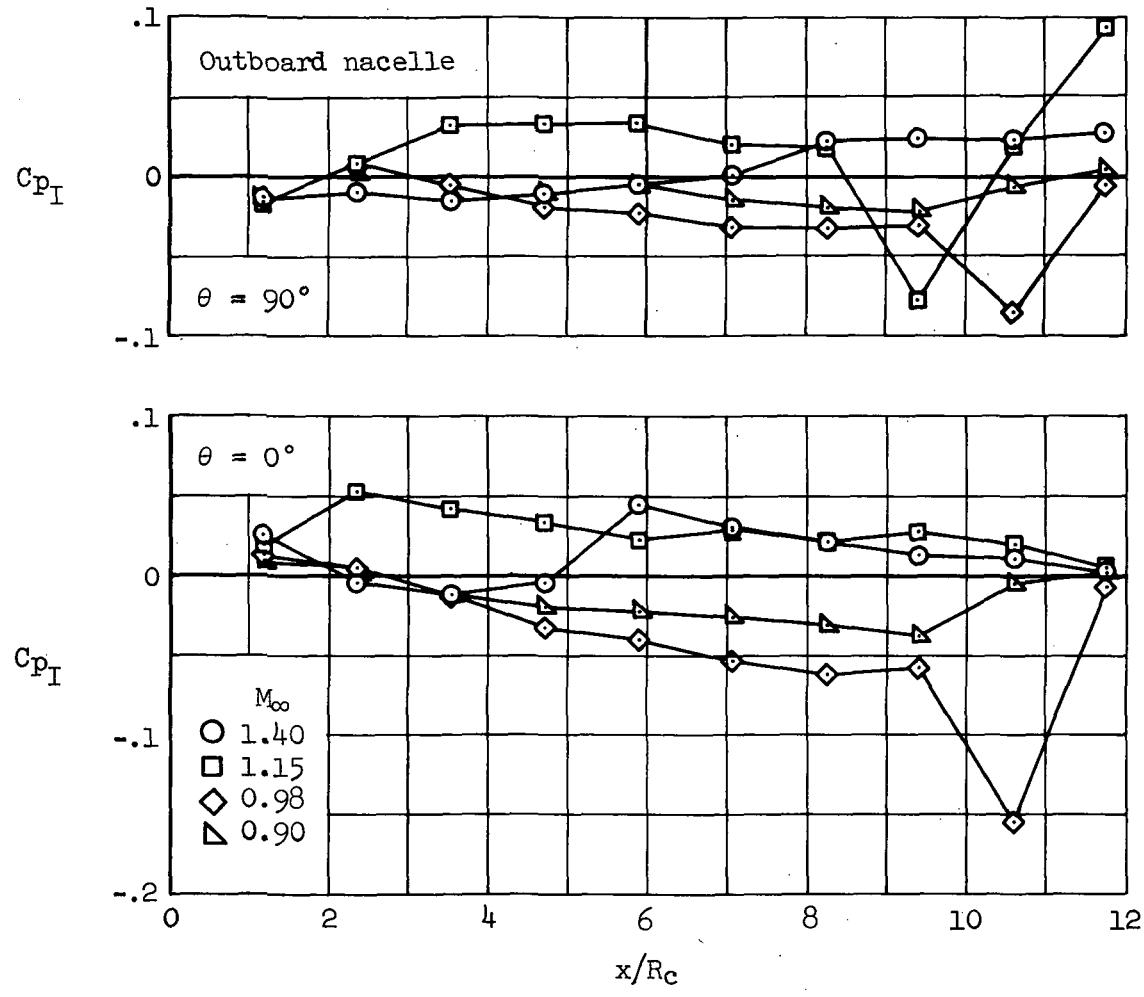

(b) Outboard nacelle, C_{p_I} at θ = 0° and 90°.

Figure 23.- Continued.

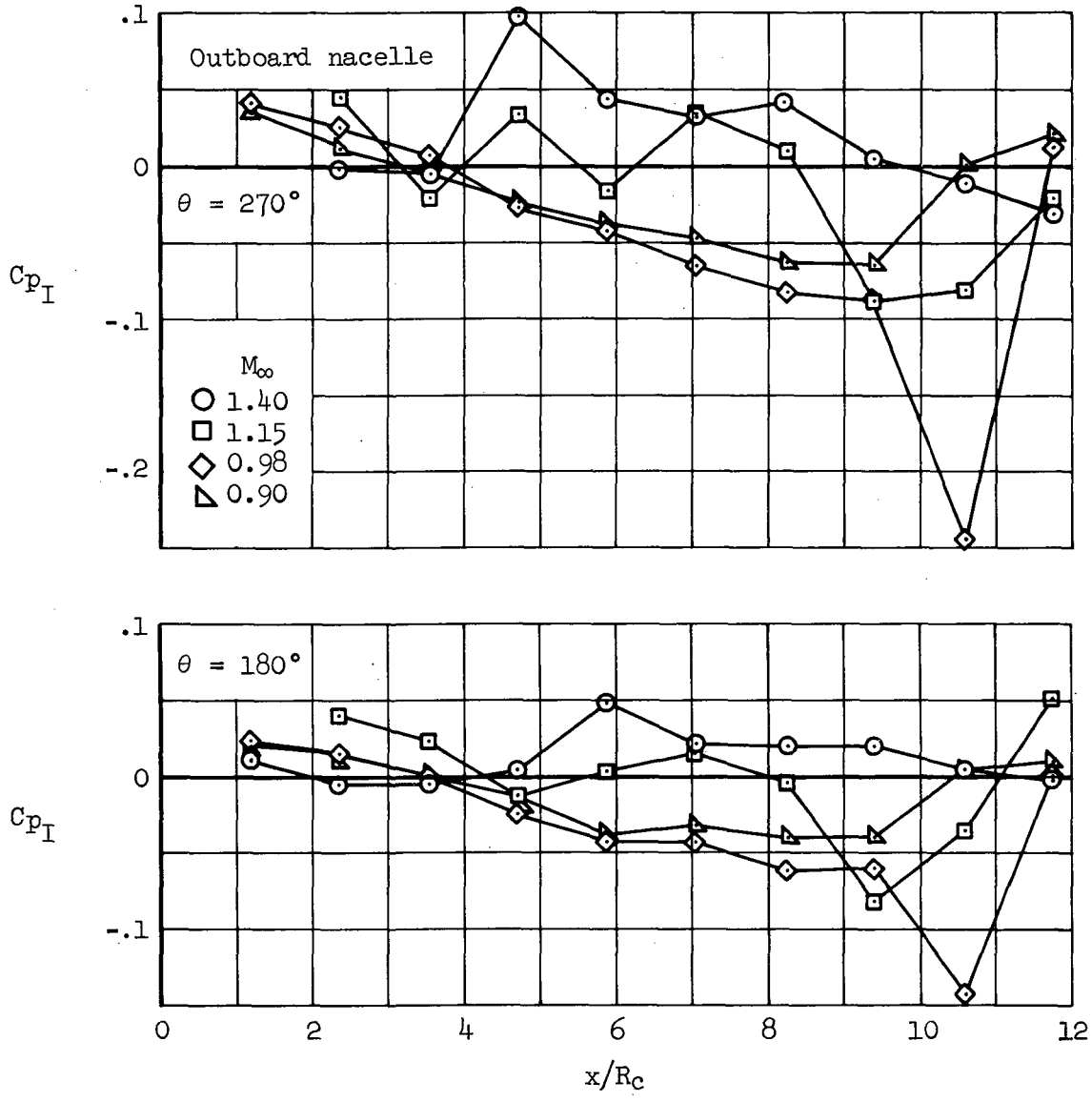

(c) Outboard nacelle, C_{p_I} at θ = 180° and 270°.

Figure 23.- Continued.

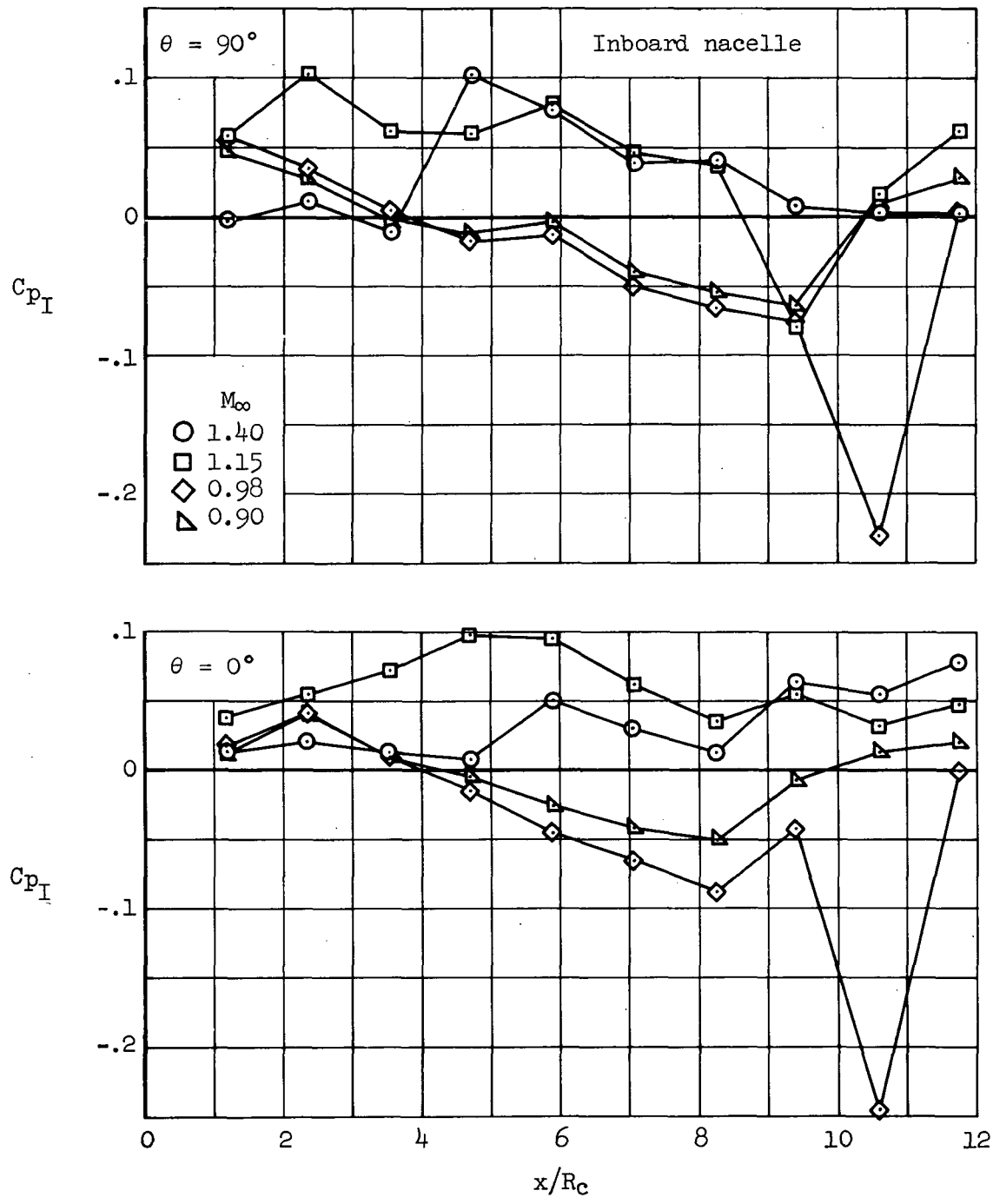

(d) Inboard nacelle, C_{p_I} at $\theta = 0°$ and 90°.

Figure 23.- Continued.

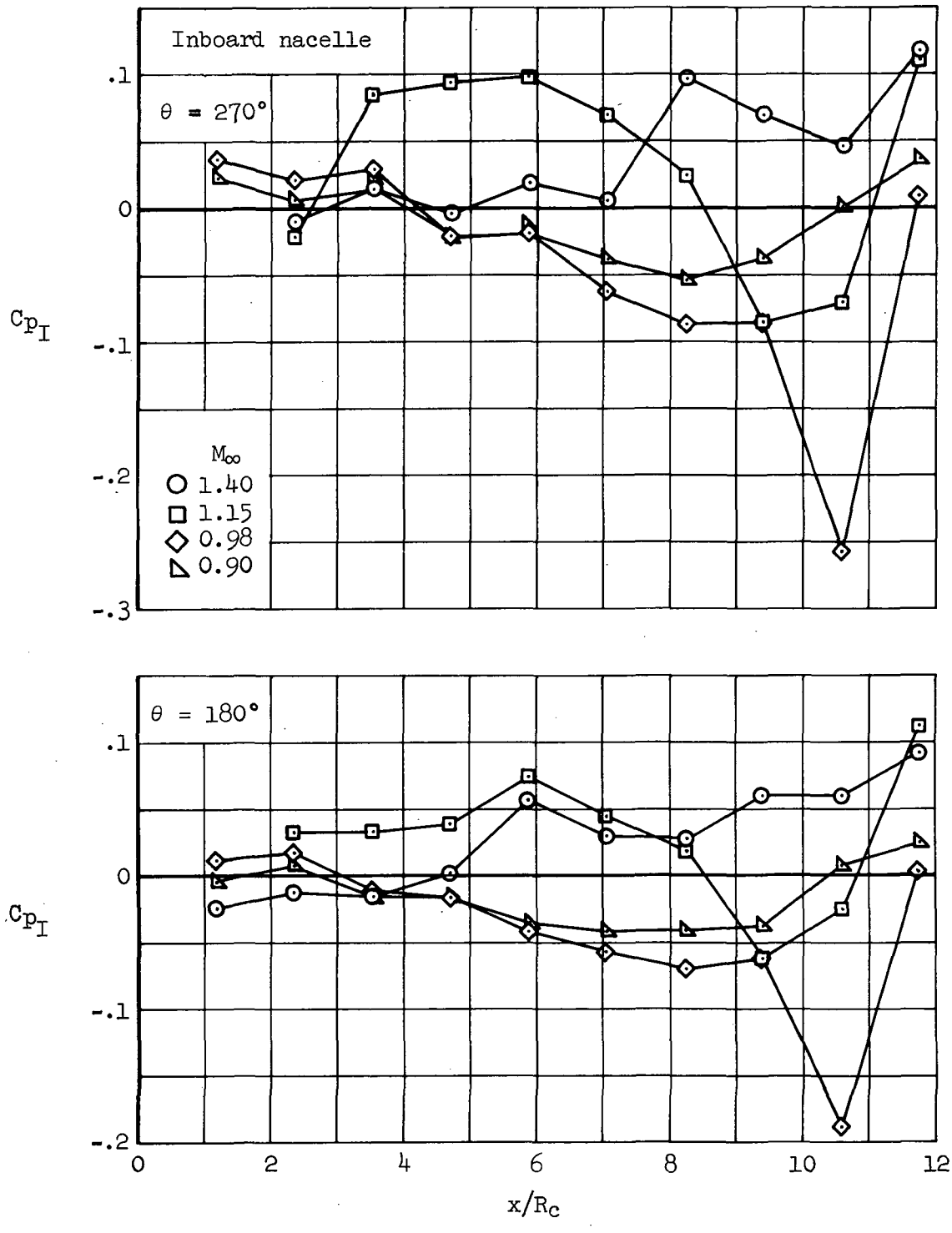

(e) Inboard nacelle, C_{p_I} at θ = 180° and 270°.

Figure 23.- Concluded.

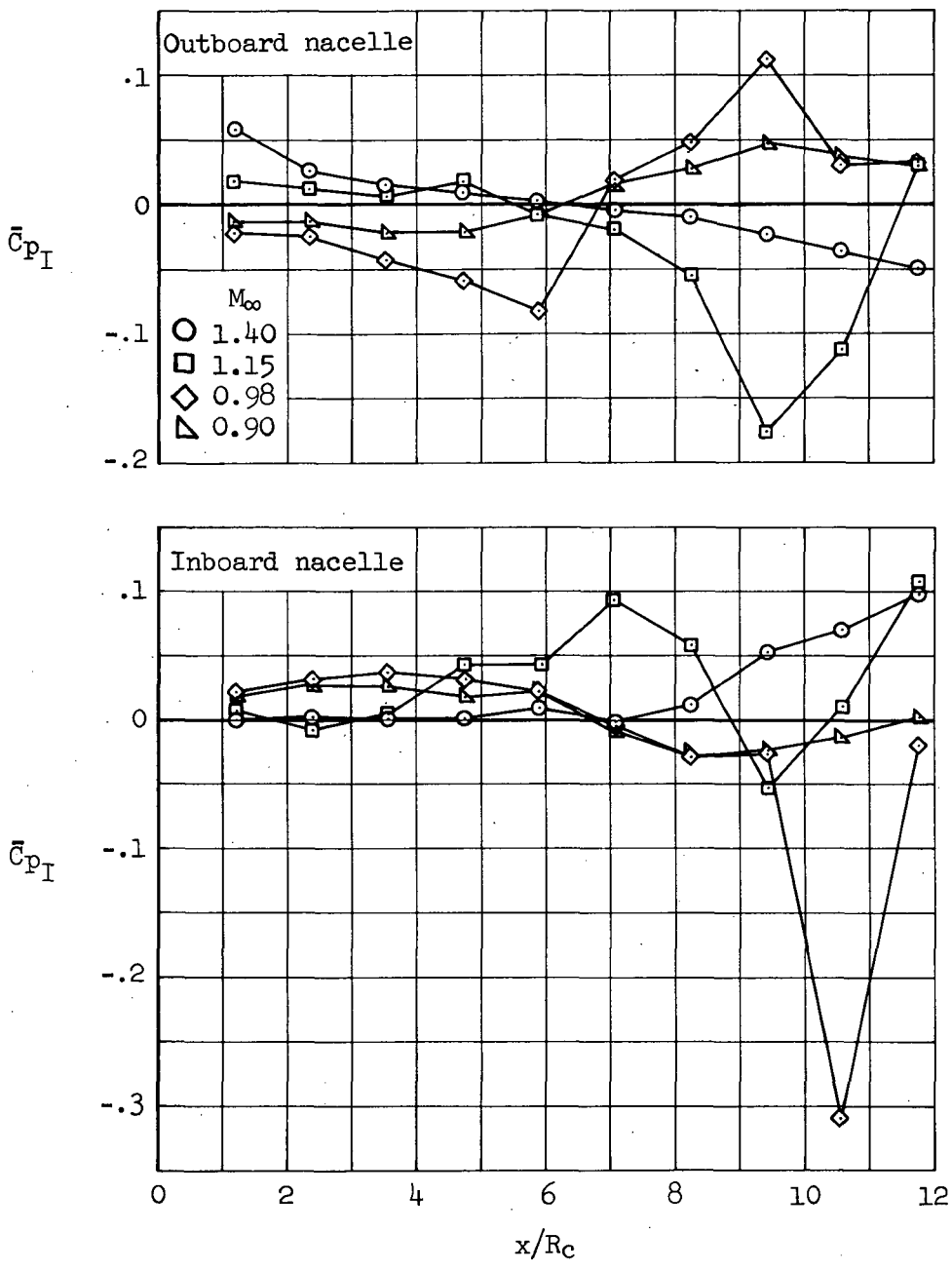

(a) Inboard and outboard nacelles, $\bar{C}_{p_I}$.

Figure 24.- Nacelle interference pressure distributions; configuration N_1N_1, $\alpha = 0°$, $\Delta X/R_c = 4.71$, $y_j' = 0.25$, $y_o' = 0.55$, maximum m/m_c.

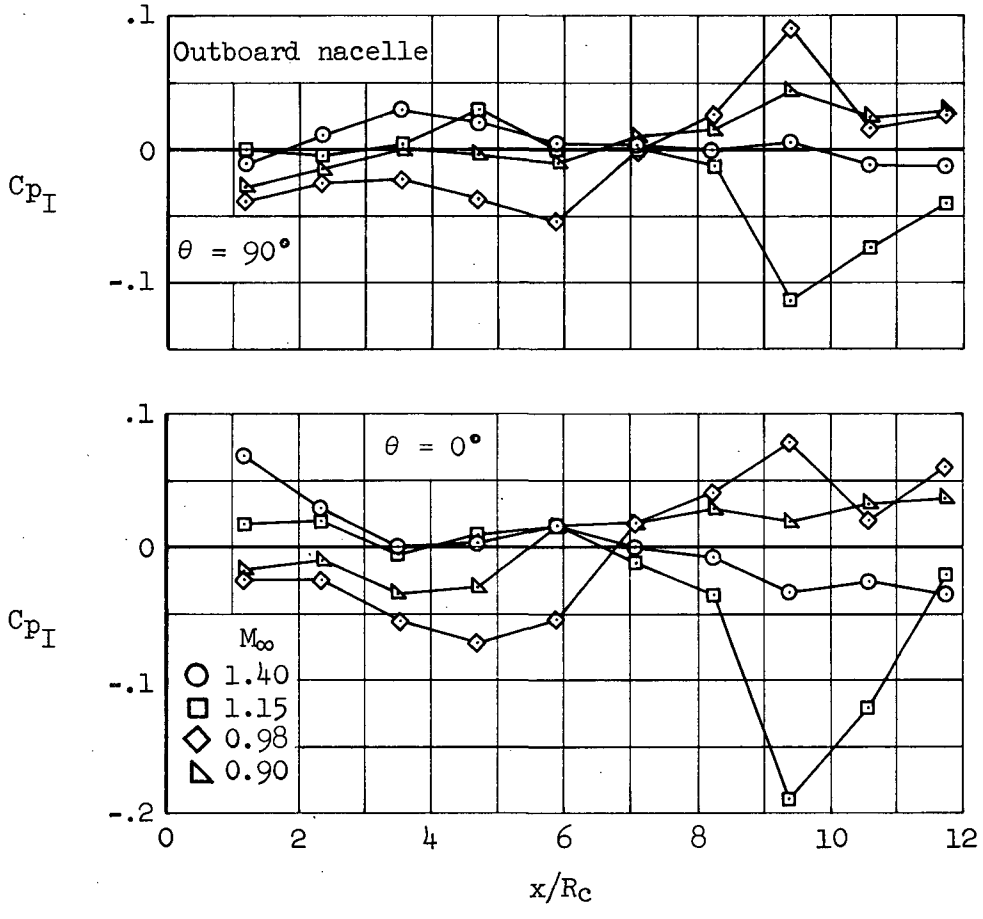

(b) Outboard nacelle, C_{p_I} at θ = 0° and 90°.

Figure 24.- Continued.

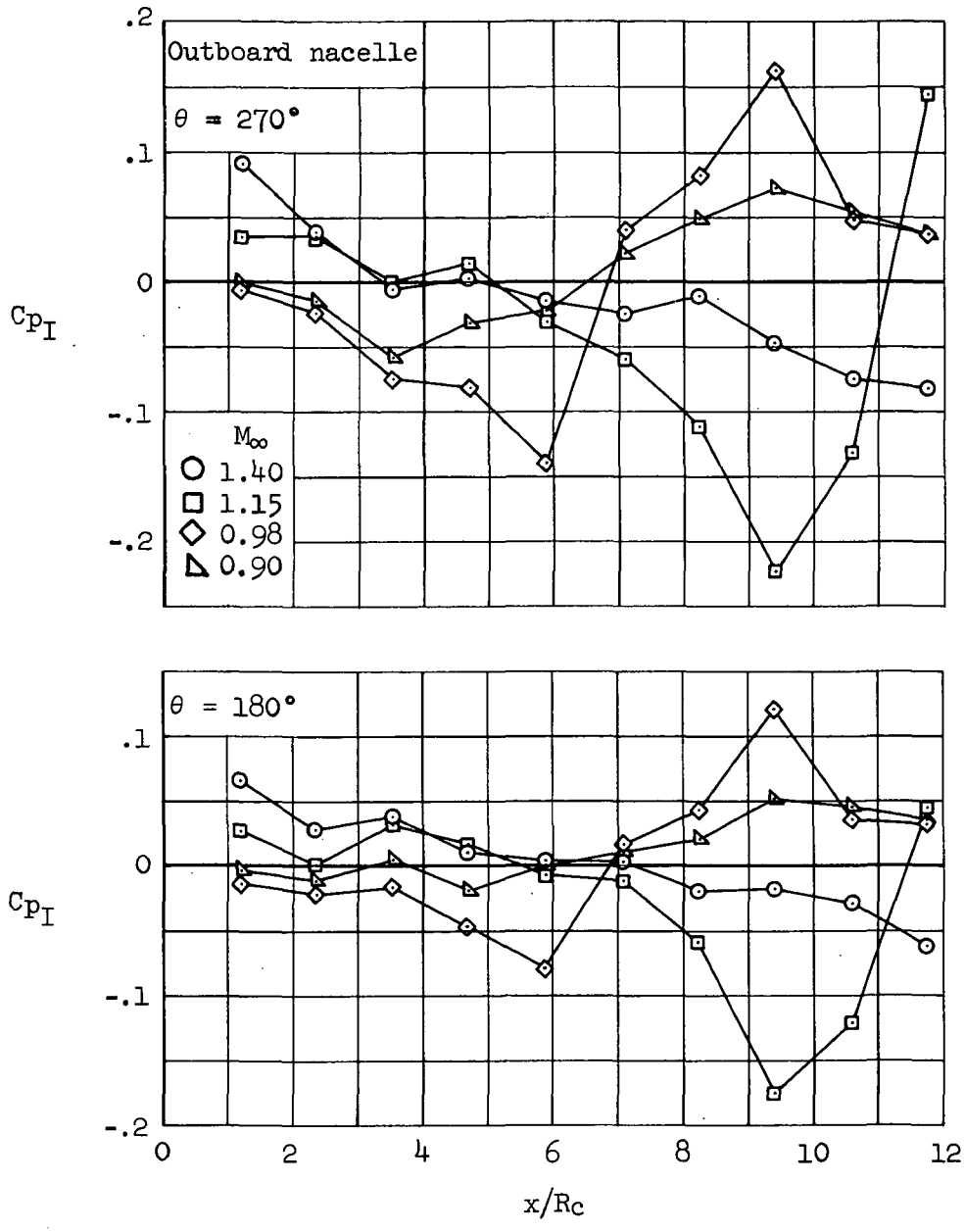

(c) Outboard nacelle, C_{p_I} at θ = 180° and 270°.

Figure 24.- Continued.

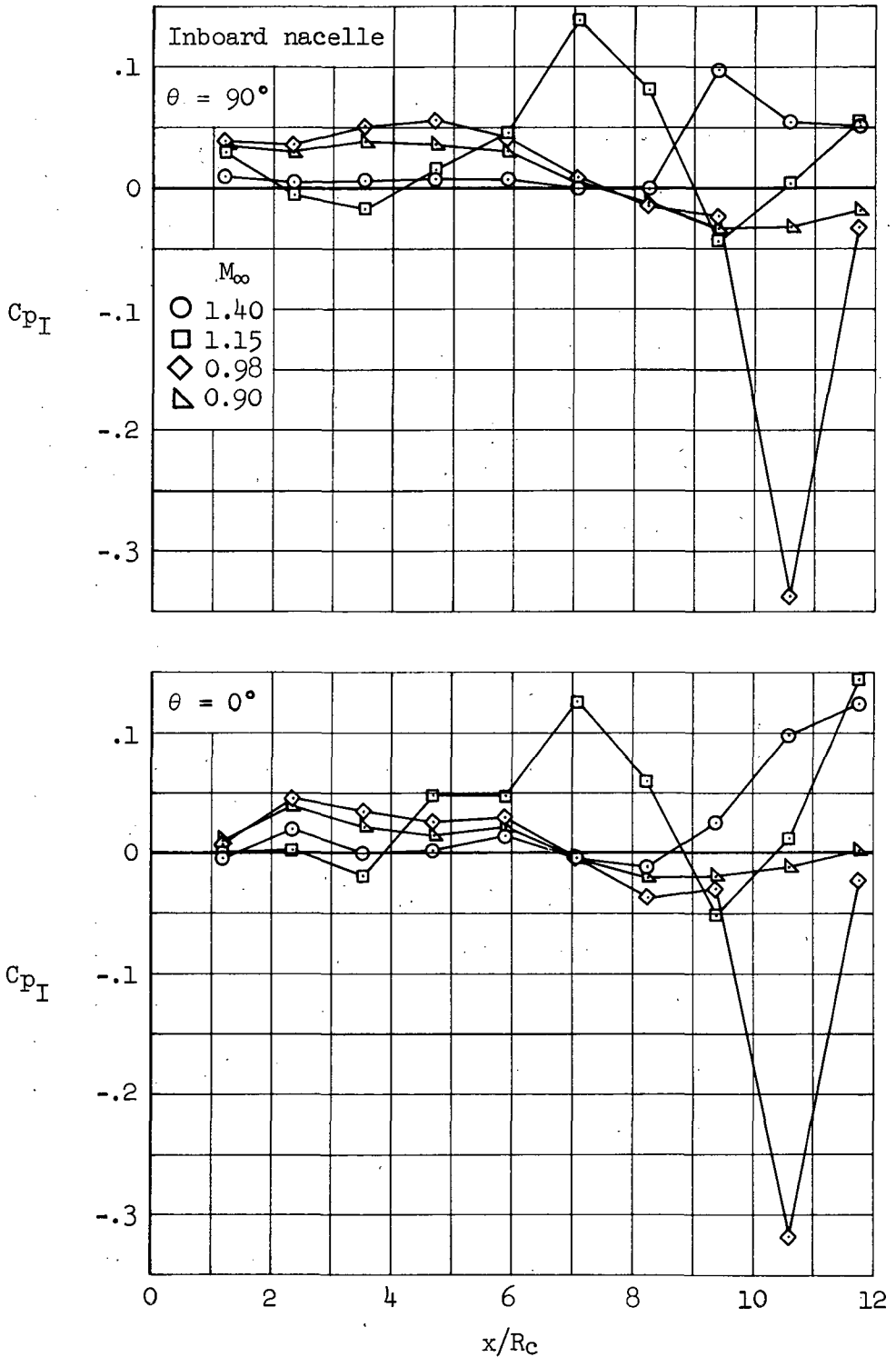

(d) Inboard nacelle, C_{p_I} at θ = 0° and 90°.

Figure 24.- Continued.

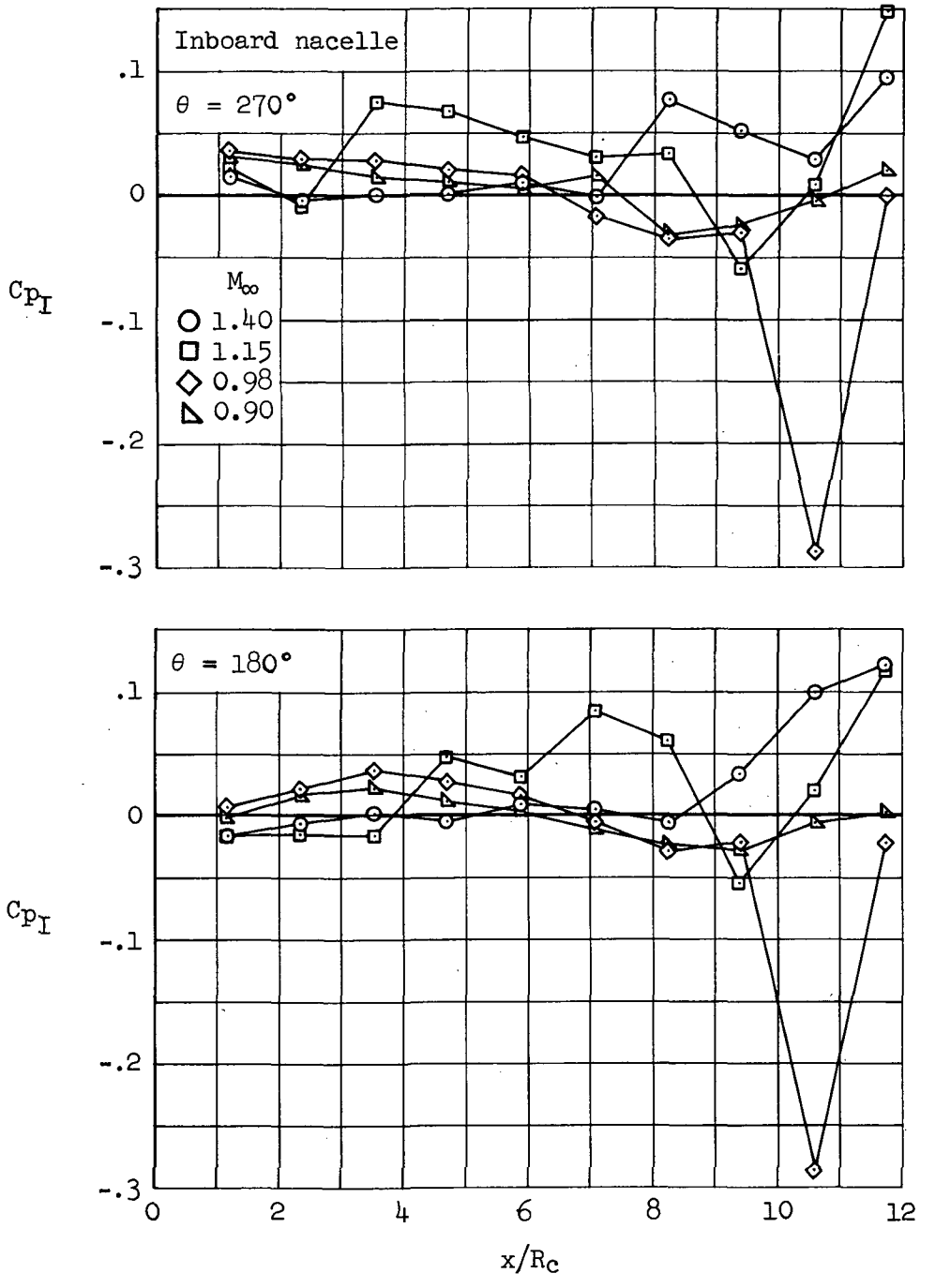

(e) Inboard nacelle, C_{p_I} at θ = 180° and 270°.

Figure 24.- Concluded.

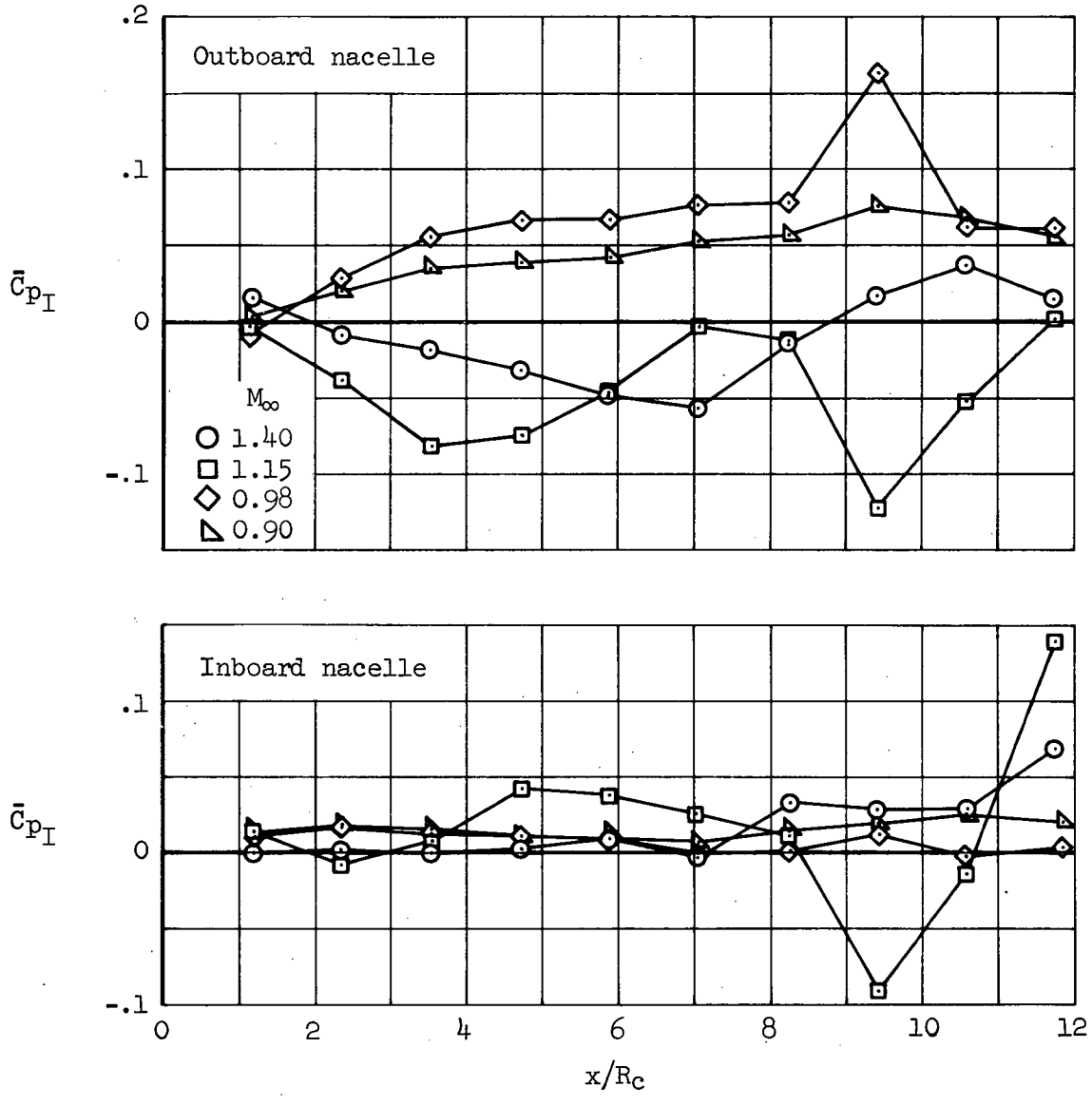

(a) Inboard and outboard nacelles, $\bar{C}_{p_I}$.

Figure 25.- Nacelle interference pressure distributions; configuration N_1N_1, $\alpha = 0°$, $\Delta X/R_c = 9.41$, $y_i' = 0.25$, $y_o' = 0.55$, maximum m/m_c.

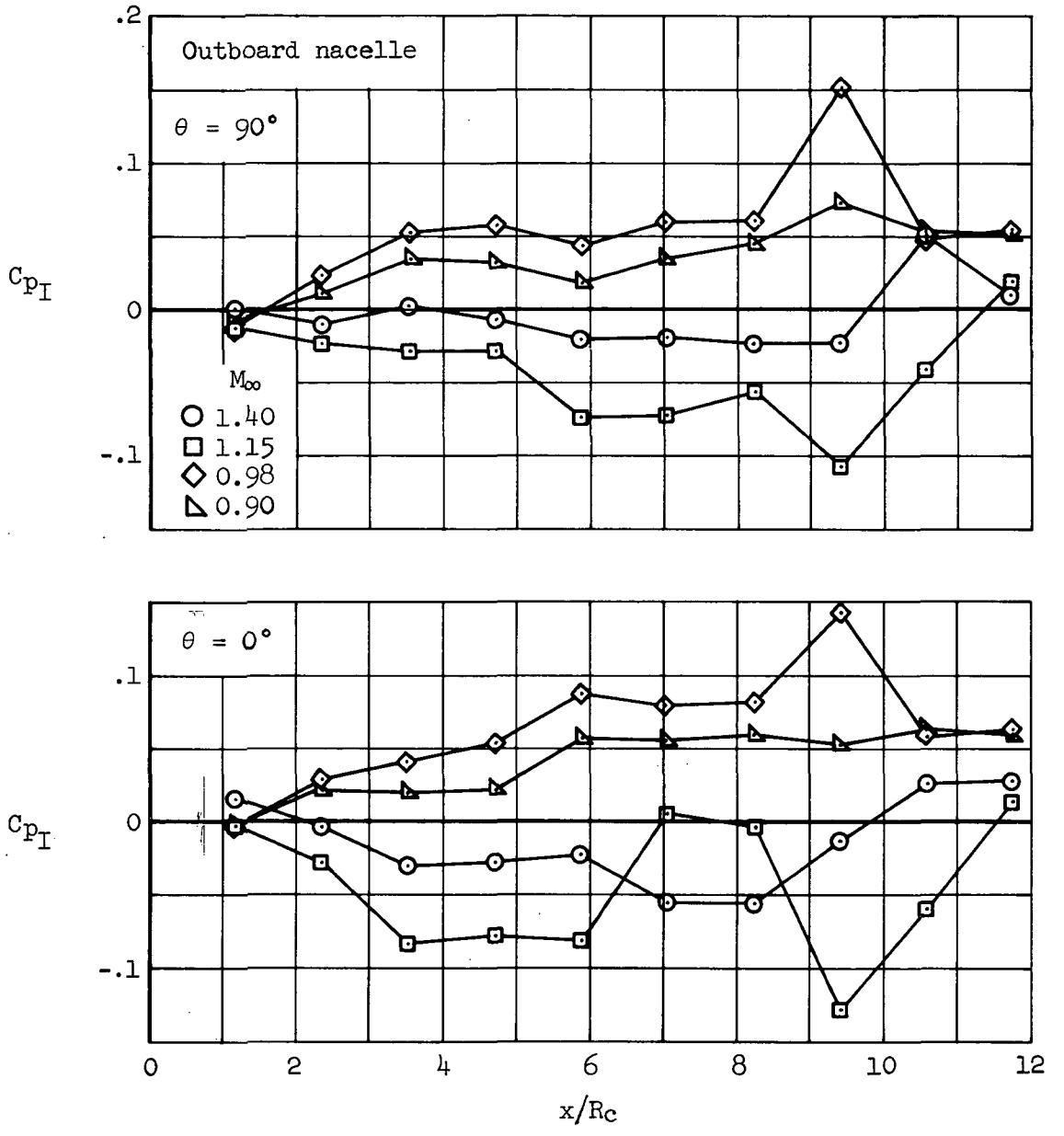

(b) Outboard nacelle; C_{p_I} at θ = 0° and 90°.

Figure 25.- Continued.

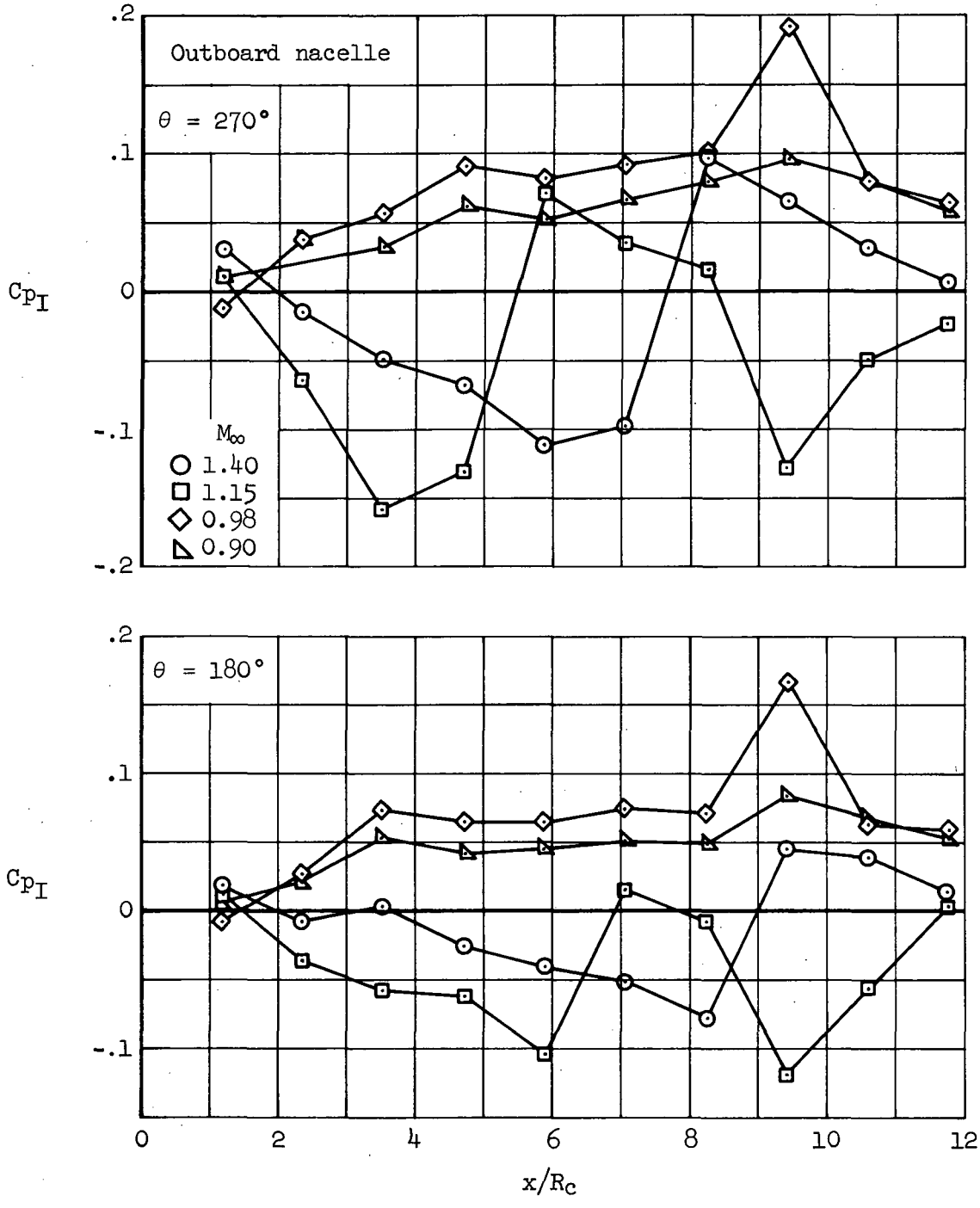

(c) Outboard nacelle, C_{p_I} at θ = 180° and 270°.

Figure 25.- Continued.

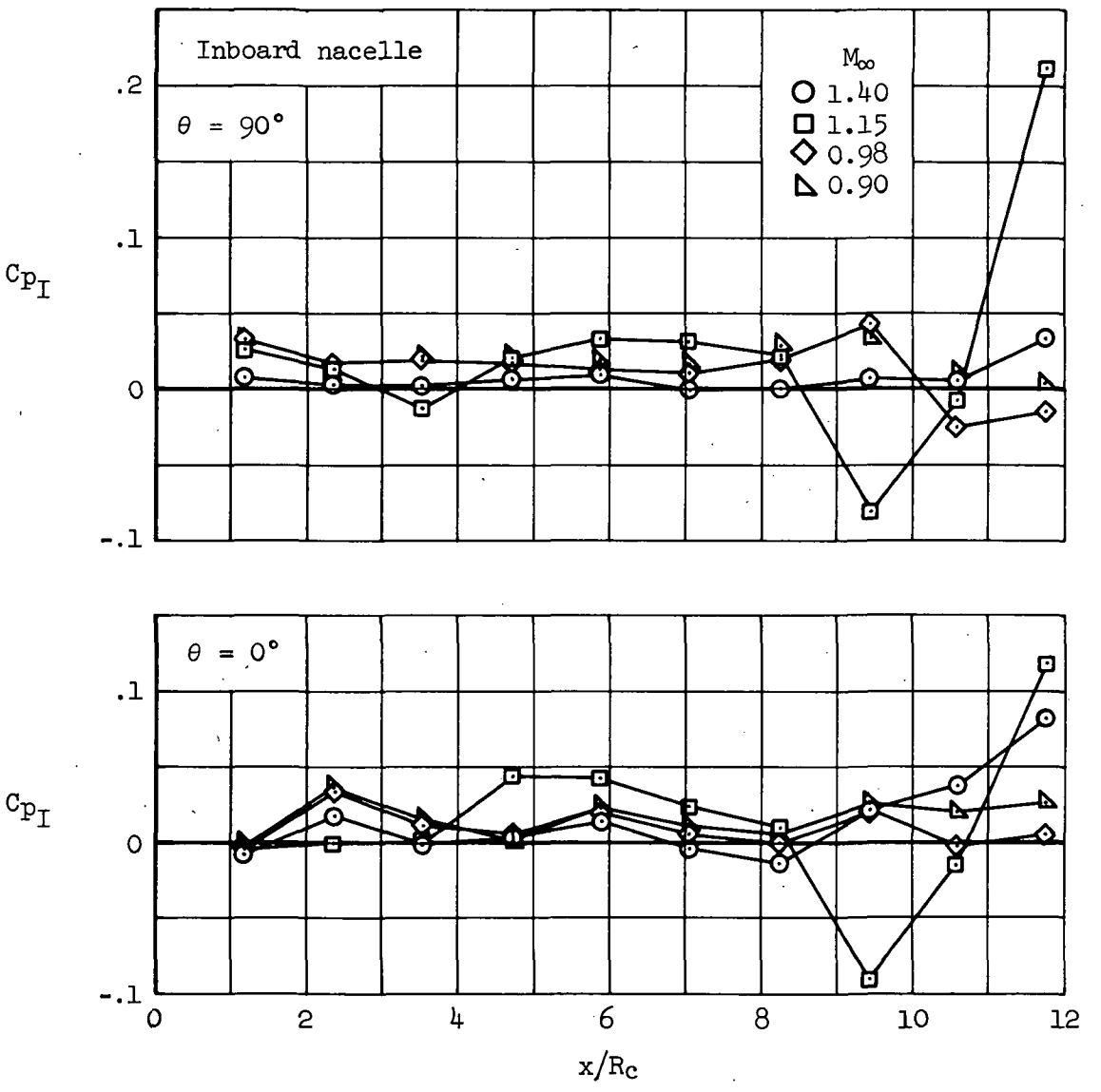

(d) Inboard nacelle, C_{p_I} at $\theta = 0°$ and 90°.

Figure 25.- Continued.

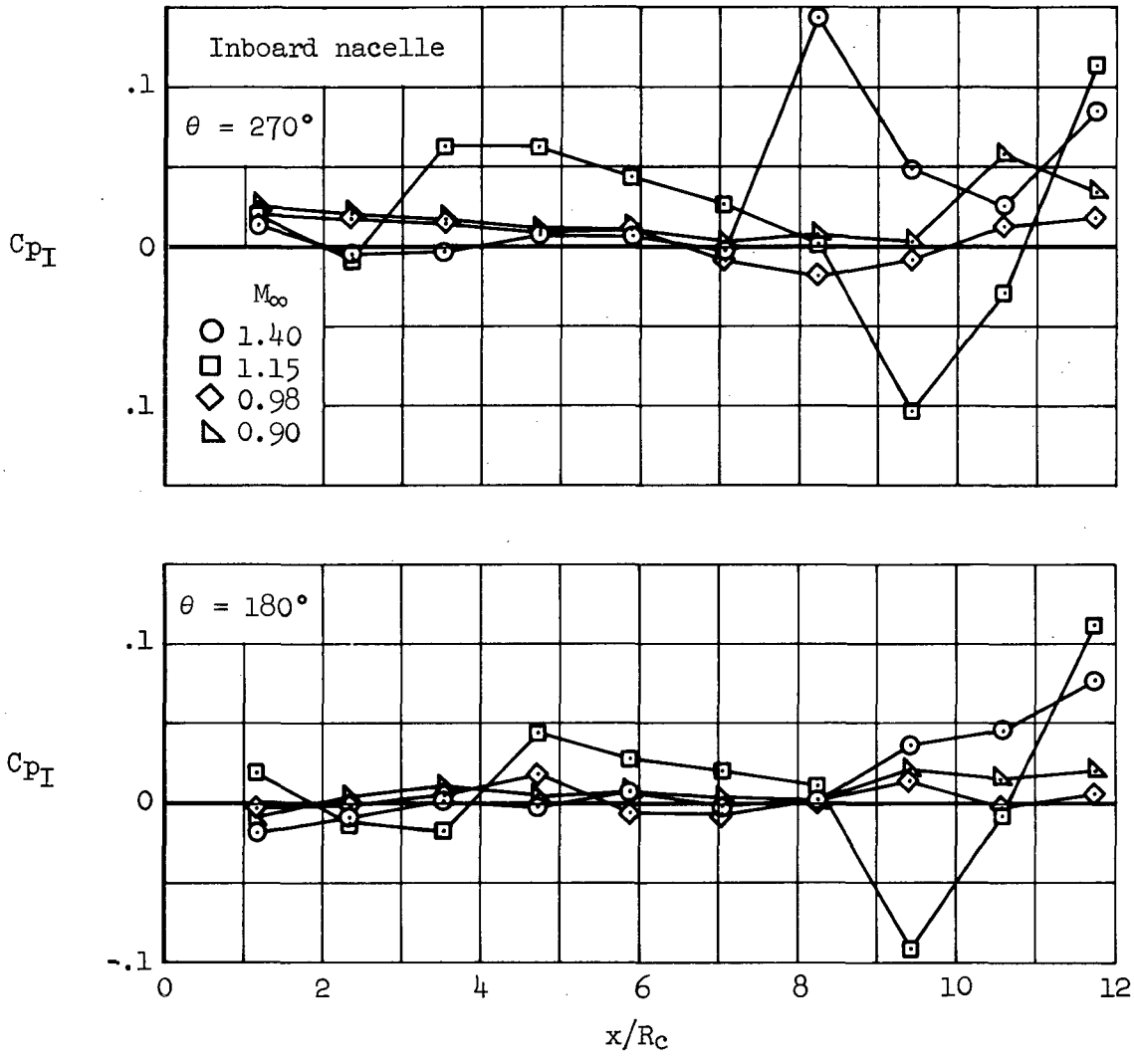

(e) Inboard nacelle, C_{p_I} at θ = 180° and 270°.

Figure 25.- Concluded.

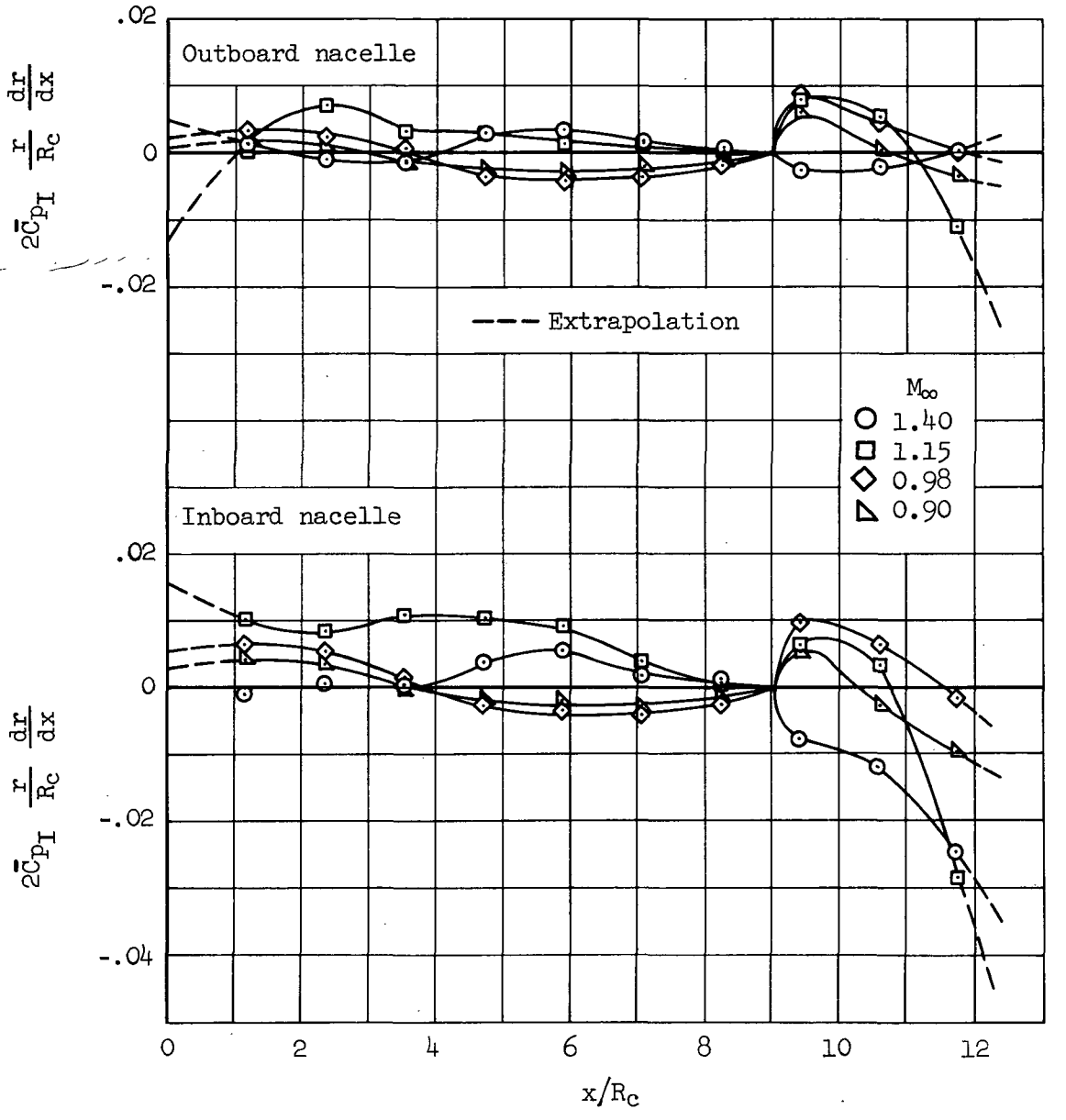

(a) $\Delta X/R_c = 0$

Figure 26.- Local nacelle interference drag coefficient; configuration N_1N_1, $\alpha = 0°$, $y_i' = 0.25$, $y_o' = 0.55$, maximum m/m_c.

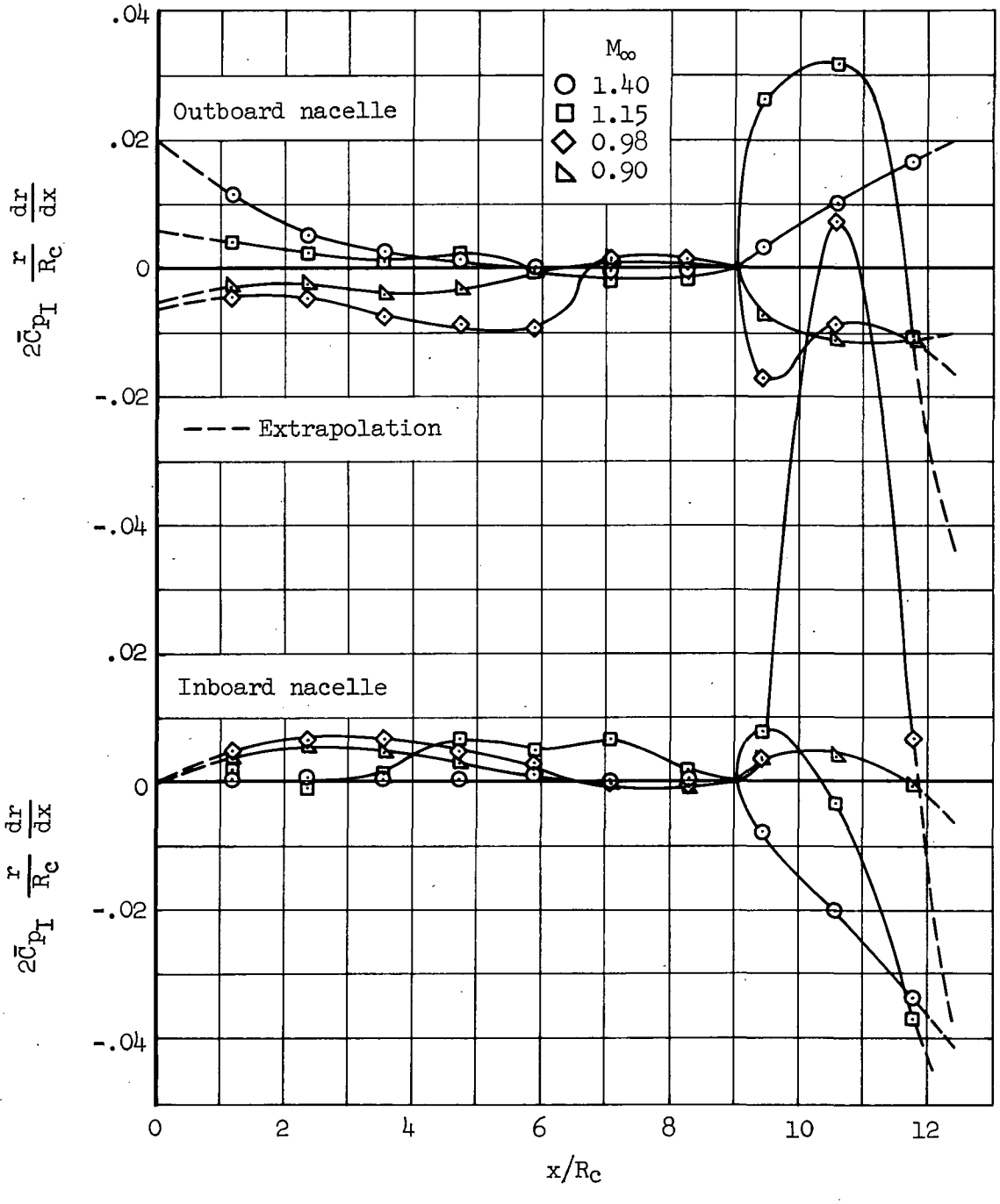

(b) $\Delta X/R_c = 4.71$

Figure 26.- Continued.

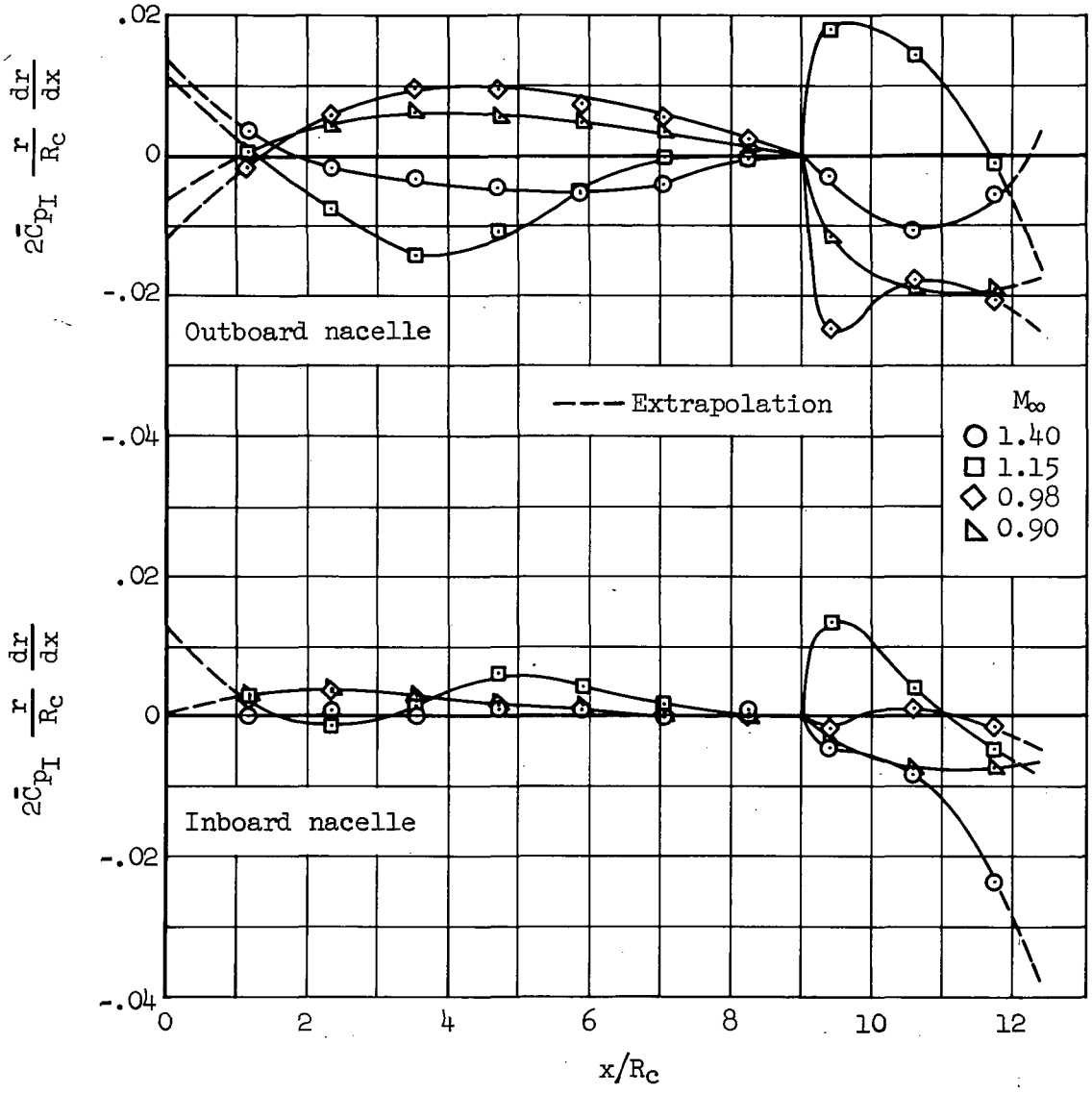

(c) $\Delta X/R_c = 9.41$

Figure 26.- Concluded.

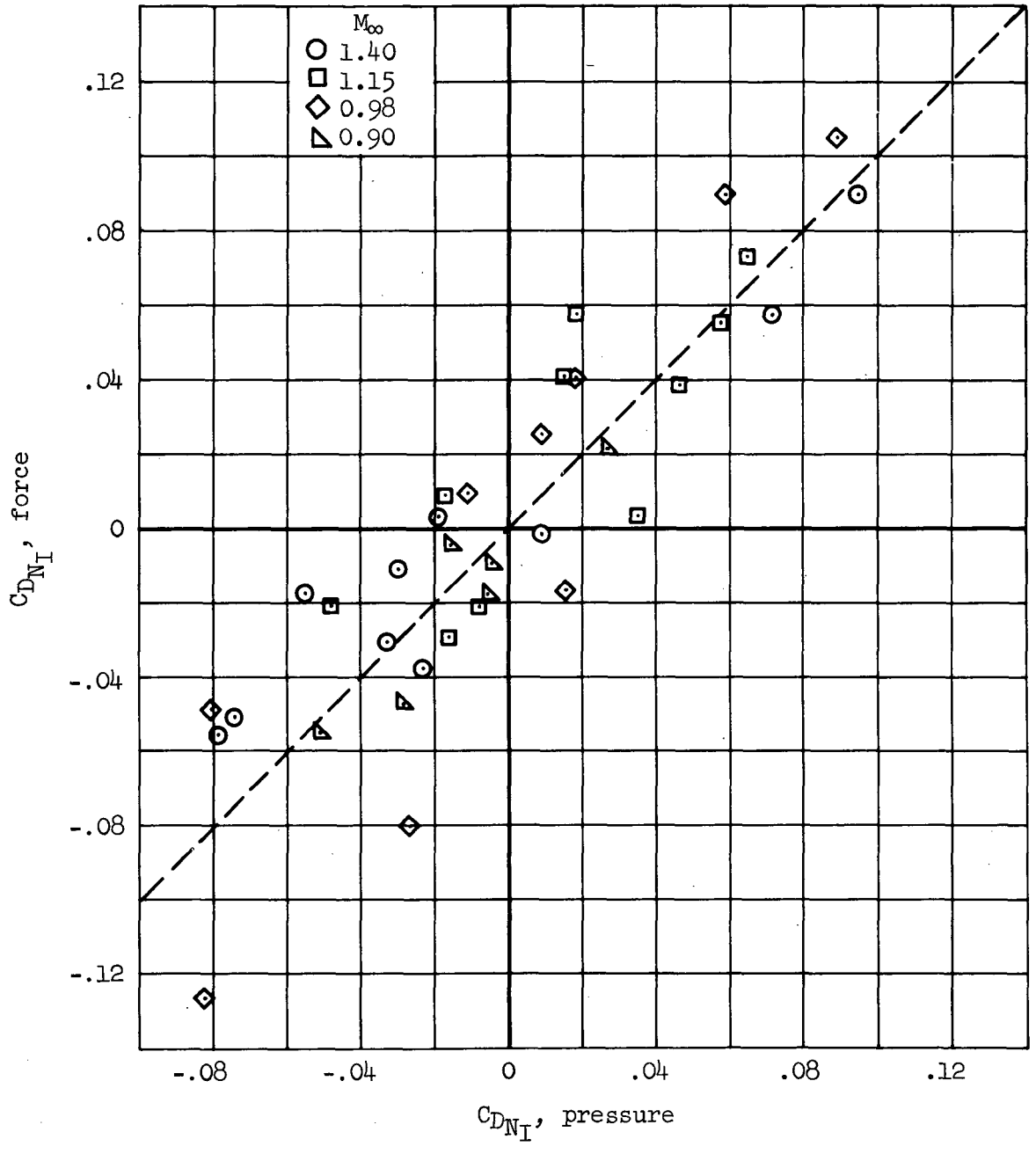

Figure 27.- Comparison of nacelle-nacelle interference drag based on force measurement and pressure integration; configuration N_1N_1, $\alpha = 0°$, $y_i' = 0.25$, $y_o' = 0.55$, maximum m/m_c.

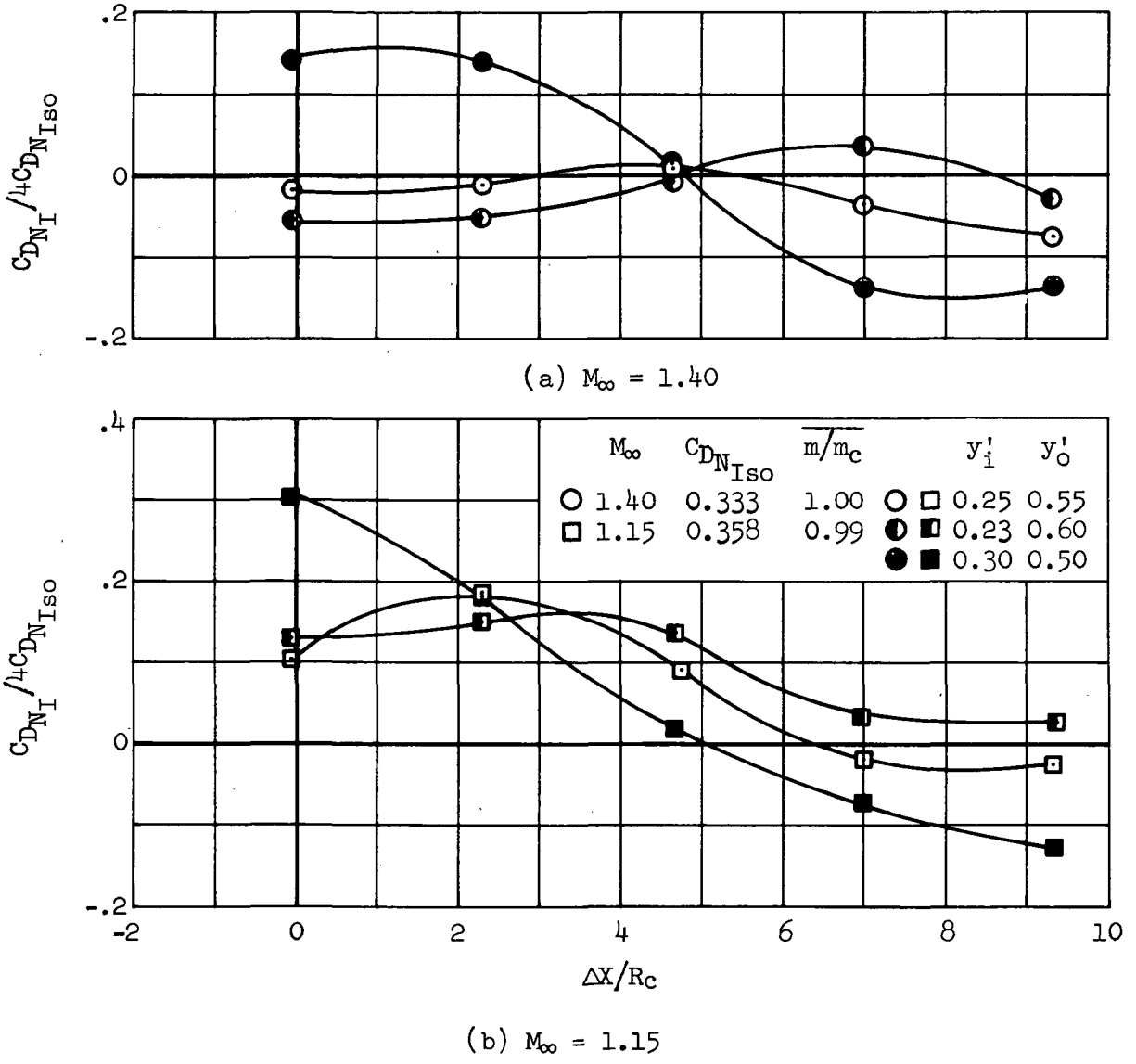

Figure 28.- Nacelle-nacelle interference drag; configuration N_1N_1, α = 0°, maximum m/m_c.

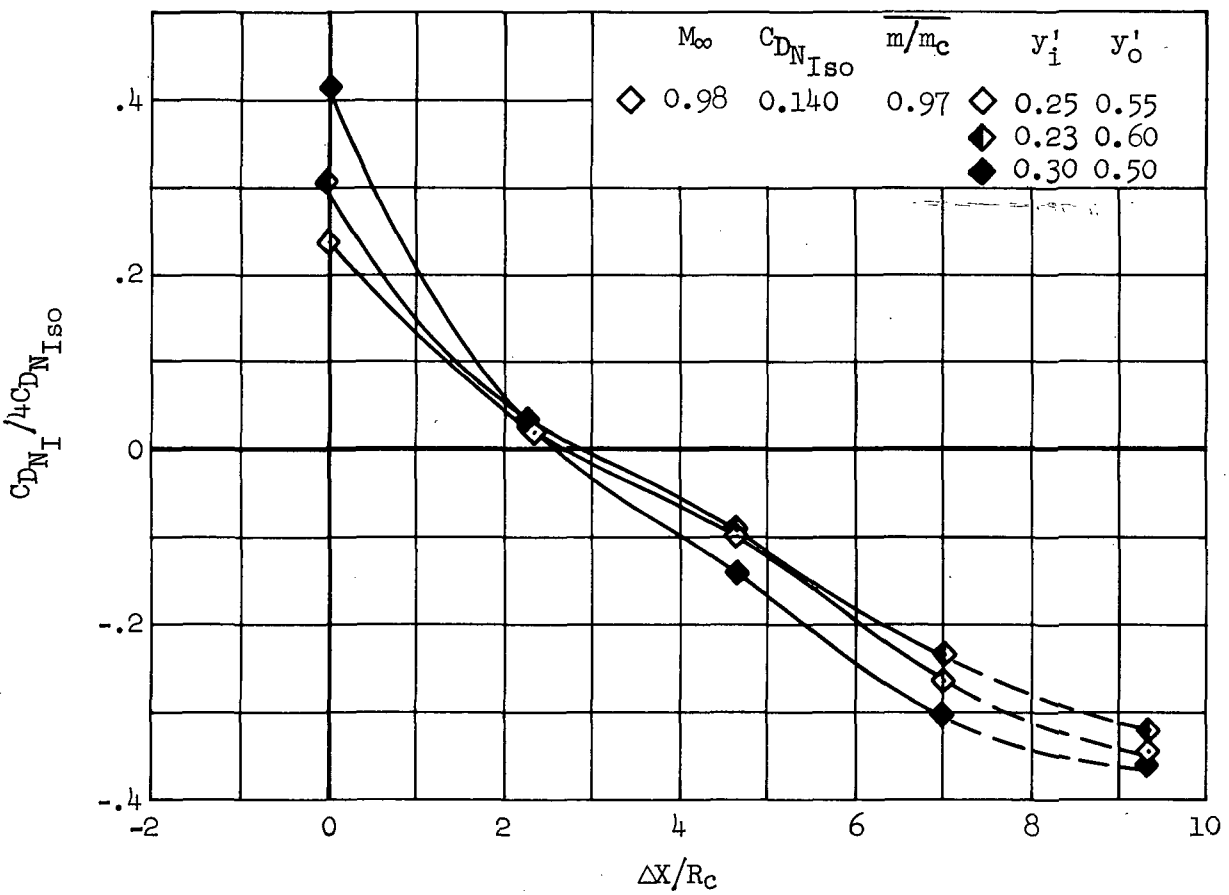

(c) $M_\infty = 0.98$

Figure 28.- Concluded.

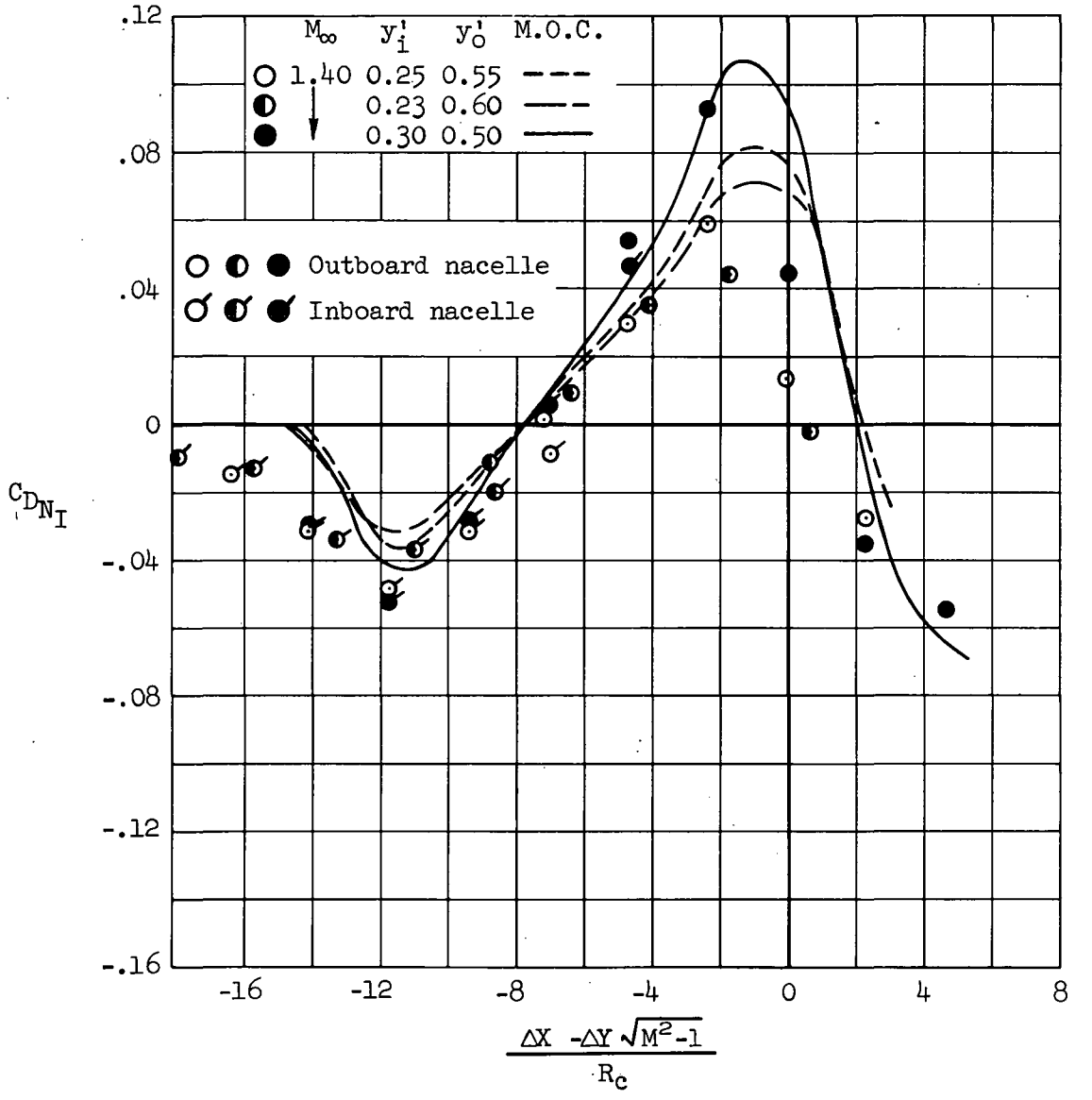

(a) $M_\infty = 1.40$

Figure 29.- Correlation of nacelle-nacelle interference drag; configuration N_1N_1, $\alpha = 0°$, maximum m/m_c.

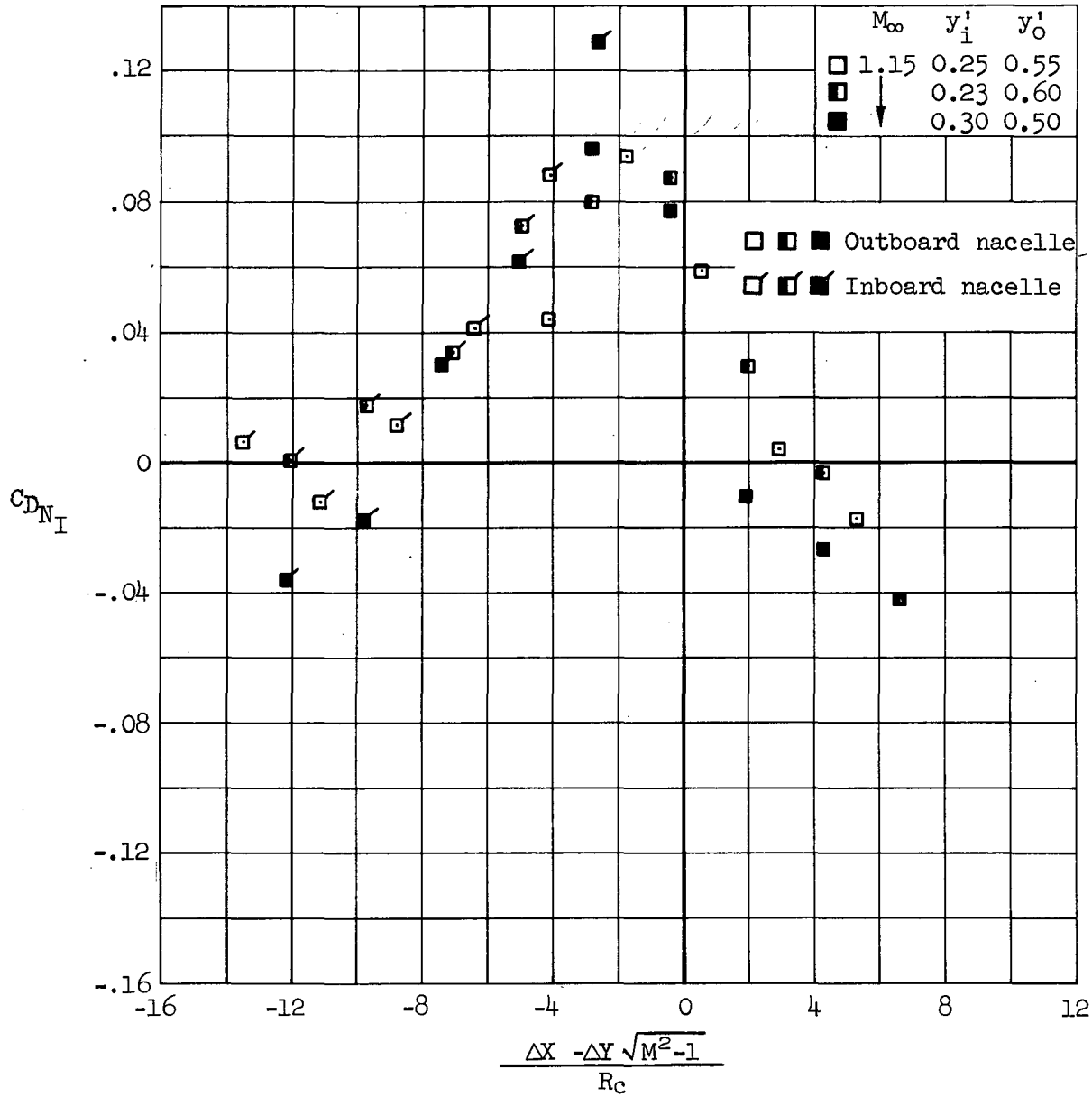

(b) $M_\infty = 1.15$

Figure 29.- Continued.

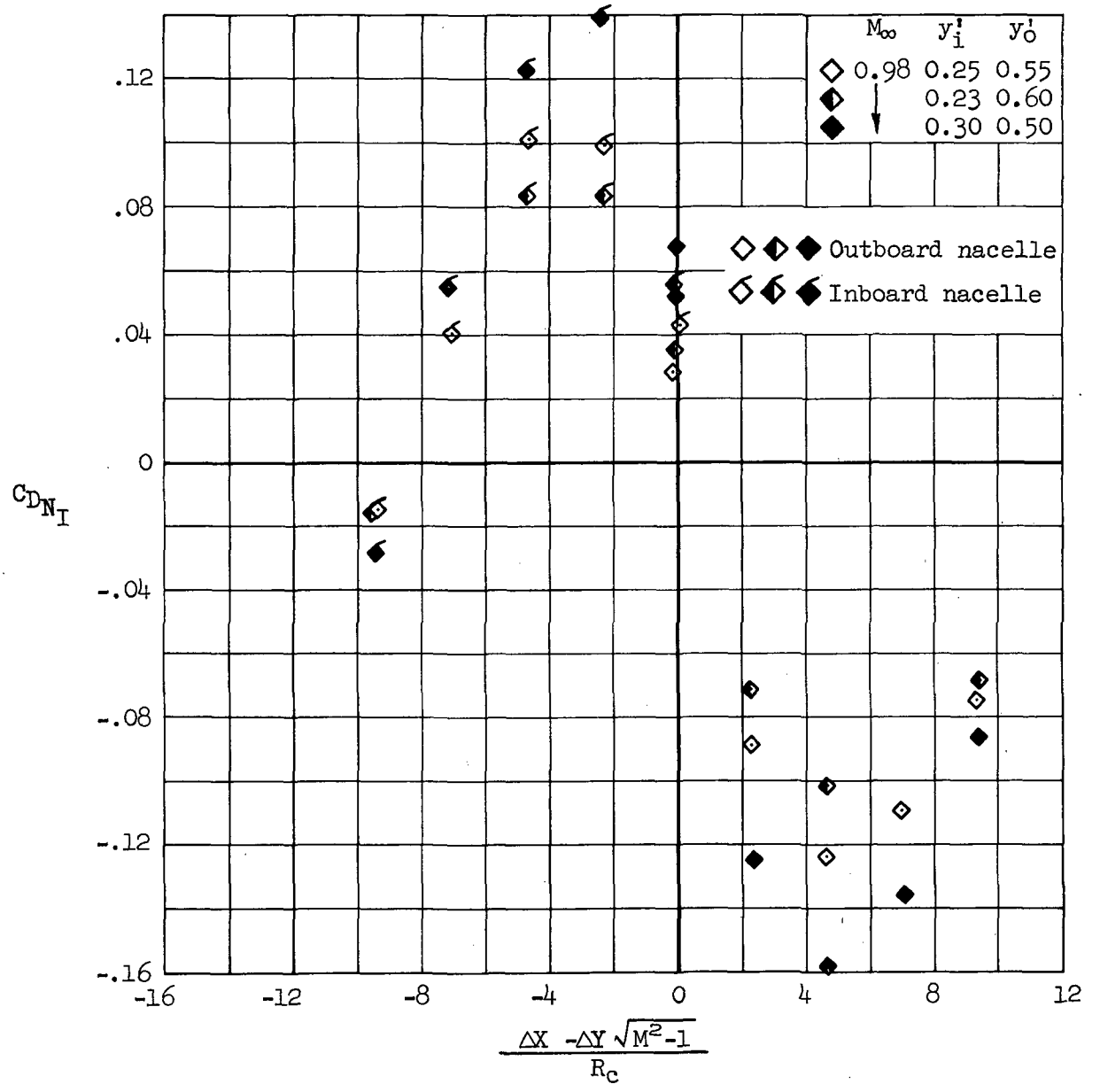

(c) $M_\infty = 0.98$

Figure 29.- Concluded.

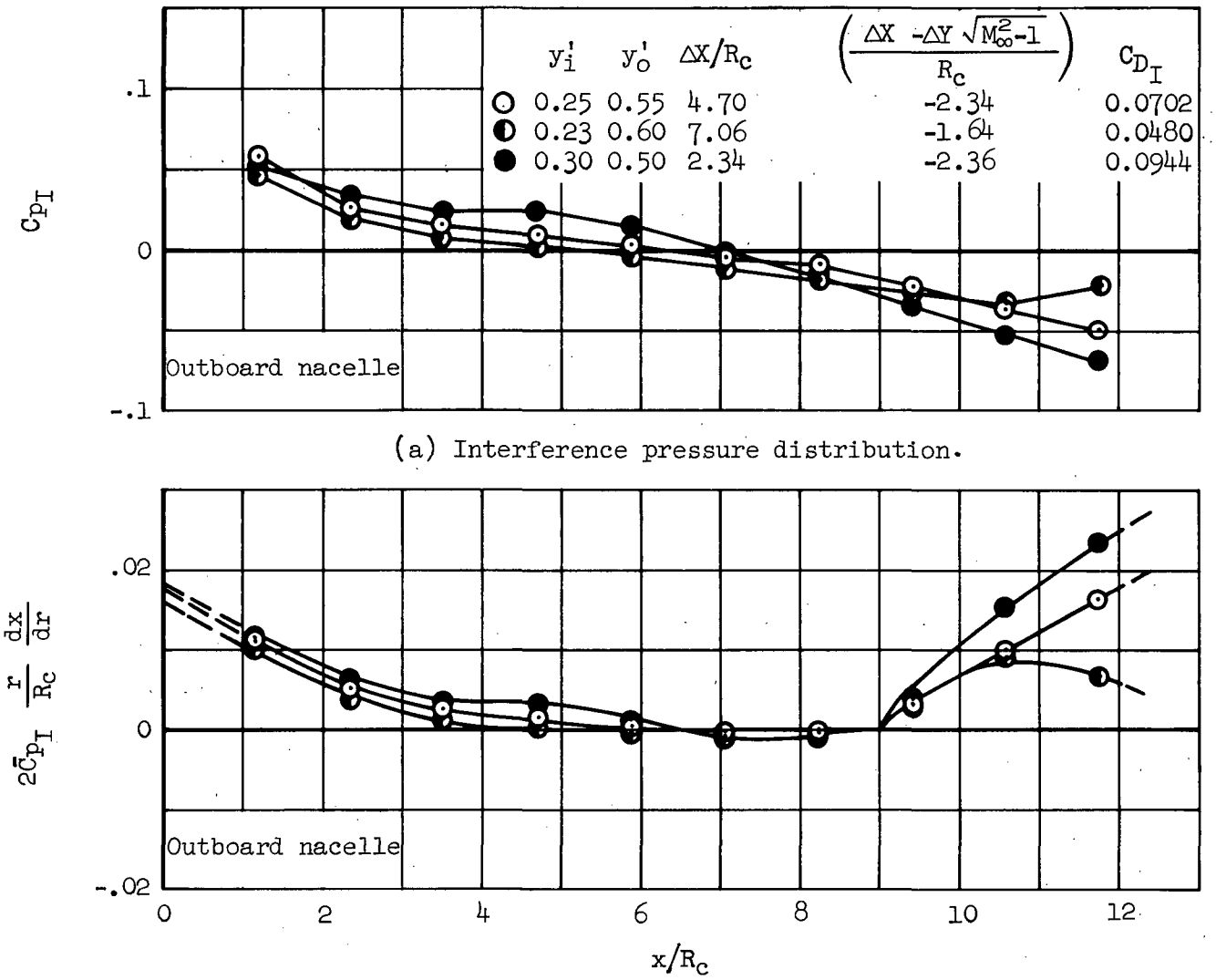

(a) Interference pressure distribution.

(b) Local interference drag coefficient.

Figure 30.- Nacelle-nacelle interference at a constant value of $\left(\Delta X - \Delta Y\sqrt{M_\infty^2-1}\right)/R_c$; configuration N_1N_1, $M_\infty = 1.40$, $\alpha = 0°$, maximum m/m_c.

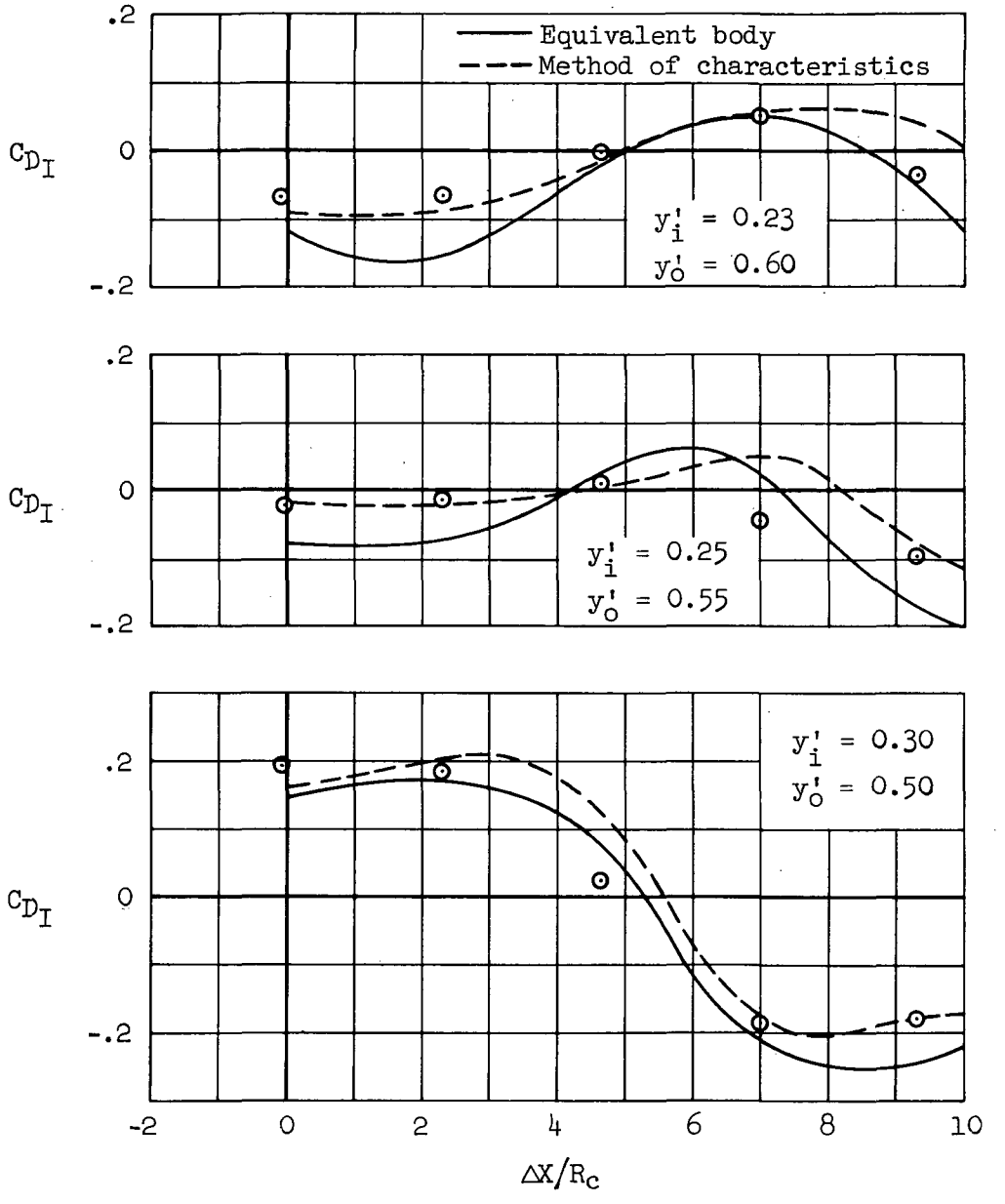

(a) $M_\infty = 1.40$

Figure 31.- Comparison between measured and predicted nacelle-nacelle interference drag; configuration N_1N_1, $\alpha = 0°$, maximum m/m_c.

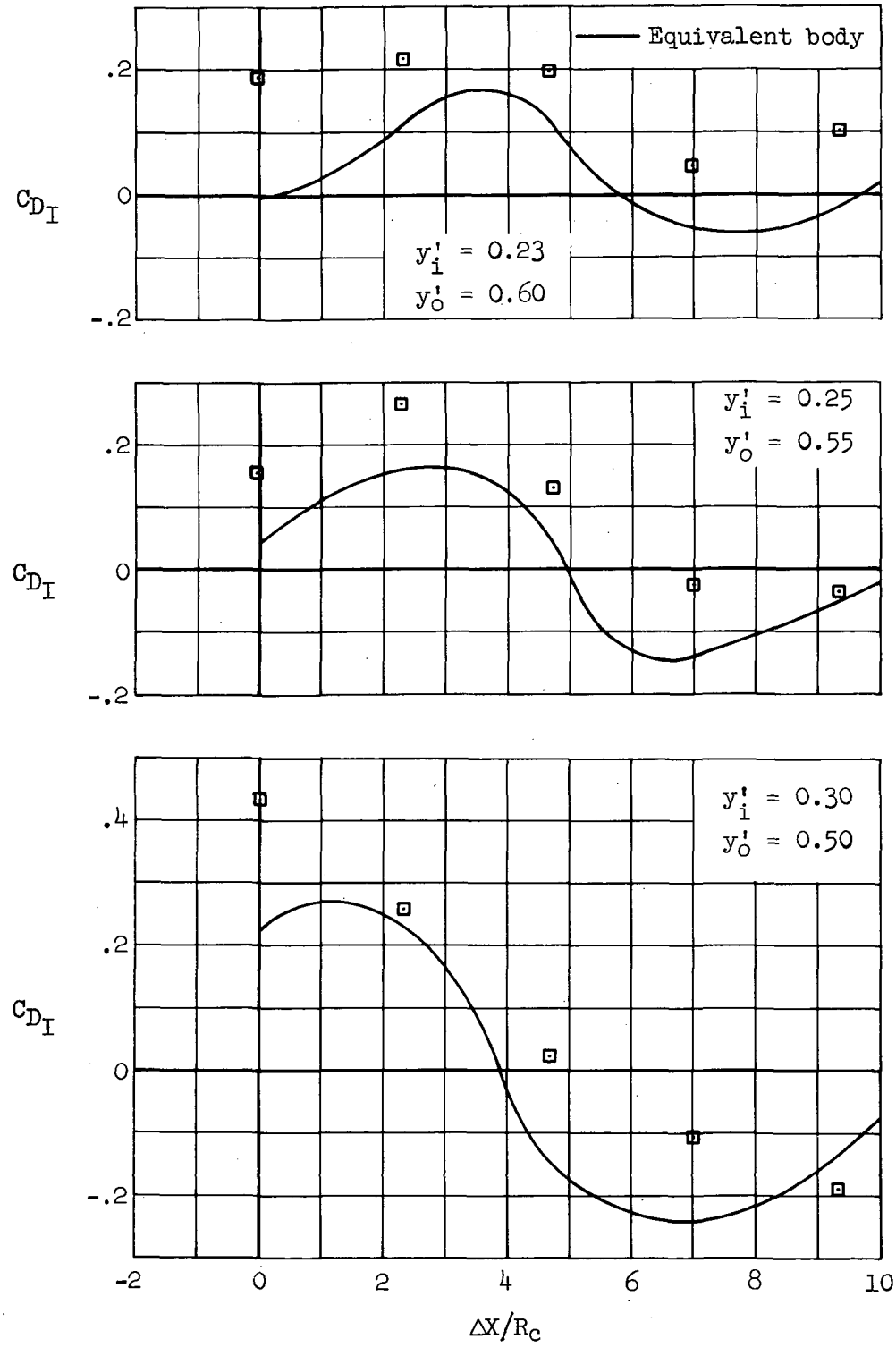

(b) $M_\infty = 1.15$

Figure 31.- Concluded.

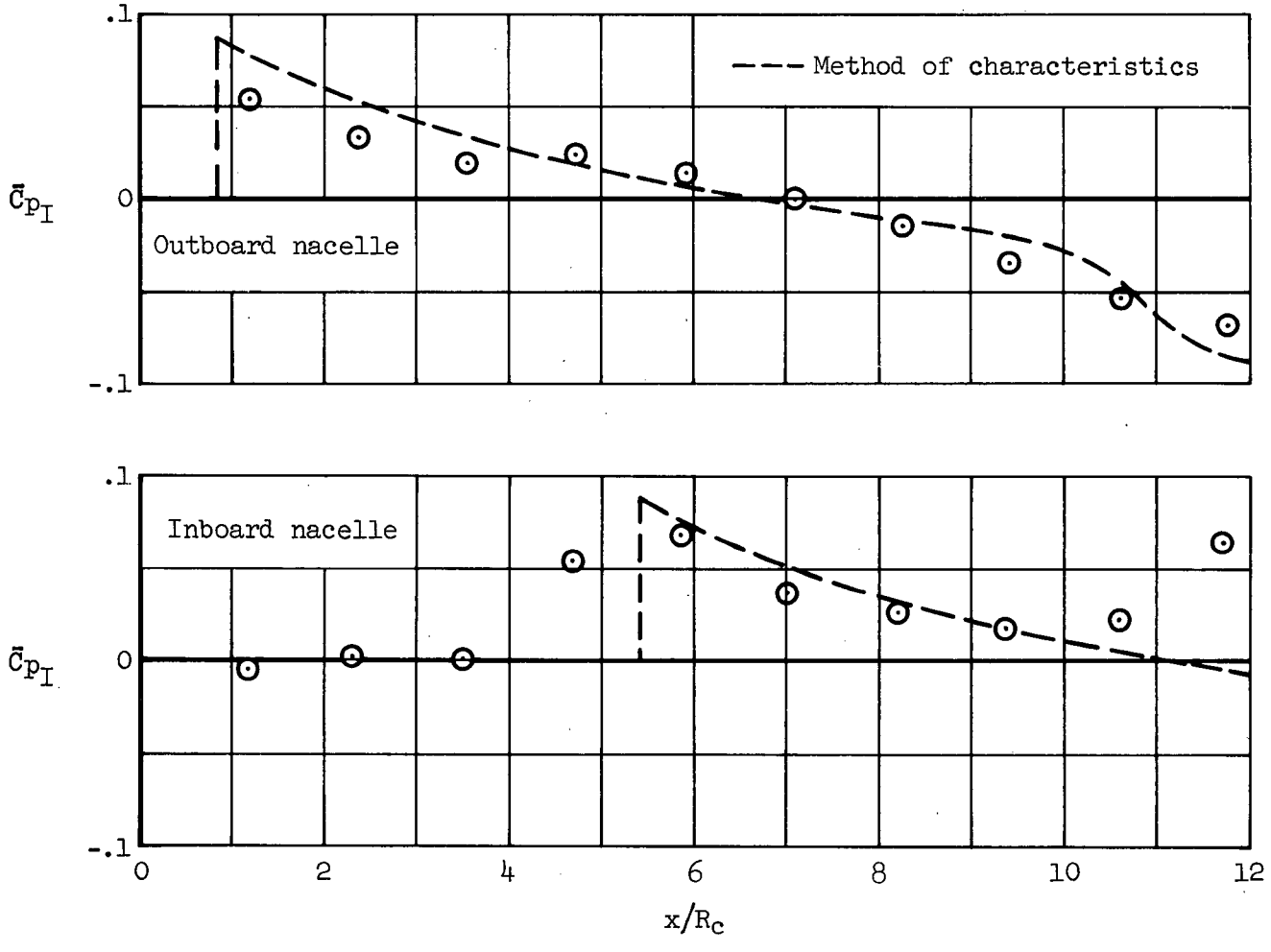

(a) $\Delta X/R_c = 2.296$

Figure 32.- Comparison between predicted and measured average nacelle-nacelle interference pressure distributions; configuration N_1N_1, $M_\infty = 1.40$, $\alpha = 0°$, $y_i' = 0.30$, $y_o' = 0.50$, maximum m/m_c.

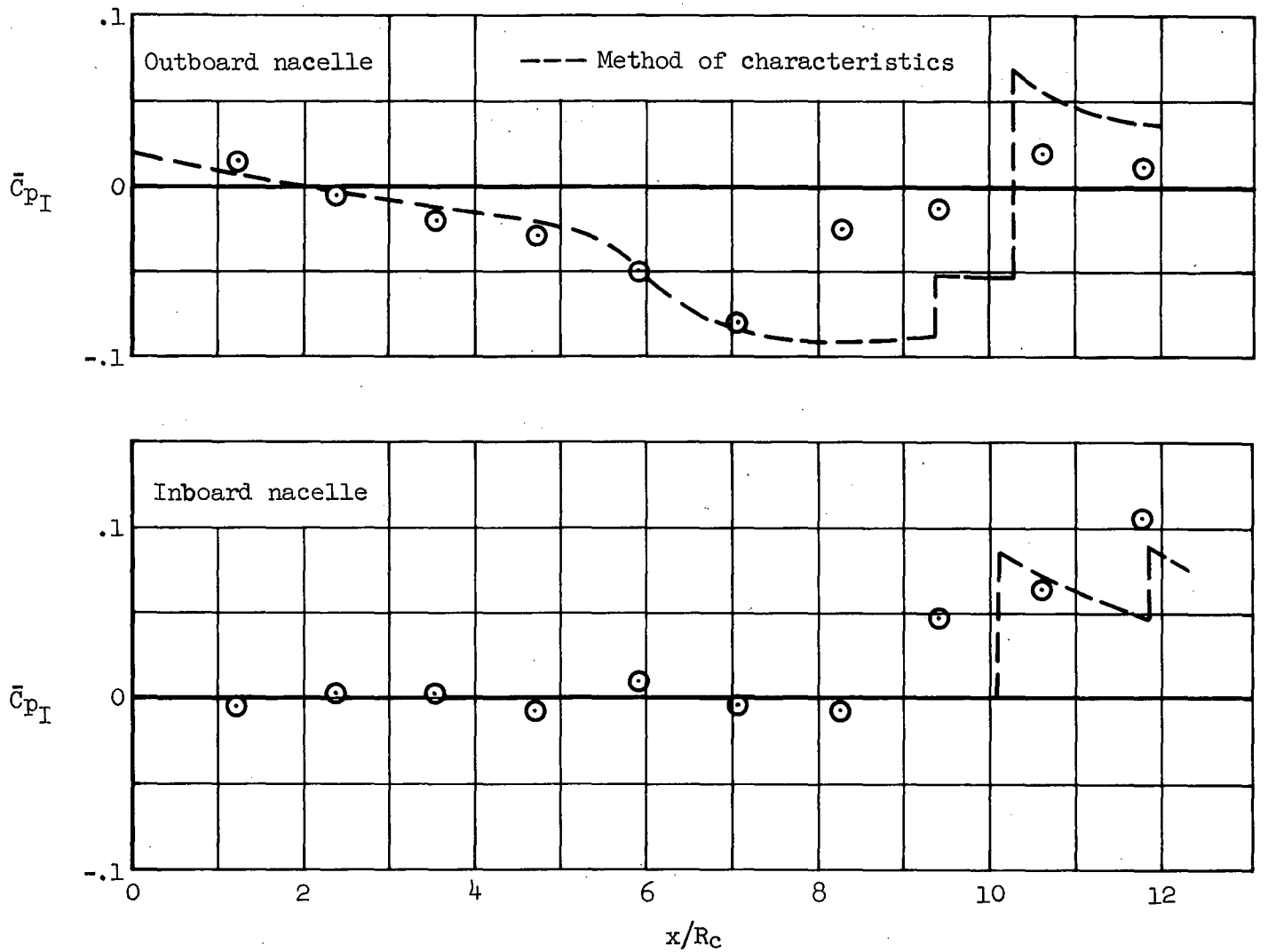

(b) $\Delta X/R_c = 6.990$

Figure 32.- Concluded.

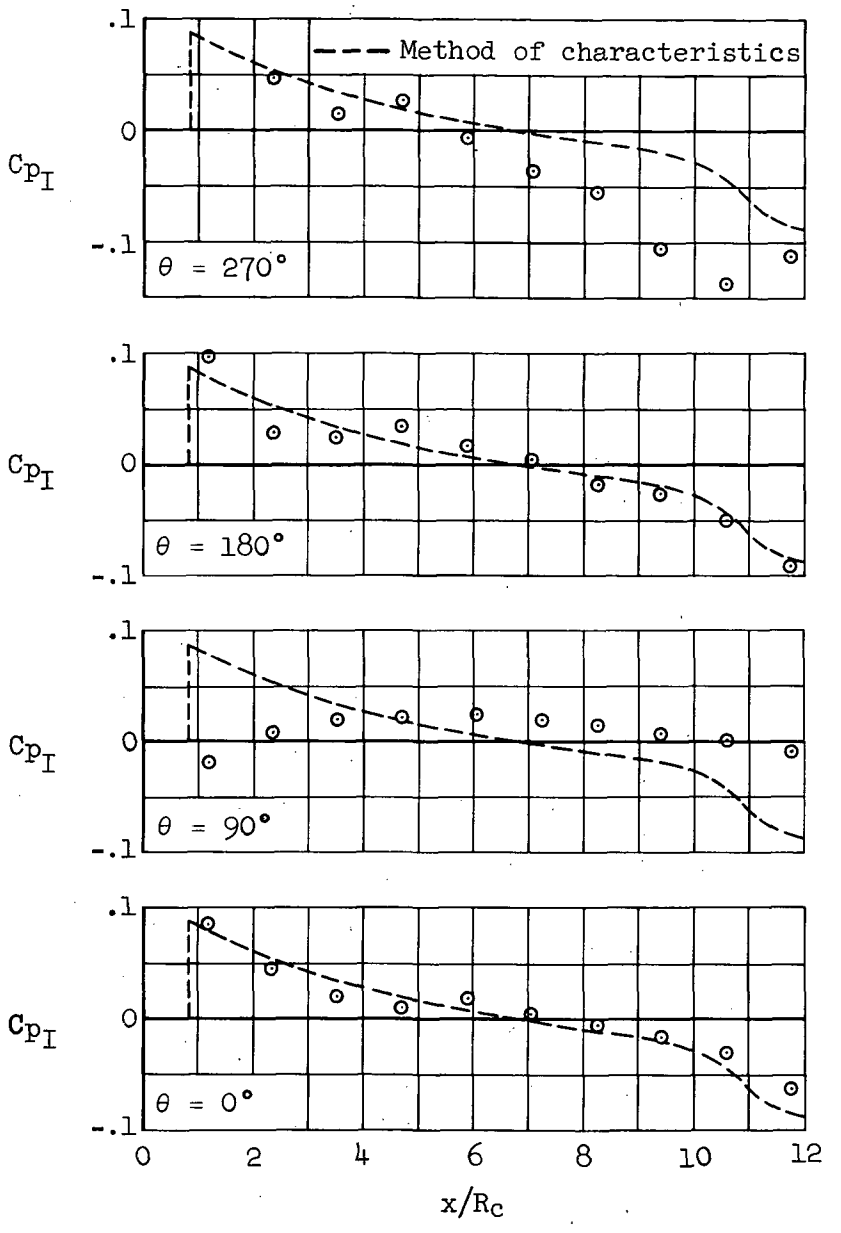

(a) Outboard nacelle, $\Delta X/R_c = 2.296$.

Figure 33.- Comparison between predicted and measured local nacelle-nacelle interference pressure distributions; configuration N_1N_1, $M_\infty = 1.40$, $\alpha = 0°$, $y_i' = 0.30$, $y_o' = 0.50$, maximum m/m_c.

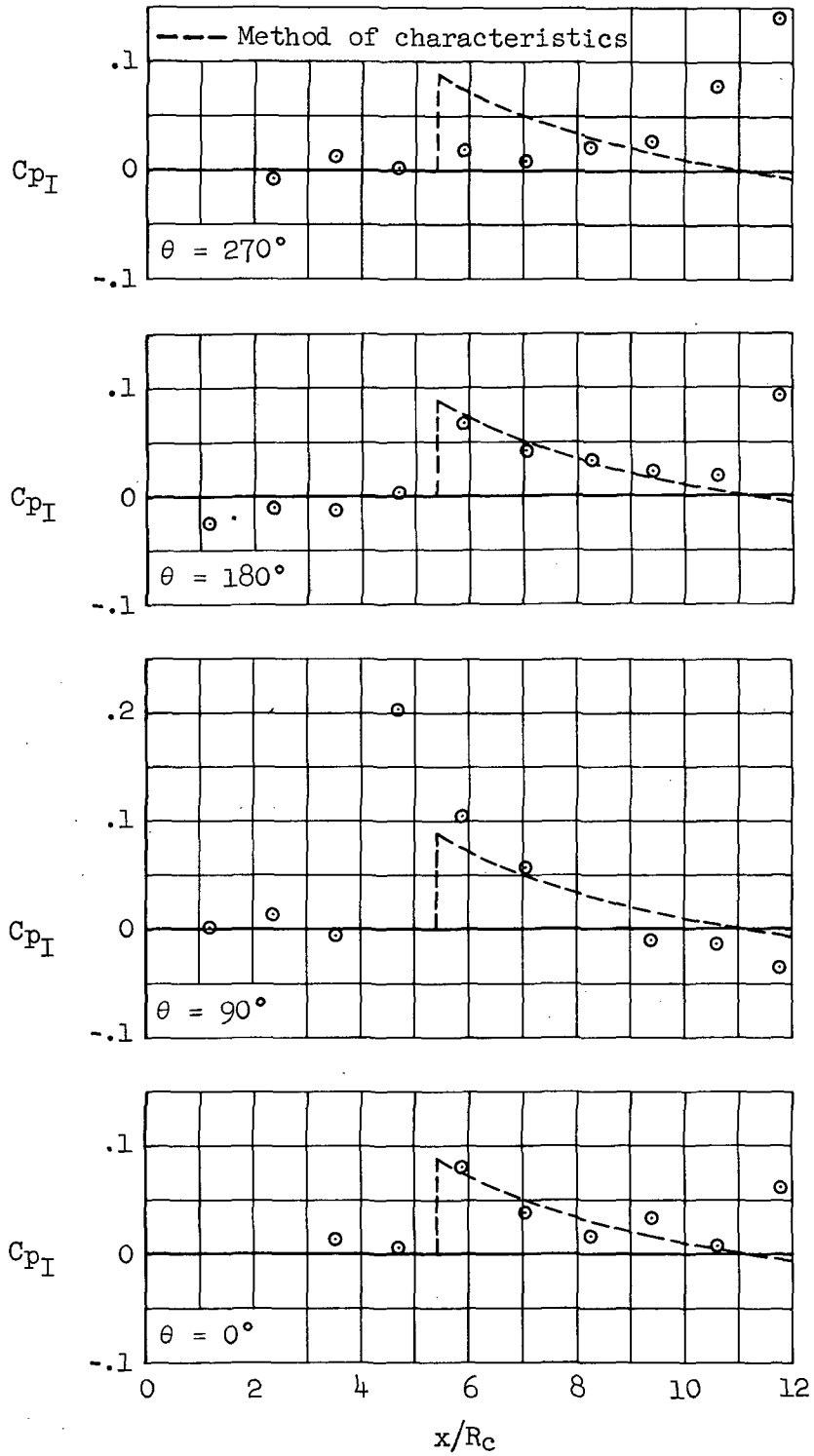

(b) Inboard nacelle, $\Delta X/R_c = 2.296$.

Figure 33.- Continued.

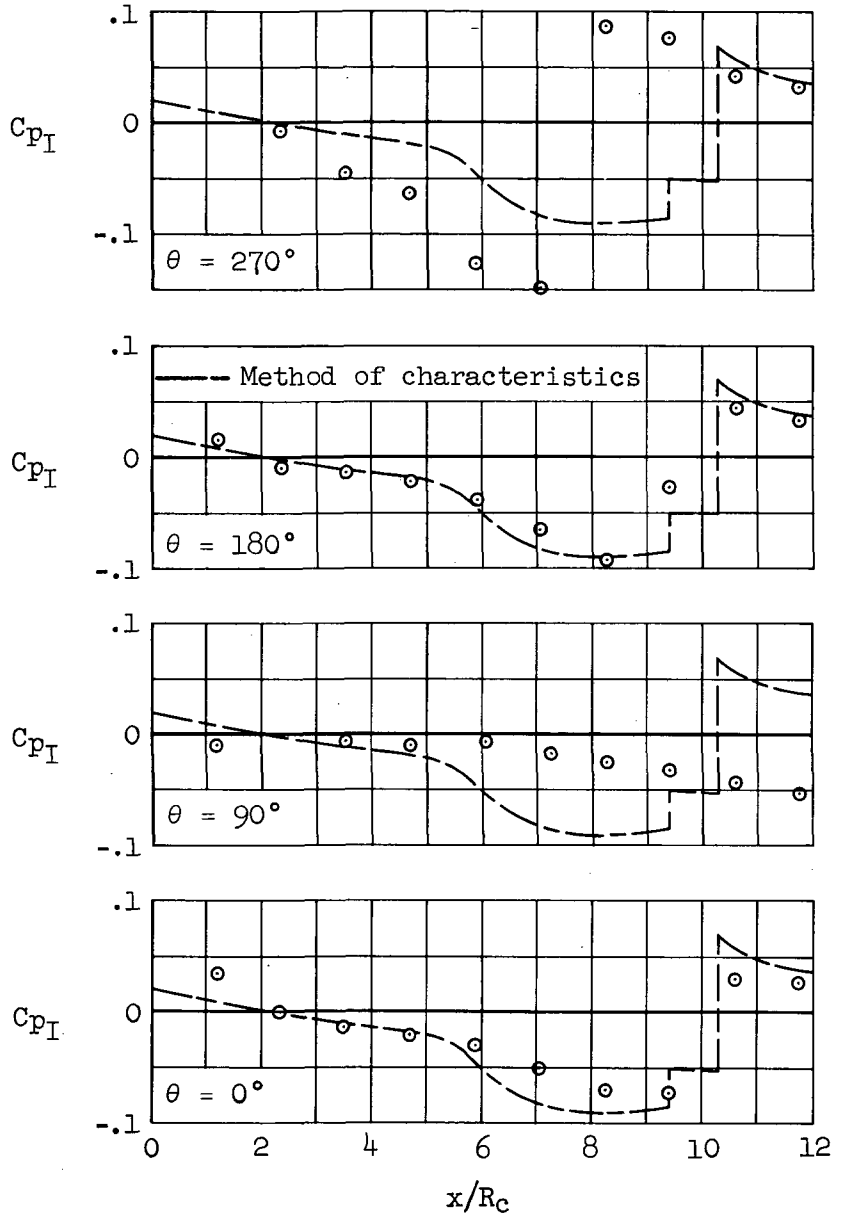

(c) Outboard nacelle, $\Delta X/R_c = 6.990$.

Figure 33.- Continued.

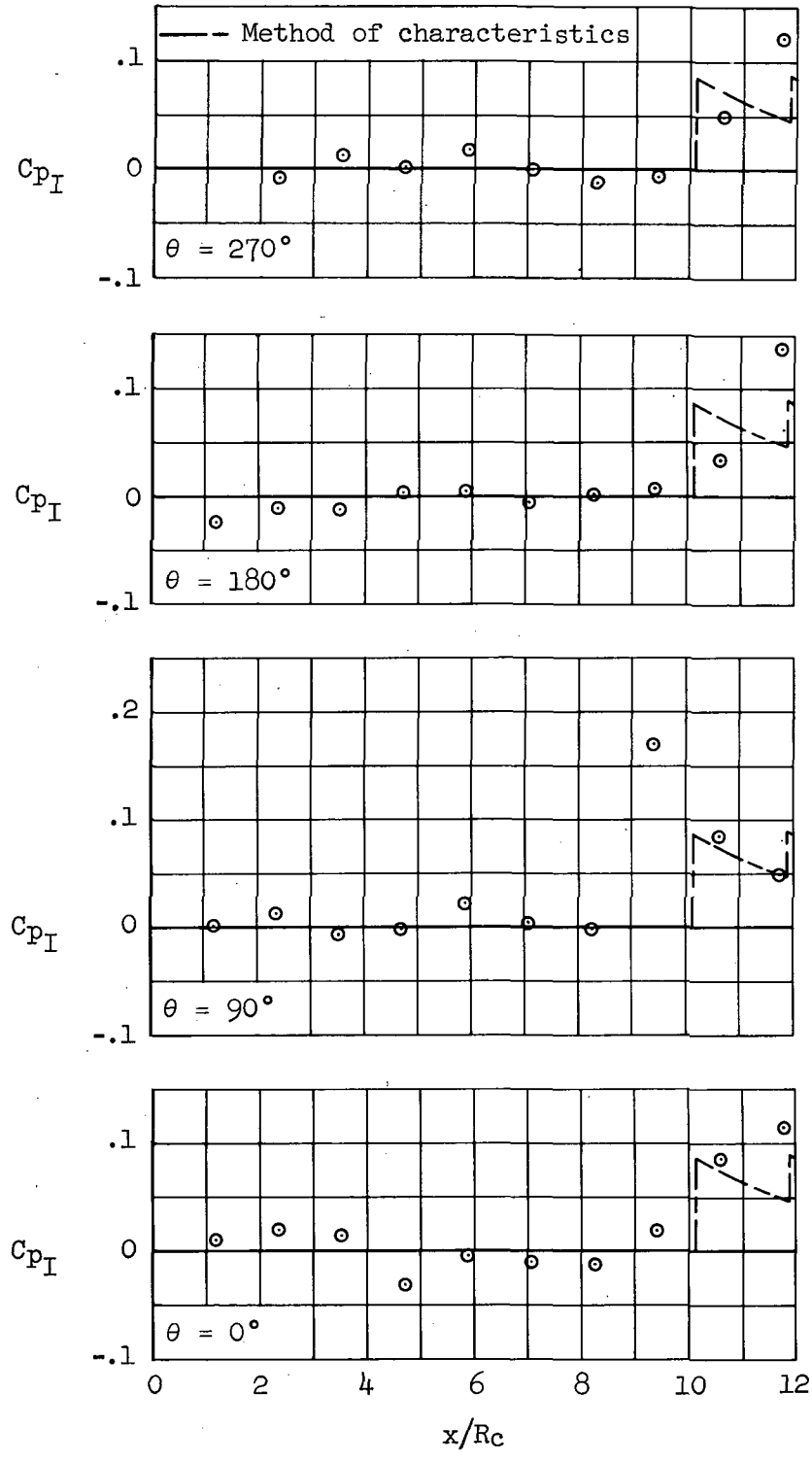

(d) Inboard nacelle, $\Delta X/R_c = 6.990$.

Figure 33.- Concluded.

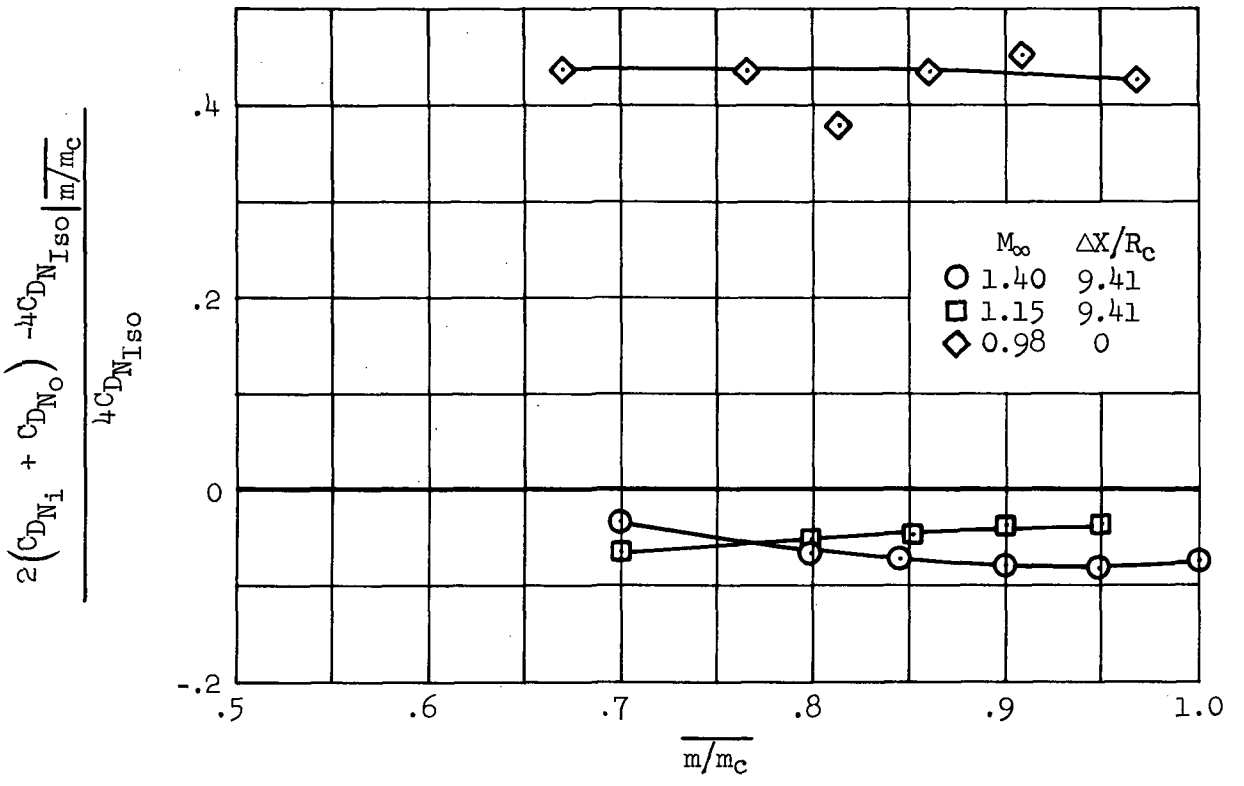

Figure 34.- Mass-flow ratio effects on nacelle-nacelle interference drag; configuration N_1N_1, $\alpha = 0°$, $y_i' = 0.25$, $y_o' = 0.55$.

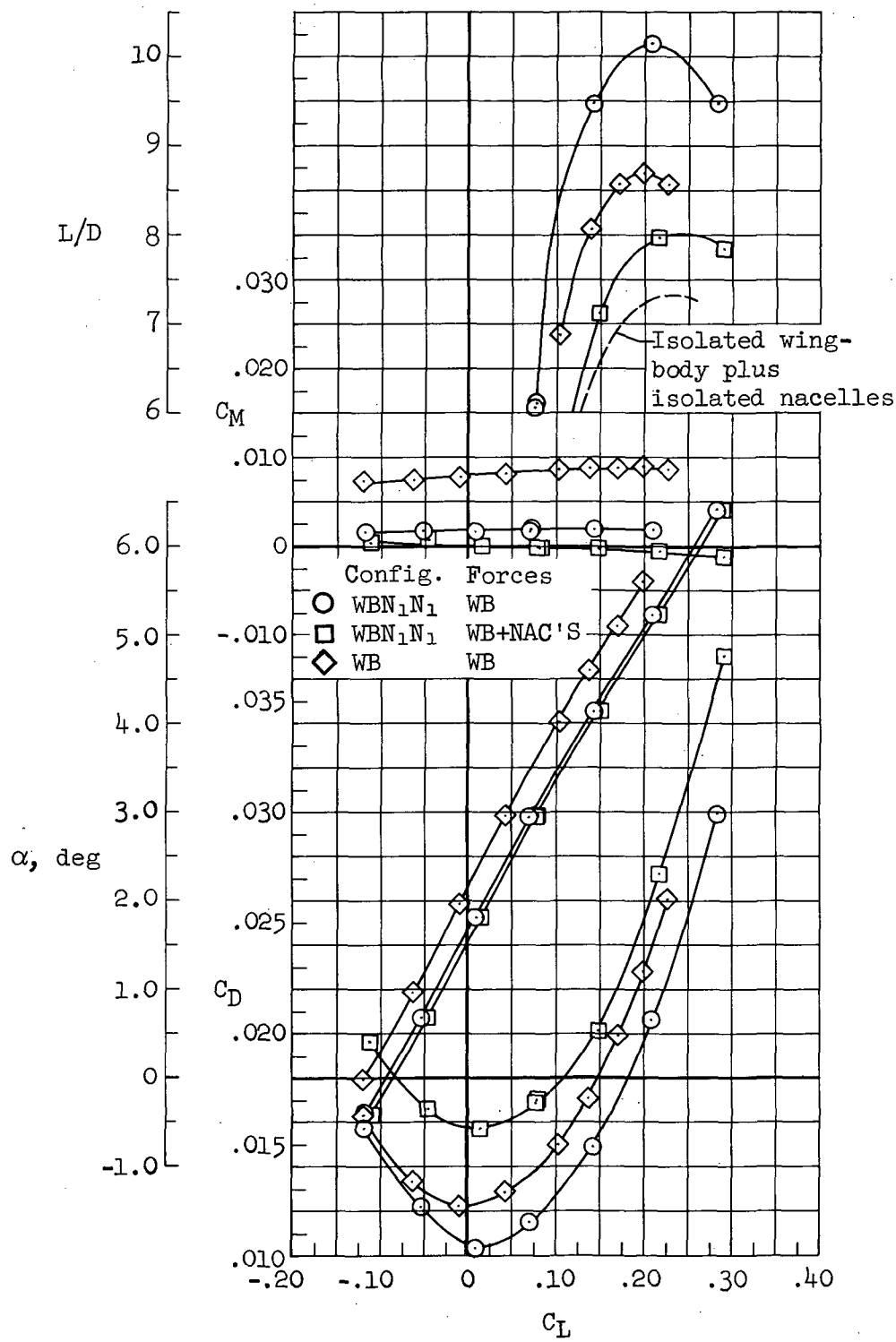

(a) $X_i = X_o = 142.2$ cm (56 in.)

Figure 35.- Longitudinal aerodynamic characteristics; configuration WBN_1N_1, $M_\infty = 1.40$, $y_i' = 0.25$, $y_o' = 0.55$, *maximum* m/m_c.

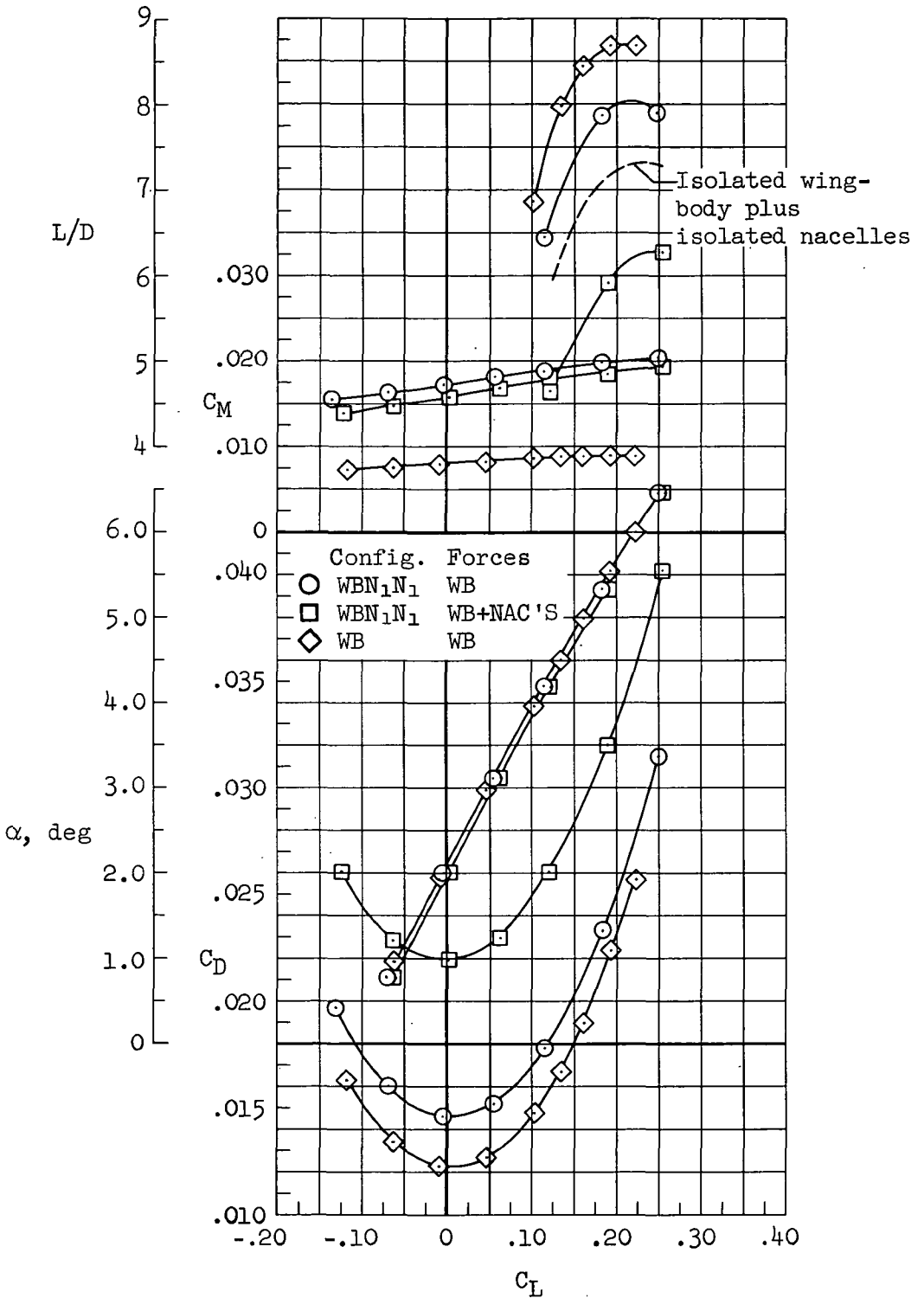

(b) $X_i = X_o$ = 121.9 cm (48 in.)

Figure 35.- Concluded.

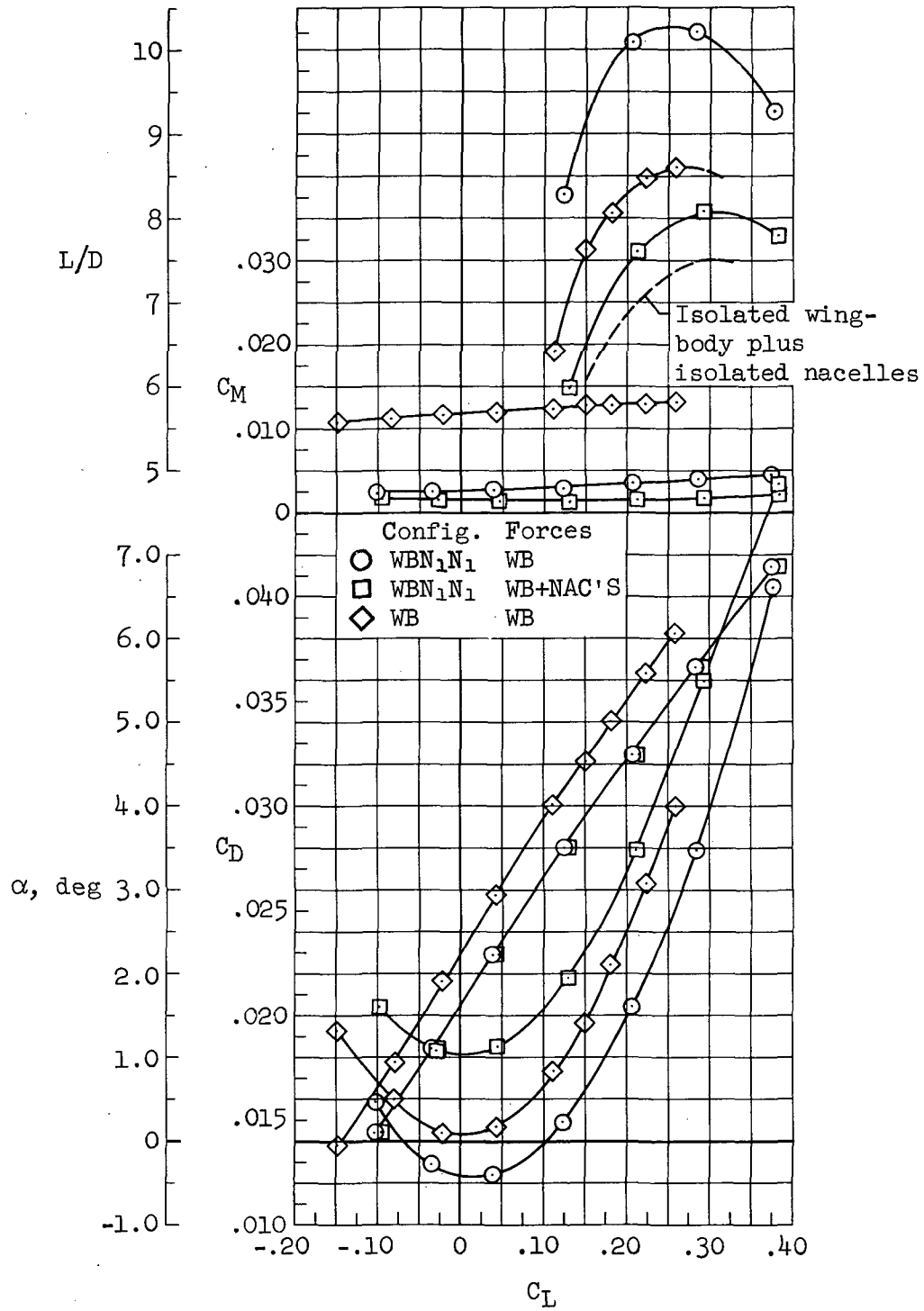

(a) $X_i = X_o = 142.2$ cm (56 in.)

Figure 36.- Longitudinal aerodynamic characteristics; configuration WBN_1N_1, $M_\infty = 1.15$, $y'_i = 0.25$, $y'_o = 0.55$, maximum m/m_c.

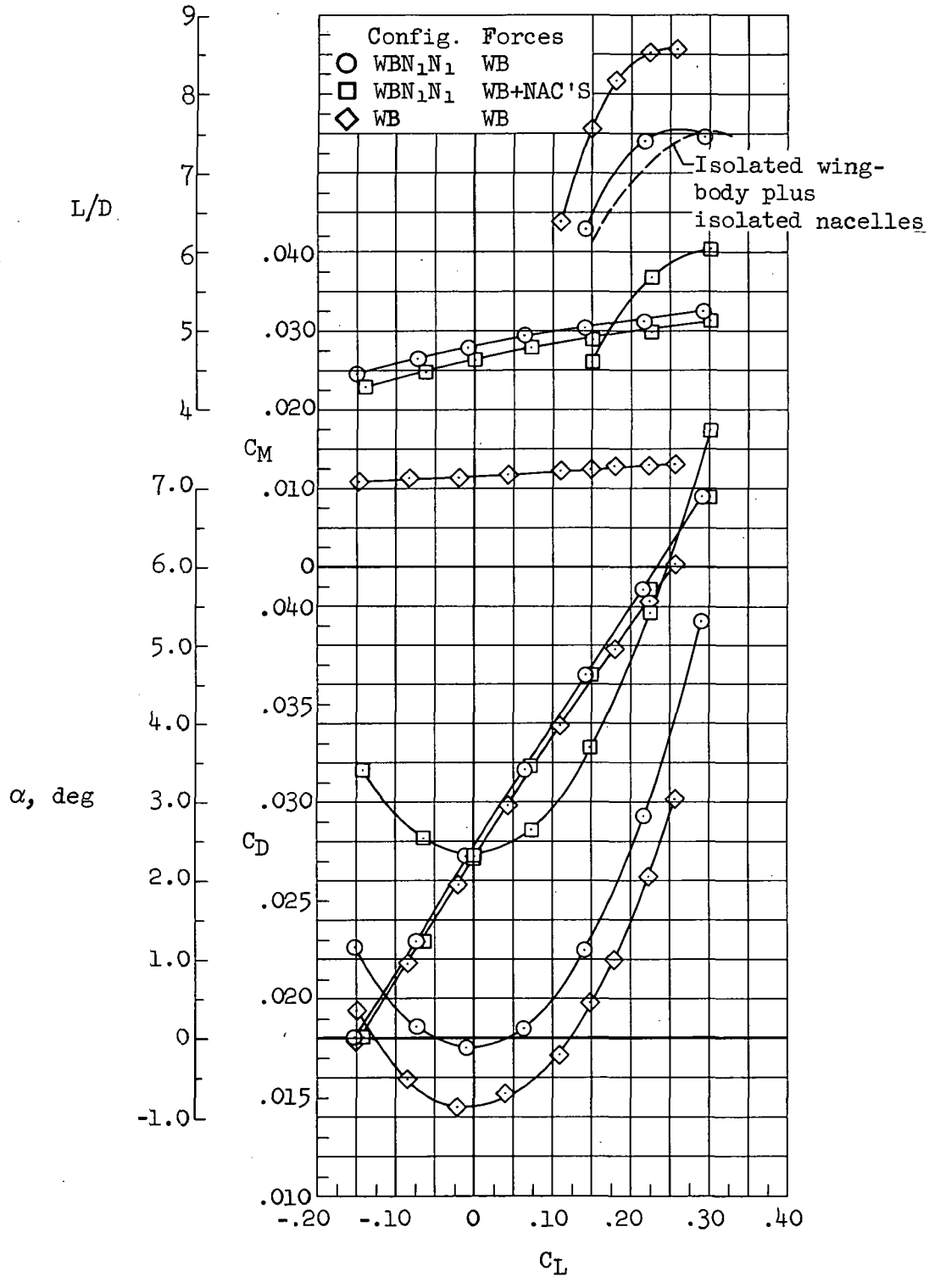

(b) $X_i = X_o$ = 121.9 cm (48 in.)

Figure 36.- Concluded.

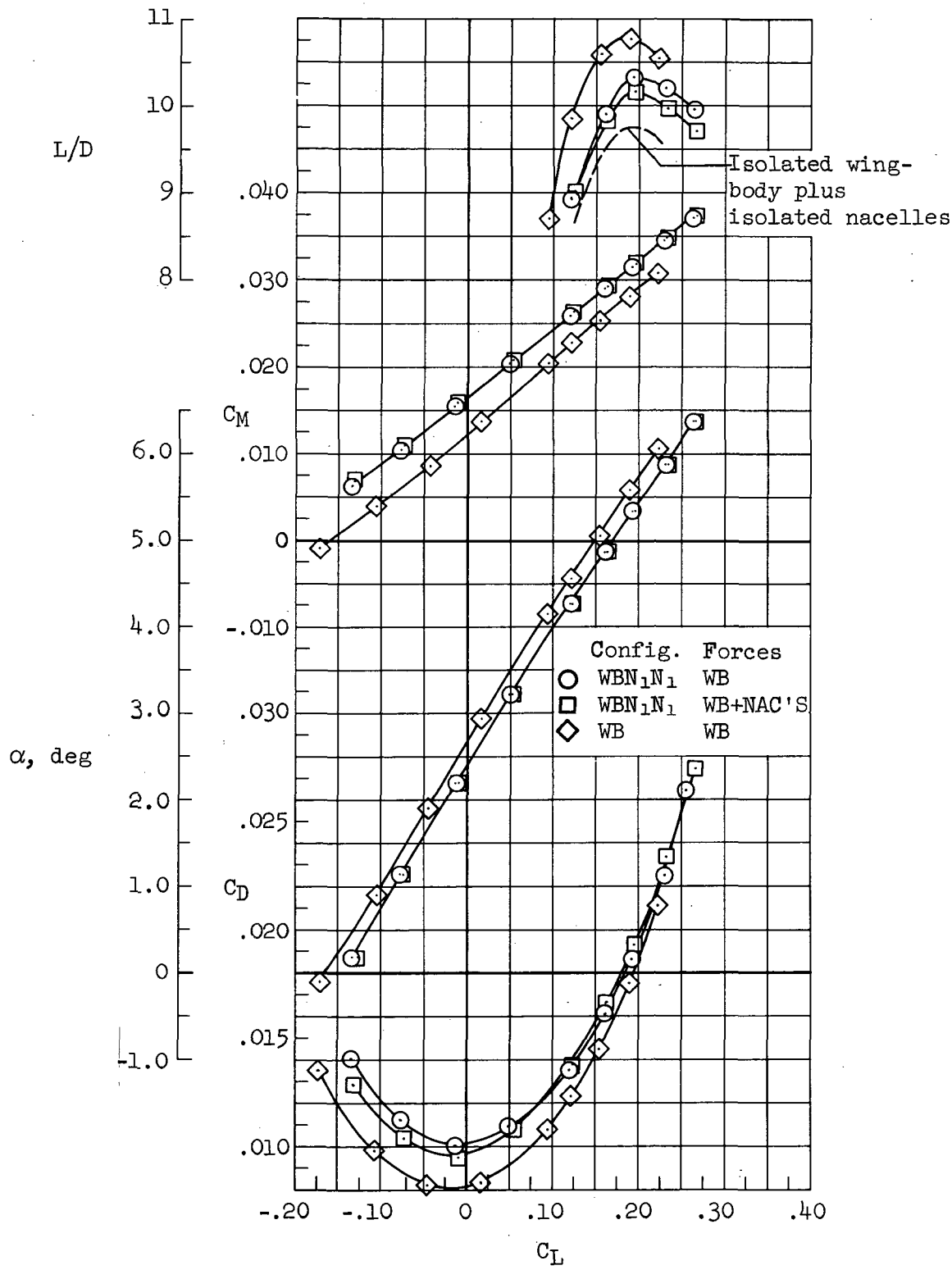

Figure 37.- Longitudinal aerodynamic characteristics; configuration WBN_1N_1, $M_\infty = 0.90$, $y_i' = 0.25$, $y_o' = 0.55$, $X_i = X_o = 142.2$ cm (56 in.), maximum m/m_c.

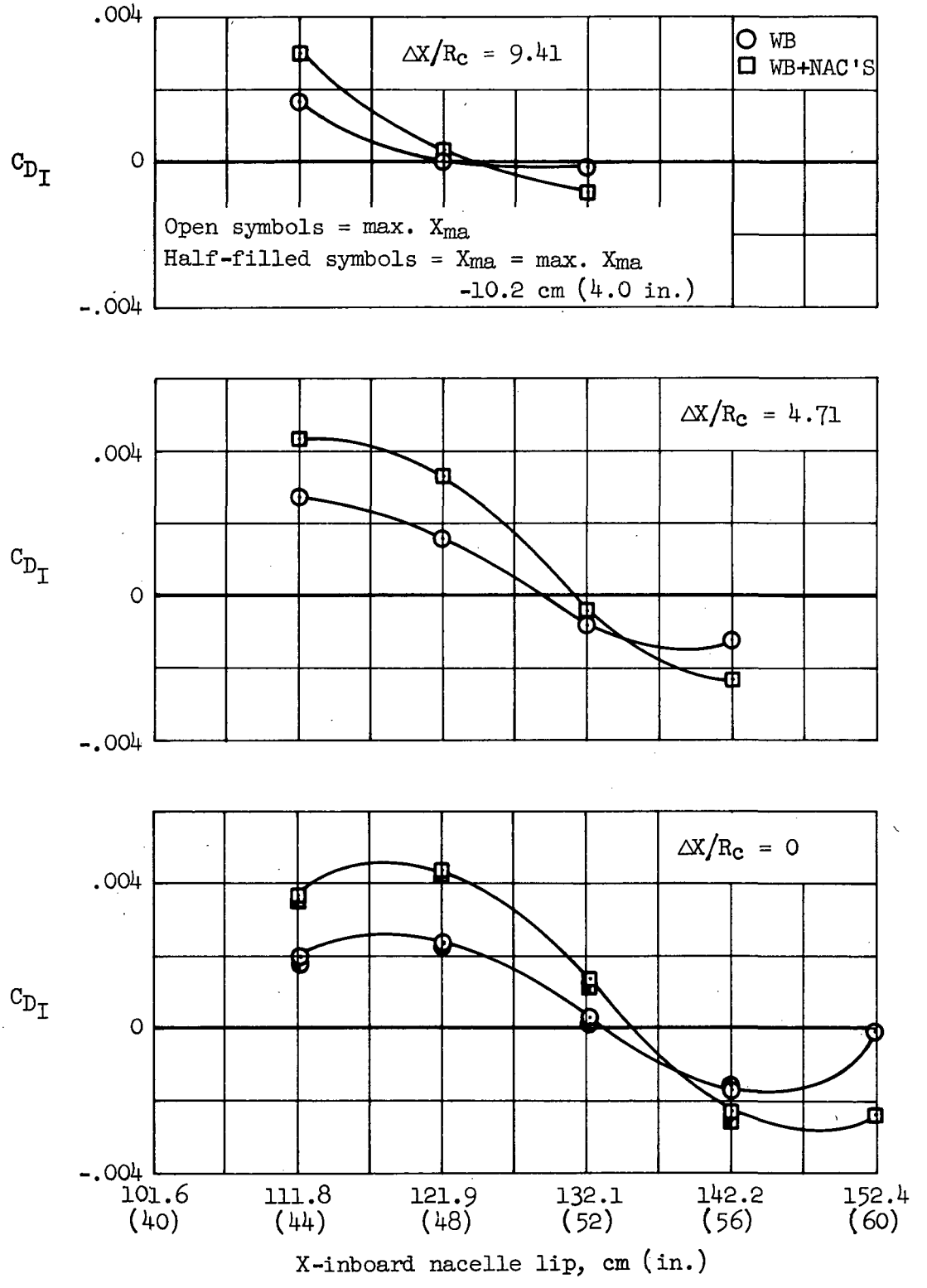

(a) Interference drag.

Figure 38.- Interference forces; configuration WBN_1N_1, M_∞ = 1.40, α = 0°, y_i' = 0.25, y_o' = 0.55, maximum m/m_c.

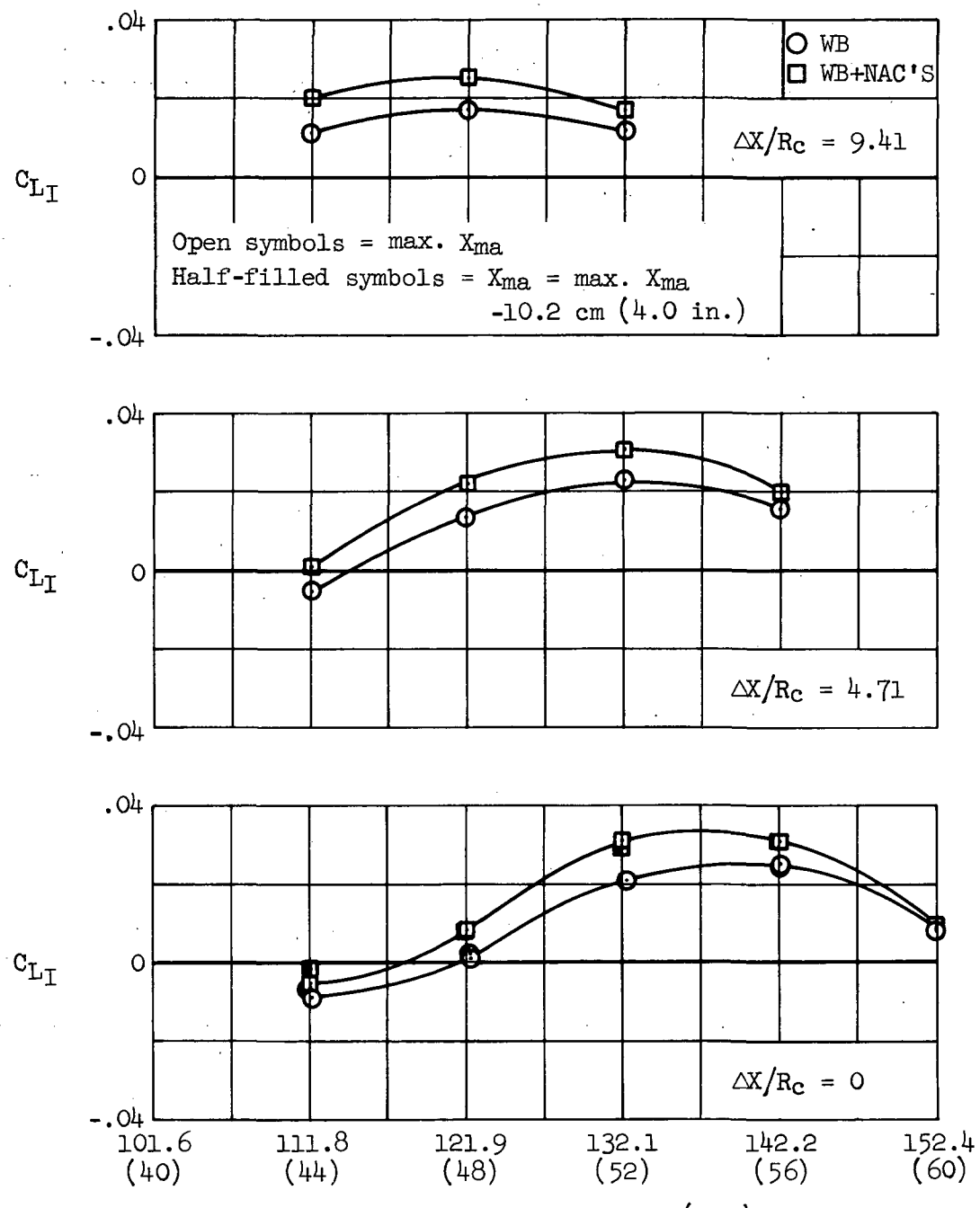

(b) Interference lift.

Figure 38.- Continued.

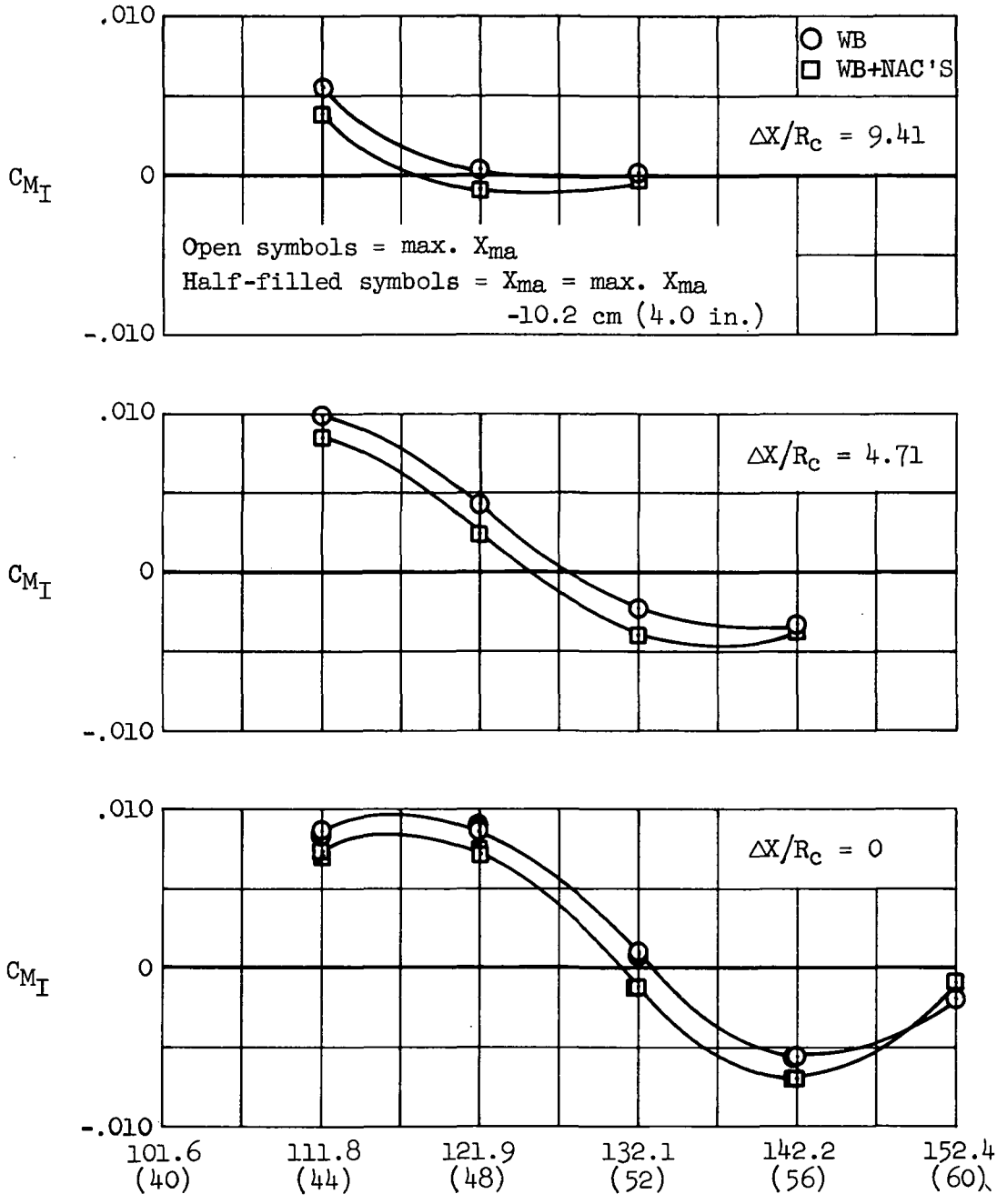

(c) Interference pitching moment.

Figure 38.- Concluded.

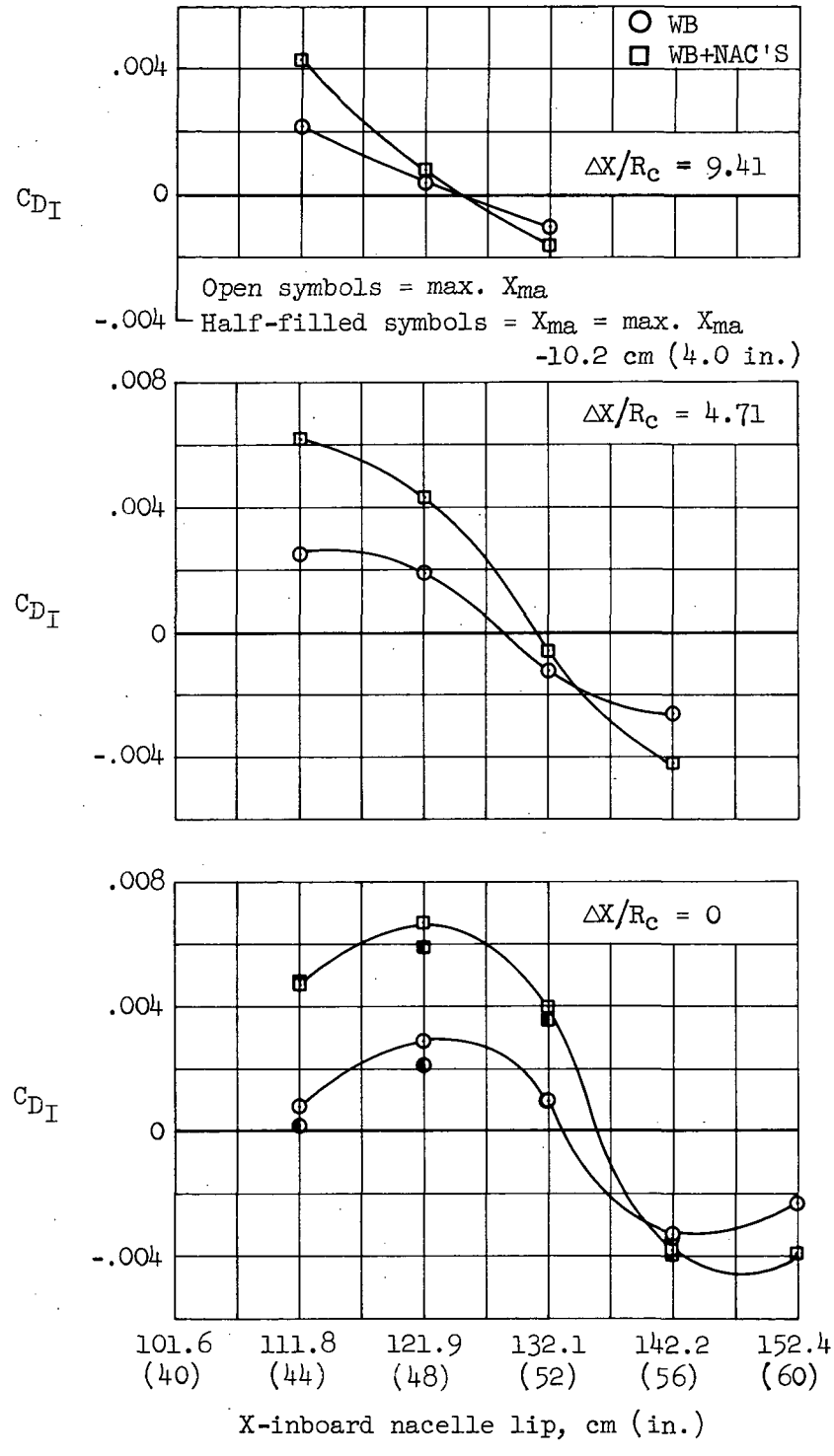

(a) Interference drag.

Figure 39.- Interference forces; configuration WBN_1N_1, $M_\infty = 1.15$, $\alpha = 0°$, $y_i' = 0.25$, $y_o' = 0.55$, maximum m/m_c.

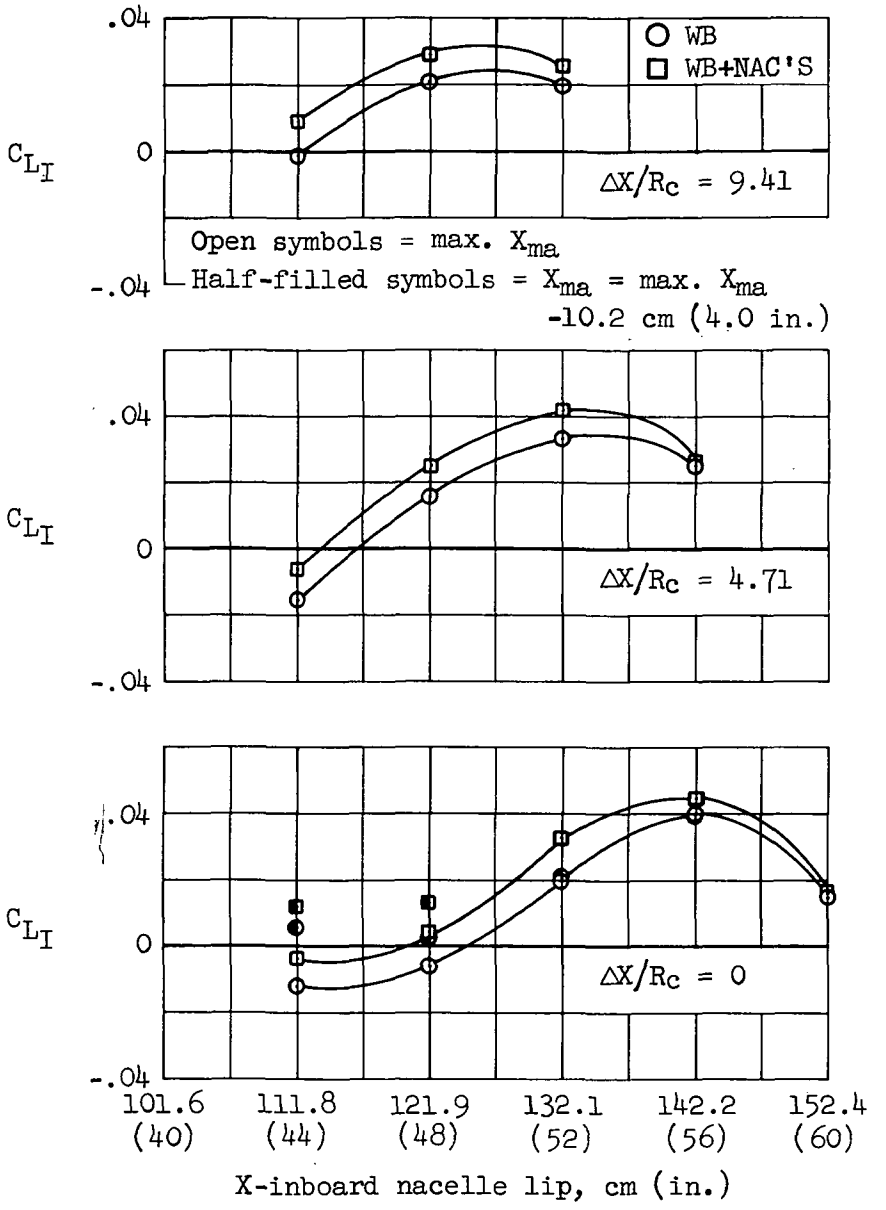

(b) Interference lift.

Figure 39.- Continued.

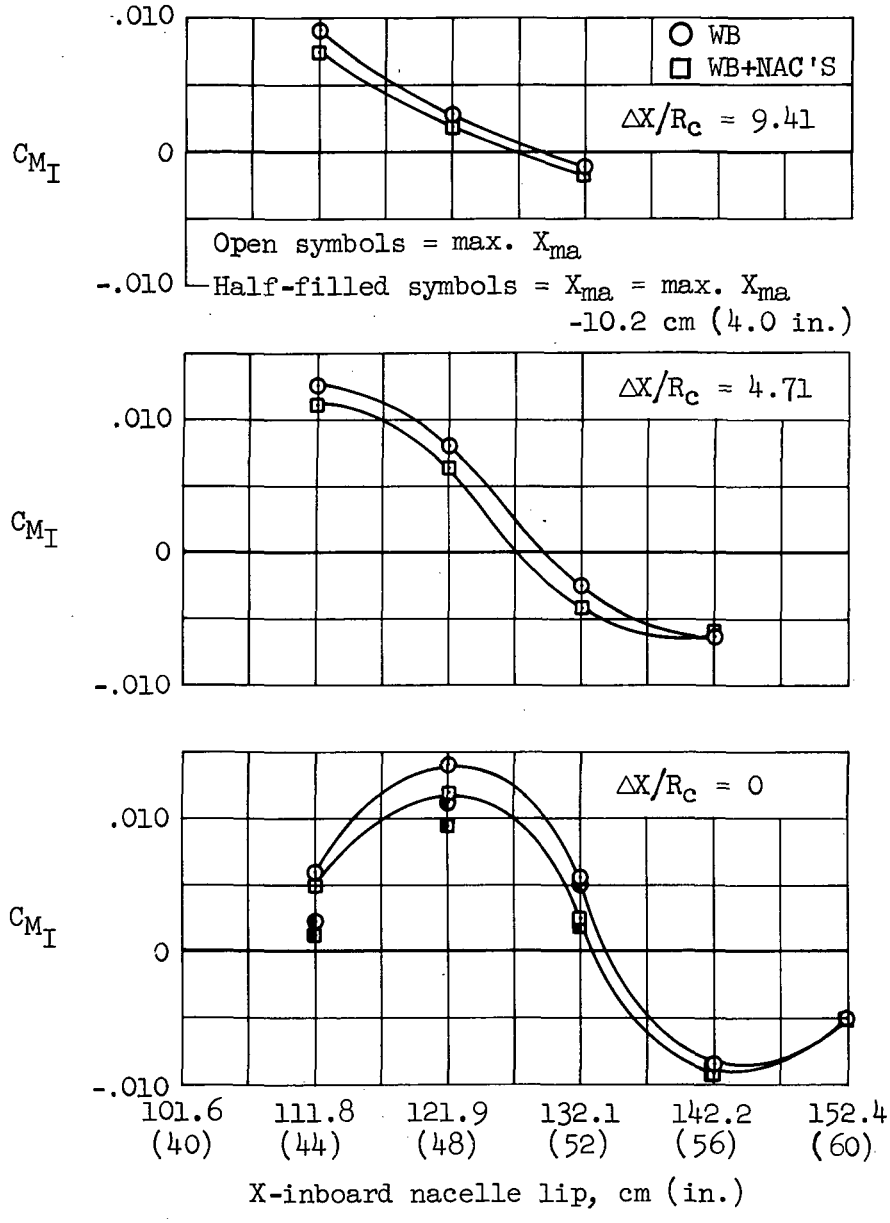

(c) Interference pitching moment.

Figure 39.- Concluded.

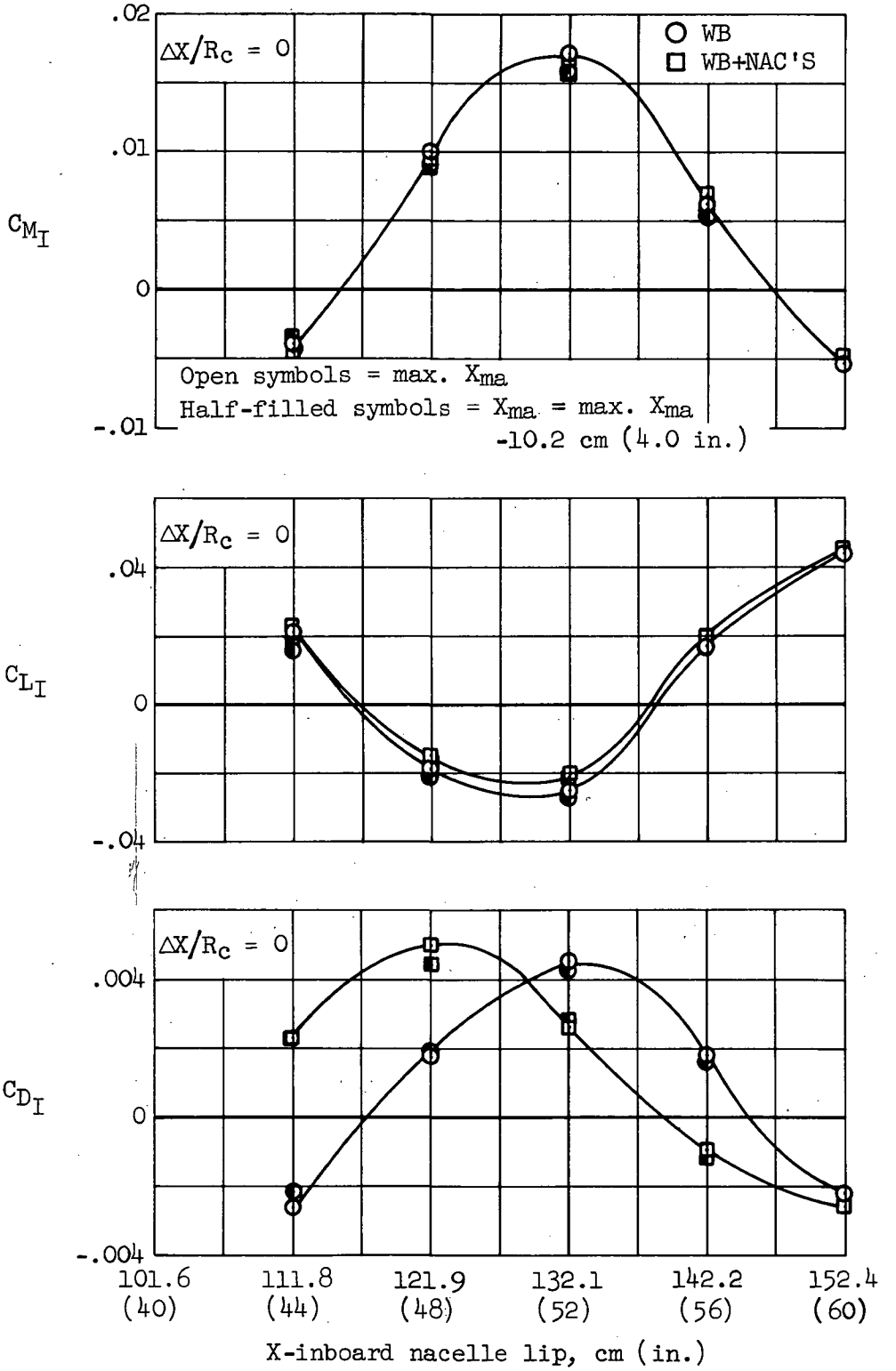

Figure 40.- Interference drag, lift and pitching moment; configuration WBN_1N_1, $M_\infty = 0.90$, $\alpha = 0°$, $y_i' = 0.25$, $y_o' = 0.55$, maximum m/m_c.

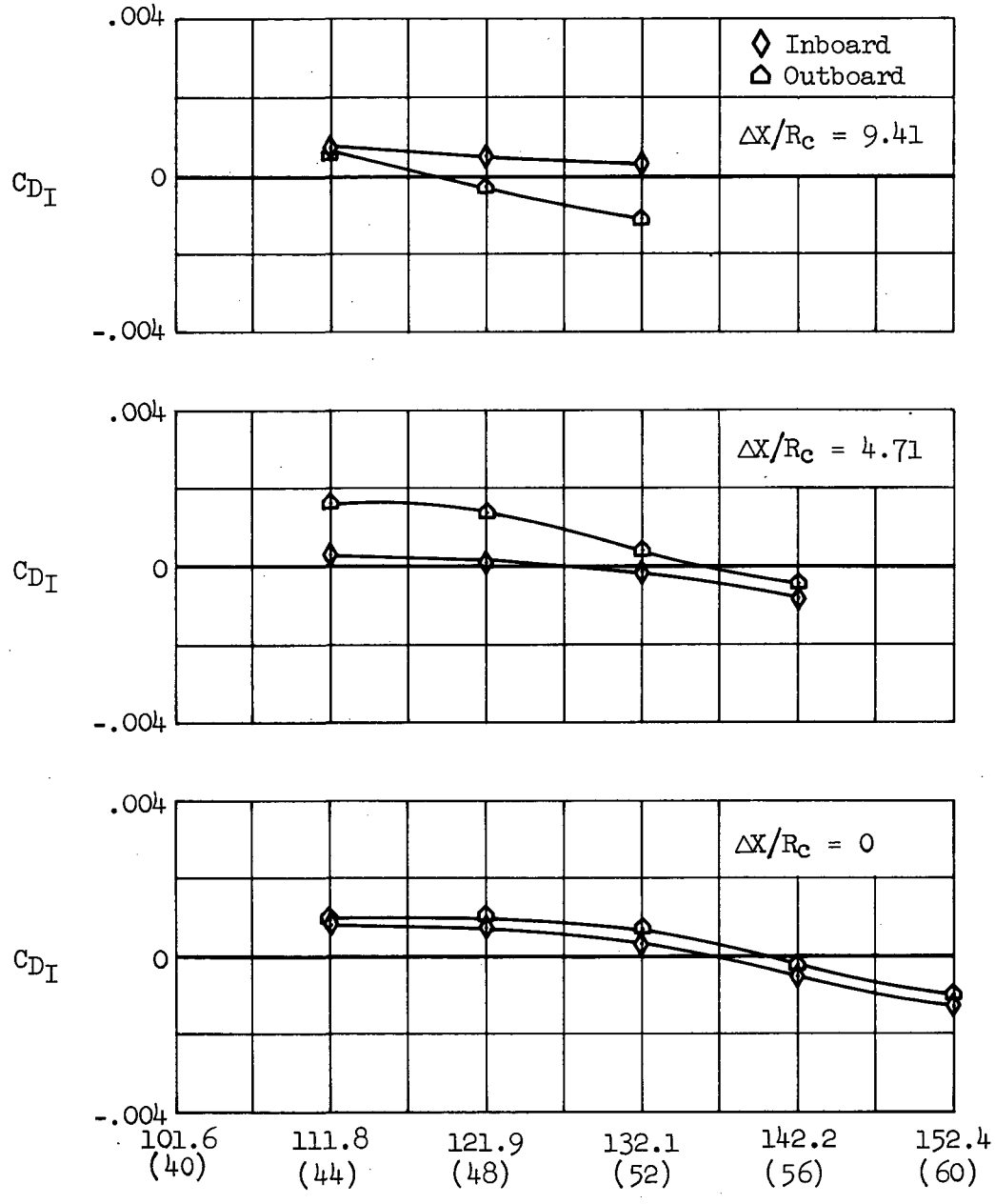

(a) Inteference drag.

Figure 41.- Interference forces on individual nacelle pairs, configuration WBN_1N_1, $M_\infty = 1.40$, $\alpha = 0°$, $y_i' = 0.25$, $y_o' = 0.55$, maximum m/m_c.

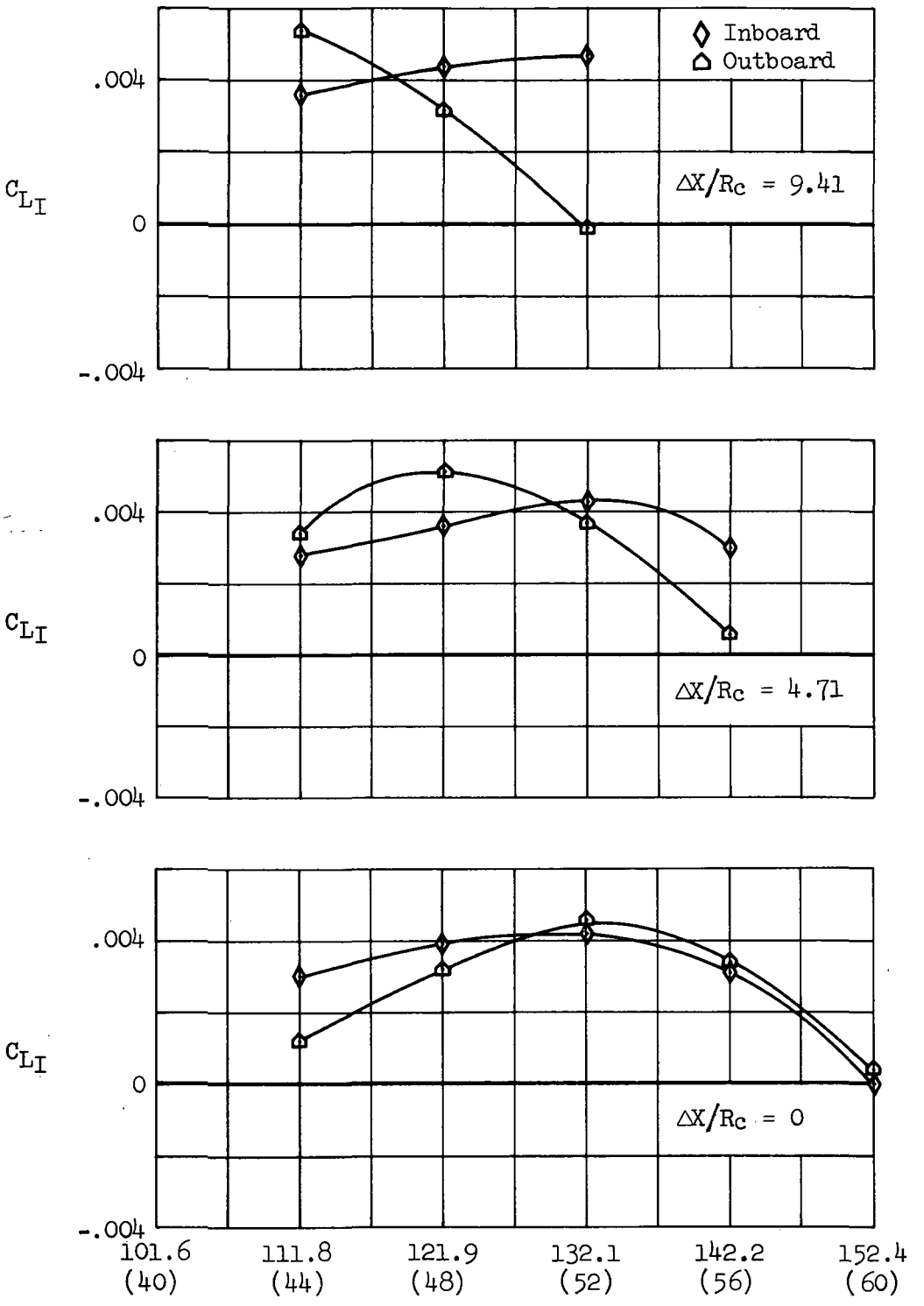

(b) Interference lift.

Figure 41.- Continued.

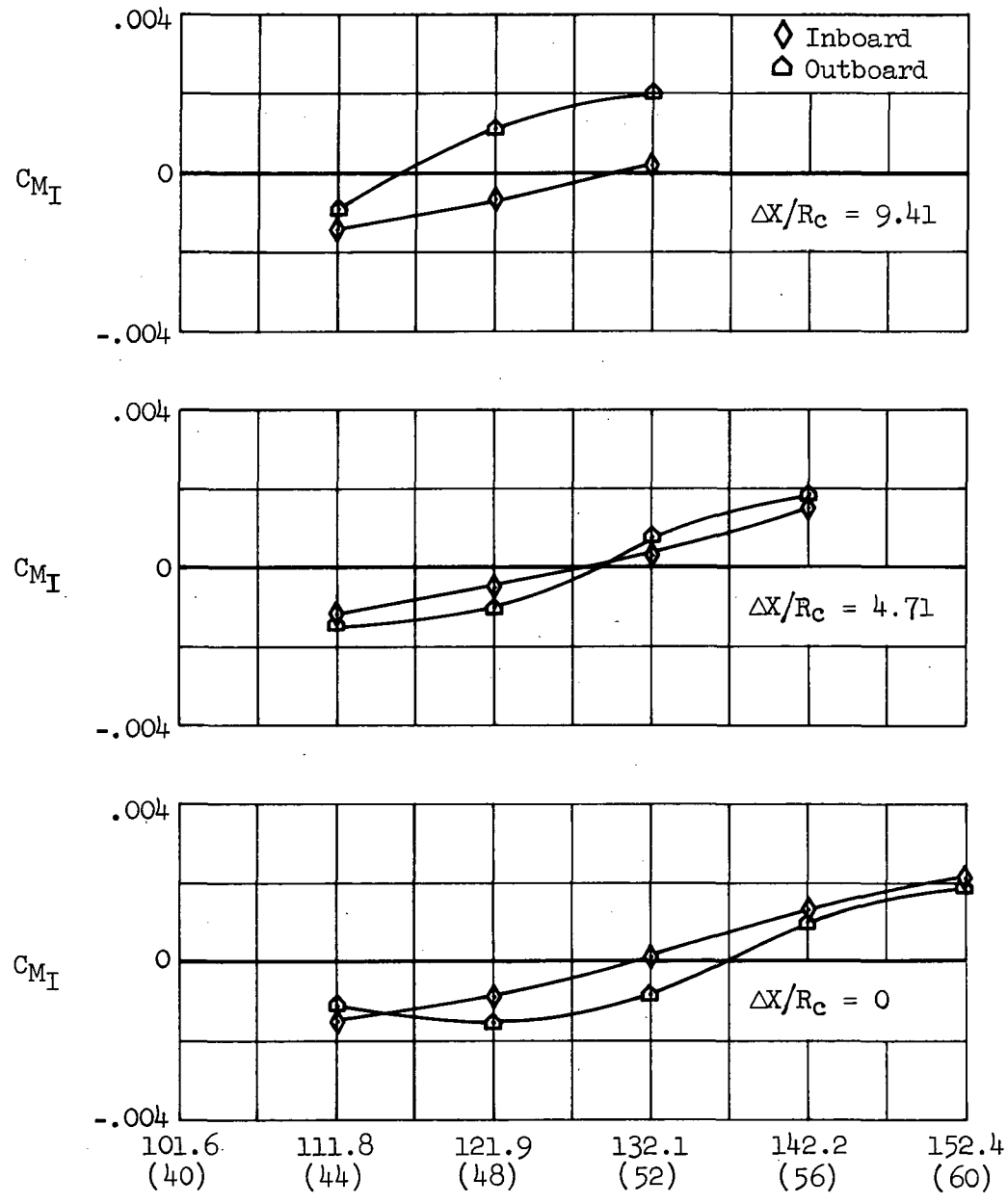

(c) Interference pitching moment.

Figure 41.- Concluded.

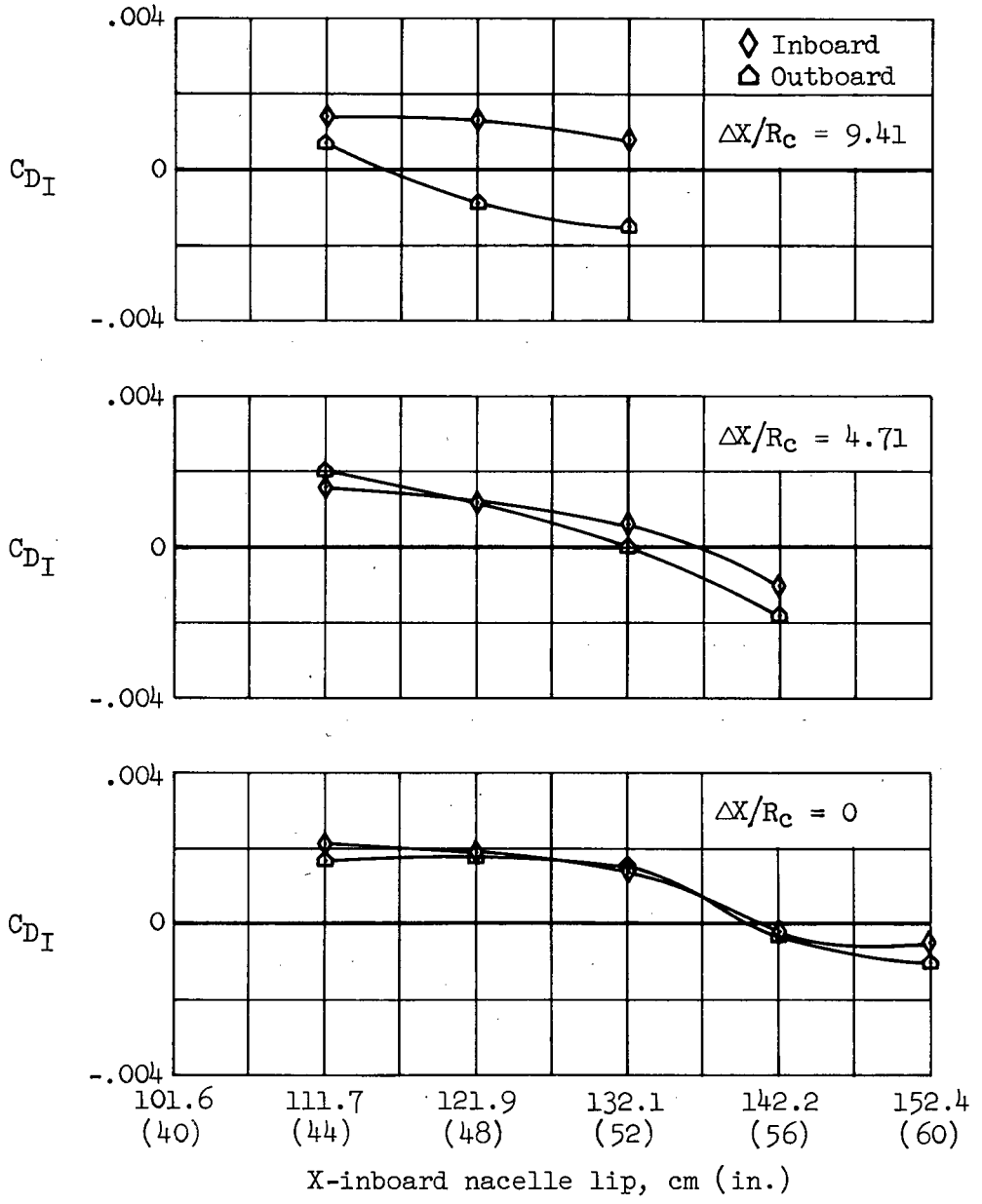

(a) Interference drag.

Figure 42.- Interference forces on individual nacelle pairs; configuration WBN_1N_1, $M_\infty = 1.15$, $\alpha = 0°$, $y_i' = 0.25$, $y_o' = 0.55$, maximum m/m_c.

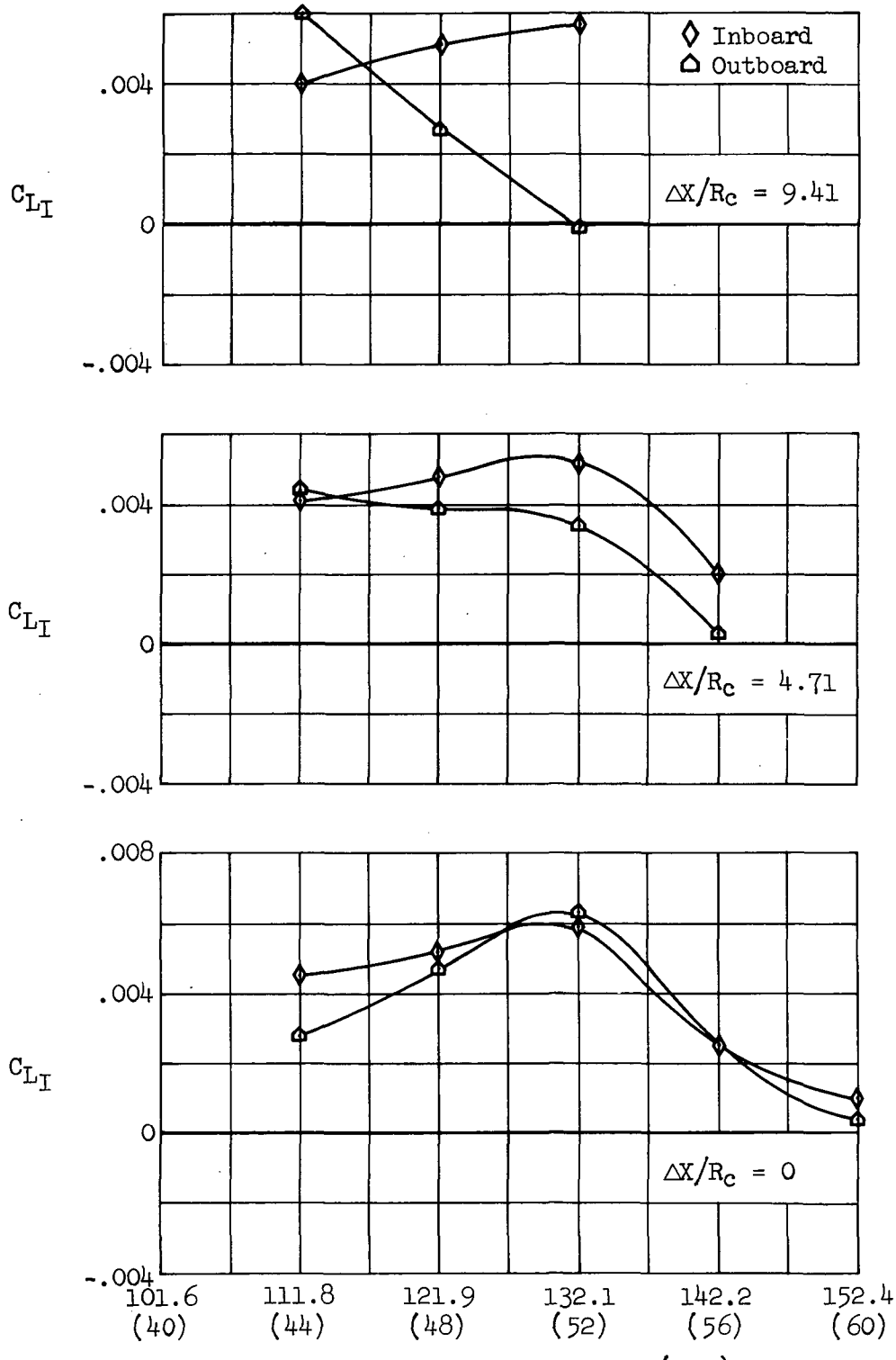

(b) Interference lift.

Figure 42.- Continued.

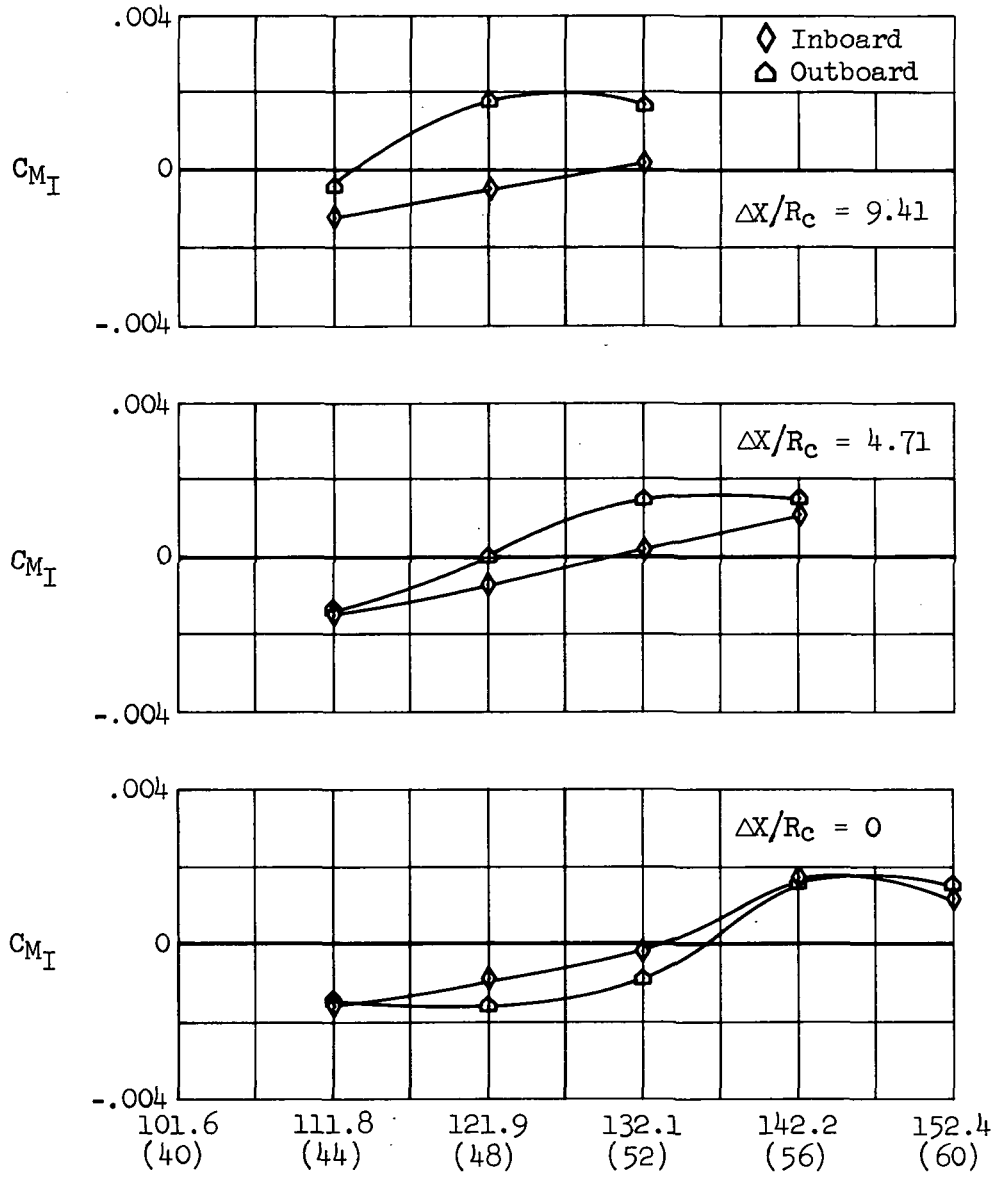

(c) Interference pitching moment.

Figure 42.- Concluded.

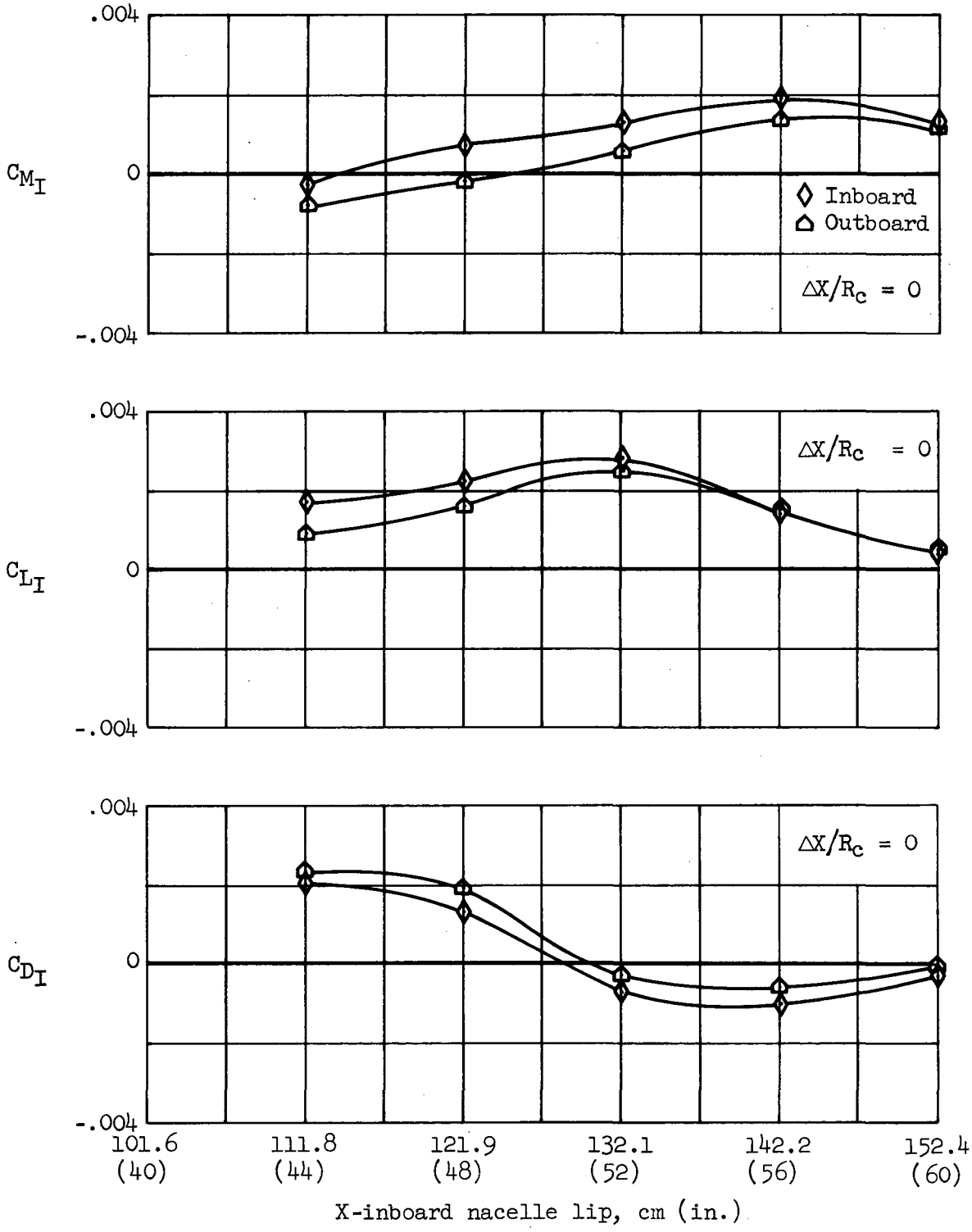

Figure 43.- Interference drag, lift, and pitching moment on individual nacelle pairs; configuration WBN_1N_1, $M_\infty = 0.90$, $\alpha = 0°$, $y_i' = 0.25$, $y_o' = 0.55$, maximum m/m_c.

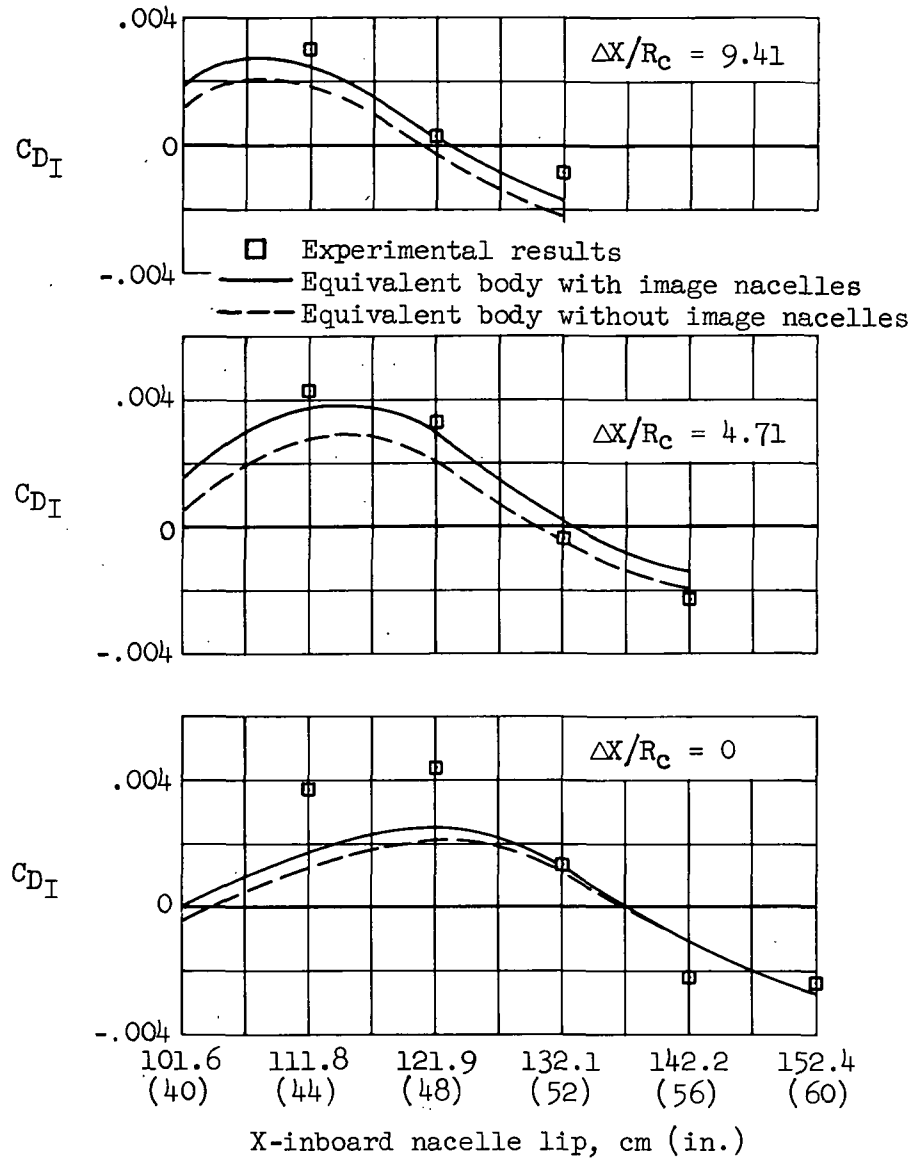

(a) $M_\infty = 1.40$

Figure 44.- Comparison between measured and predicted interference drag; configuration WBN_1N_1, $\alpha = 0°$, $y_i' = 0.25$, $y_o' = 0.55$ maximum m/m_c.

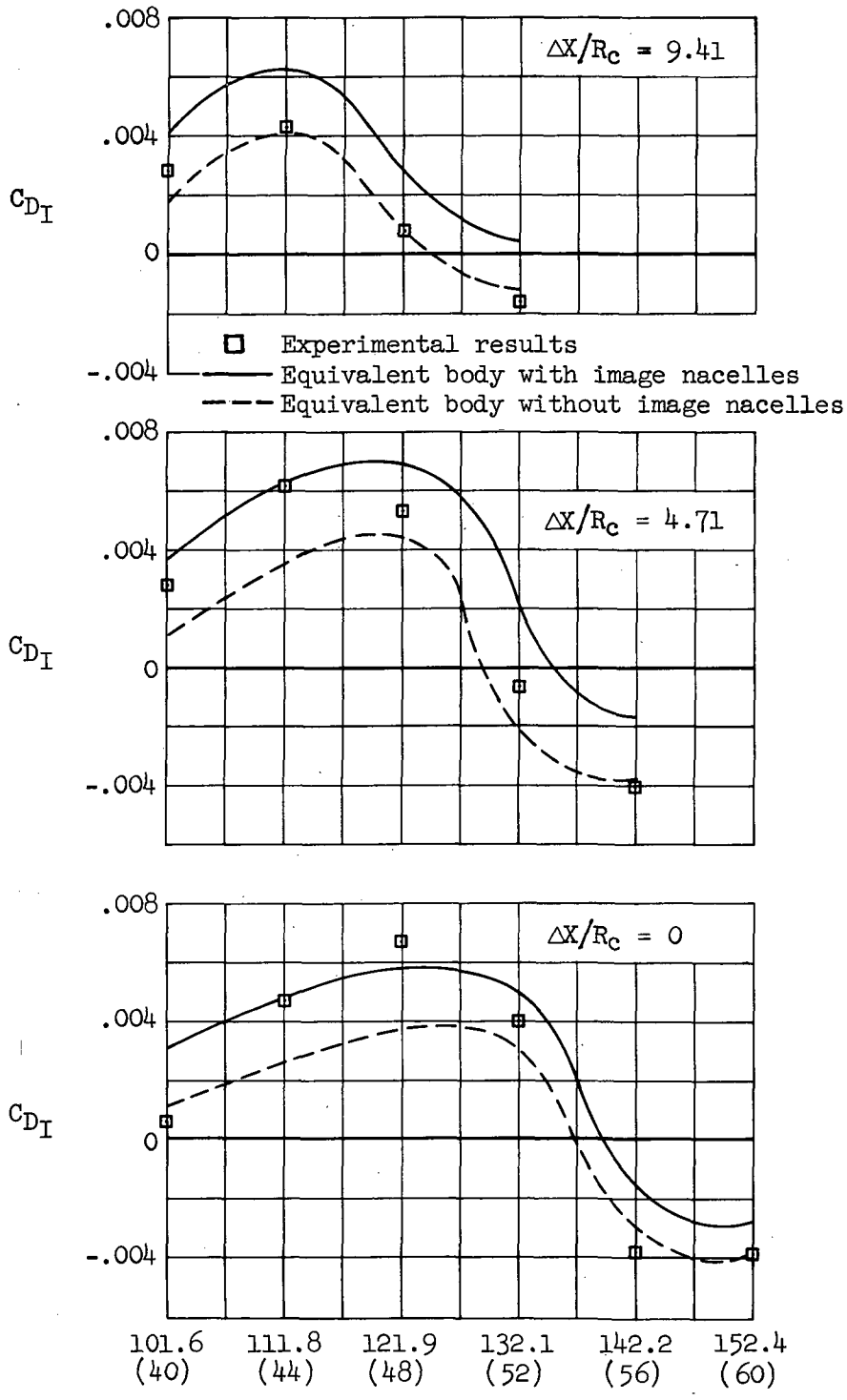

(b) M_∞ = 1.15

Figure 44.- Concluded.

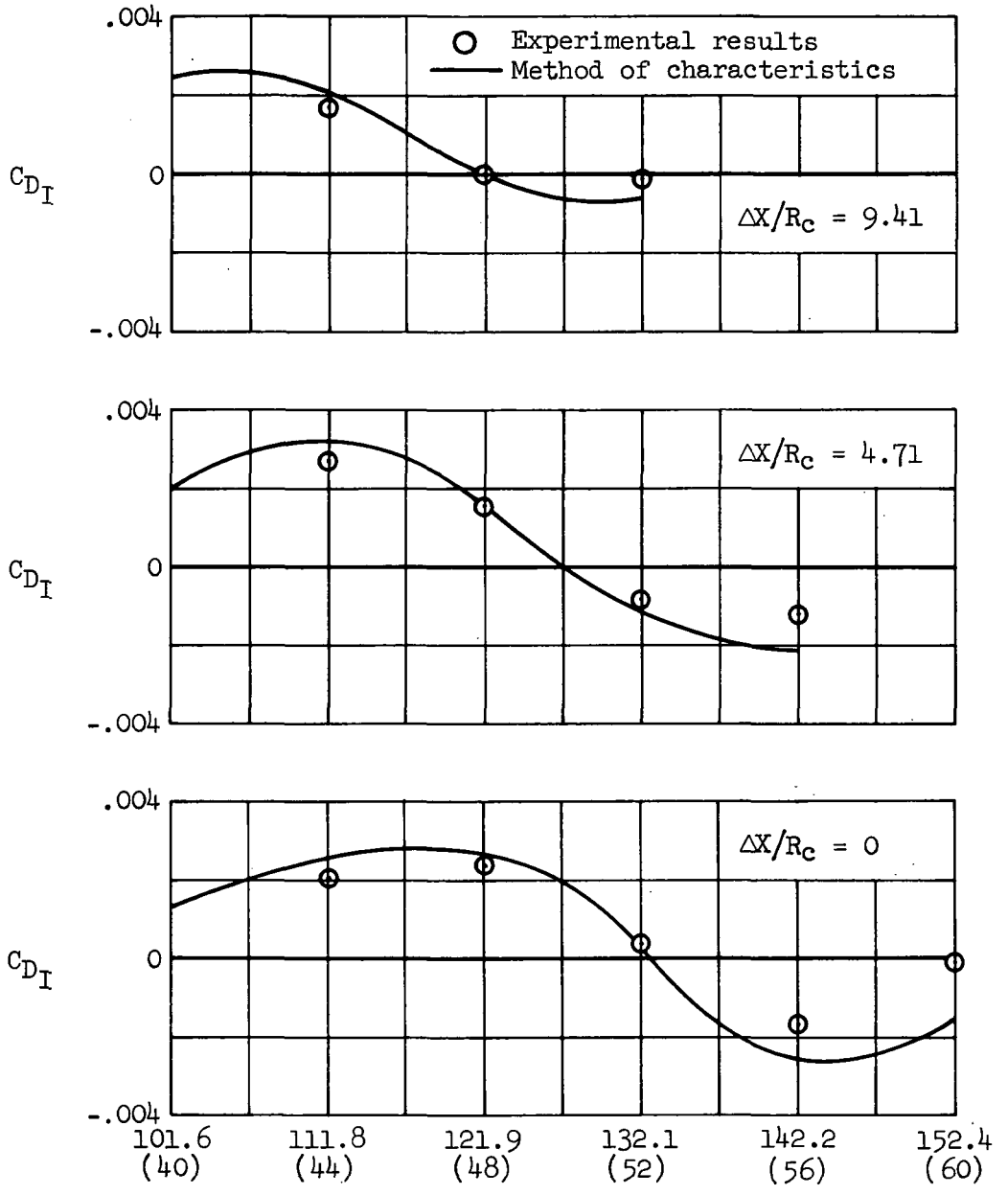

(a) Interference drag.

Figure 45.- Comparison between measured and predicted interference forces on the wing-body combination; configuration WBN_1,N_1, $M_\infty = 1.40$, $\alpha = 0°$, $y_i' = 0.25$, $y_o' = 0.55$, maximum m/m_c.

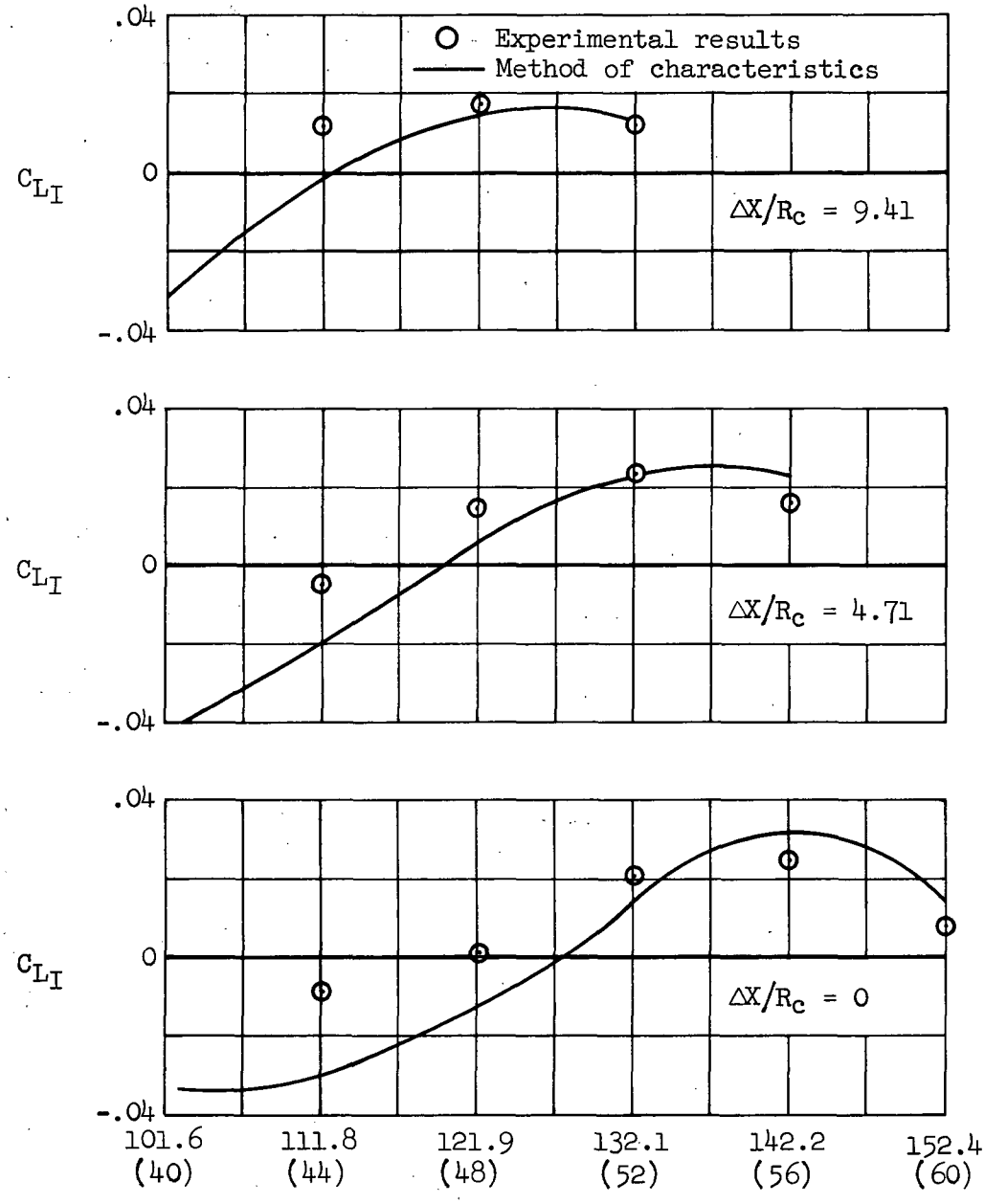

(b) Interference lift.

Figure 45.- Continued.

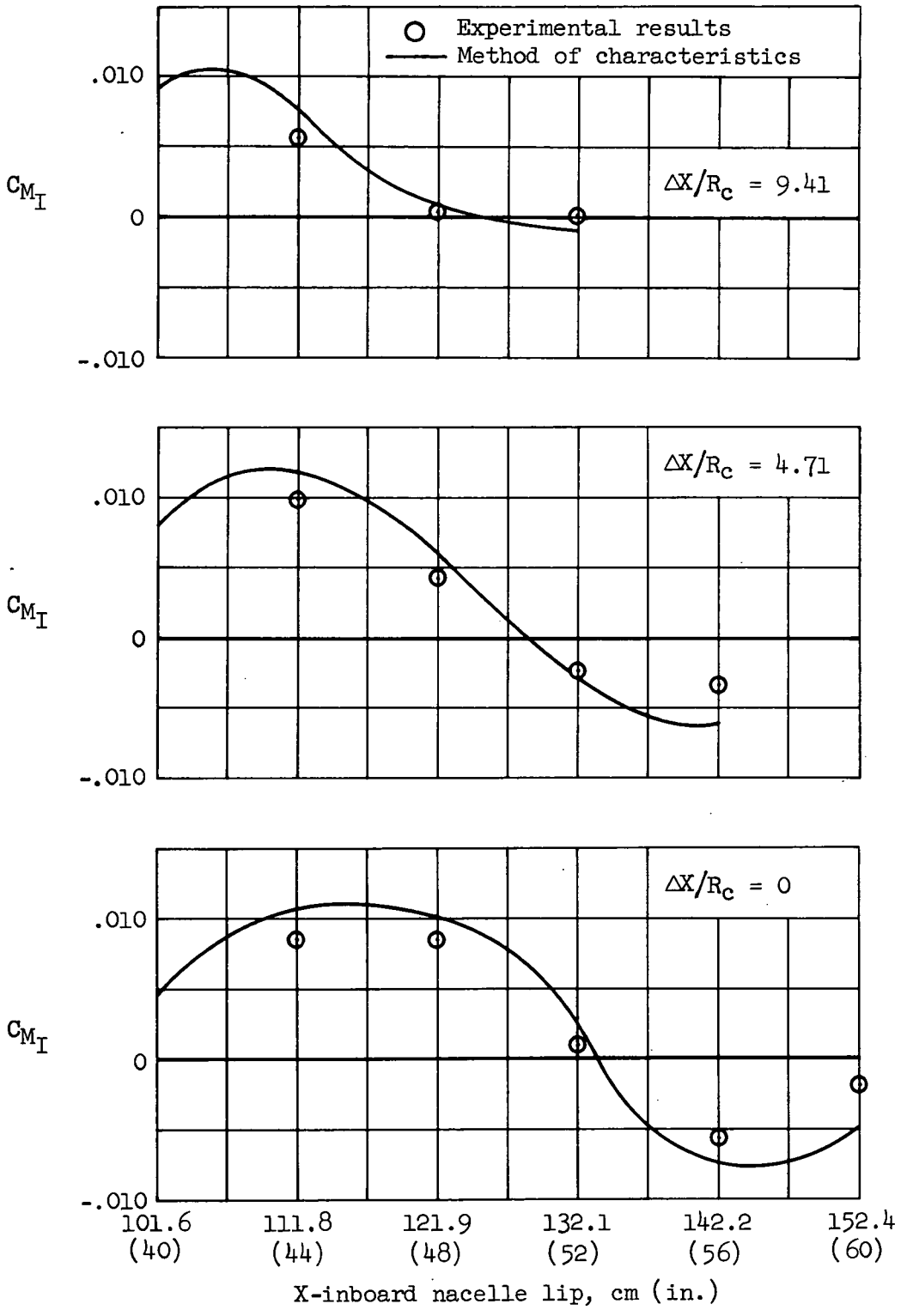

(c) Interference pitching moment.

Figure 45.- Concluded.

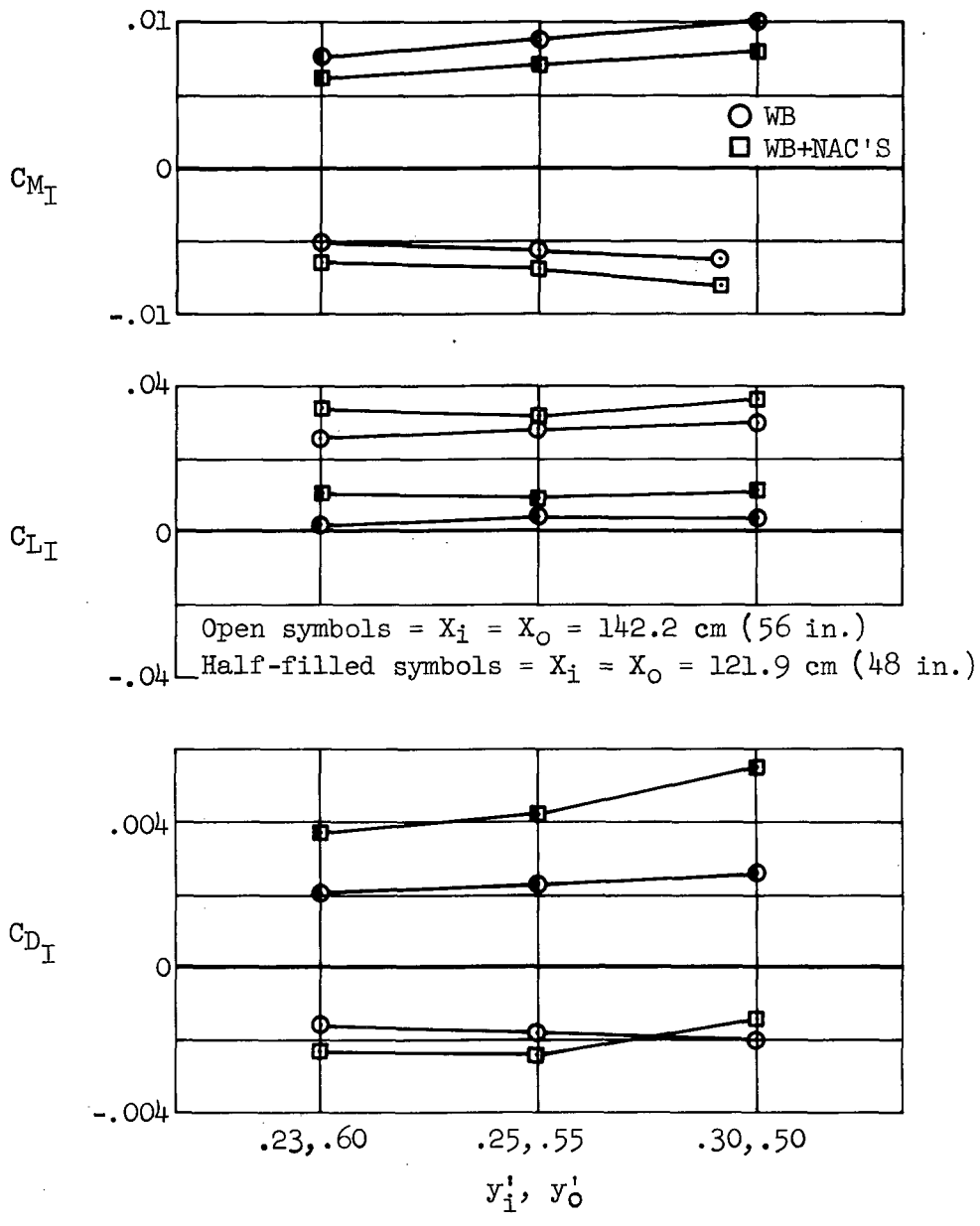

(a) $M_\infty = 1.40$

Figure 46.- Effects of spanwise nacelle position on interference drag, lift, and pitching moment; configuration WBN_1N_1, $\alpha = 0°$, $\Delta X/R_c = 0$, maximum m/m_c.

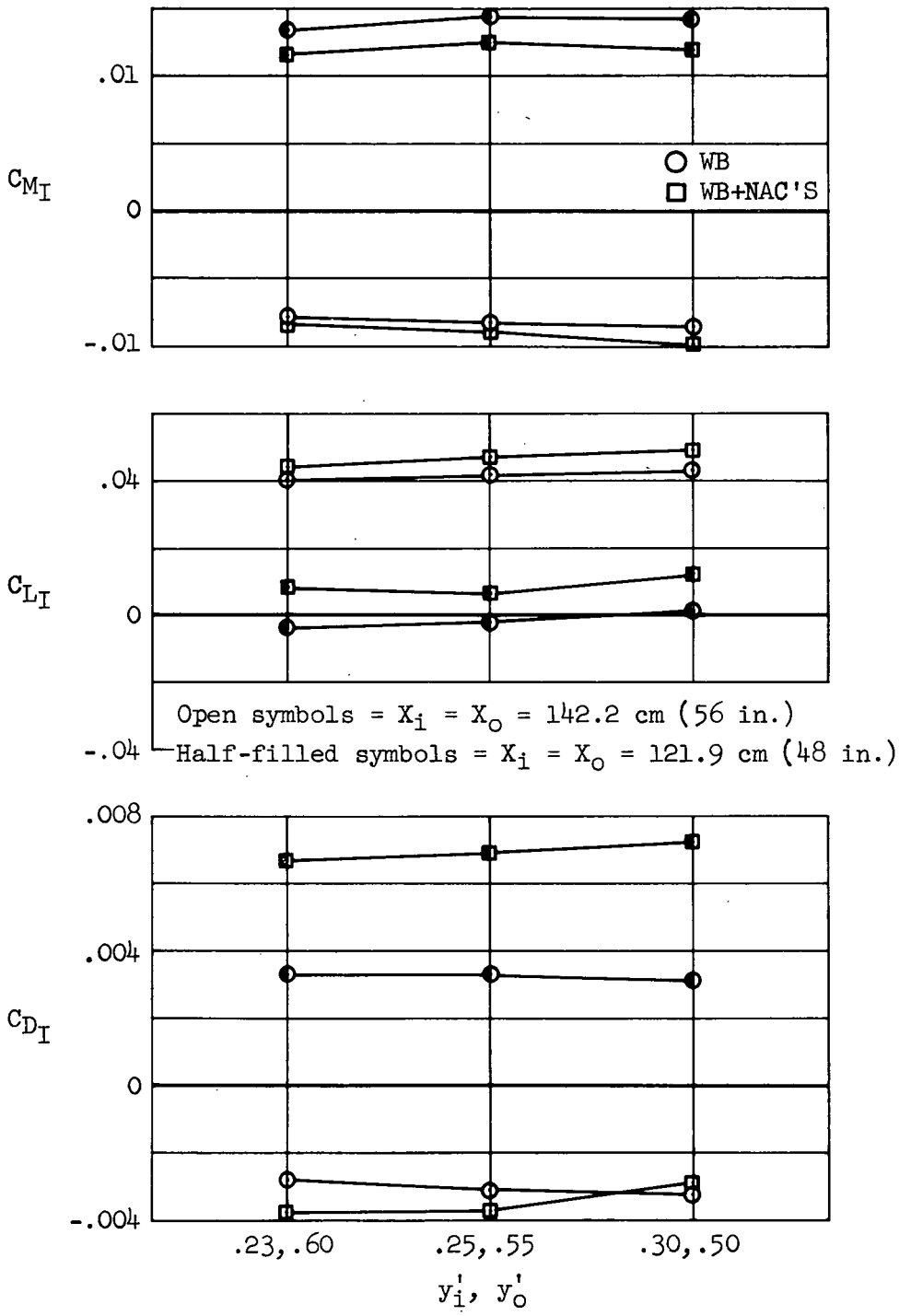

(b) M_∞ = 1.15

Figure 46.- Concluded.

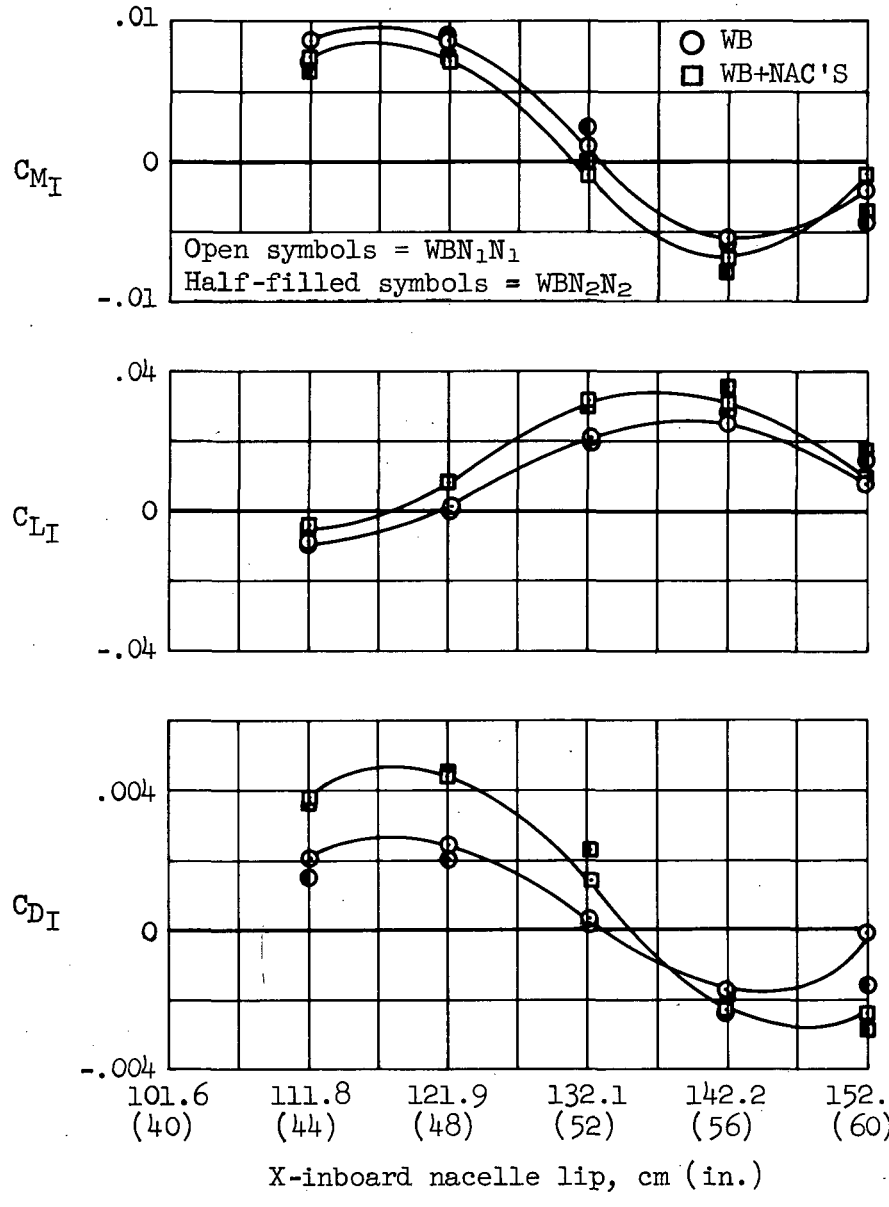

(a) $M_\infty = 1.40$

Figure 47.- Effects of nacelle contours on interference drag, lift, and pitching moment; $\alpha = 0°$, $y_i' = 0.25$, $y_o' = 0.55$, $\Delta X/R_c = 0$, maximum m/m_c.

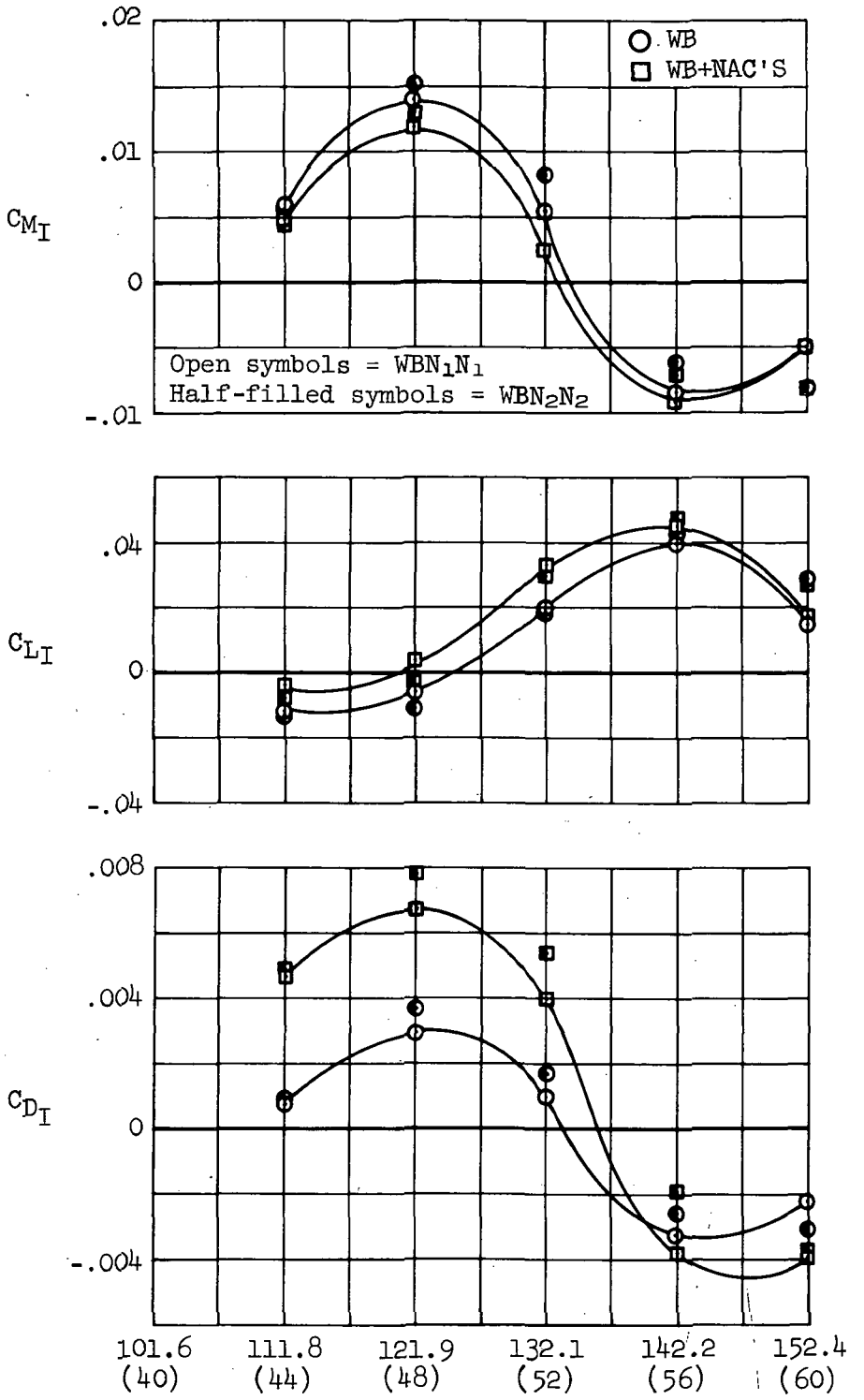

(b) $M_\infty = 1.15$

Figure 47.- Concluded.

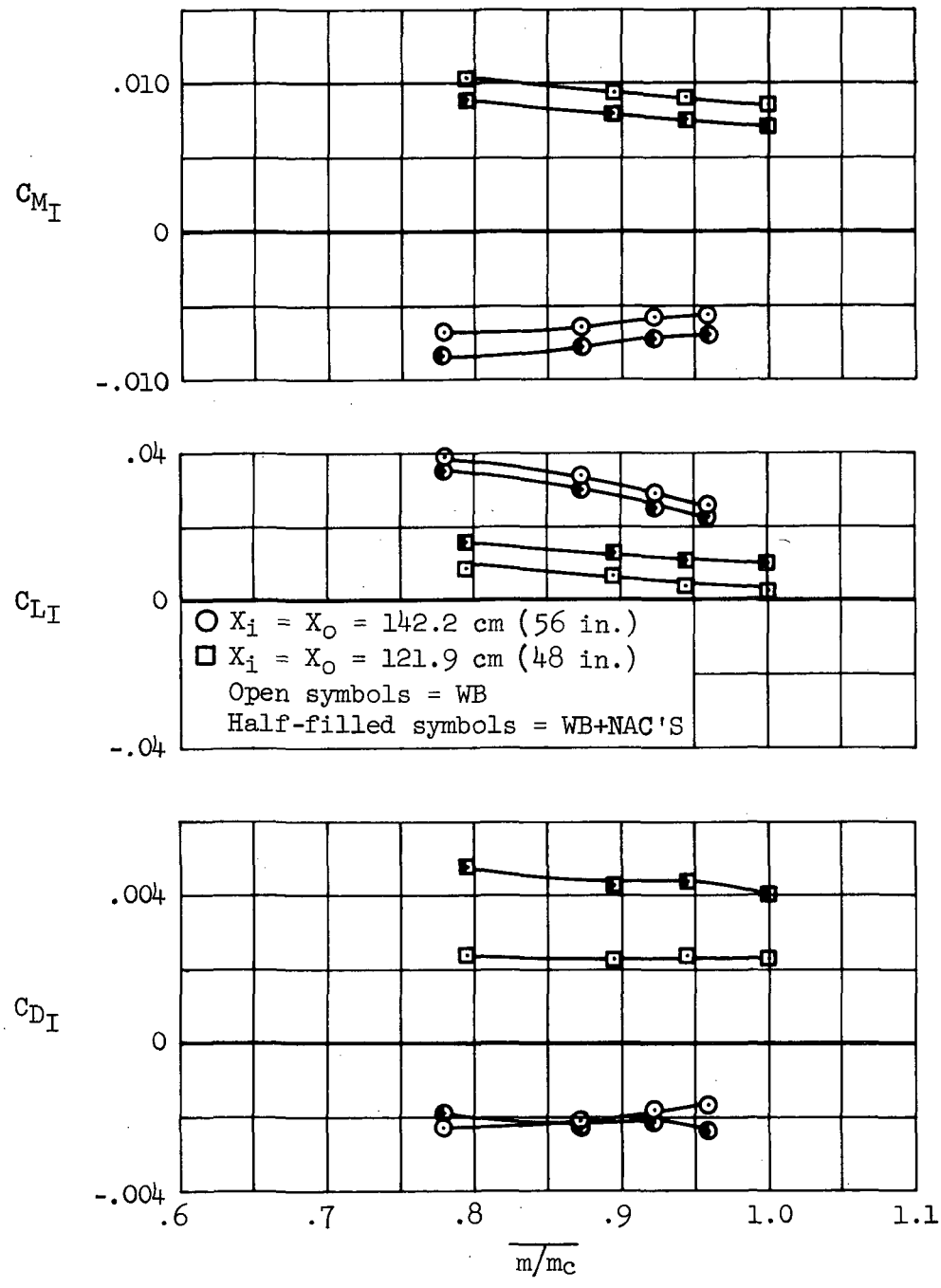

(a) $M_\infty = 1.40$

Figure 48.- Effects of mass-flow ratio on interference drag, lift, and pitching moment; configuration WBN_1N_1, $\alpha = 0°$, $y_i' = 0.25$, $y_o' = 0.55$, $\Delta X/R_c = 0$.

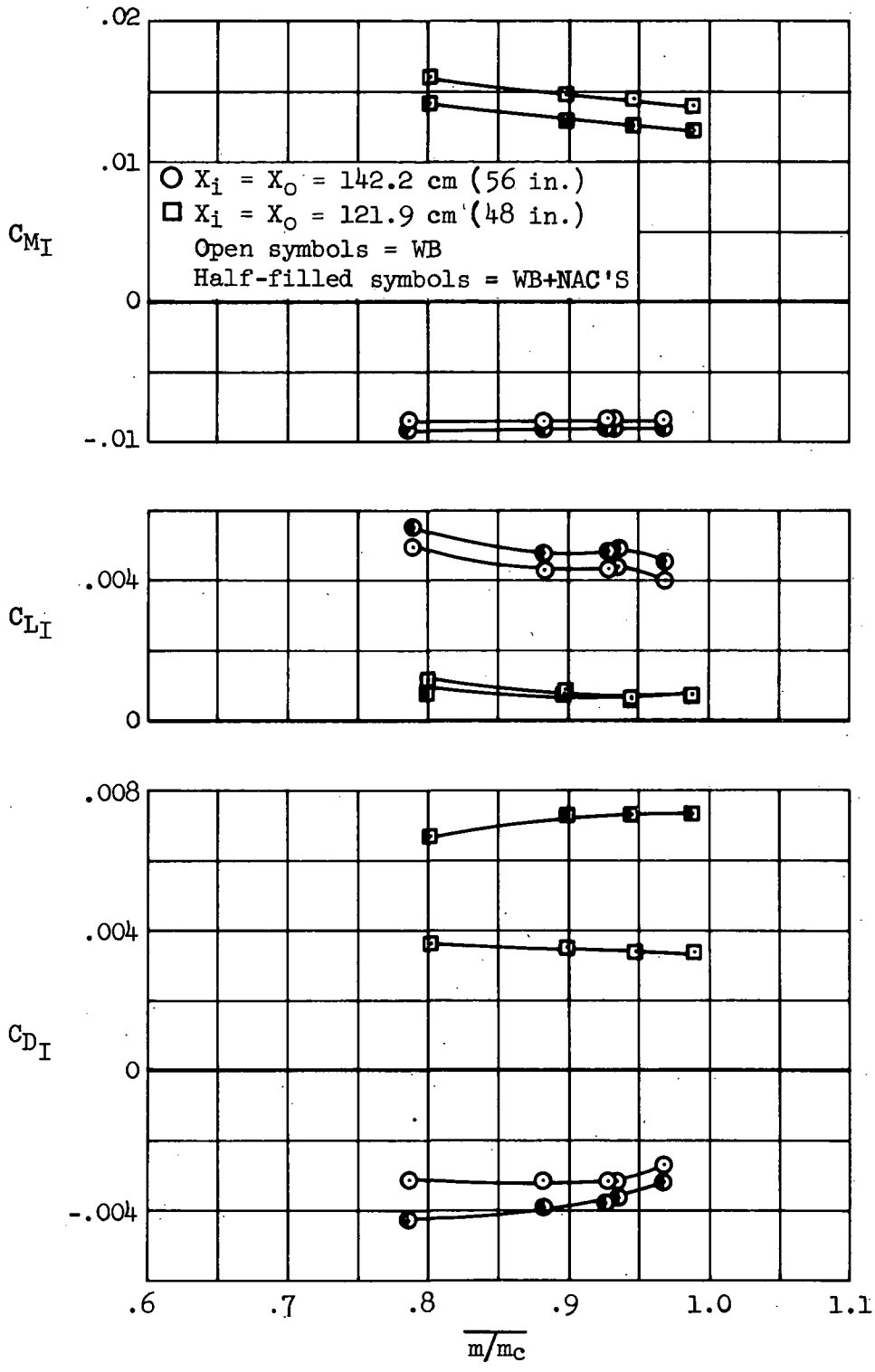

(b) $M_\infty = 1.15$

Figure 48.- Continued.

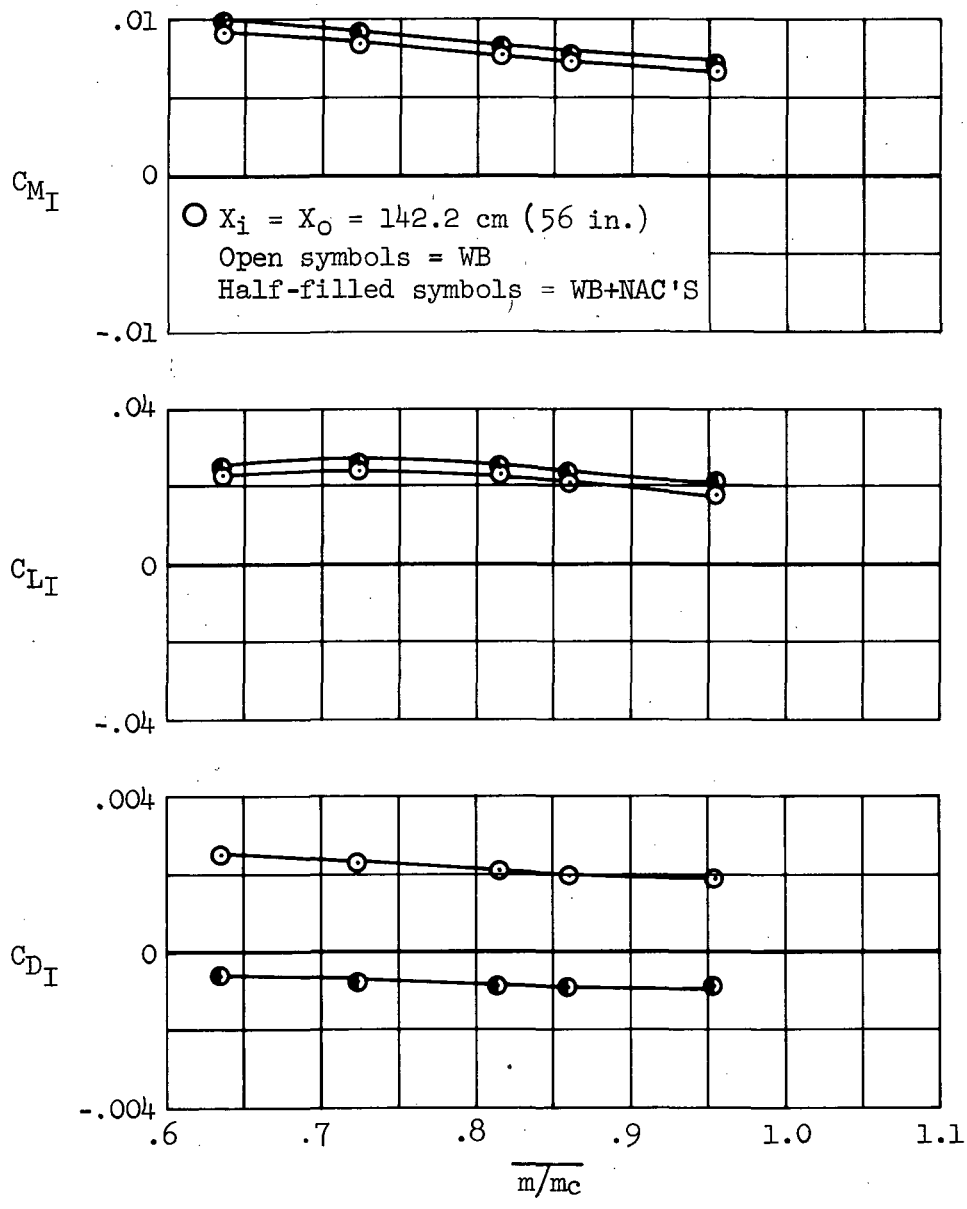

(c) $M_\infty = 0.90$

Figure 48.- Concluded.

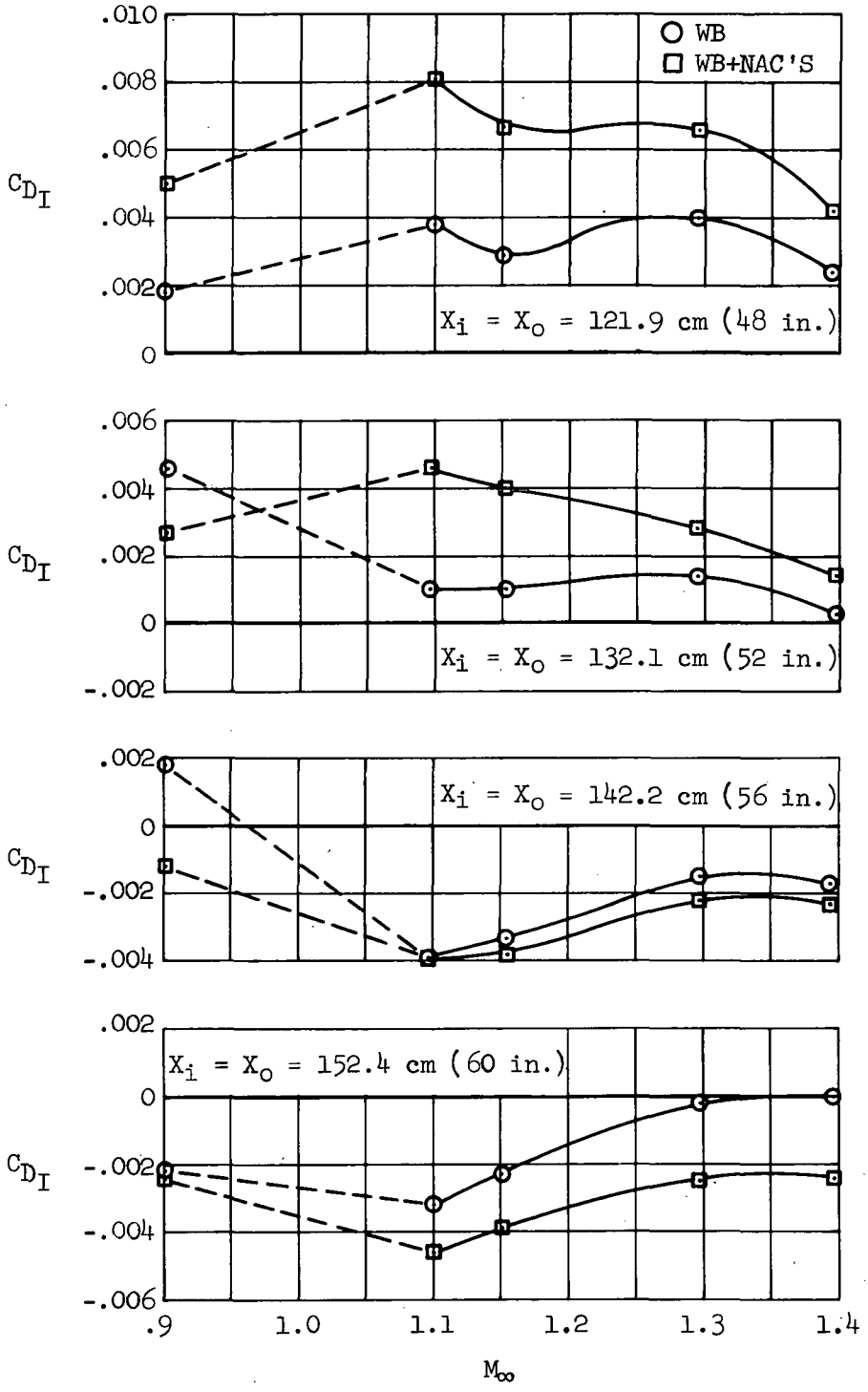

(a) Interference drag.

Figure 49.- Influence of Mach number on the interference forces; configuration WBN_1N_1, $\alpha = 0°$, $y_i' = 0.25$, $y_o' = 0.55$, $\Delta X/R_c = 0$, maximum m/m_c.

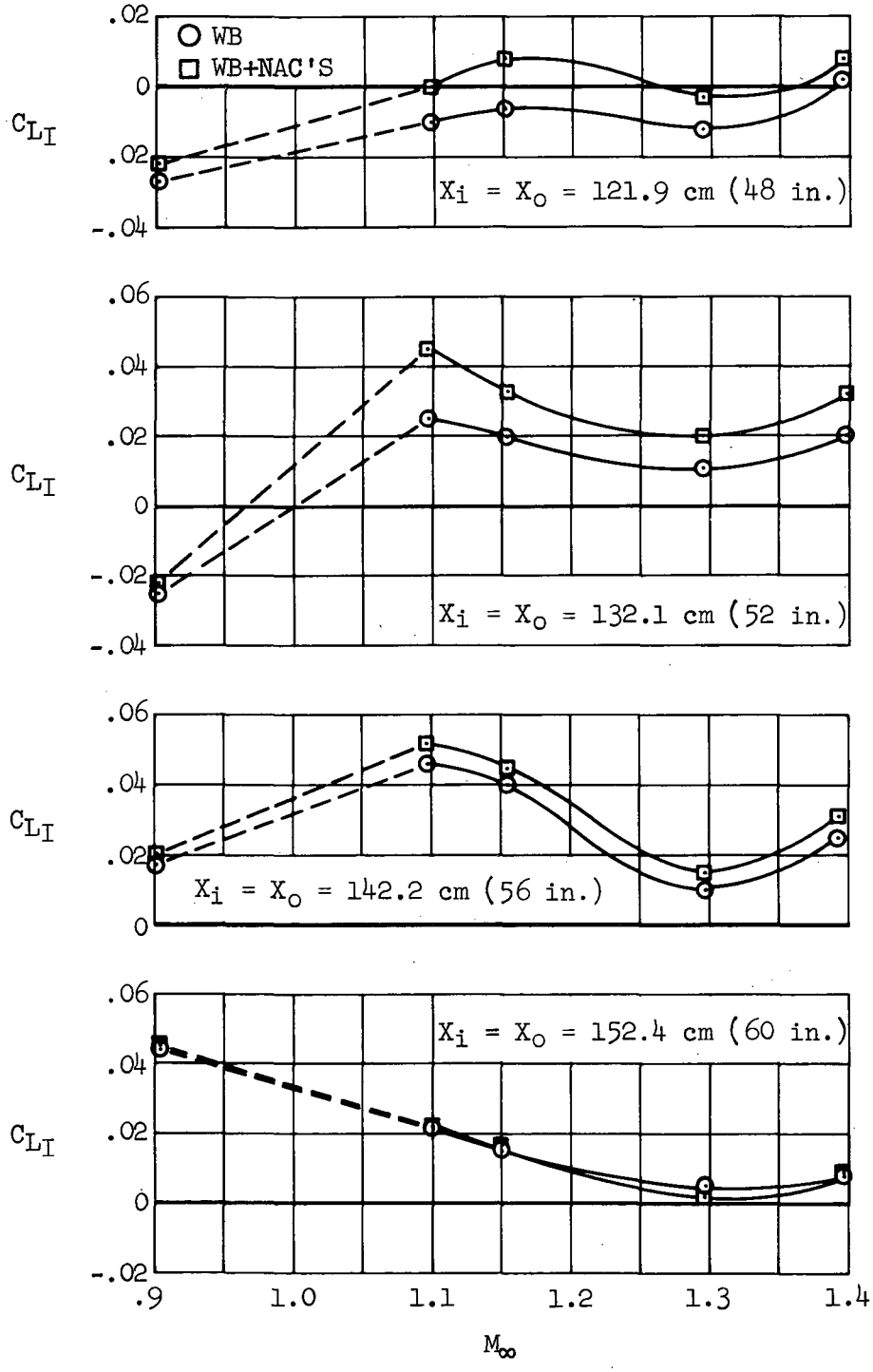

(b) Interference lift.

Figure 49.- Continued.

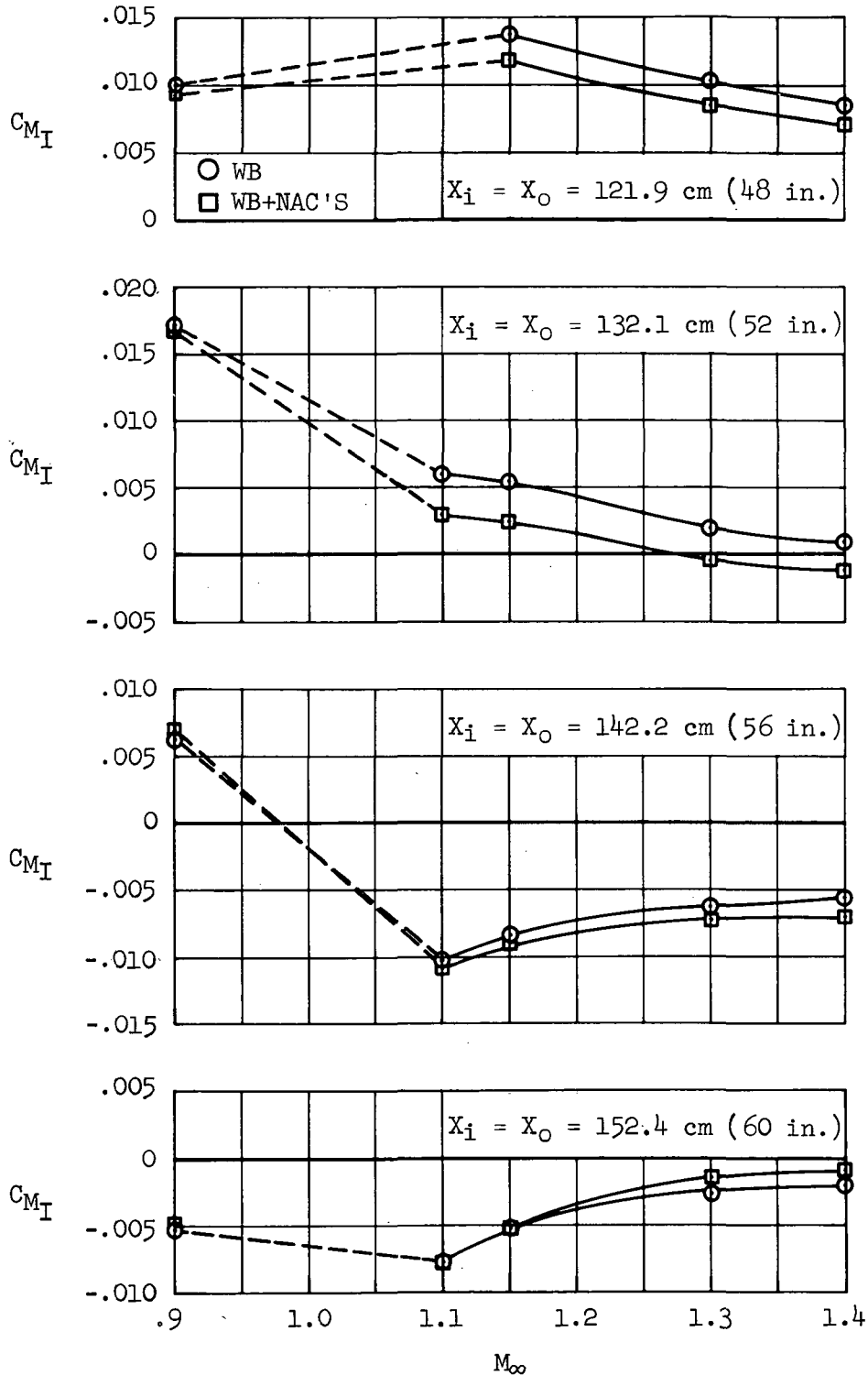

(c) Interference pitching moment.

Figure 49.- Concluded.

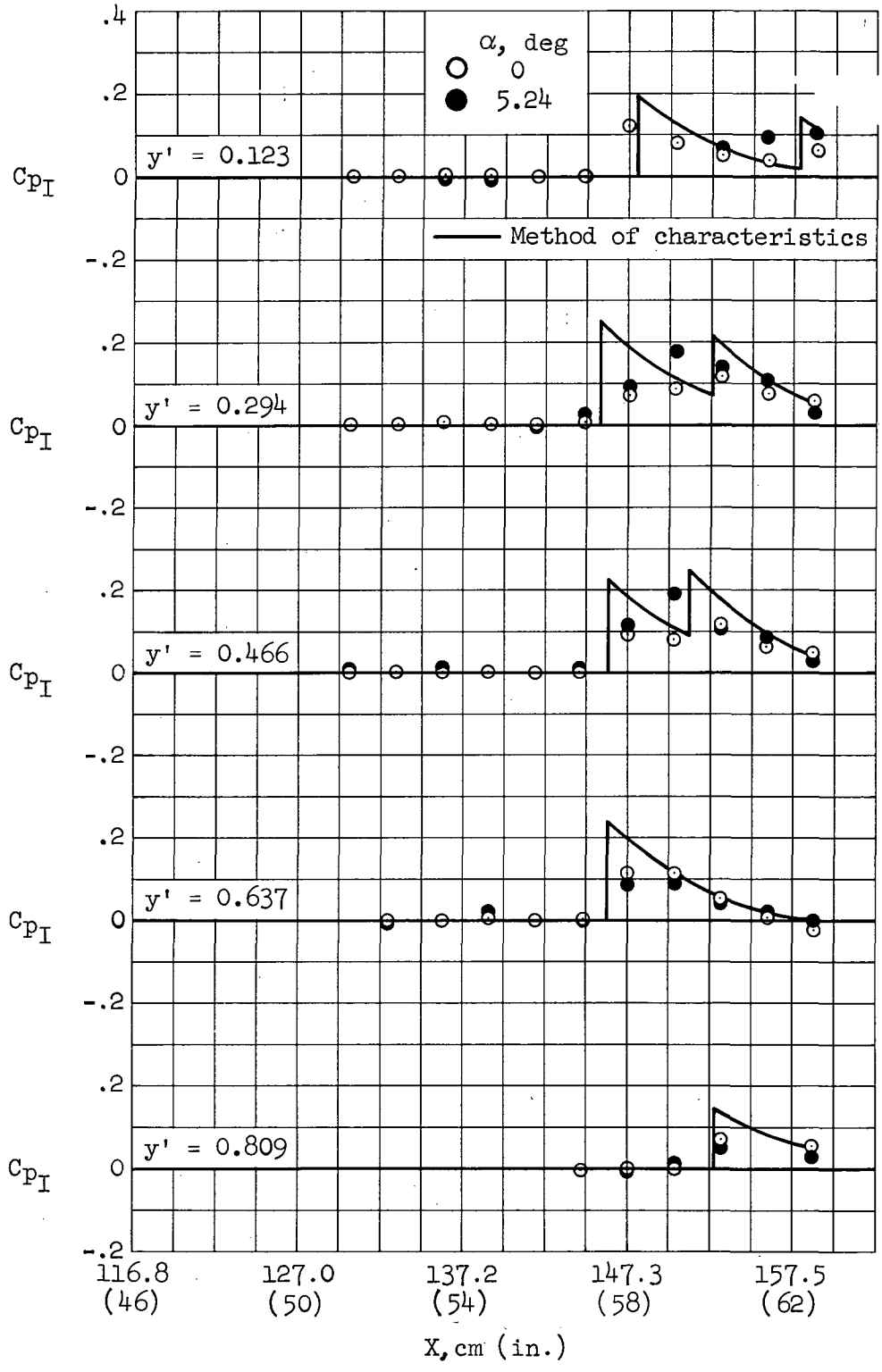

Figure 50.- Comparison between measured and predicted lower wing surface interference pressure distributions; configuration WBN_1N_1, $M_\infty = 1.40$, $y_i' = 0.25$, $y_o' = 0.55$, $X_i = X_o = 142.2$ cm (56 in.).

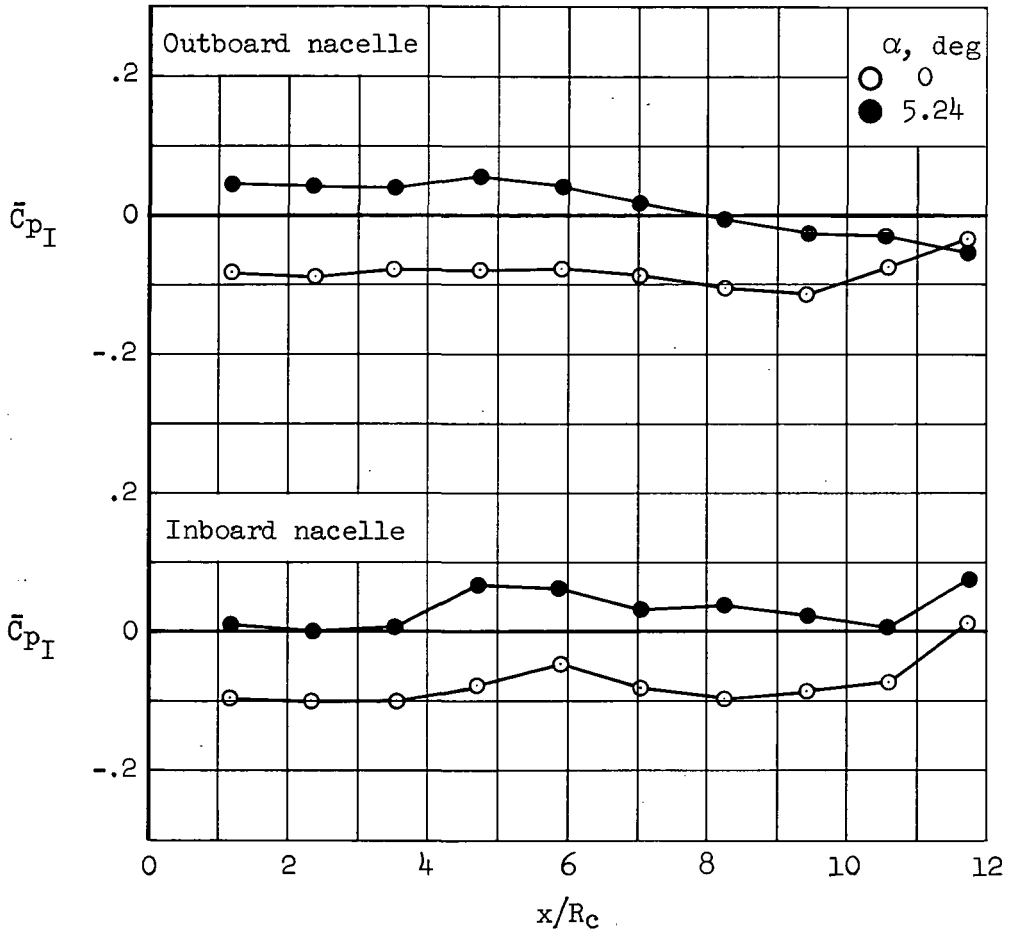

(a) $\bar{C}_{p_I}$, inboard and outboard nacelles.

Figure 51.- Nacelle interference pressure distributions; configuration WBN_1N_1, $M_\infty = 1.40$, $y_i' = 0.25$, $y_o' = 0.55$, $X_i = X_o = 142.2$ cm (56 in.).

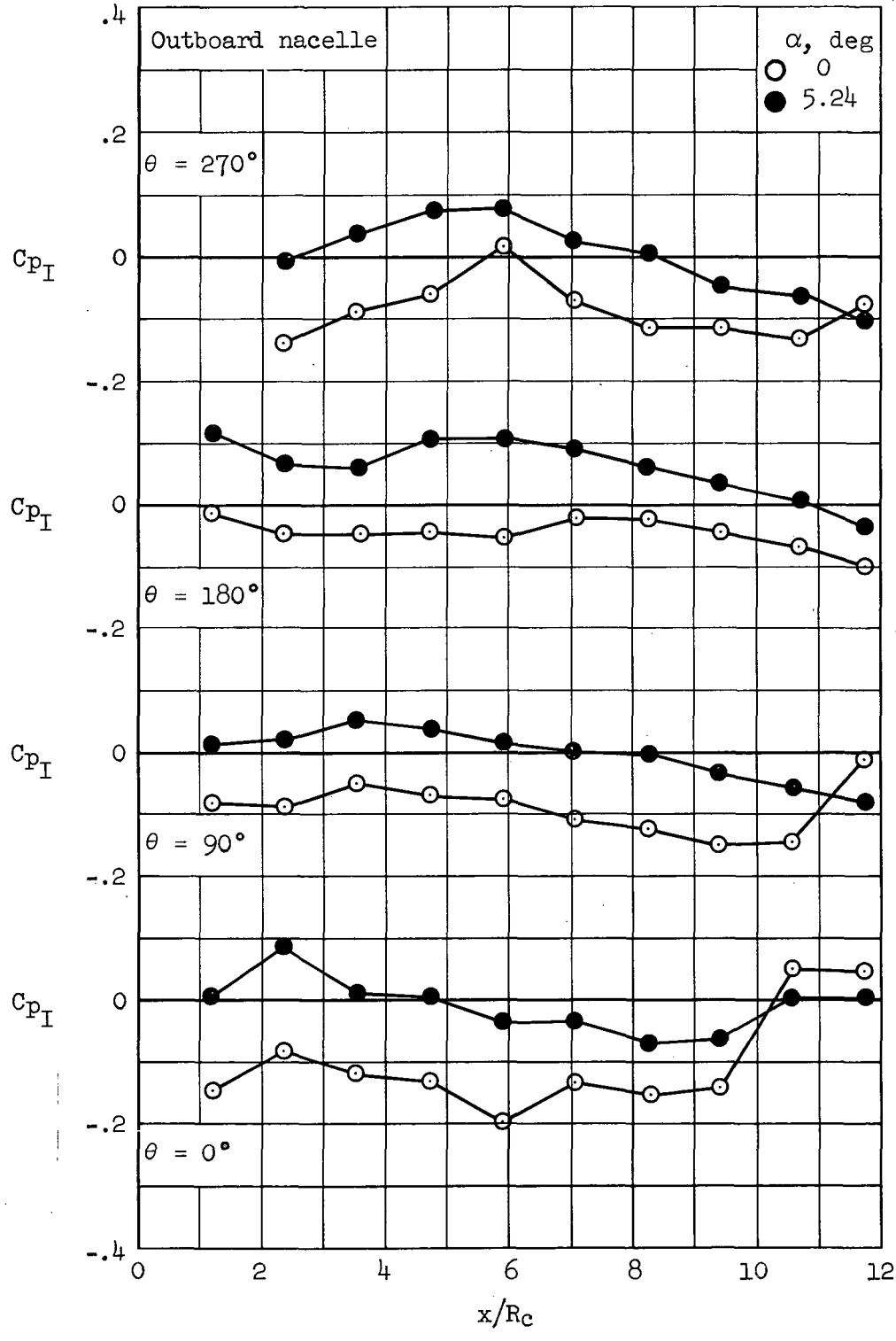

(b) Outboard nacelle, C_{p_I} at θ = 0°, 90°, 180°, 270°.

Figure 51.- Continued.

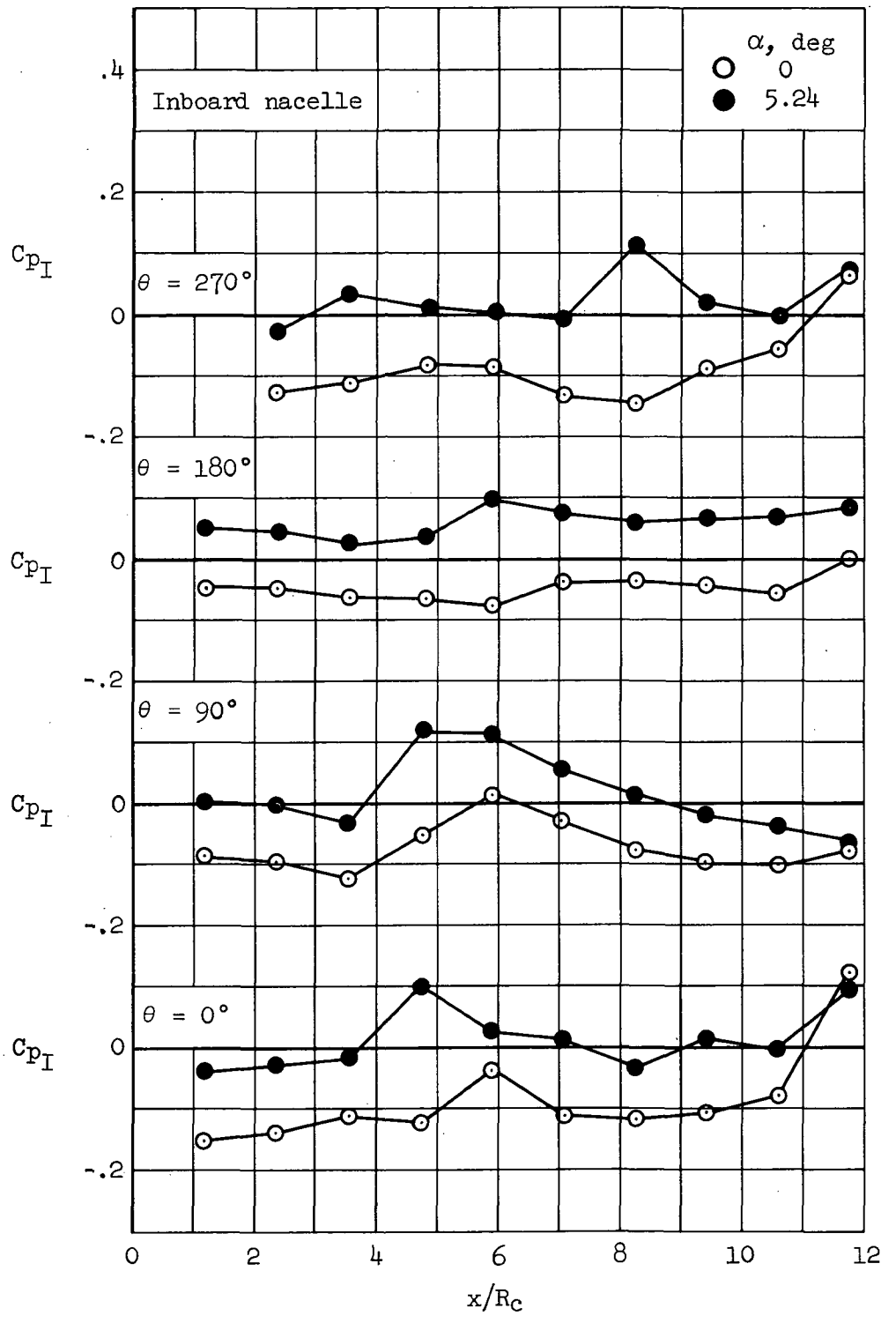

(c) Inboard nacelle, C_{p_I} at θ = 0°, 90°, 180°, 270°.

Figure 51.- Concluded.

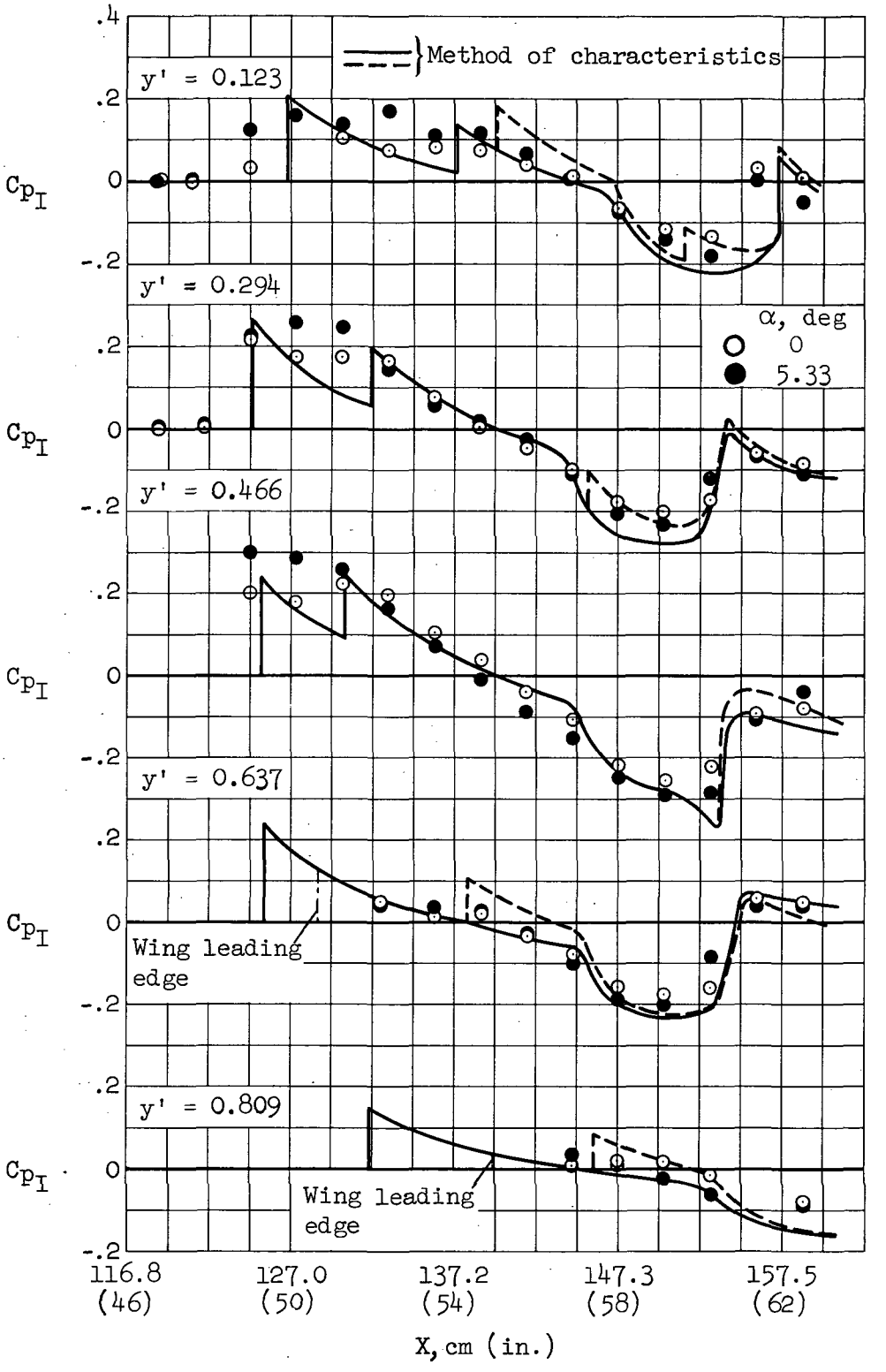

Figure 52.- Comparison between measured and predicted lower wing surface interference pressure distributions; configuration WBN_1N_1, $M_\infty = 1.40$, $y_i' = 0.25$, $y_o' = 0.55$, $X_i = X_o = 121.9$ cm (48 in.).

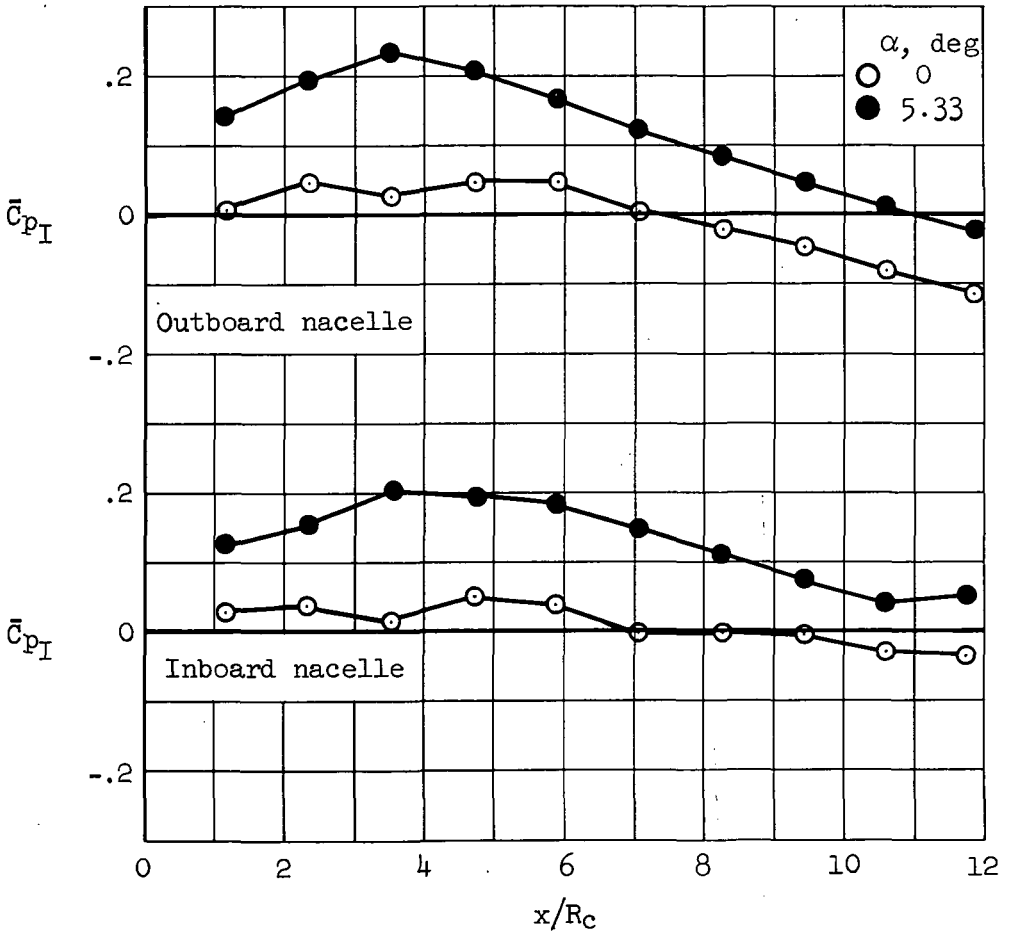

(a) $\bar{C}_{p_I}$, inboard and outboard nacelles.

Figure 53.- Nacelle interference pressure distributions; configuration WBN_1N_1, $M_\infty = 1.40$, $y_i' = 0.25$, $y_o' = 0.55$, $X_i = X_o = 121.9$ cm (48 in.).

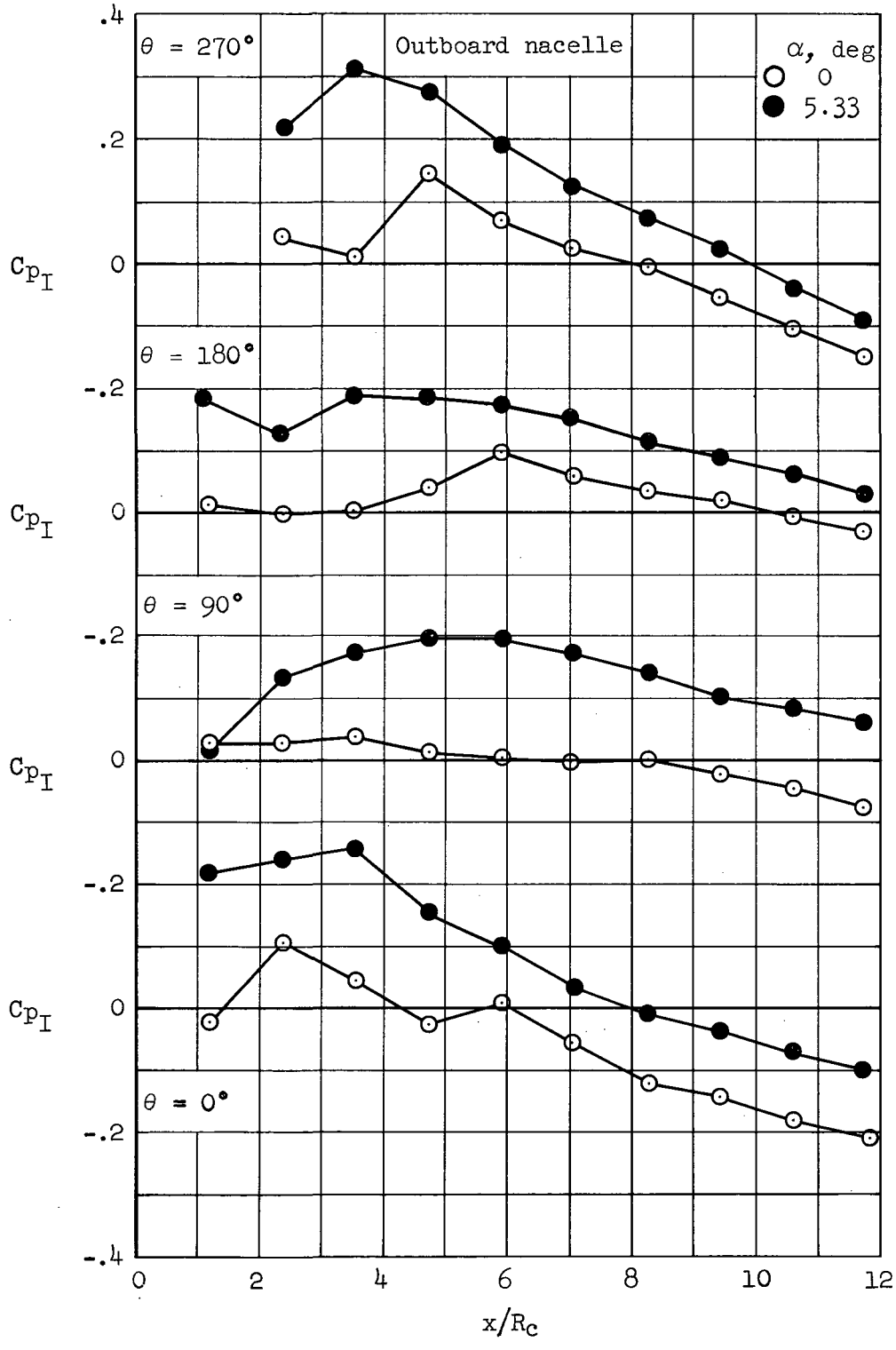

(b) Outboard nacelle, C_{p_I} at θ = 0°, 90°, 180°, 270°.

Figure 53.- Continued.

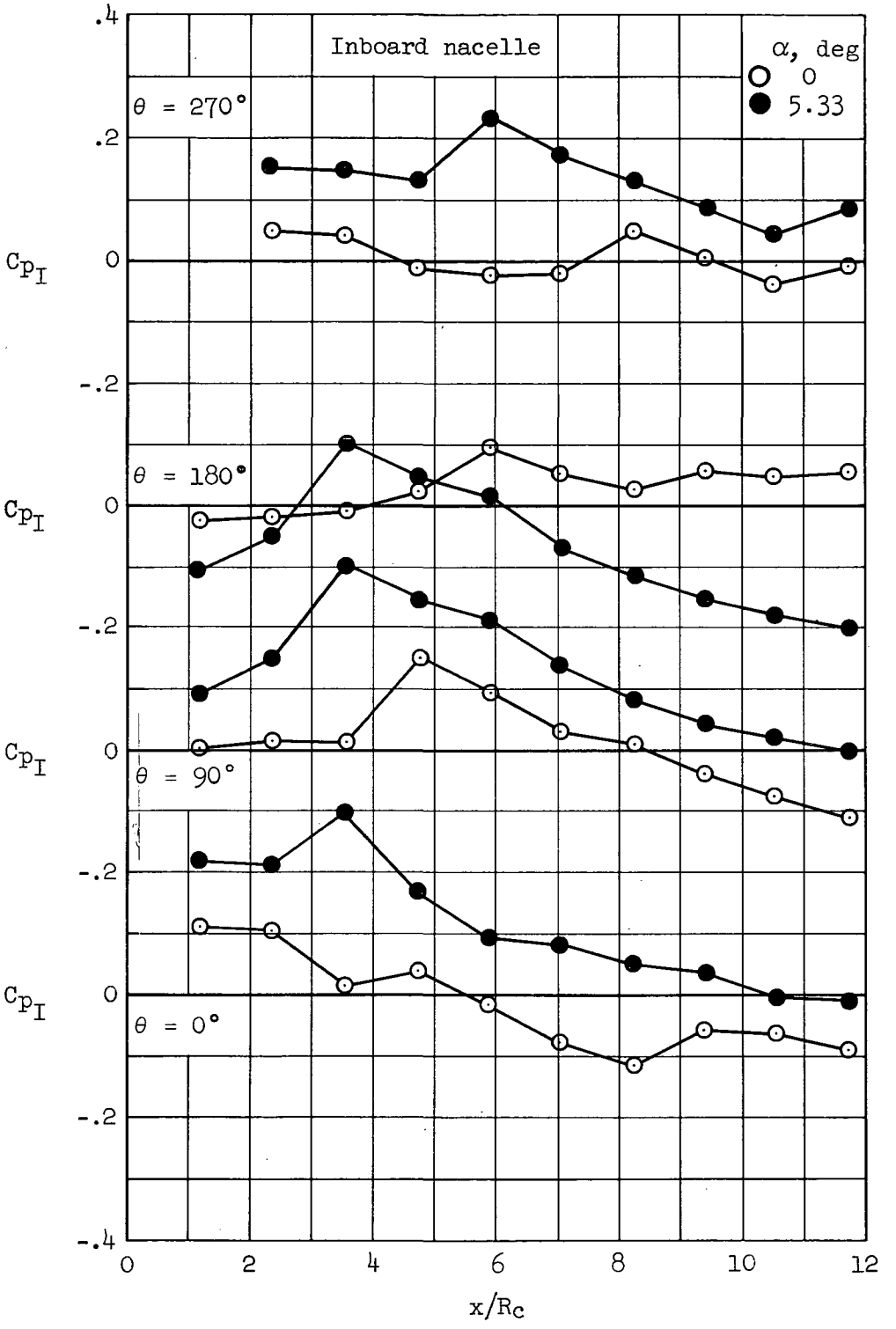

(c) Inboard nacelle, C_{p_I} at θ = 0°, 90°, 180°, 270°.

Figure 53.- Concluded.

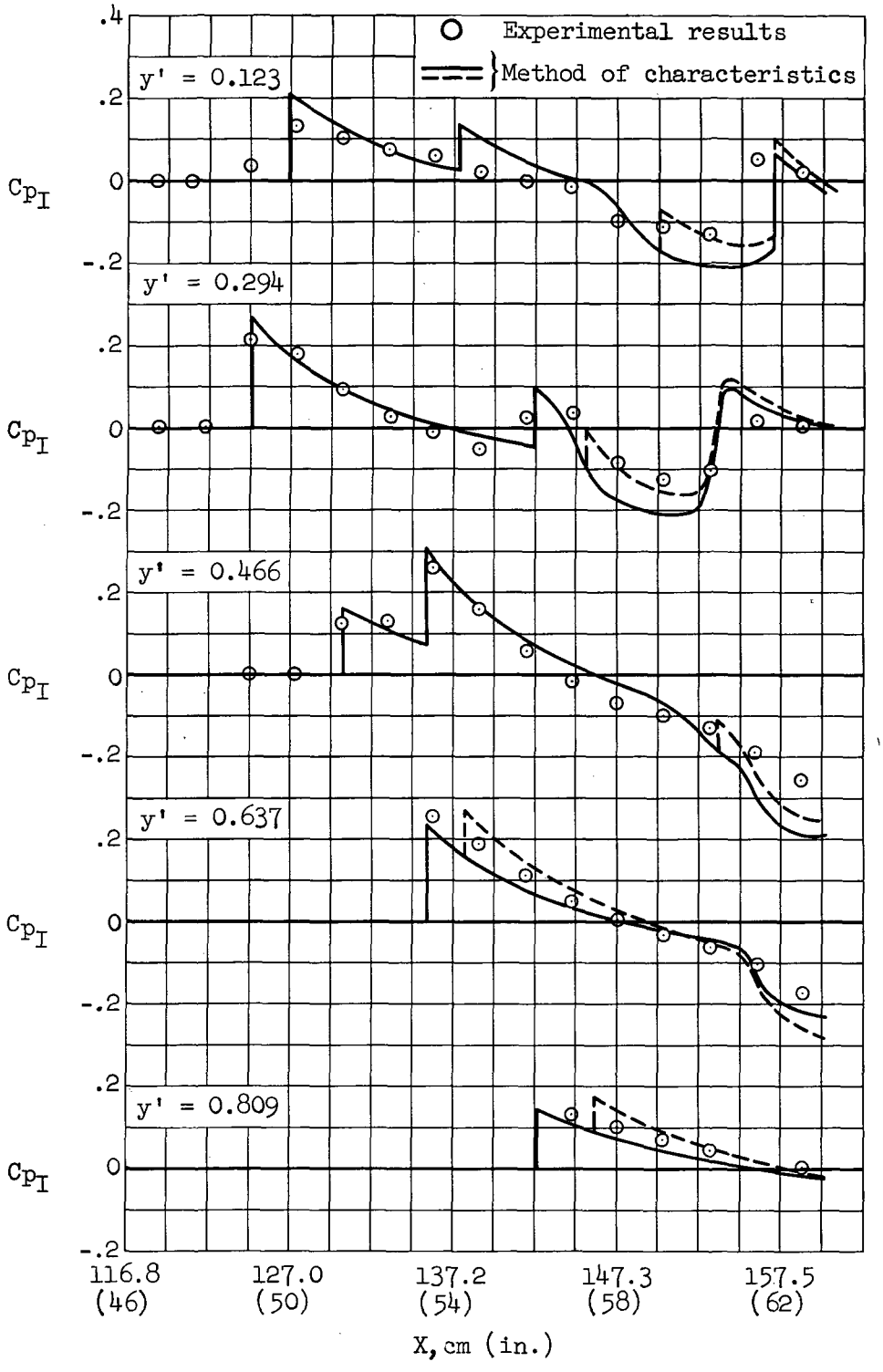

Figure 54.- Comparison between measured and predicted lower wing surface interference pressure distributions; configuration WBN_1N_1, $M_\infty = 1.40$, $\alpha = 0.32°$, $y_i' = 0.25$, $y_o' = 0.55$, $X_i = 121.9$ cm (48 in.), $X_o = 132.1$ cm (52 in.).

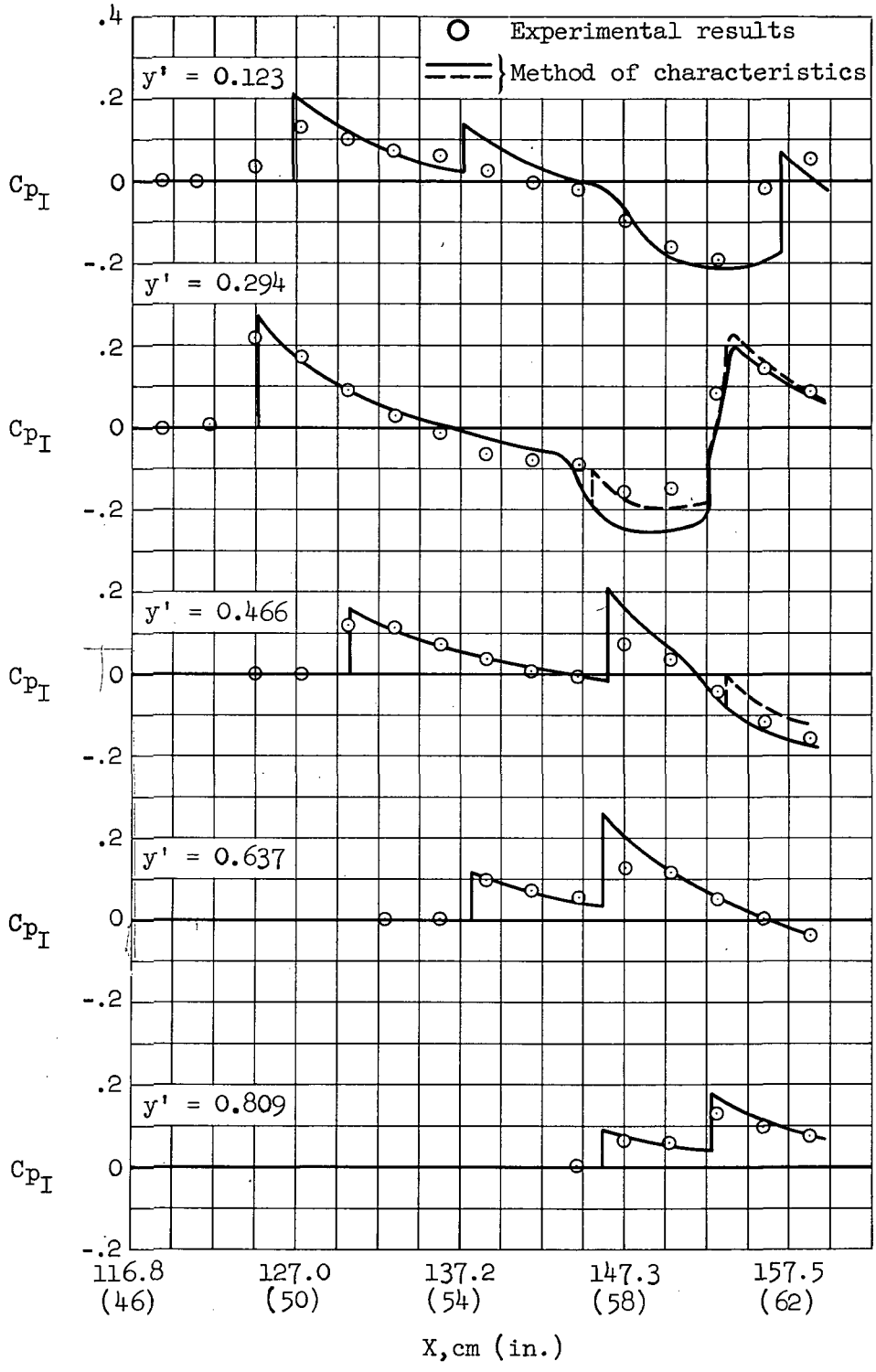

Figure 55.- Comparison between measured and predicted lower wing surface interference pressure distributions; configuration WBN_1N_1, $M_\infty = 1.40$, $\alpha = 0.02°$, $y_i' = 0.25$, $y_o' = 0.55$, $X_i = 121.9$ cm (48 in.), $X_o = 142.2$ cm (56 in.).

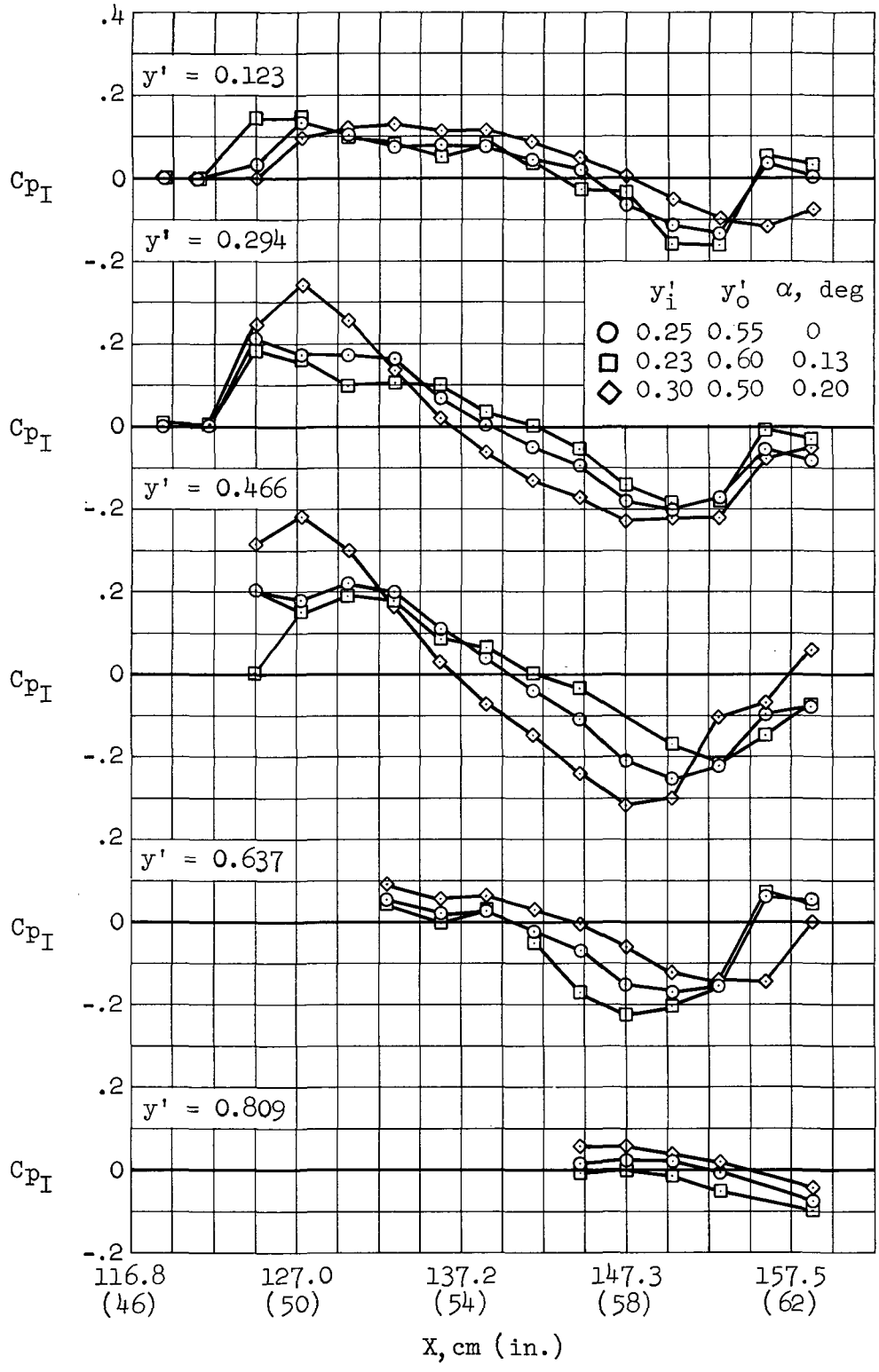

Figure 56.- Lower wing surface interference pressure distributions for various spanwise nacelle positions; configuration WBN_1N_1, $M_\infty = 1.40$, $X_i = X_o = 121.9$ cm (48 in.).

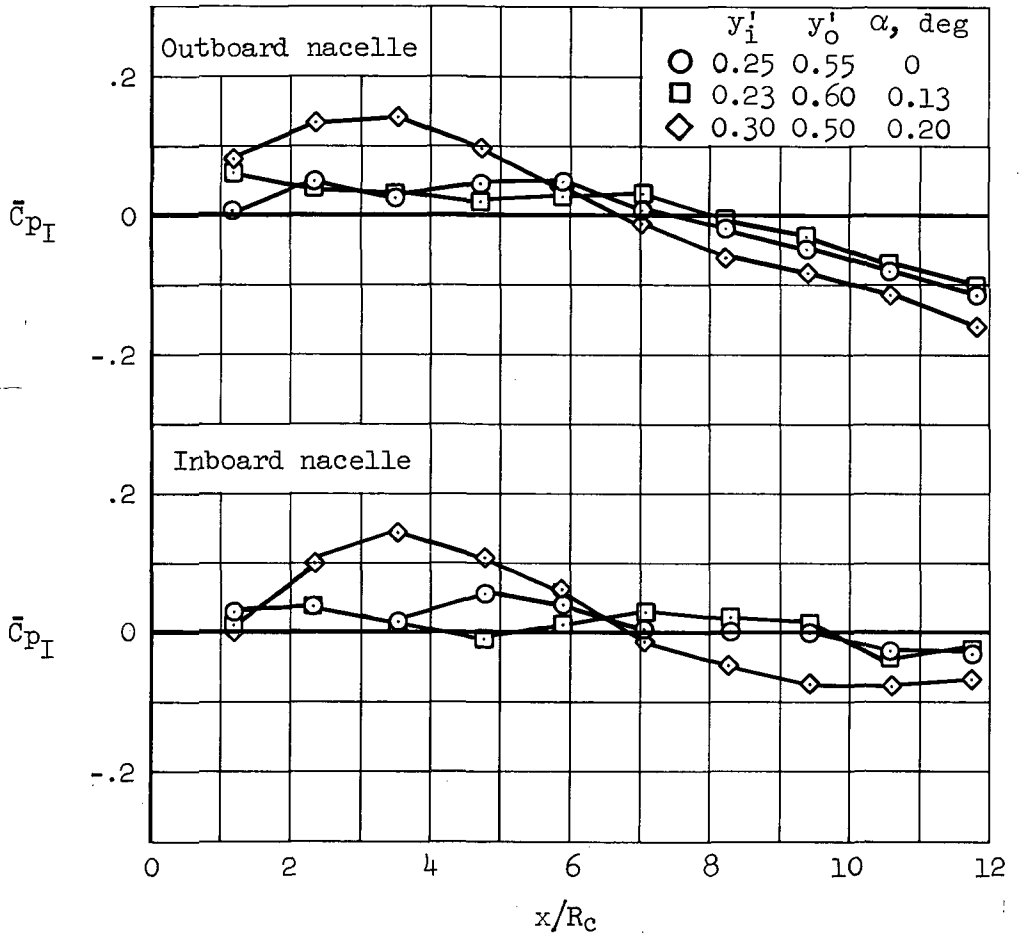

(a) $\bar{C}_{p_I}$, inboard and outboard nacelles.

Figure 57.- Nacelle interference pressure distributions for various spanwise nacelle positions; configuration WBN_1N_1, $M_\infty = 1.40$, $X_i = X_o = 121.9$ cm (48 in.).

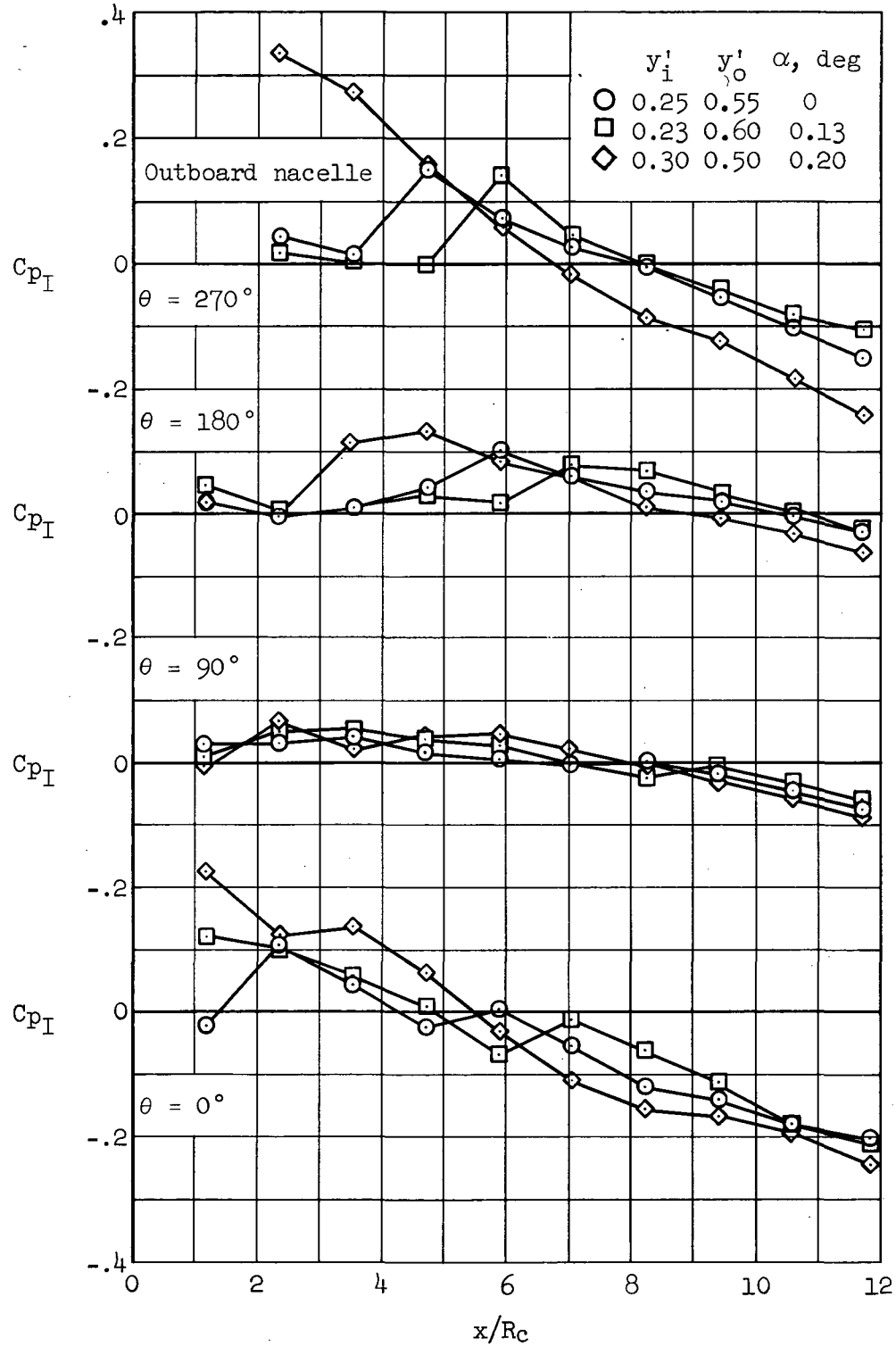

(b) Outboard nacelle, C_{p_I} at θ = 0°, 90°, 180°, 270°.

Figure 57.- Continued.

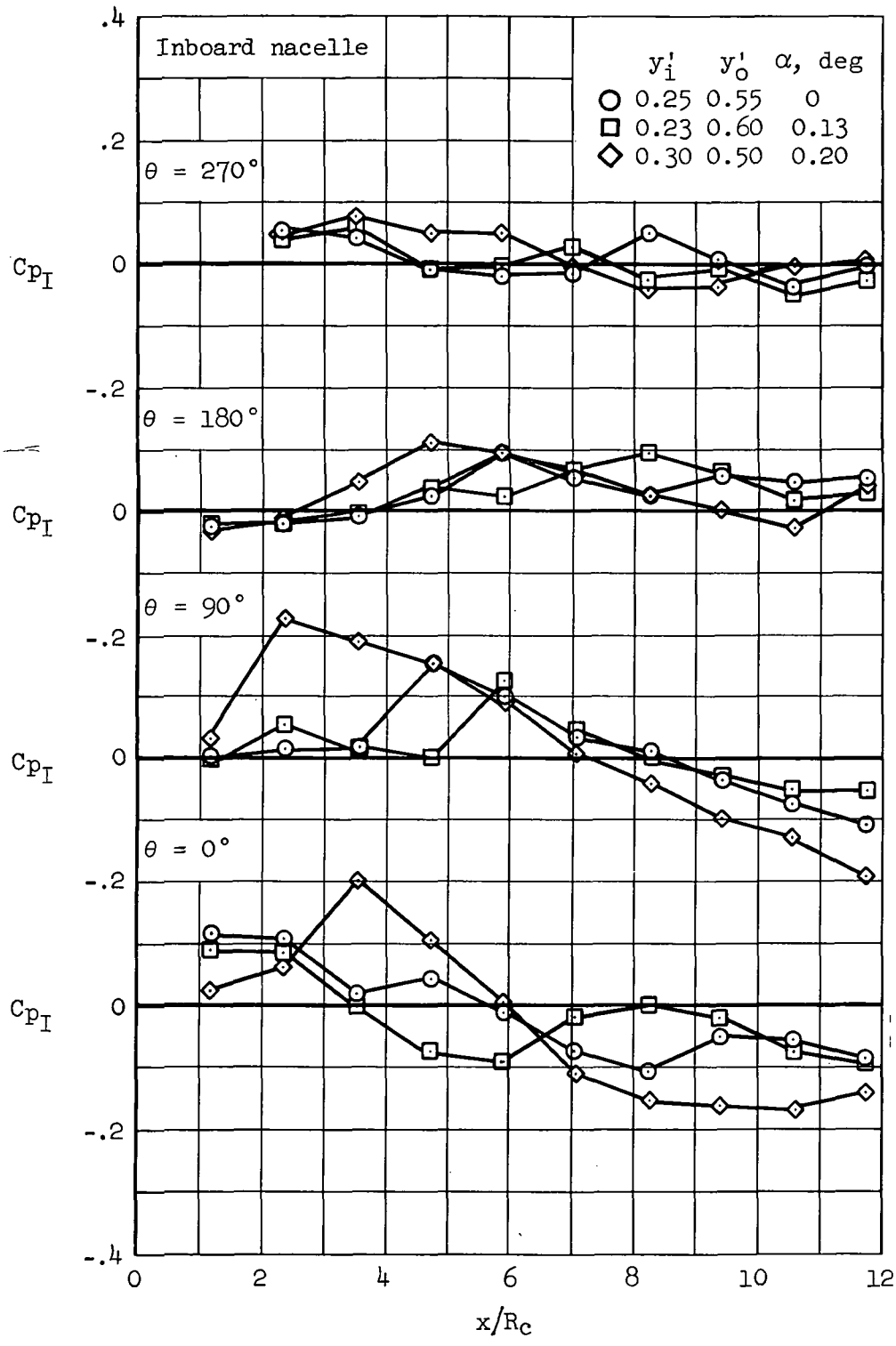

(c) Inboard nacelle, C_{p_I} at θ = 0°, 90°, 180°, 270°.

Figure 57.- Concluded.

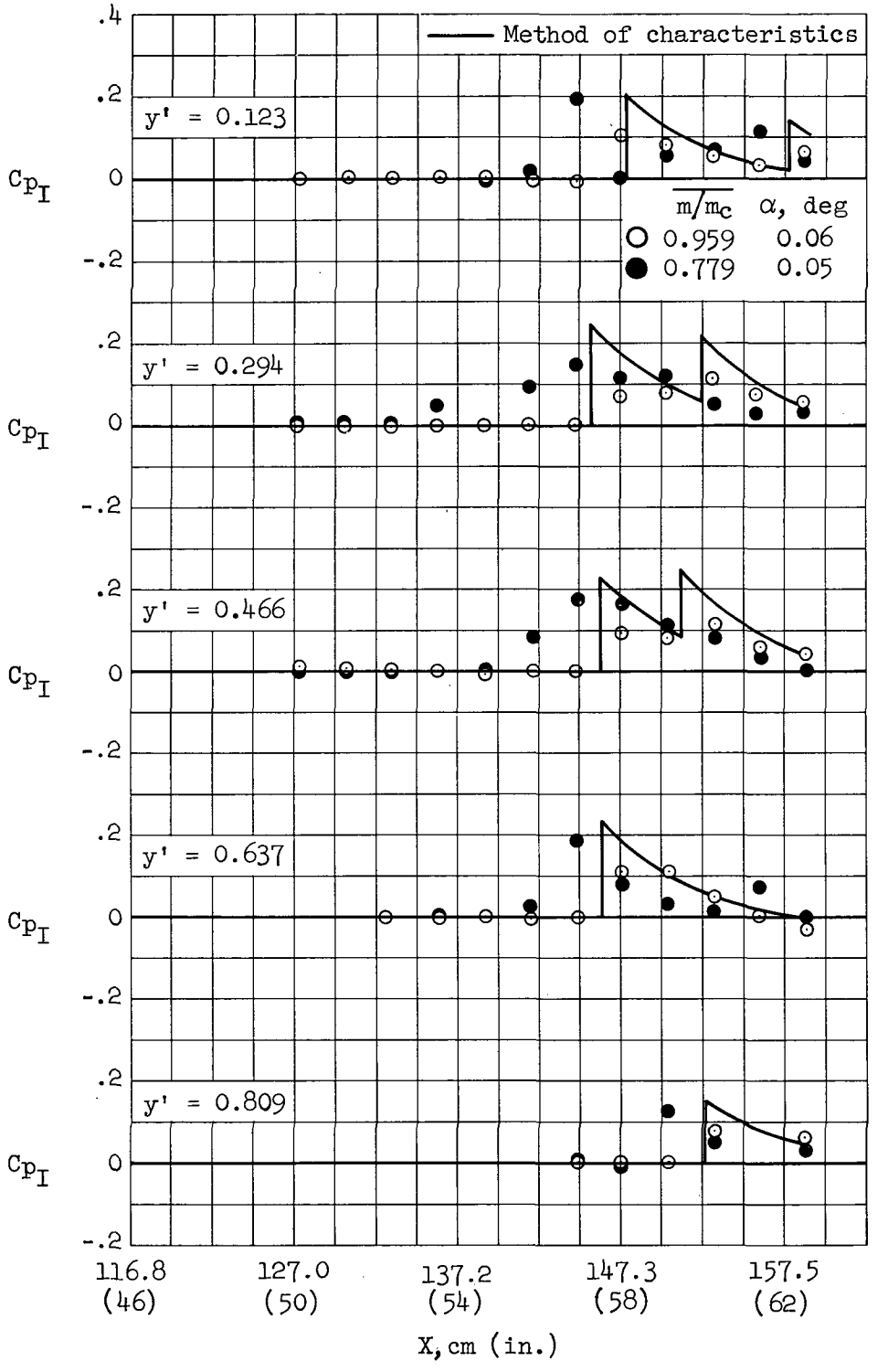

(a) $X_i = X_o = 142.2$ cm (56 in.)

Figure 58.- Lower wing surface interference pressure distributions at two nacelle mass flow ratios; configuration WBN_1N_1, $M_\infty = 1.40$, $y_i' = 0.25$, $y_o' = 0.55$.

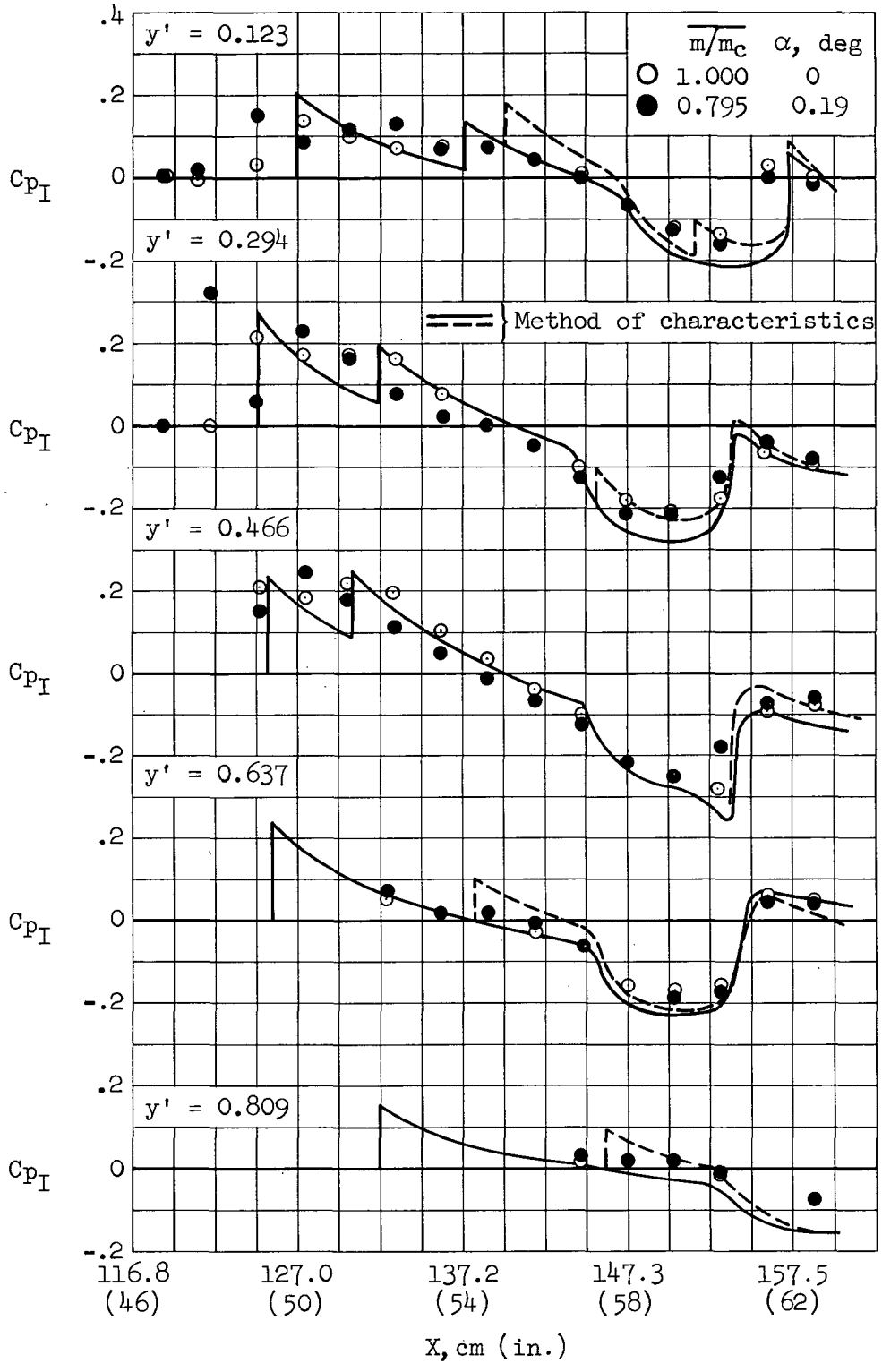

(b) $X_i = X_o = 121.9$ cm (48 in.)

Figure 58.- Concluded.

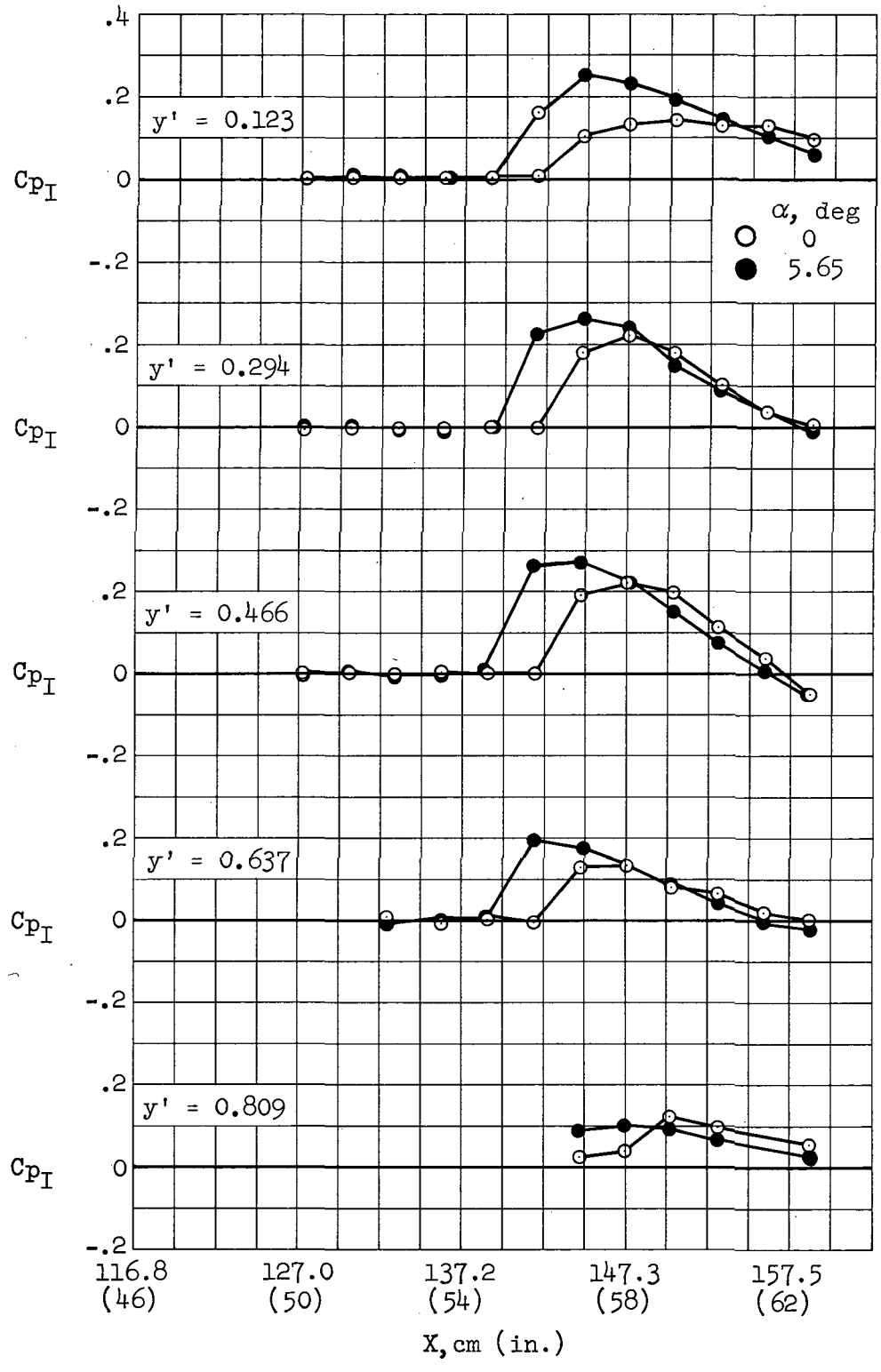

Figure 59.- Lower wing surface interference pressure distributions; configuration WBN_1N_1, $M_\infty = 1.15$, $y_i' = 0.25$, $y_o' = 0.55$, $X_i = X_o = 142.2$ cm (56 in.).

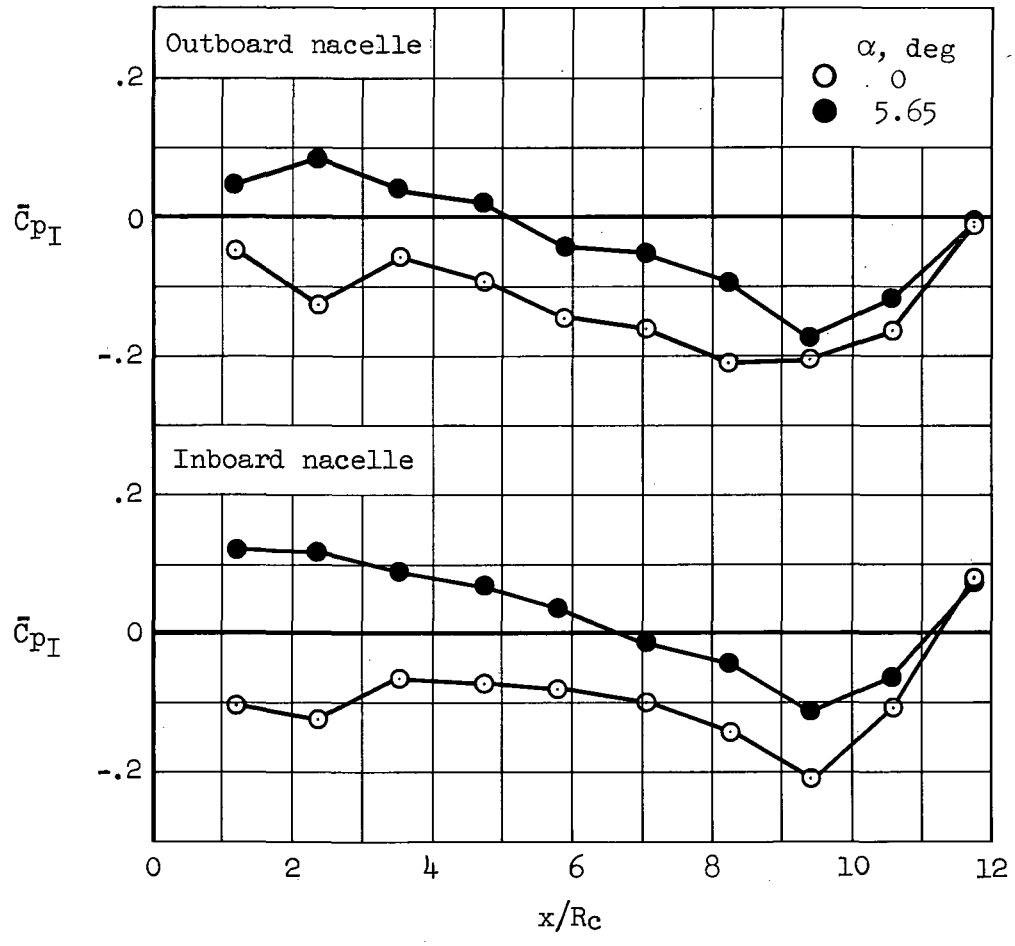

(a) $\bar{C}_{p_I}$, inboard and outboard nacelles.

Figure 60.- Nacelle interference pressure distributions; configuration WBN_1N_1, $M_\infty = 1.15$, $y_i' = 0.25$, $y_o' = 0.55$, $X_i = X_o = 142.2$ cm (56 in.).

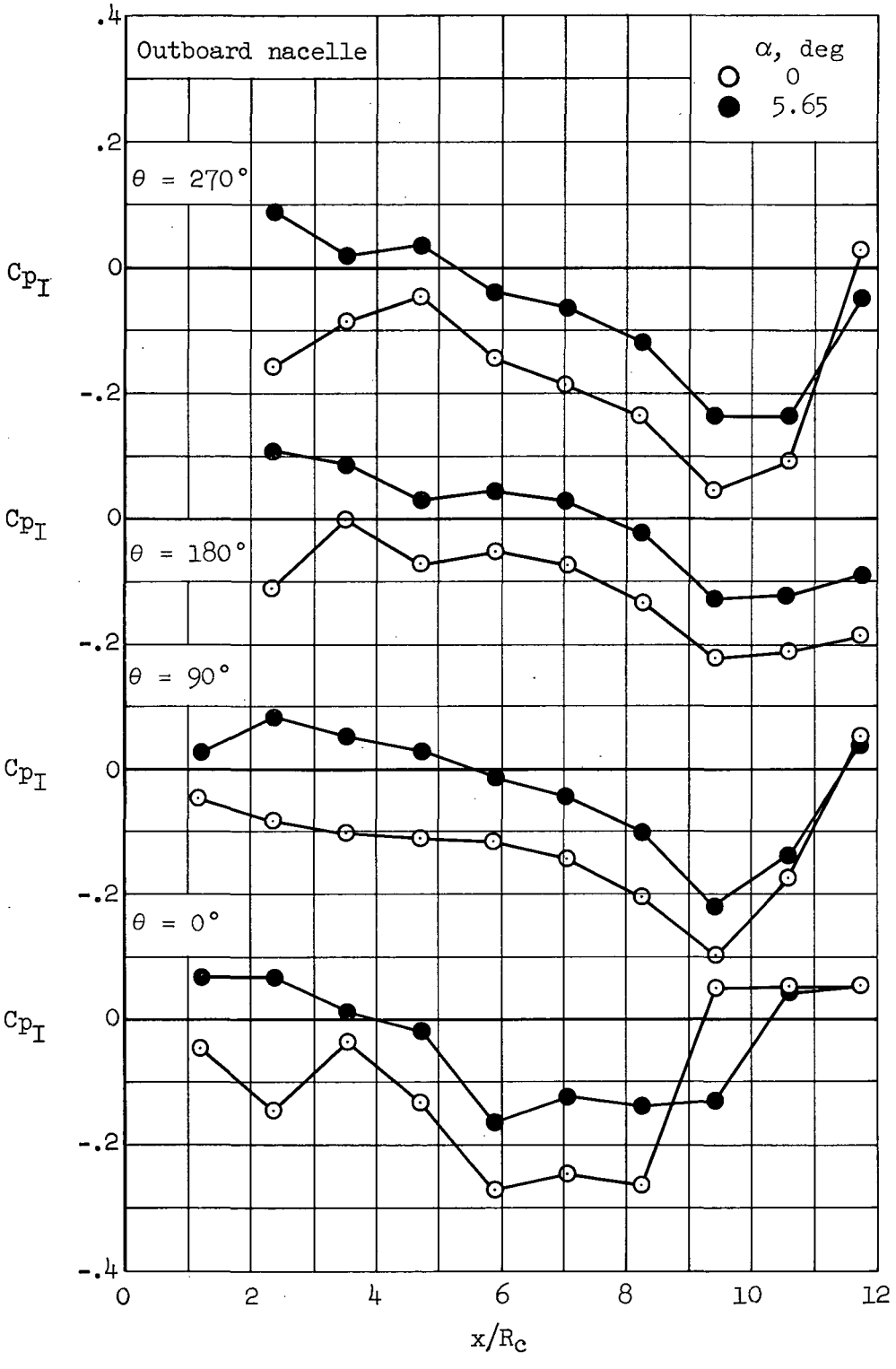

(b) Outboard nacelle, C_{p_I} at θ = 0°, 90°, 180°, 270°.

Figure 60.- Continued.

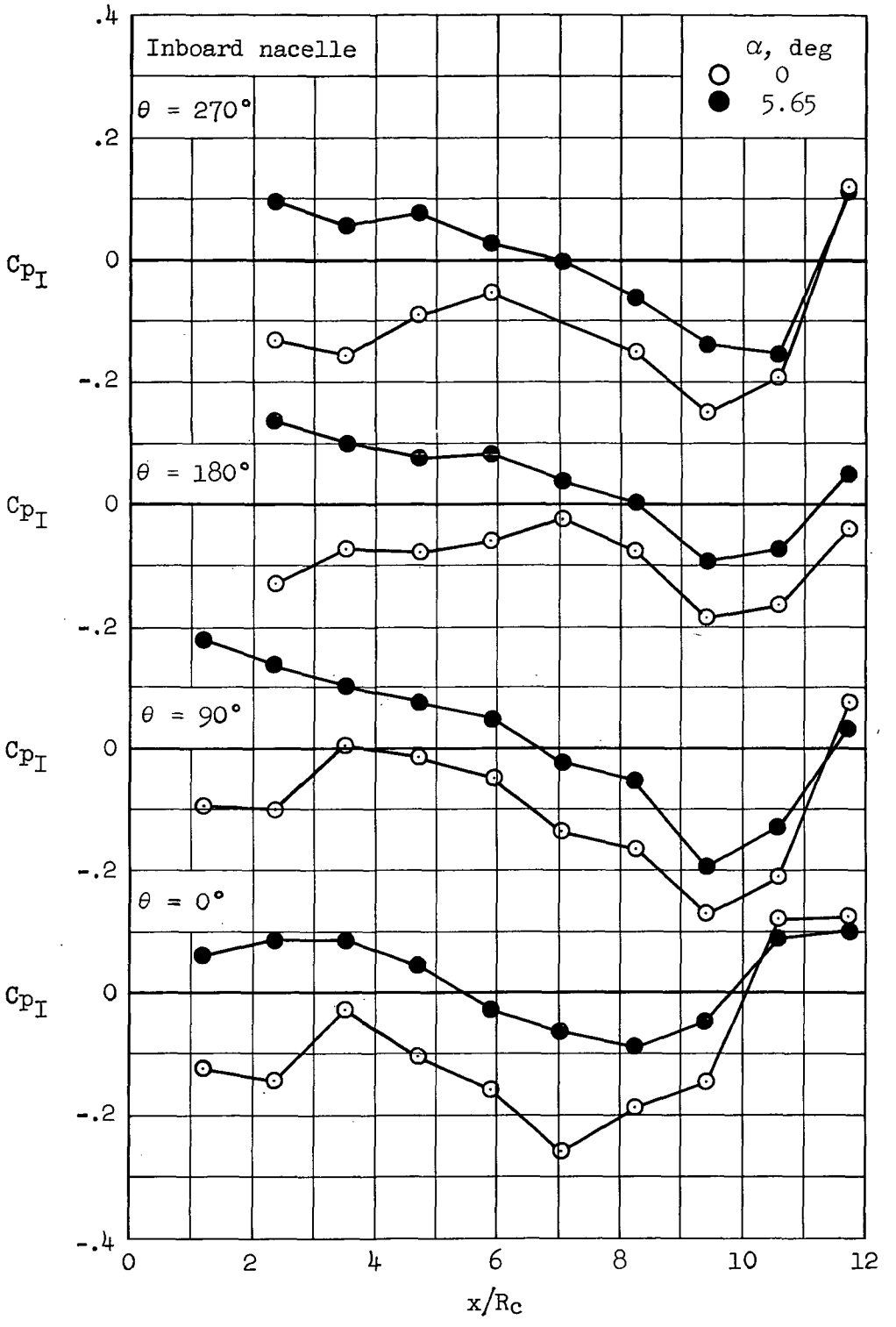

(c) Inboard nacelle, C_{p_I} at θ = 0°, 90°, 180°, 270°.

Figure 60.- Concluded.

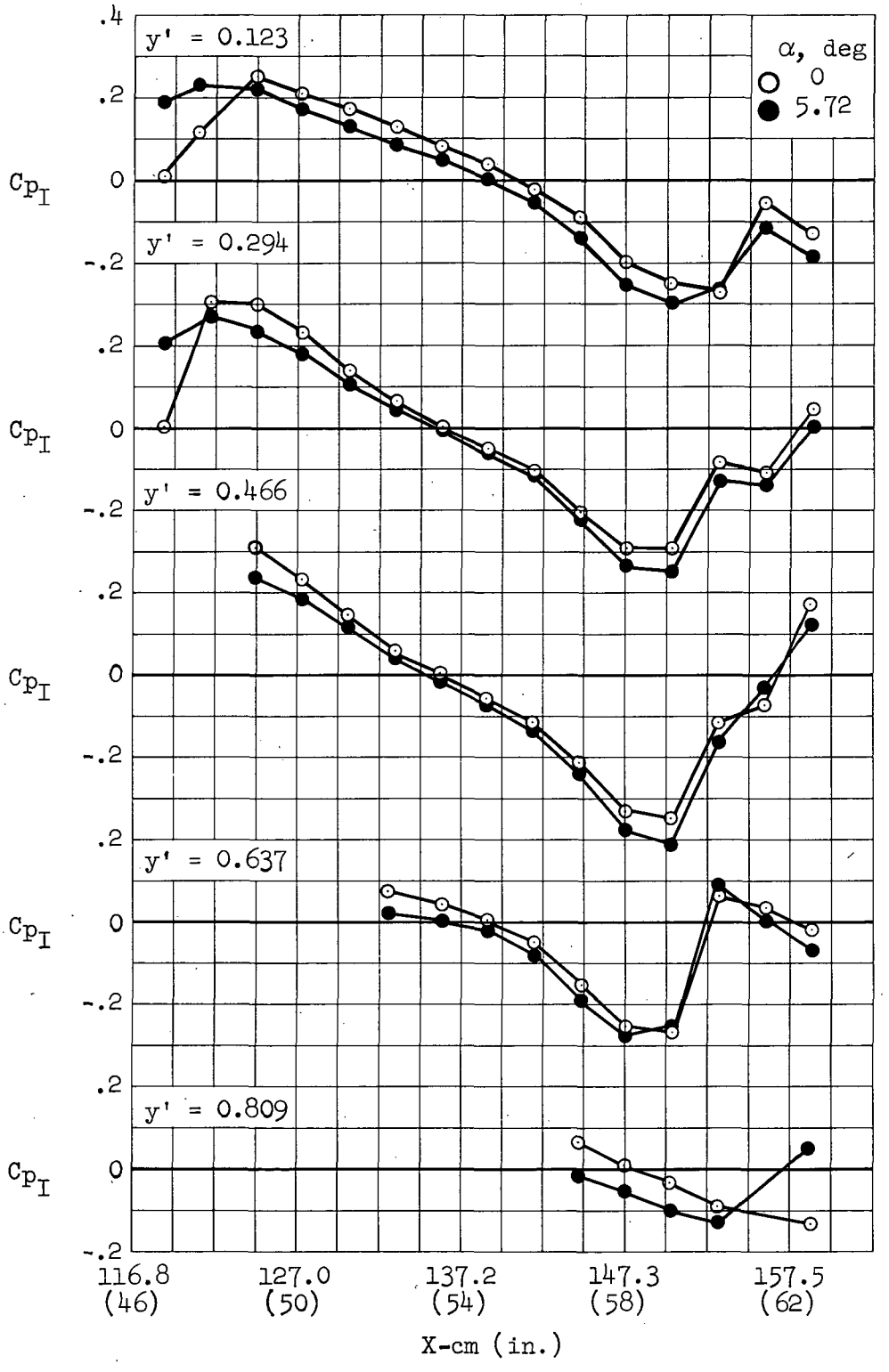

Figure 61.- Lower wing surface interference pressure distributions; configuration WBN_1N_1, $M_\infty = 1.15$, $y_i' = 0.25$, $y_o' = 0.55$, $X_i = X_o = 121.9$ cm (48 in.).

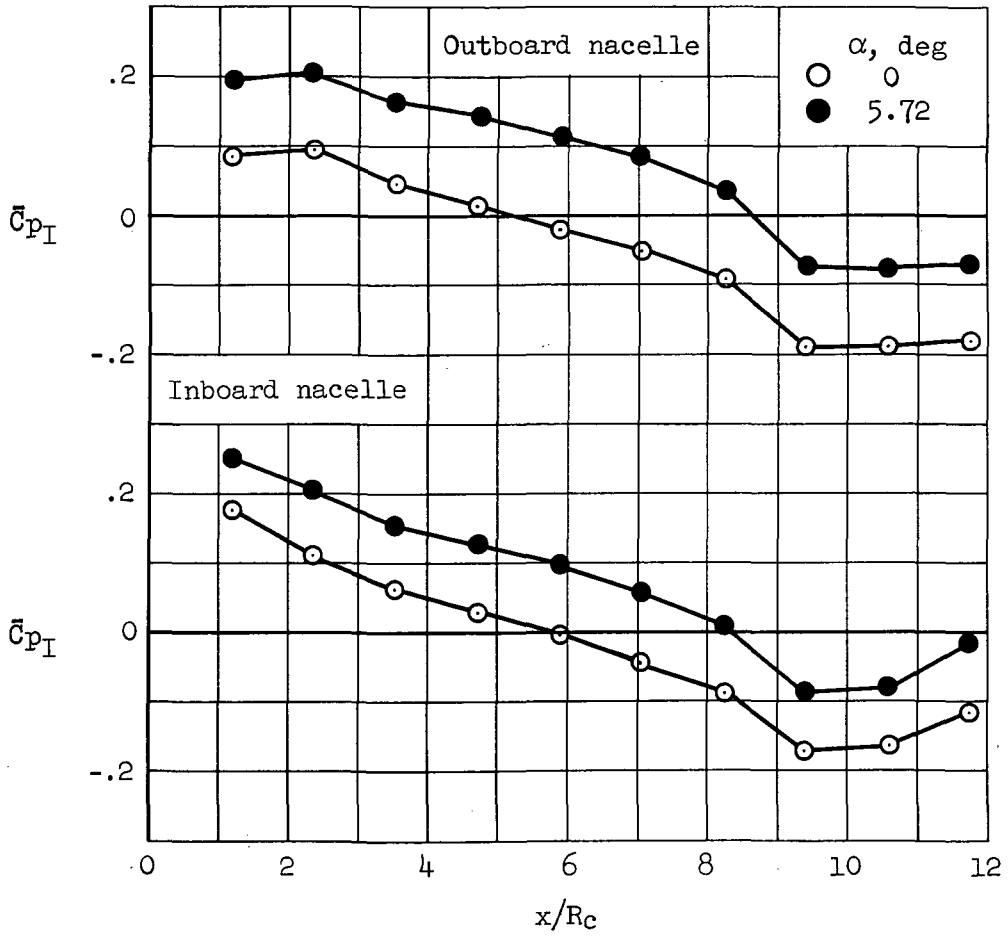

(a) $\bar{C}_{p_I}$, inboard and outboard nacelles.

Figure 62.- Nacelle interference pressure distributions; configuration WBN_1N_1, $M_\infty = 1.15$, $y_i' = 0.25$, $y_o' = 0.55$, $X_i = X_o = 121.9$ cm (48 in.).

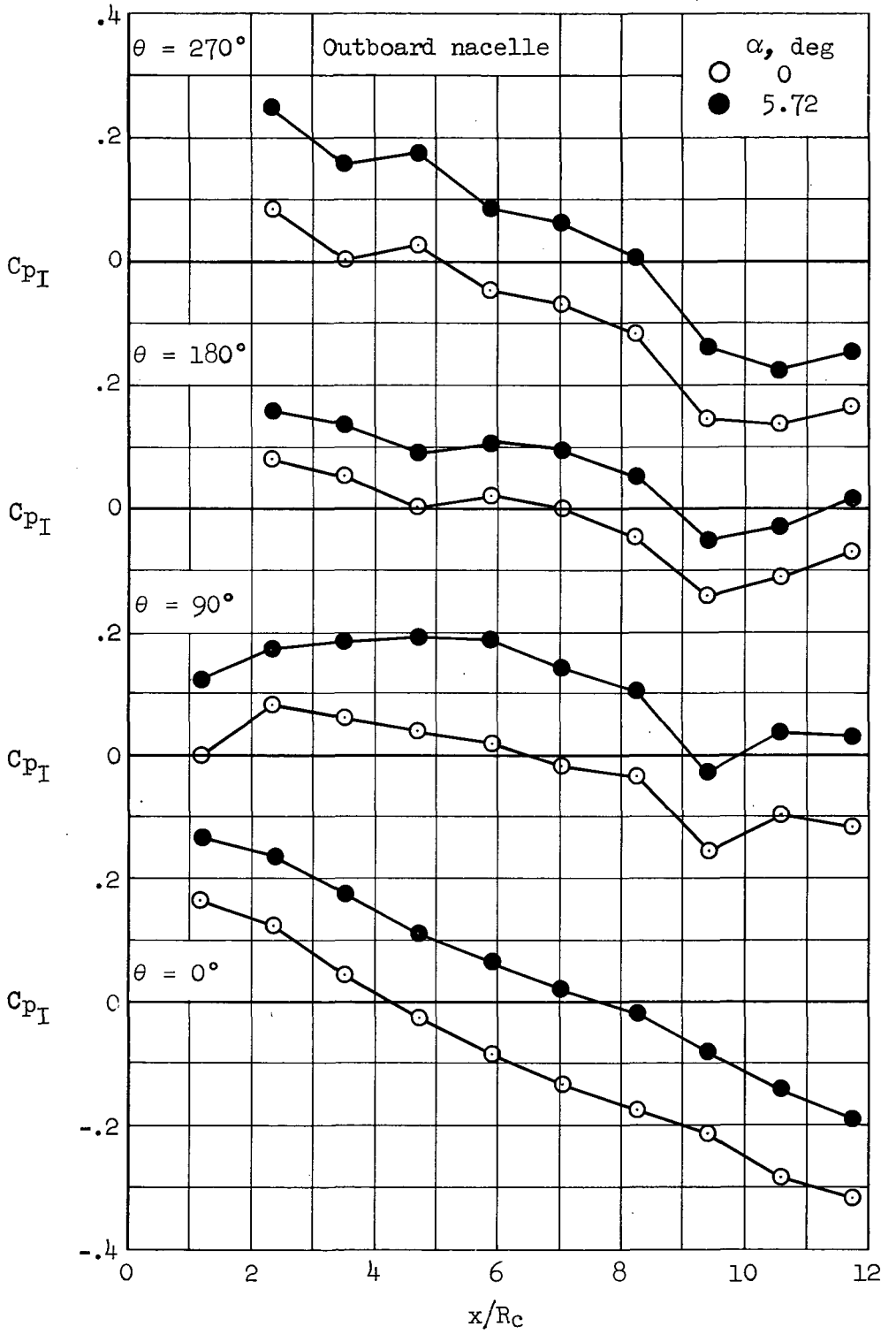

(b) Outboard nacelle, C_{p_I} at θ = 0°, 90°, 180°, 270°.

Figure 62.- Continued.

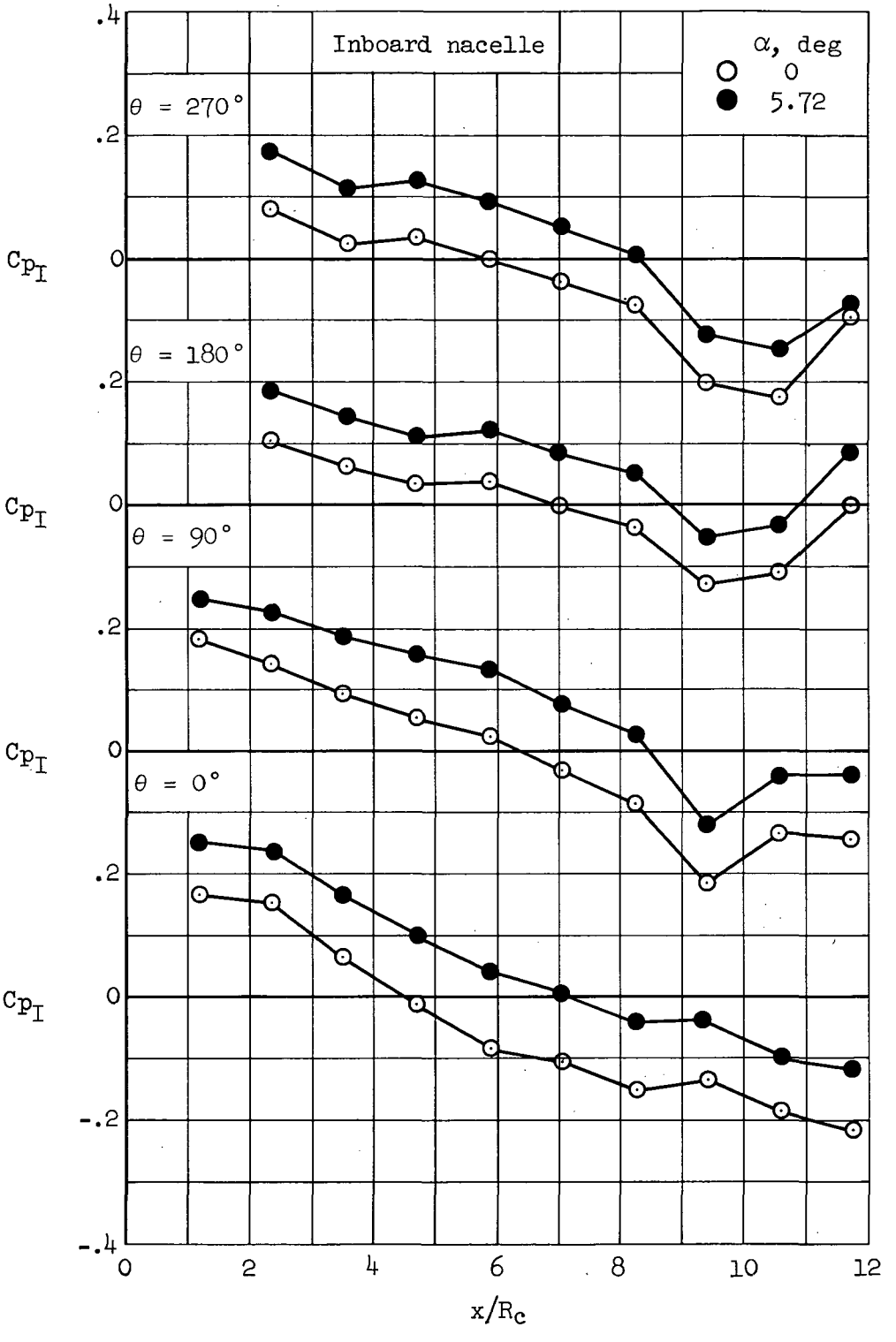

(c) Inboard nacelle, C_{p_I} at θ = 0°, 90°, 180°, 270°.

Figure 62.- Concluded.

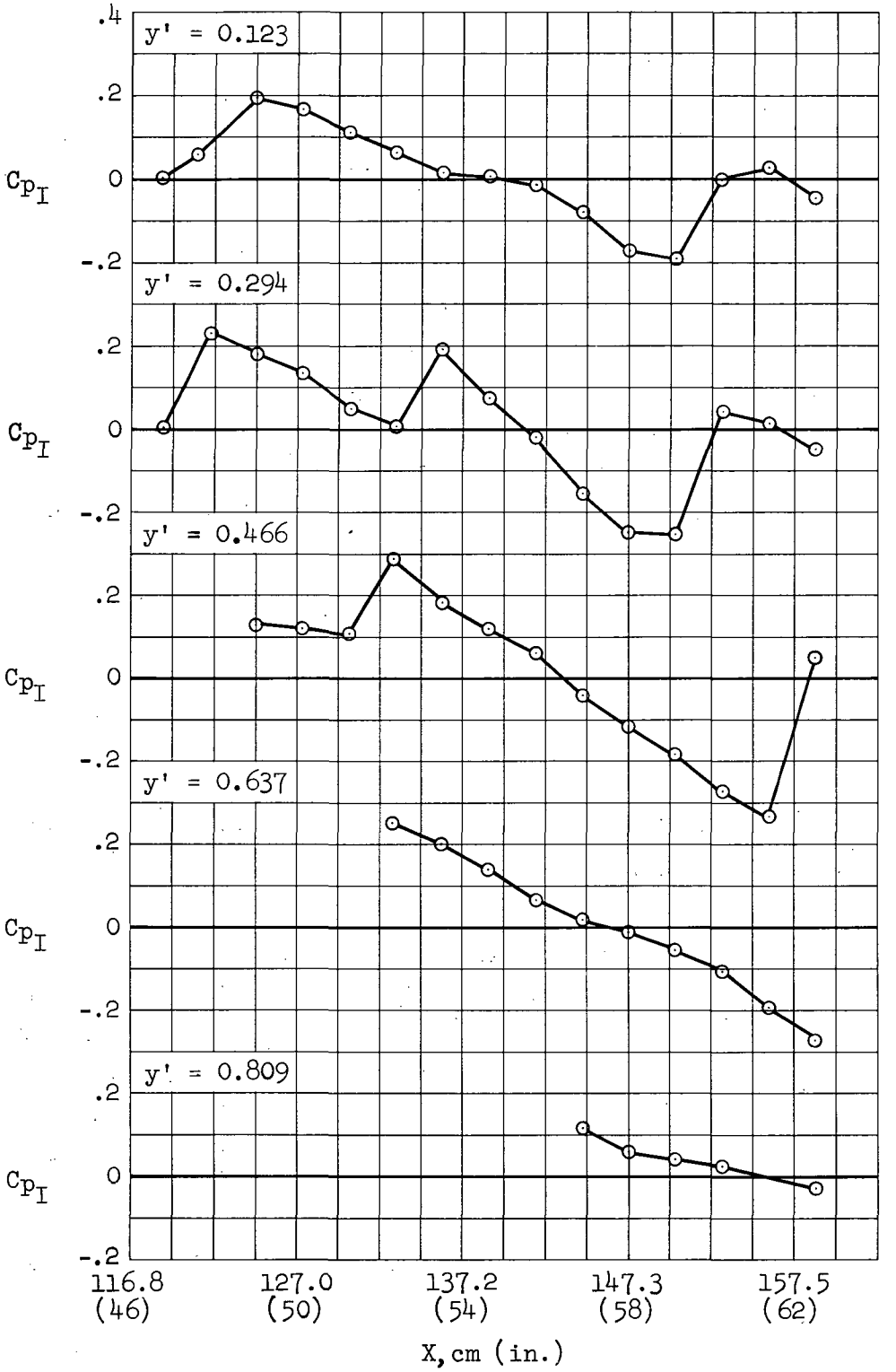

Figure 63.- Lower wing surface interference pressure distributions; configuration WBN_1N_1, $M_\infty = 1.15$, $y'_i = 0.25$, $y'_o = 0.55$, $X_i = 121.9$ cm (48 in.), $X_o = 132.1$ cm (52 in.).

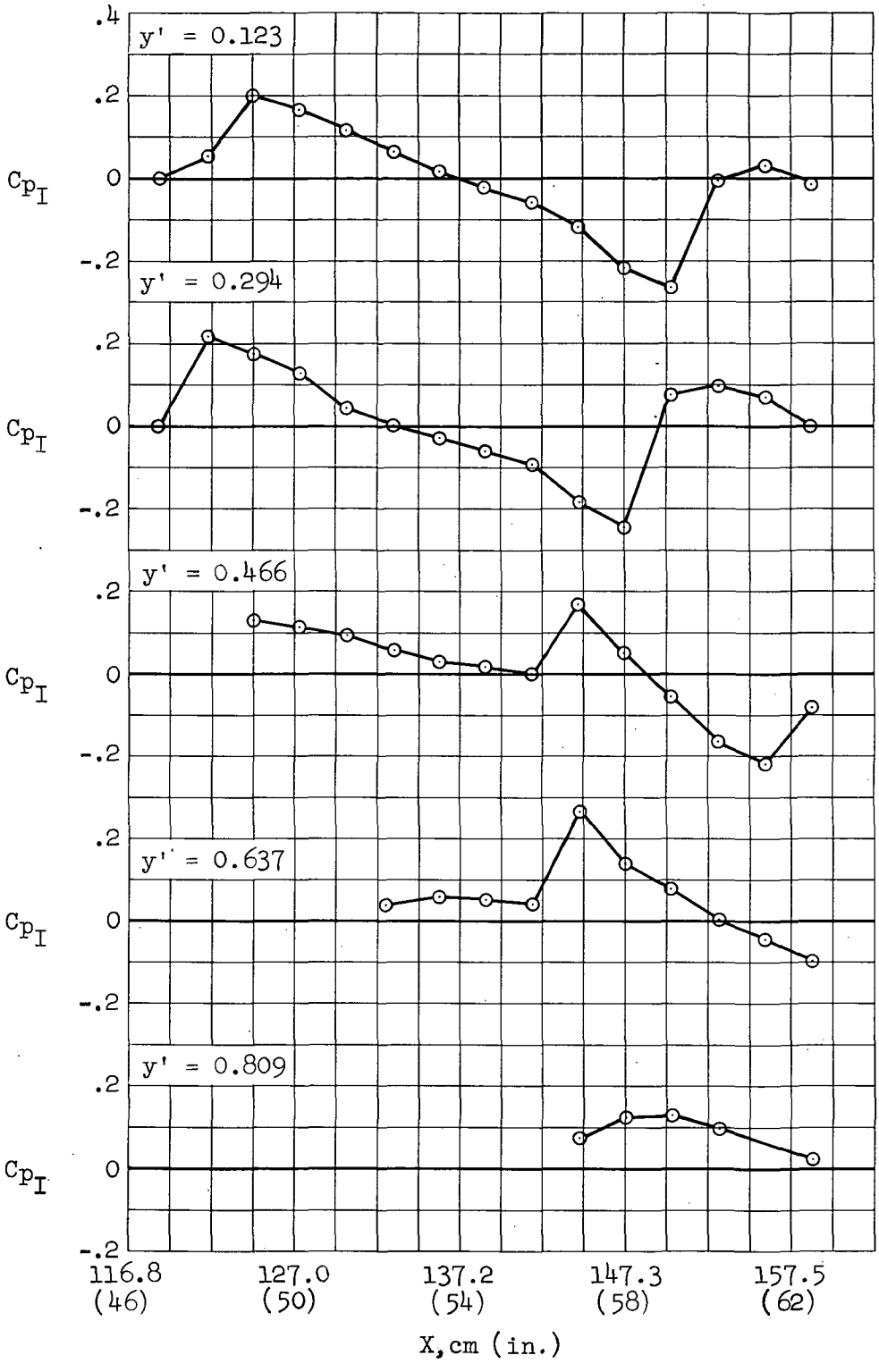

Figure 64.- Lower wing surface interference pressure distributions; configuration WBN_1N_1, $M_\infty = 1.15$, $y'_i = 0.25$, $y'_o = 0.55$, $X_i = 121.9$ cm (48 in.), $X_o = 142.2$ cm (56 in.).

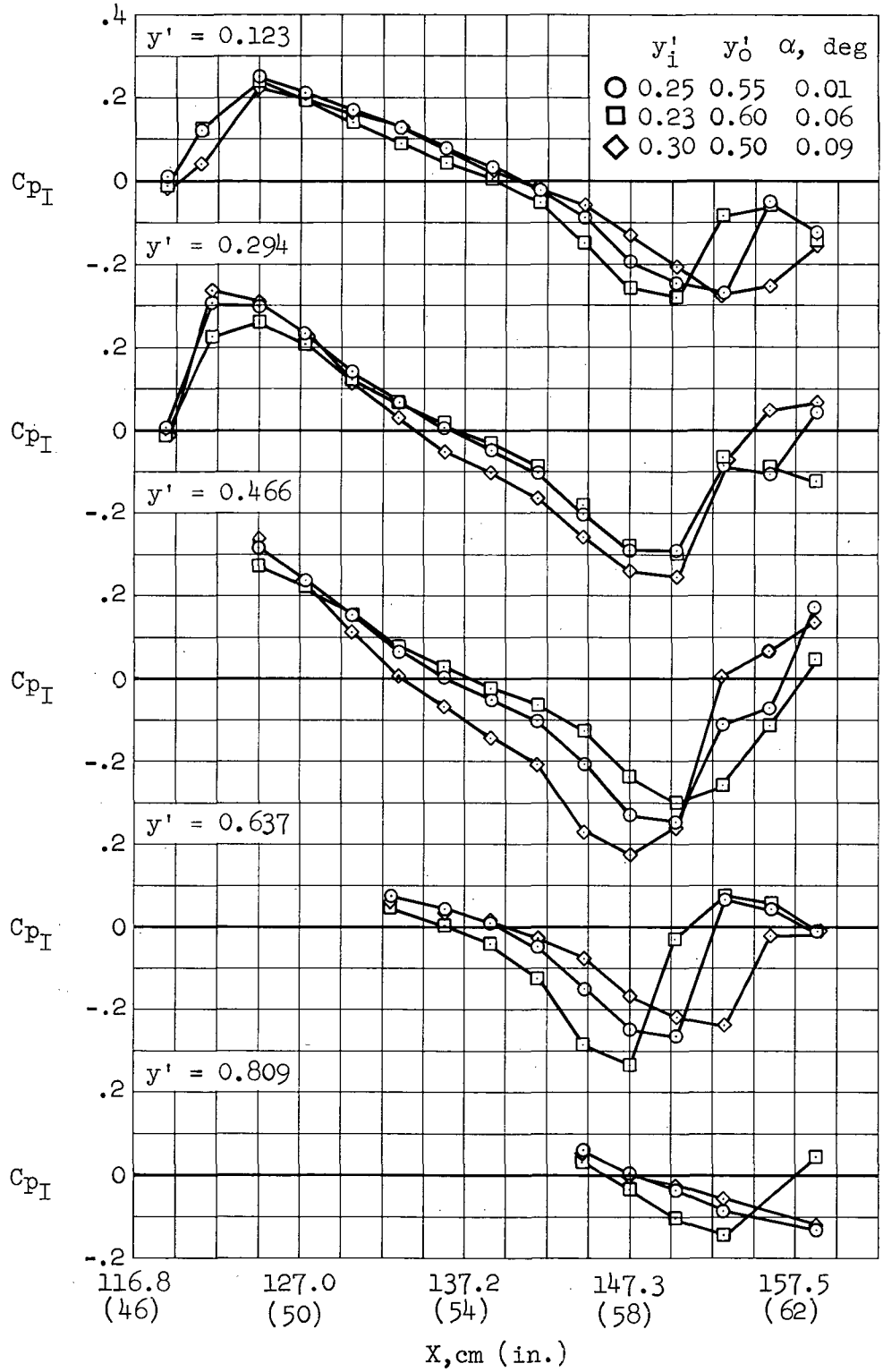

Figure 65.- Lower wing surface interference pressure distributions for various spanwise nacelle positions; configuration WBN_1N_1, $M_\infty = 1.15$, $X_i = X_o = 121.9$ cm (48 in.).

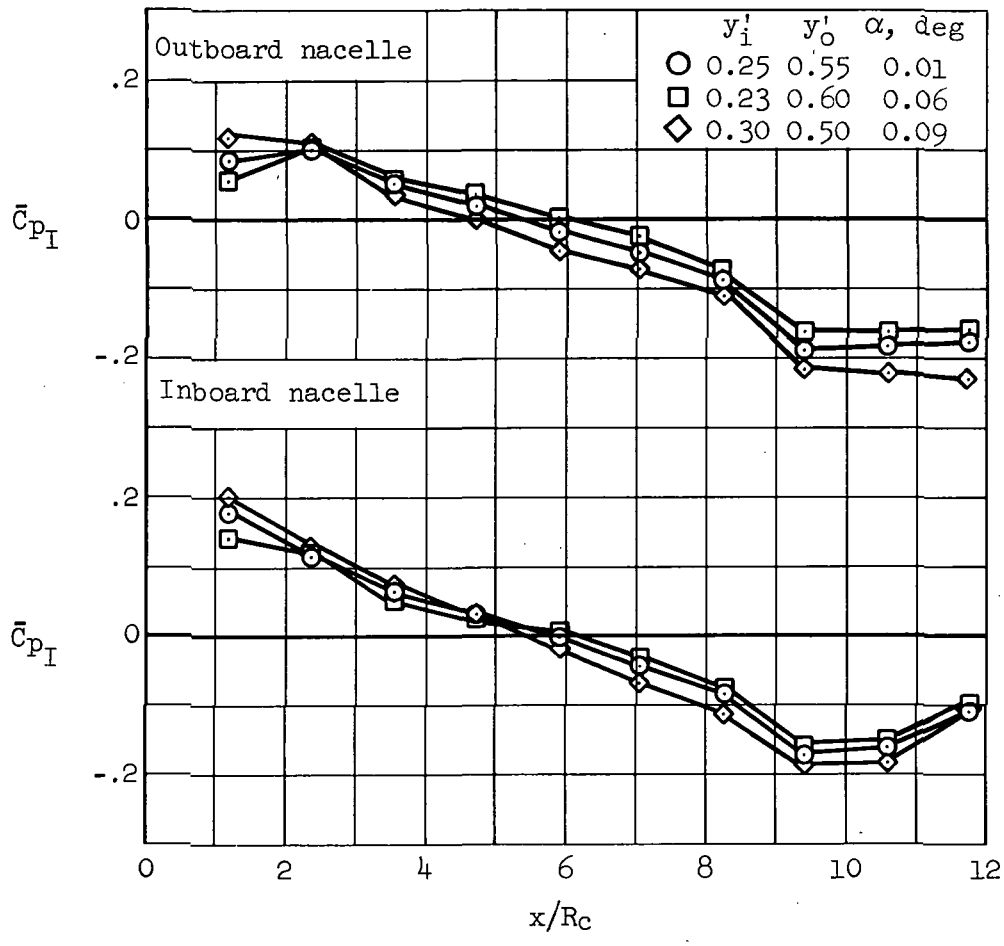

(a) $\bar{C}_{p_I}$, inboard and outboard nacelles.

Figure 66.- Nacelle interference pressure distributions for various spanwise nacelle positions; configuration WBN_1N_1, $M_\infty = 1.15$, $X_i = X_o = 121.9$ cm (48 in.).

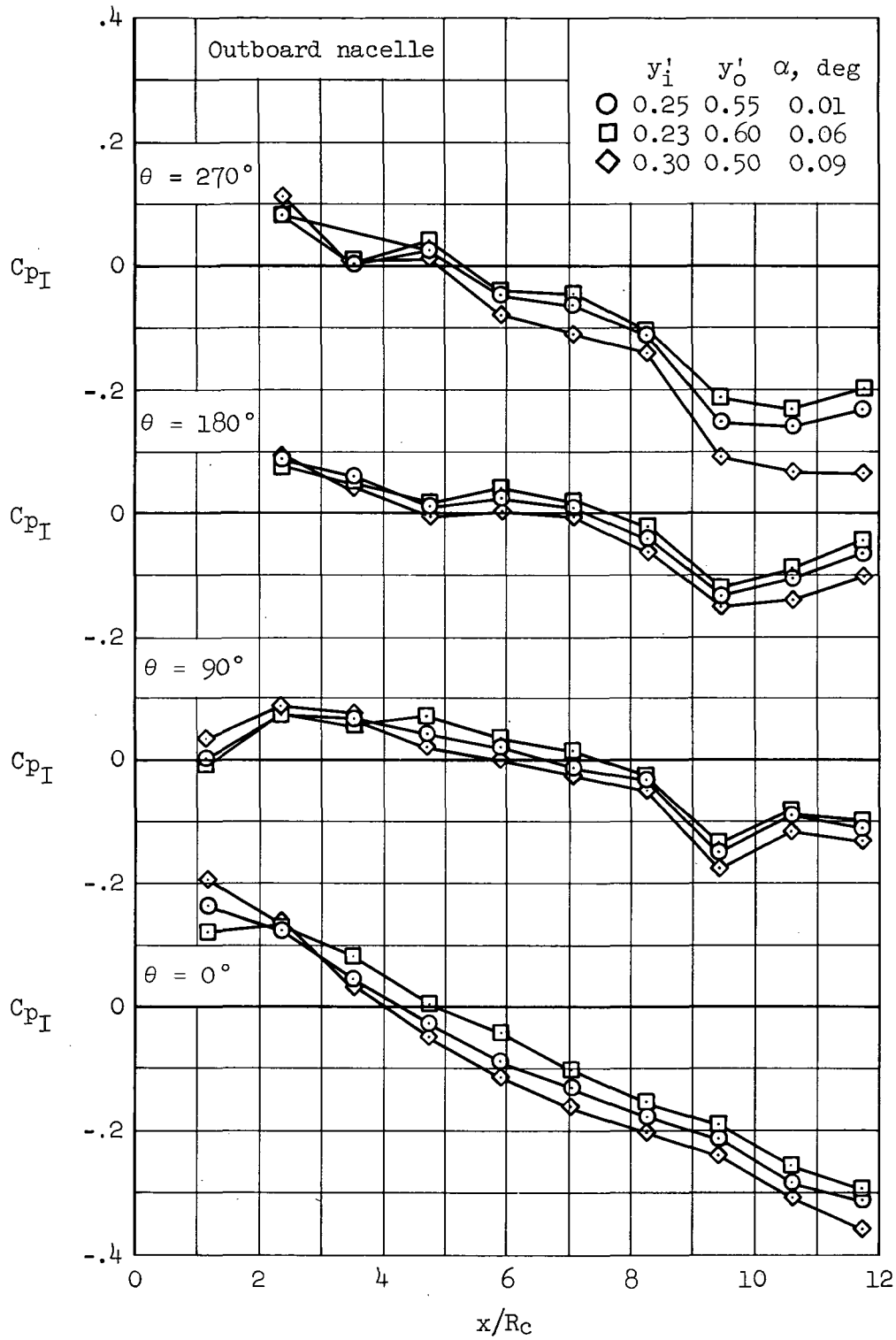

(b) Outboard nacelle, C_{p_I} at θ = 0°, 90°, 180°, 270°.

Figure 66.- Continued.

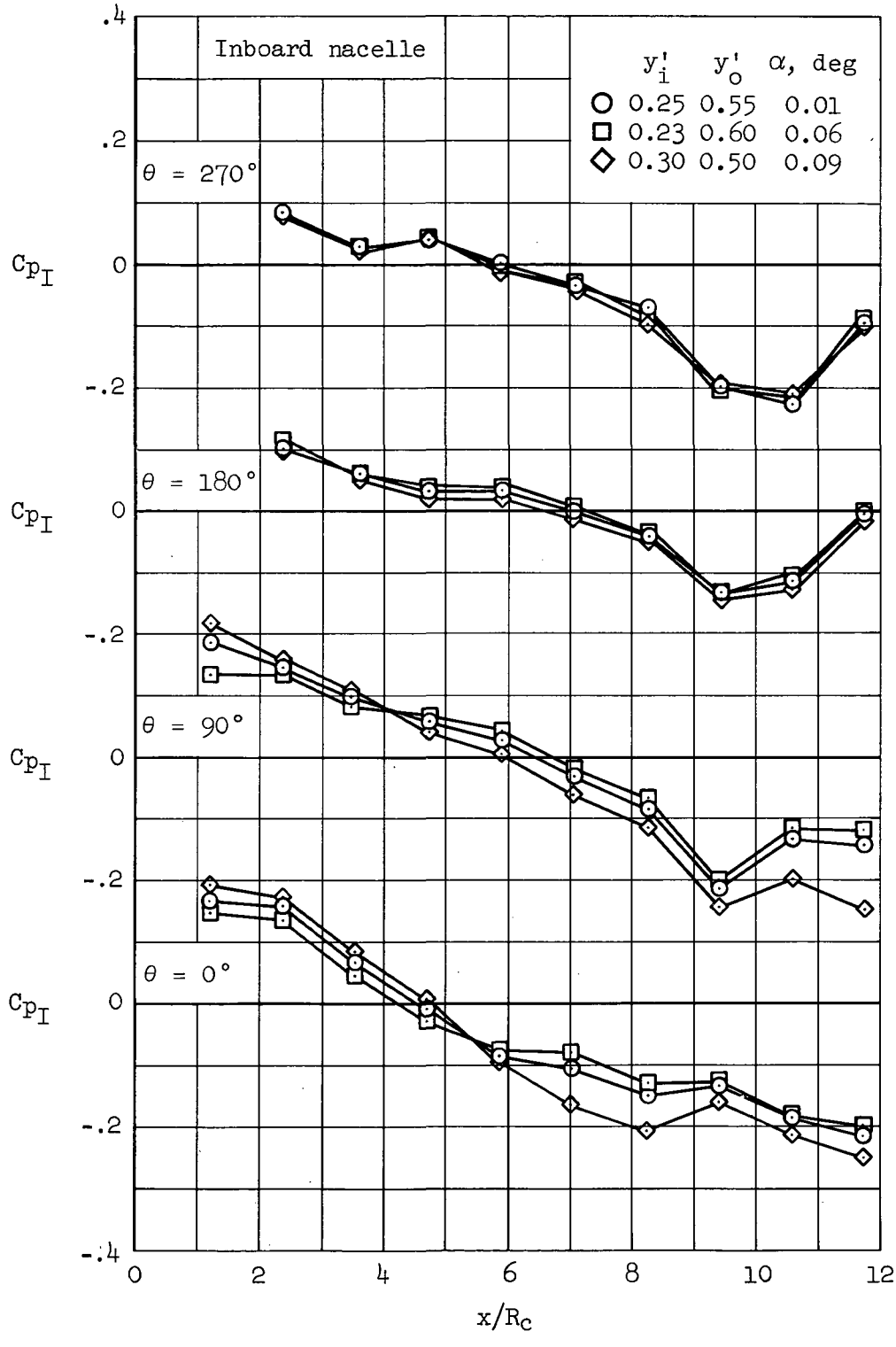

(c) Inboard nacelle, C_{p_I} at θ = 0°, 90°, 180°, 270°.

Figure 66.- Concluded.

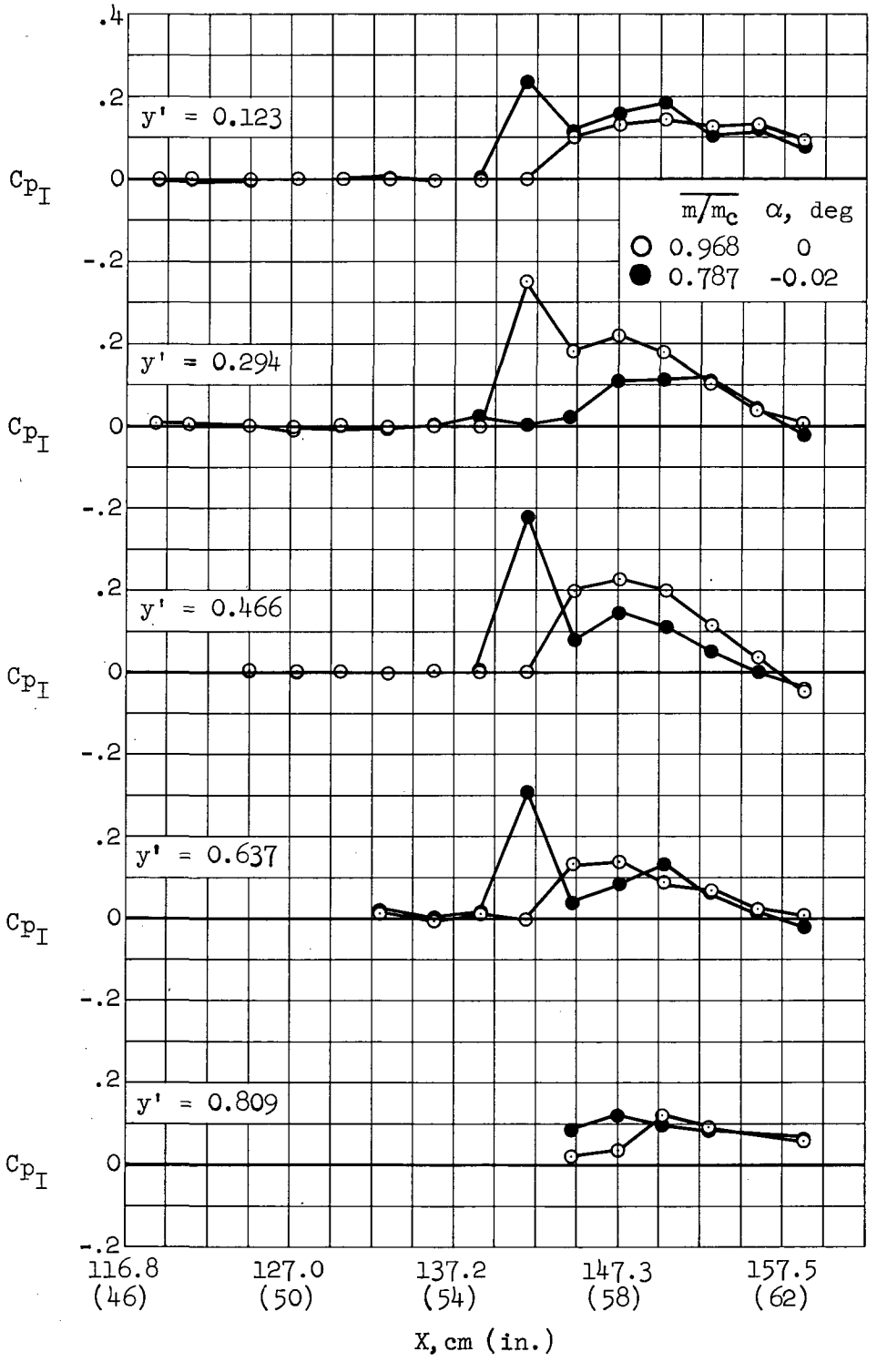

(a) $X_i = X_o = 142.2$ cm (56 in.)

Figure 67.- Lower wing surface interference pressure distributions at two nacelle mass flow ratios; configuration WBN_1N_1, $M_\infty = 1.15$, $y_i' = 0.25$, $y_o' = 0.55$.

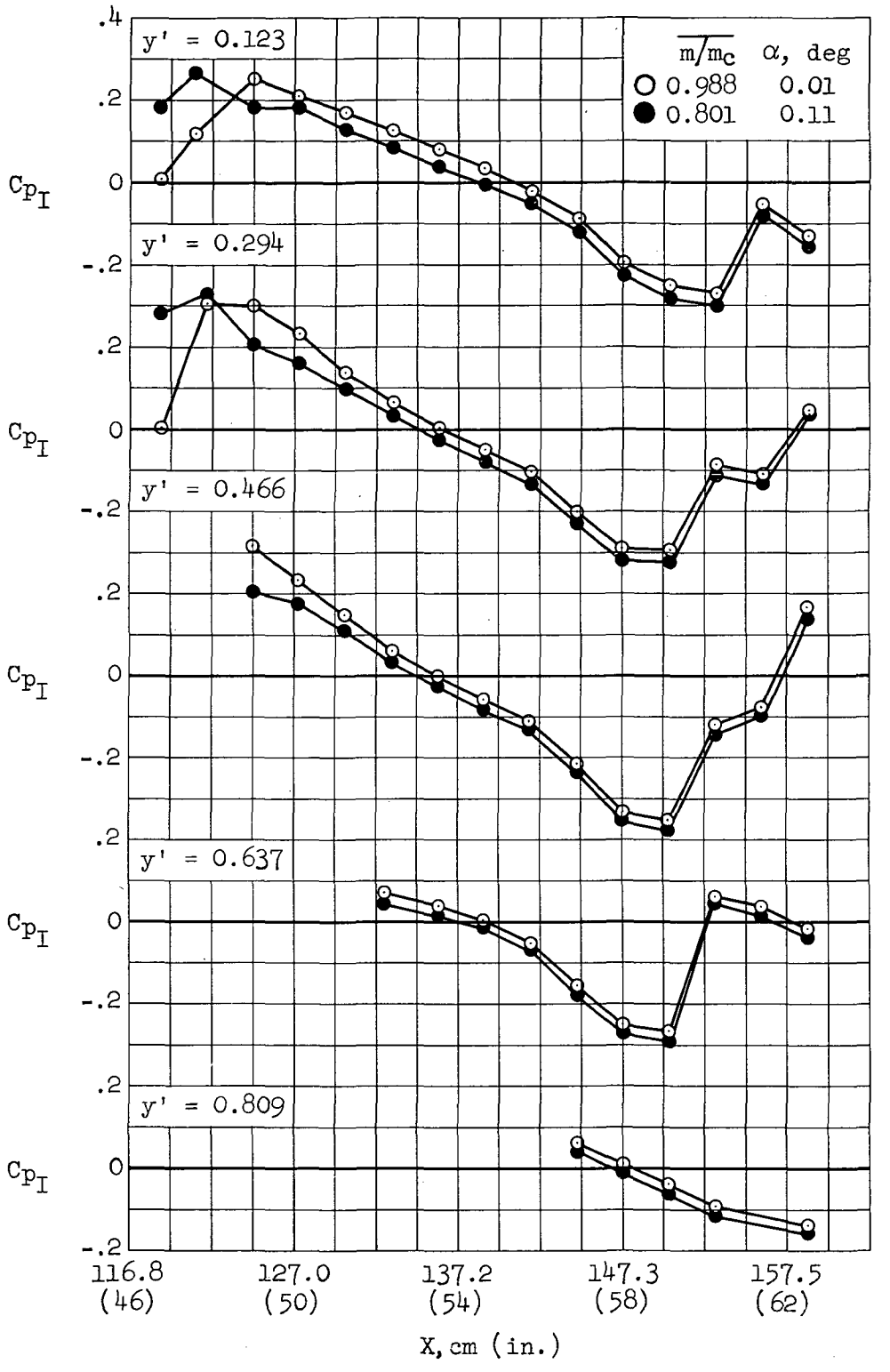

(b) $X_i = X_o$ = 121.9 cm (48 in.)

Figure 67.- Concluded.

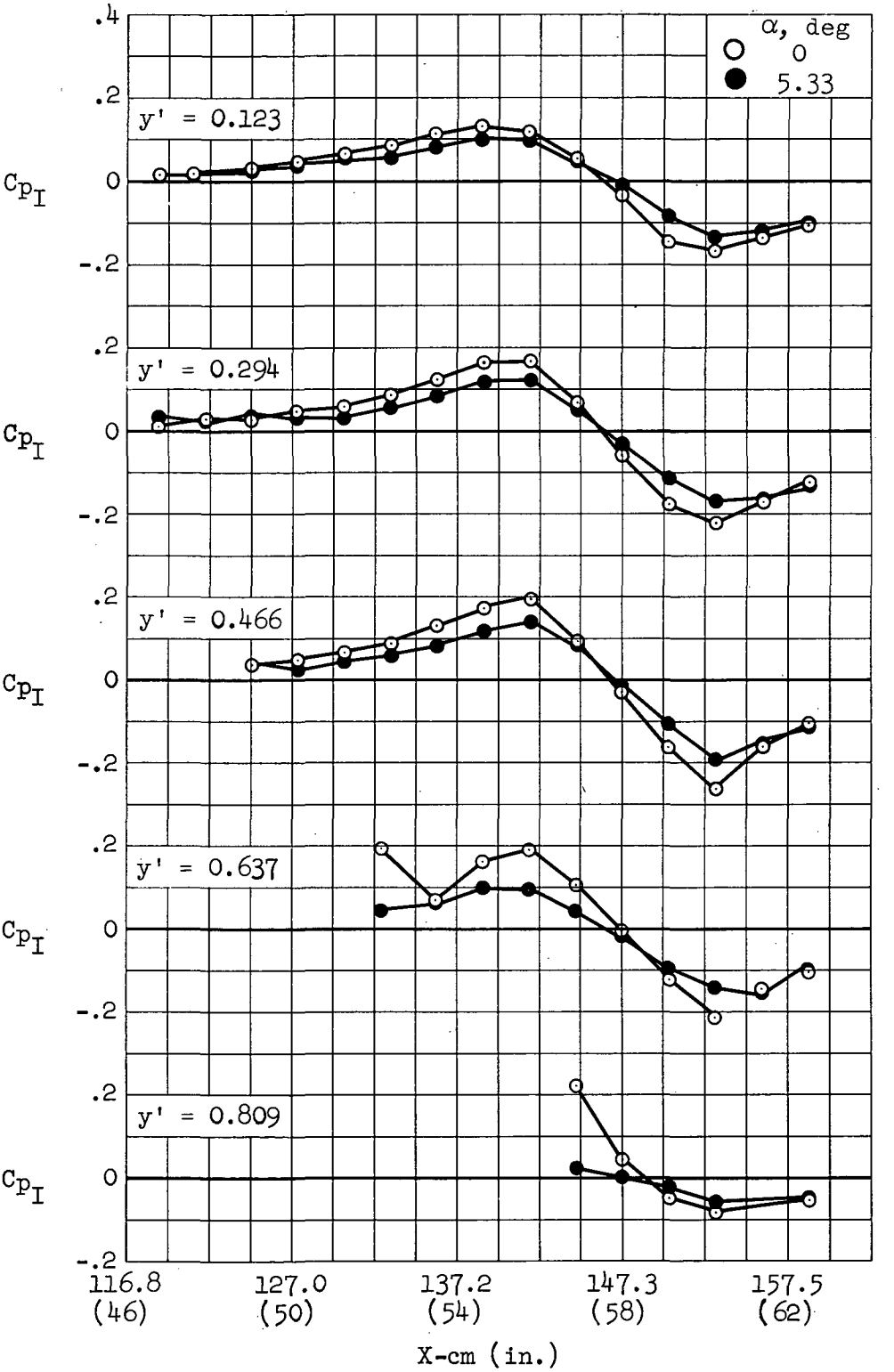

Figure 68.- Lower wing surface interference pressure distributions; configuration WBN_1N_1, $M_\infty = 0.90$, $y_i' = 0.25$, $y_o' = 0.55$, $X_i = X_o = 142.2$ cm (56 in.).

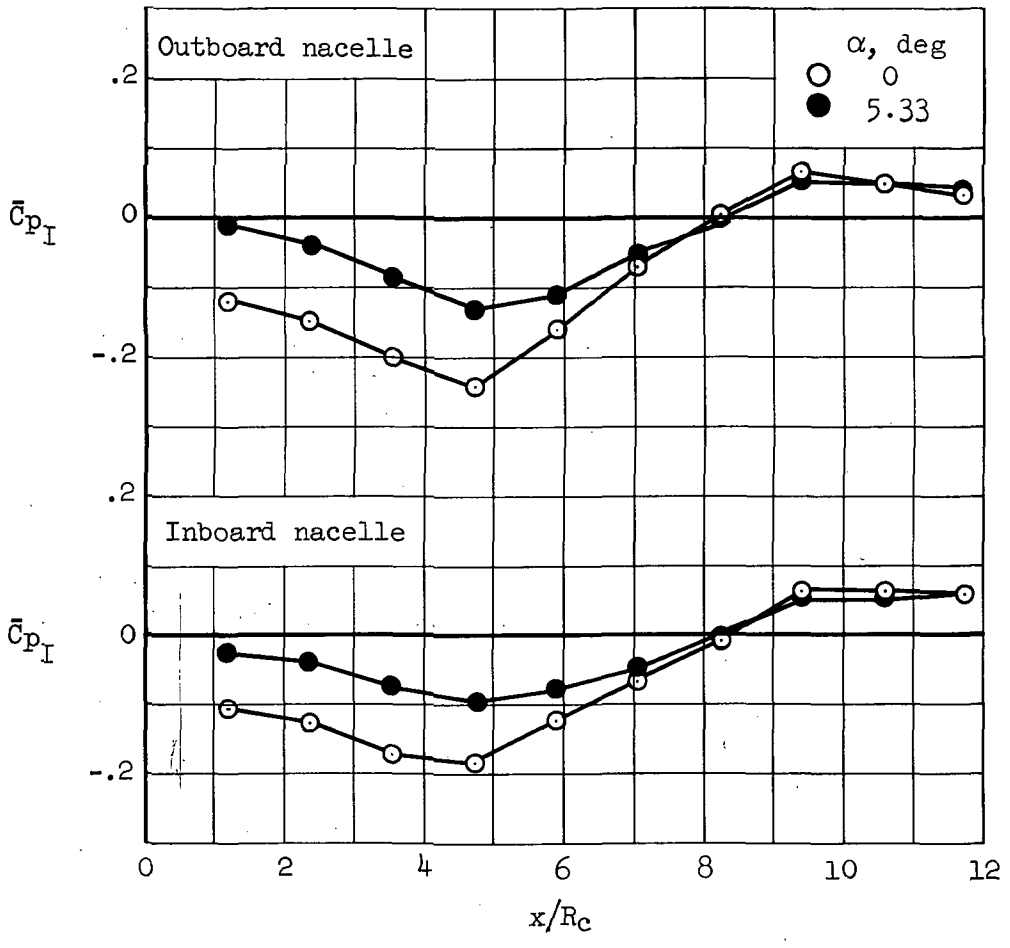

(a) $\bar{C}_{p_I}$, inboard and outboard nacelles.

Figure 69.- Nacelle interference pressure distributions; configuration WBN_1N_1, $M_\infty = 0.90$, $y_i' = 0.25$, $y_o' = 0.55$, $X_i = X_o = 142.2$ cm (56 in.).

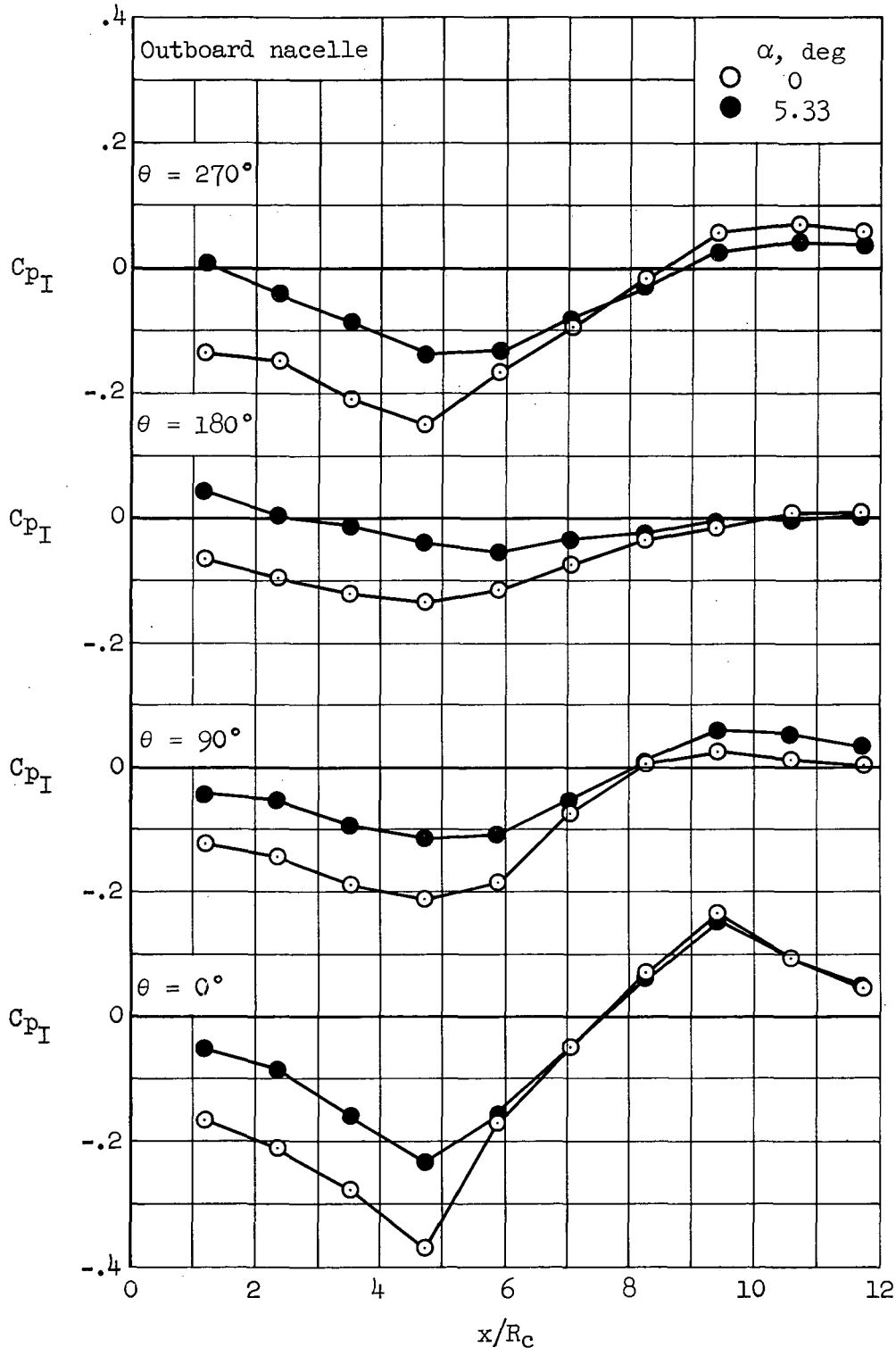

(b) Outboard nacelle, C_{p_I} at θ = 0°, 90°, 180°, 270°.

Figure 69.- Continued.

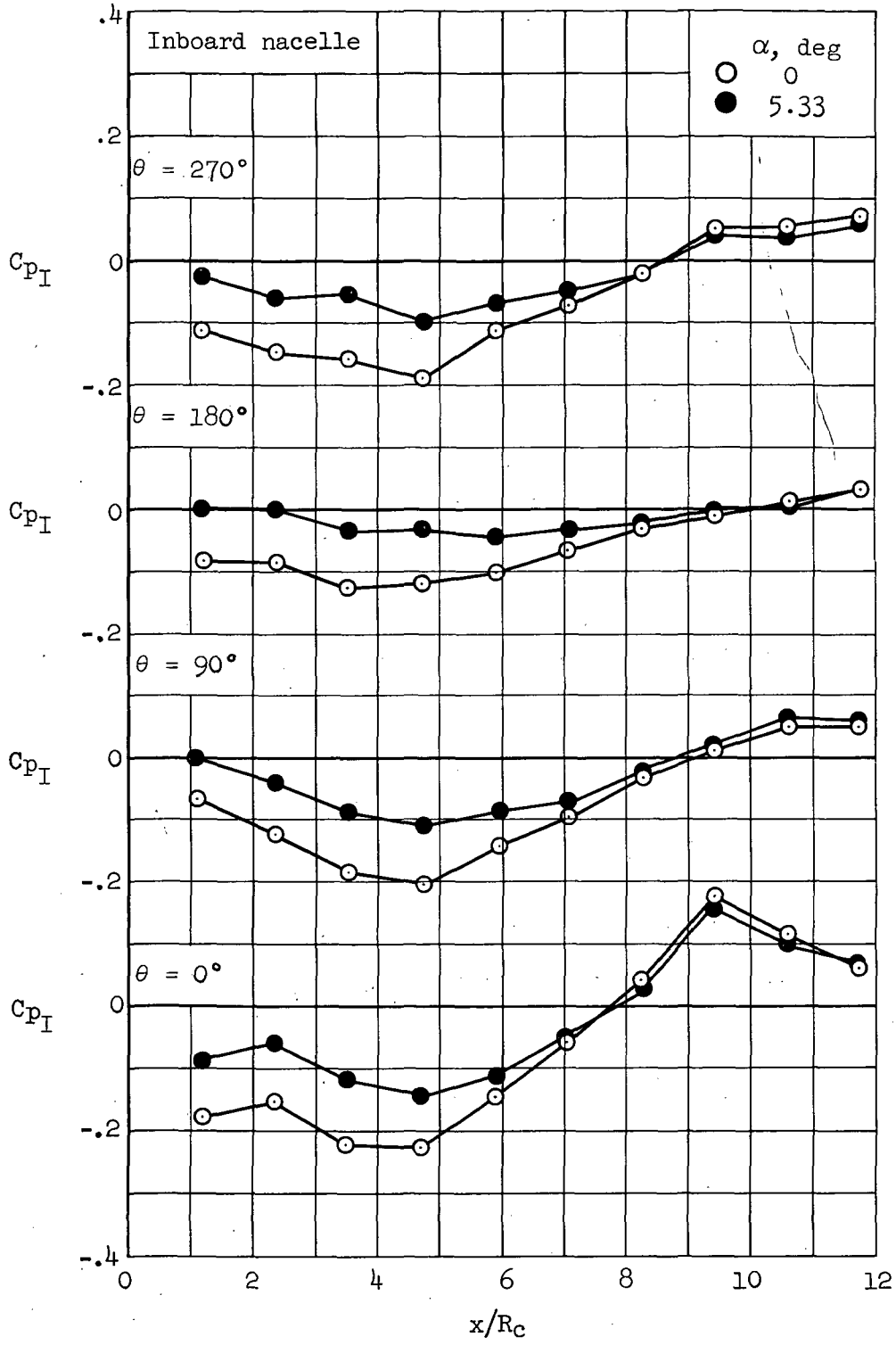

(c) Inboard nacelle, C_{p_I} at θ = 0°, 90°, 180°, 270°.

Figure 69.- Concluded.

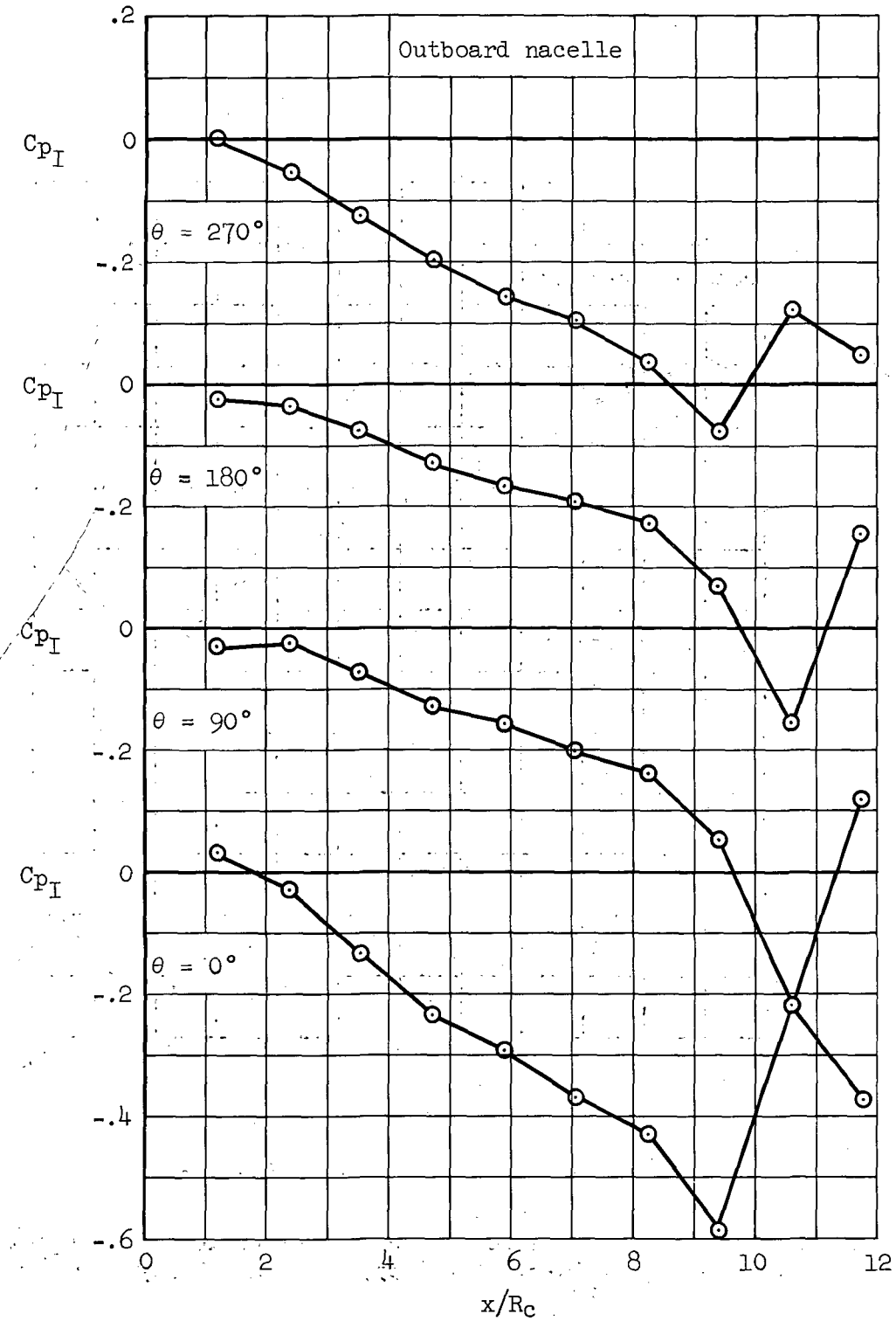

(b) Outboard nacelle, C_{p_I} at θ = 0°, 90°, 180°, 270°.

Figure 71.- Continued.

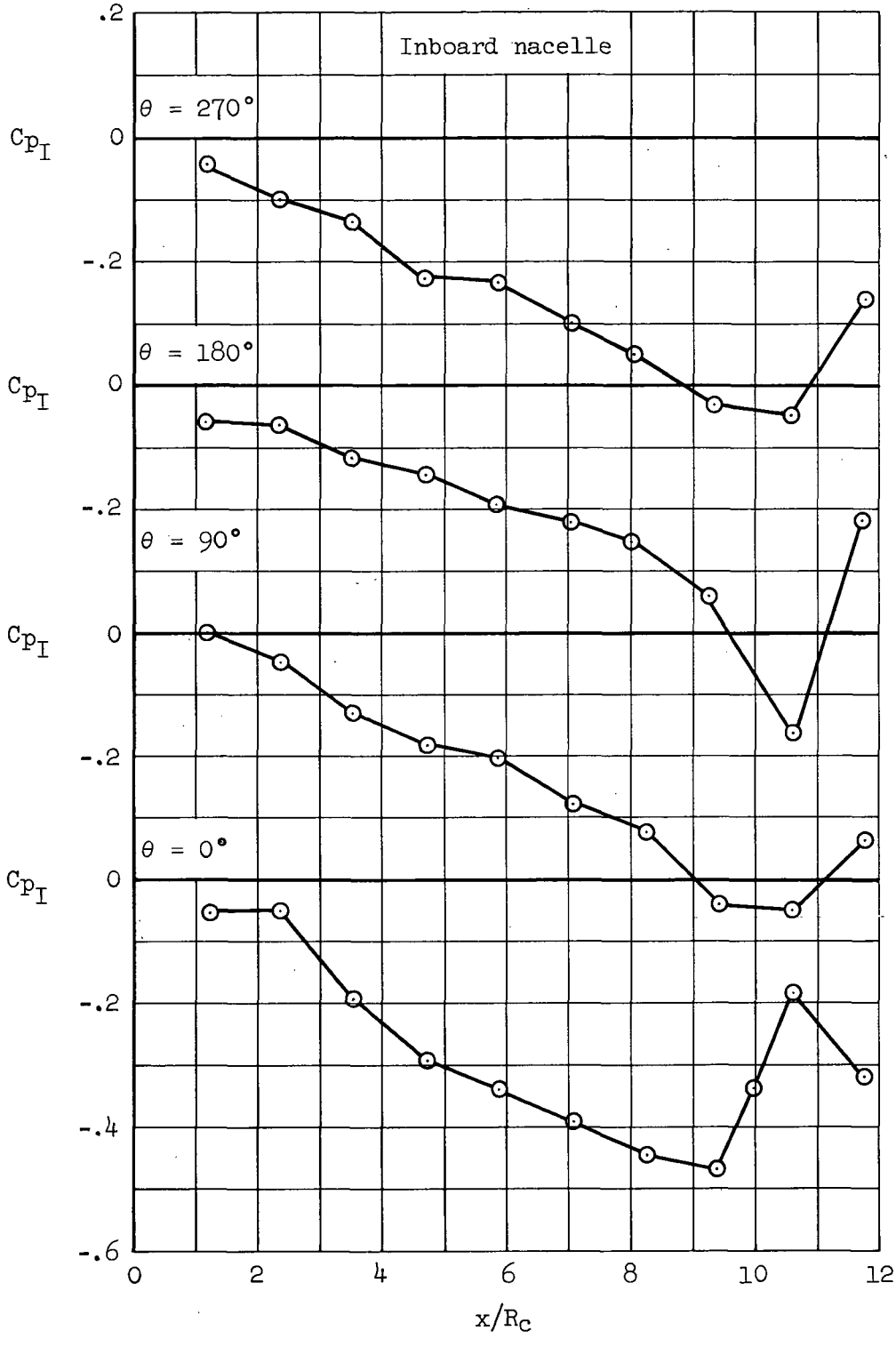

(c) Inboard nacelle, C_{p_I} at θ = 0°, 90°, 180°, 270°.

Figure 71.- Concluded.

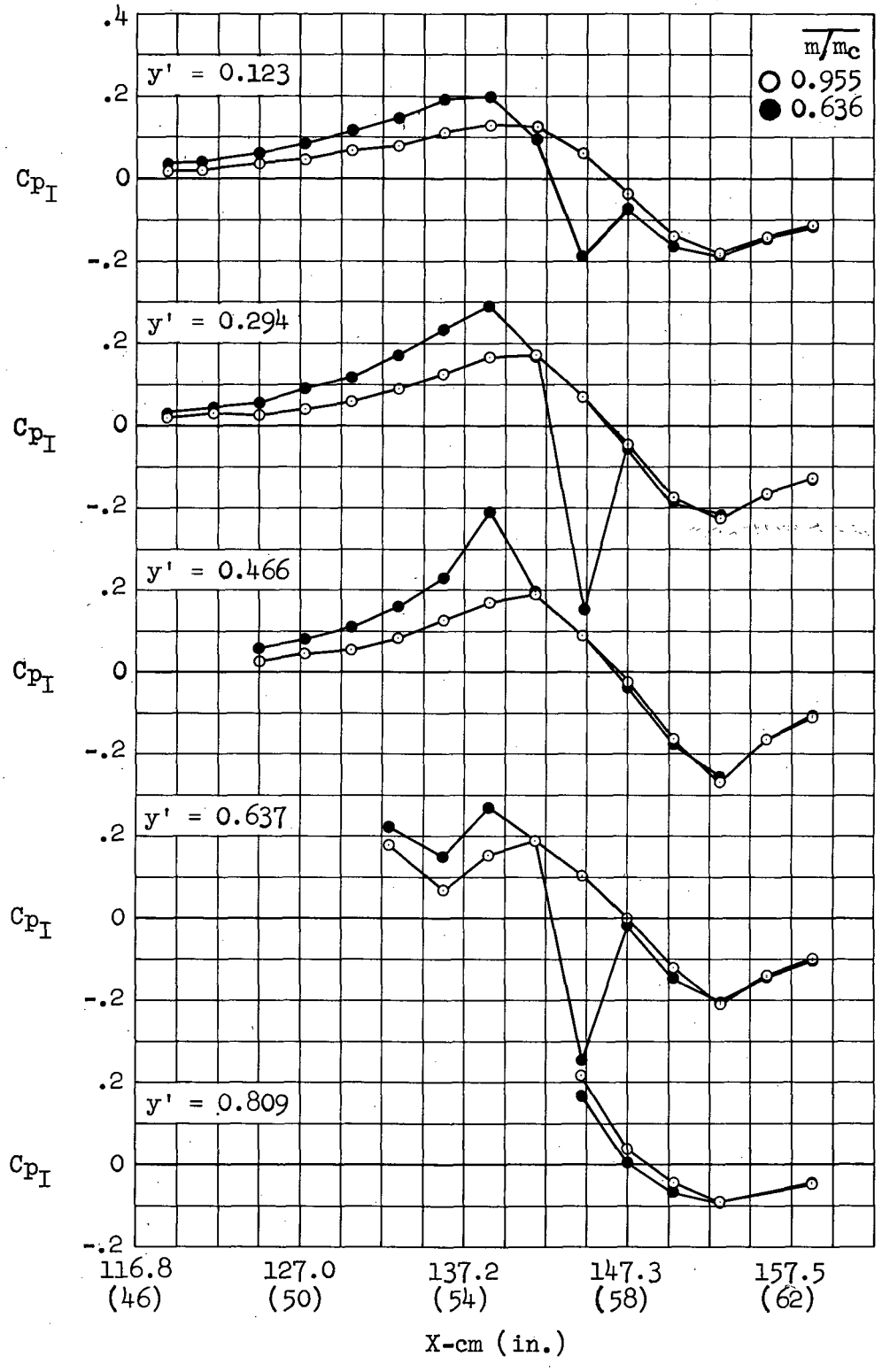

Figure 72.- Lower wing surface interference pressure distribution at two nacelle mass flow ratios; configuration WBN_1N_1, $M_\infty = 0.90$, $y_i' = 0.25$, $y_o' = 0.55$; $X_i = X_o = 142.2$ cm (56 in.).

NATIONAL AERONAUTICS AND SPACE ADMINISTRATION
WASHINGTON, D.C. 20546

OFFICIAL BUSINESS
PENALTY FOR PRIVATE USE $300

SPECIAL FOURTH-CLASS RATE
BOOK

POSTAGE AND FEES PAID
NATIONAL AERONAUTICS AND
SPACE ADMINISTRATION
451

U.S.MAIL

POSTMASTER : If Undeliverable (Section 15
Postal Manual) Do Not Retu

"The aeronautical and space activities of the United States shall be conducted so as to contribute . . . to the expansion of human knowledge of phenomena in the atmosphere and space. The Administration shall provide for the widest practicable and appropriate dissemination of information concerning its activities and the results thereof."

—NATIONAL AERONAUTICS AND SPACE ACT OF 1958

NASA SCIENTIFIC AND TECHNICAL PUBLICATIONS

TECHNICAL REPORTS: Scientific and technical information considered important, complete, and a lasting contribution to existing knowledge.

TECHNICAL NOTES: Information less broad in scope but nevertheless of importance as a contribution to existing knowledge.

TECHNICAL MEMORANDUMS: Information receiving limited distribution because of preliminary data, security classification, or other reasons. Also includes conference proceedings with either limited or unlimited distribution.

CONTRACTOR REPORTS: Scientific and technical information generated under a NASA contract or grant and considered an important contribution to existing knowledge.

TECHNICAL TRANSLATIONS: Information published in a foreign language considered to merit NASA distribution in English.

SPECIAL PUBLICATIONS: Information derived from or of value to NASA activities. Publications include final reports of major projects, monographs, data compilations, handbooks, sourcebooks, and special bibliographies.

TECHNOLOGY UTILIZATION PUBLICATIONS: Information on technology used by NASA that may be of particular interest in commercial and other non-aerospace applications. Publications include Tech Briefs, Technology Utilization Reports and Technology Surveys.

Details on the availability of these publications may be obtained from:

SCIENTIFIC AND TECHNICAL INFORMATION OFFICE

NATIONAL AERONAUTICS AND SPACE ADMINISTRATION

Washington, D.C. 20546